University of Alberta

Modification of the Stress-Strain Curve for High-Strength Line Pipe Steel

by

Katherine Jonsson

A thesis submitted to the Faculty of Graduate Studies and Research
in partial fulfillment of the requirements for the degree of

Master of Science
in
Materials Engineering

Department of Chemical and Materials Engineering

Spring 2013
Edmonton, Alberta

This page was intentionally left blank

Abstract

This thesis presents work performed to improve the work hardening behaviour of an X80 microalloyed steel through various Interrupted Thermal Treatments (ITT). The aim of this work was to determine the relationships between thermal history, microstructure and mechanical properties through both qualitative and quantitative measures. Prior to the ITT experiments, a continuous cooling transformation (CCT) diagram was constructed under no-strain conditions to identify the transformation temperatures and products that are achievable in X80 steel.

The thermal treatments were applied using a Gleeble thermal-mechanical simulator to generate a variety of microstructures in various fractions and morphologies. Scanning electron microscopy (SEM) and transmission electron microscopy (TEM) were used to investigate and quantify the microstructures in terms of phase fraction and grain size. The ITT experiments successfully generated microstructures comprised of ferrite, bainitic ferrite, martensite and martensite-austenite (M-A) without the addition of strain. The effect of cooling rates, interrupt temperature, re-heat temperature and hold times were investigated and the mechanical performance was correlated with the quantified microstructures. Although the ITT experiments did not improve the strength relative to a continuously cooled sample, the work hardening coefficient was increased as a result of the interrupted thermal treatments.

This page was intentionally left blank

Acknowledgements

There are several people that I would like to thank for their support, love, motivation and belief in me and my abilities. First and most importantly, I would like to thank Martin Kupsta. Not only was he directly involved in my work through TEM sample preparation, but he also supported my work and supported me throughout the stressful, emotional and lengthy writing process. He encouraged me out of my research slump and pushed me to accomplish more than I ever thought I could achieve. He has been an instrumental part of this work and I thank him for everything he has done to make me, and this thesis, the best that they can be.

I would also like to thank my family for their unwavering support and genuine belief in me. Even though they may not have understood the technical intricacies of my work, they were always interested; or at least they tolerated my rants and bouts of excitement over successful experiments. I never would have made it as far as I have without my family, and I acknowledge their contributions to my success in every aspect of my life.

Thank you, Dr. Ivey and Dr. Henein, for taking me on as a graduate student and for providing unequivocal and unmeasurable guidance and knowledge. I have enjoyed my experience in graduate school and I am thankful that I worked with two incredible supervisors. Dr. Ivey - thank you for the TEM work that became the cornerstone of this thesis. Thank you also for your constructive feedback, your

technical knowledge and, of course, the beer. Dr. Henein - thank you for always reminding me of the bigger picture, for encouraging my interaction with the global Materials community, and for always supporting my work through all the challenges we encountered.

I would like to thank my industry sponsors, Dr. Laurie Collins and Shahrooz Nafisi, for their invaluable expertise. Their comments, questions and feedback provoked further questions that stretched my mental capacity and helped me be more humble. They were gracious hosts and provided a wonderful facility for me to conduct experiments, and they never rejected my persistent requests for more samples, more SEM time and more tests. Thank you for challenging me and for helping me at every step of the way, even when we all didn't know the answers. I would also like to thank Lorne Good for his assistance with the Gleeble samples and for his guidance, mentorship and patience with repetitive polishing, etching and imaging iterations. Lorne was a exceptional colleague and I am truly thankful for his participation and input in this work.

I would like to thank Warren Poole and Thomas Garcin at the University of British Columbia for allowing me access to and for teaching me how to operate the Gleeble thermomechanical simulator.

For everyone else who supported me and respected my anti-social behaviour during the writing process, I thank you.

Contents

List of Symbols

α	Low temperature iron phase (ferrite) with bcc crystal structure
γ	Intermediate temperature iron phase (austenite) with fcc crystal structure
δ	High temperature iron phase (delta ferrite) with bcc crystal structure
Fe_3C	Iron carbide
A_{e1}	Upper boundary of the α–Fe_3C phase field under equilibrium conditions, units = [°C]
A_{e3}	Boundary between the α–γ and γ regions under equilibrium conditions, units = [°C]
A_{em}	Boundary between the γ and γ-Fe_3C phase fields under equilibrium conditions, units = [°C]
A_{c1}	Temperature at which the α to γ begins under cooling conditions, units = [°C]
A_{c3}	Temperature at which the α to γ is complete under cooling conditions, units = [°C]
B_1	Acicular ferrite with intralath or plate-like cementite, equivalent to lower bainite
B_2	Acicular ferrite with interlath particles of cementite and/or austenite films, equivalent to upper bainite

B_3 ..... Acicular ferrite containing a constituent of discrete austenite and/or martensite islands

M_s ..... Martensite start temperature, units = [°C]

M_f ..... Martensite finish temperature, units = [°C]

d ..... Mean grain diameter, units = [m]

d_0 ..... Initial mean grain diameter, units = [m]

K ..... Rate constant for grain growth equation, units = [m/s]

K_0 ..... Constant used to calculate K for grain growth modeling, units = [m/s]

Q_G ..... Activation energy for grain growth, units = [kJ/mol]

T ..... Temperature, units = [°C or K]

R ..... Ideal gas constant, units = [kJ/mol K]

σ_y ..... Yield strength, units = [MPa]

σ_0 ..... Yield strength of a single crystal of the same purity, units = [MPa]

k_y ..... Grain boundary strengthening coefficient

n ..... Work hardening coefficient

α_i ..... Half-angle of the oblique light rays that enter the front lens of the objective lens

n_i ..... Minimum refraction index of the material between the specimen and the lens

NA ..... Numerical aperture

λ ..... Wavelength of the incident light , units = [nm]

N_i ..... Number of intercepts/intersections counted on the field of view for grain size determination

L ..... Total length of the test line for grain size determination, units = [m]

M ..... Magnification of the image used for grain size determination

$\bar{l}$ ..... The mean linear intercept for the entire sample based on several field counts, units = [m]

l_i ..... The sum of the lineal intercepts for each area, units = [m]

n_g ..... The number of areas that were measured for grain size determination

n_{tot} ..... The number of grains that were counted for grain area calculation

s ..... The standard deviation of the individual measurements for grain size determination

E ..... Young's Modulus of elasticity, units = [GPa]

s ..... The standard deviation of the individual measurements for grain size determination

H_0 ..... Constant used for the Hall-Petch hardness relationship

K_H ..... Constant used for the Hall-Petch hardness relationship

σ_{eng} ..... Engineering stress, units = [MPa]

A_0 ..... Original cross sectional area of the tensile test piece, units = [m^2]

F ..... Instantaneous uniaxial load during tensile testing, units = [N]

ϵ_{eng} ..... Engineering strain, units = [mm/mm]

l ..... Measured extension during tensile testing, units = [mm]

l_0 ..... Original gauge length of the tensile test specimen, units = [mm]

σ_{true} ..... True stress, units = [MPa]

ϵ_{true} ..... True strain, units = [mm/mm]

f ..... Fraction transformed

y_T ..... Experimental dilation value at a given temperature T, units = [mm]

$y_{1(T)}$ ..... Dilation value of the low tangent (α region) at temperature T, units = [mm]

$y_{2(T)}$ ..... Dilation value of the high tangent (γ region) at temperature T, units = [mm]

List of Abbreviations

CCT	Continuous Cooling Transformation
ITT	Interrupted Thermal Treatment
HOP	Heat-treatment Online Process
SEM	Scanning Electron Microscopy
TEM	Transmission Electron Microscopy
fcc	Face Centered Cubic
bcc	Body Centered Cubic
bct	Body Centered Tetragonal
M-A	Martensite-Austenite constituent
SE	Secondary Electrons
BSE	Back Scattered Electrons
TEC	Thermal Expansion Coefficient
AF	Acicular Ferrite
GB	Granular Bainite

UTS ..... Ultimate Tensile Strength

YS ..... Yield Strength

TMCP ..... Thermo-Mechanical Controlled Process(ing)

HSLA ..... High Strength Low Alloy

UHV ..... Ultra High Vacuum

FE ..... Field Emission

EBSD ..... Electron Back Scattered Diffraction

FIB ..... Focused Ion Beam

BF ..... Bright Field

DF ..... Dark Field

EDX ..... Energy Dispersive X-ray Spectroscopy

SAD ..... Selected Area Diffraction

ZA ..... Zone Axis

DP ..... Diffraction Pattern

List of Tables

This page was intentionally left blank

List of Figures

Chapter 1

Introduction

The demand for high strength line pipe steel for arctic pipeline applications such as the MacKenzie Valley pipeline has increased substantially in recent years. Microalloyed steels are prime candidates for such applications due to their high yield and ultimate strengths, good weldability, good toughness at low temperatures, excellent strain hardening behaviour and corrosion resistance. A high degree of work hardening is desirable for strain-based pipeline steels due to the high levels of compressive and tensile stresses that result from ground movements in permafrost regions. Buckling resistance is achieved with a high work hardening coefficient and a round stress-strain curve and, as a result, is highly dependent on microstructure. Studies performed by JFE Steel suggest that an on-line heat treatment process between accelerated cooling and rolling procedures facilitates a fine-grained dual-phase microstructure that increases the work hardening coefficient while maintaining a high yield strength [Nobuyuki 06, Mitsuhiro 08, Shikanai 08]. This thesis presents research exploring the effect of interrupted thermal treatments (ITT) on the microstructure development and resulting mechanical properties for a microalloyed steel in efforts to enhance work hardening characteristics. The goal

of this study was not to replicate the results presented by JFE Steel, but rather to determine whether the microstructure could be manipulated and controlled using thermal treatments under no strain conditions. The microalloyed steel investigated in this work was an X80 grade (where 'X' refers to pipeline grade steel and '80' refers to the minimum yield strength requirement of 80 ksi or 550 MPa).

Chapter 2 provides theoretical background on microalloyed steels, including the historical development and current processing techniques used to enhance strength, toughness and work hardening characteristics. The relationships between processing techniques and microstructure are discussed, as are the relationships between microstructure and mechanical properties. Furthermore, an introduction to the important experimental techniques are introduced and the project goals are defined.

Chapter 3 details the experimental techniques and results for the development of the continuous cooling transformation (CCT) diagram for the X80 steel used in this study. The dilatometry techniques used to determine transformation temperatures during continuous cooling are discussed and the results are compared with the microstructures observed for each sample. An in-depth microstructural investigation using transmission electron microscopy (TEM) is presented and the results are used to correctly identify individual constituents in the microstructure. The microstructures are quantified using image analysis techniques and the grain size is also determined according to ASTM E112 [AST 10]. The hardness values are presented and compared with the microstructures for each cooling rate.

Chapter 4 presents the experimental conditions and results for the ITT trials. The microstructures are presented and discussed using both qualitative and quantitative measures. The grain size and phase fractions for each sample were determined and the effect of thermal treatment on microstructural development is addressed. The hardness and tensile data for each ITT specimen are included and the relation-

ships between microstructure and mechanical performance is discussed.

Chapter 5 provides a summary of the research presented in this thesis and the future work that would be explored. Important conclusions are presented and discussed with particular focus on the mechanical performance of the ITT trials and the successful generation of a multi-phase microstructure under conditions of no strain.

Appendices A through F include supplementary information that was not included in the bulk of the thesis. Appendix A presents the isothermal transformation kinetics for the ITT specimens. Appendix B details the color metallography and ion etching experiments and Appendix C presents the nanoindentation results. Appendices D and E include the complete set of scanning electron microscope (SEM) micrographs are included for both the CCT curve and the ITT trials, respectively. The phase quantification procedure using image analysis is specified in Appendix F.

This page was intentionally left blank

Chapter 2

Theory and Background

2.1 Steel

Steel is one of the most important materials used in engineering design due to its low cost, good mechanical properties (including high strength, toughness and ductility) and wide applicability in numerous industrial sectors. As a basic definition, steel is an alloy containing a minimum of 50 wt% iron and at least one alloying element such as carbon, manganese, silicon, nickel, vanadium, titanium, niobium, chromium, molybdenum and other trace elements [Vander Voort 92]. Various combinations of alloying elements are added to achieve different properties such as corrosion resistance, increased strength and increased toughness. There are numerous classification systems for steel based on chemistry, manufacturing, product type, microstructure, strength requirements and heat treatment [Krauss 05].

2.1.1 Iron-Carbon Phase Diagram

In order to understand the numerous types of steels, it is first necessary to understand the basic constituent of steel; more specifically, the iron-carbon phase

diagram. The iron-carbon phase diagram is an equilibrium diagram, which means that the lines and temperatures are theoretical in nature as they were obtained from infinitely slow heating and cooling cycles to simulate near-equilibrium conditions. Furthermore, the phase diagram is a thermodynamic representation of the solubility of carbon in iron. As a result, the kinetics of phase transformations are ignored and only the thermodynamically permitted reactions are shown.

Iron as a pure element has two stable crystal structures: α-ferrite, which exists as a body-centered cubic (bcc) structure between room temperature and 912 °C (1675 °F); and γ-iron, also known as austenite, which is a face-centered cubic (fcc) phase that is stable between 912 °C (1675 °F) and 1394 °C (2540 °F). There is also a high temperature bcc structure known as δ-ferrite, which is stable from 1394 °C (2540 °F) to the melting point of iron which occurs at 1530 °C (2785 °F) [Bramfitt 98]. These solubility temperatures apply to iron with no carbon added; the addition of carbon varies the temperatures which will be discussed shortly. Fcc austenite is a closer packed structure than α-ferrite and, as such, is more dense. The austenite to α-ferrite transformation therefore results in a volume increase.

Ferrite can exist in multiple forms, such as acicular ferrite or bainitic ferrite. Acicular ferrite is generally defined as "a highly substructured, non-equiaxed ferrite that forms in continuous cooling by a mixed diffusion and shear mode of transformation that begins at a temperature slightly higher than the upper bainite transition temperature" [Krauss 05]. Bainitic ferrite is ferrite that contains small lath-like structures but does not contain iron carbides (which would be true for bainite). More specifically, bainitic ferrite "consists of packets of parallel ferrite laths (or plates) separated by low-angle boundaries (which contain) very high dislocation densities" [Cizek 01].

Carbon is added to steel to provide strength through precipitation hardening,

solid solution hardening and transformation behaviour. It is the principal hardening element in all steel products [Krauss 05]. Alloys containing less than 2 wt% carbon are arbitrarily classified as steels. Most carbon steels contain less than 1 wt% carbon and in fact the largest percentage of steels manufactured contain only 0.2 - 0.3 wt% carbon [Abbaschian 94]. The low carbon content is maintained to ensure high ductility, high toughness and good weldability. High carbon contents are detrimental to weld quality due to the formation of a hard and brittle metastable phase known as martensite.

Carbon is an austenite stabilizer and, as such, extends the temperature range in which austenite is stable. The solubility of carbon is higher in austenite (2.11 wt%) than in ferrite (0.0218 wt%), and is temperature-dependent for both phases. When the solubility of carbon in the ferrite lattice is exceeded, a new phase is created, termed cementite or iron carbide (Fe_3C), which has an orthorhombic crystal structure. The temperature dependence of carbon solubility in ferrite and austenite accounts for the wide array of microstructures that is observed in steel products.

Figure 2.1 shows the partial Fe-C phase diagram for carbon concentrations up to 6.67 wt% carbon , which is the carbon concentration corresponding to Fe_3C. Fe_3C is a metastable phase; therefore, Figure 2.1 is a metastable phase diagram, although it is used as if it were a stable equilibrium phase diagram. The solid lines indicate the Fe-C phase diagram and the dashed lines show the Fe-graphite phase diagram, which will not be discussed here. Another view of the Fe-C diagram illustrating the carbon solubility in ferrite (up to 0.025 wt%) as a function of temperature is shown in Figure 2.2 [Bramfitt 98, Krauss 05].

The lowest temperature for which austenite is stable under equilibrium conditions is 727 °C (depending on composition) and, as such, austenite must transform to other phases and microconstituents upon cooling. According to Figure 2.2, slow

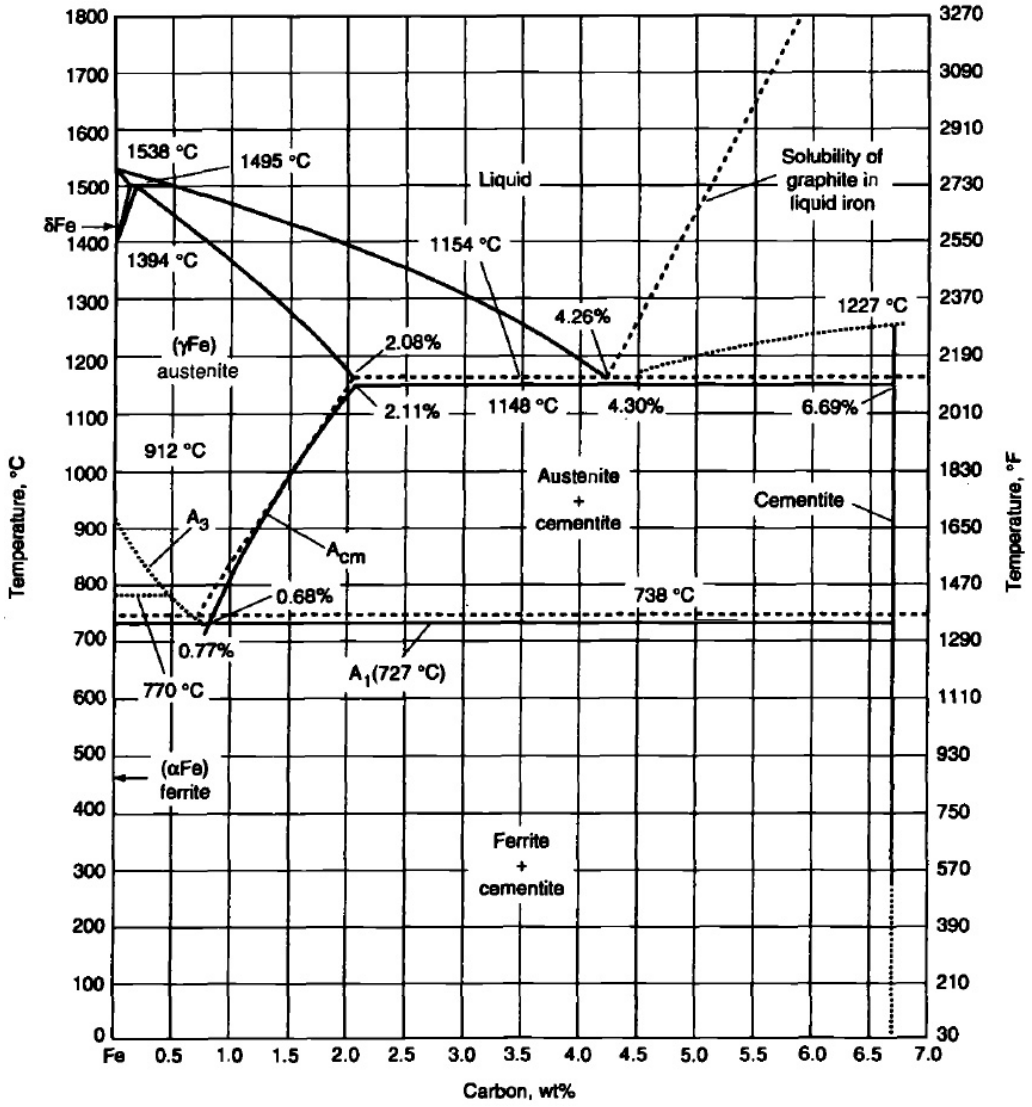

Figure 2.1: Fe-Fe_3C equilibrium phase diagram [Bramfitt 98].

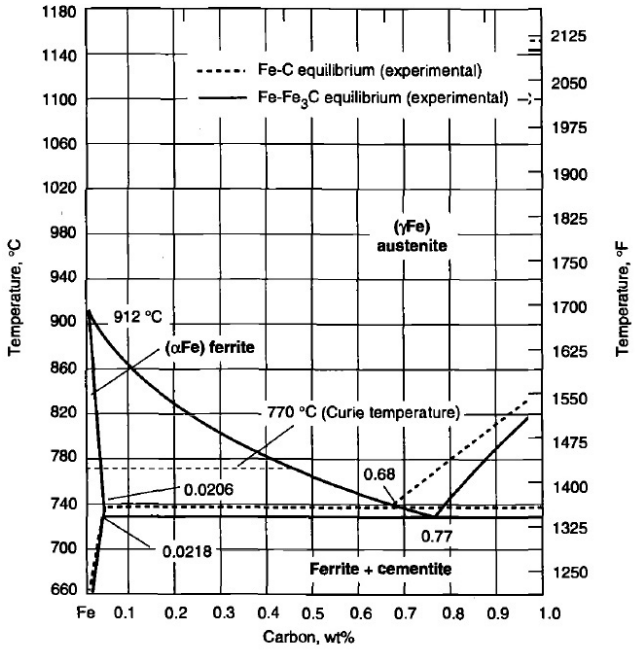

Figure 2.2: Carbon solubility in ferrite in Fe-Fe_3C phase diagram [Krauss 05].]

cooling of austenite will form mixtures of ferrite and cementite. Other transformation products such as martensite and bainite are attainable from cooling austenite to lower temperatures, and will be discussed in the next section. These transformation products are the result of diffusion-controlled or diffusionless processes that occur outside of equilibrium conditions. The phase fields identified in Figure 2.1 include boundaries that are determined by carbon content as a function of temperature. These boundaries are labeled as "A" and indicate changes in slope or thermal arrests in the heating and cooling curves. Under equilibrium conditions, the subscript 'e' is included. For example, A_{e1}, A_{e3} and A_{ecm} (or simply A_1, A_3, and A_{cm}) indicate the upper boundary of the ferrite-cementite phase field (727 °C in Figure 2.1), the boundary between the ferrite-austenite and austenite regions (the curved line between 912 °C and 727 °C in Figure 2.1) and the boundary be-

tween the austenite and austenite-cementite phase fields (from 1148 °C to 727 °C in Figure 2.1), respectively. During heating conditions, the subscript 'c'[1] is used, whereas the subscript 'r'[2] corresponds to cooling conditions. The critical temperature during heating is higher than the equilibrium temperature and, similarly, the critical temperature during cooling is less than the equilibrium temperature due to the non-equilibrium conditions, which is due to the insufficient amount of time required for diffusion-controlled transformations (such as the austenite to ferrite transformation) [Bramfitt 98].

The addition of alloying elements affects the phase fields shown in Figure 2.1. Elements such as manganese and nickel are austenite stabilizers, which suppress the critical temperatures and increase the size of the stable austenite zone. Other elements, including silicon, chromium and molybdenum, are ferrite stabilizers and also promote the formation of stable carbides [Bramfitt 98]. Ferrite stabilizers increase the critical temperatures and hence decrease the size of the stable austenite zone. Microalloying elements including titanium, niobium and vanadium are strong carbide, nitride and carbonitride formers in the austenite region. The solubility of carbides, nitrides and complex carbonitrides is highly temperature dependent [Krauss 05]. It is therefore important to understand the chemistry of the steel product to understand how alloying additions affect the location of the phase field boundaries.

2.1.2 Microconstituents

As mentioned in Section 2.1.1, there are numerous transformation products that can form when austenite is cooled below the critical transformation temperature, including pearlite, bainite and martensite. Ferrite is a solid solution of iron with car-

[1] derived from the French word chauffant
[2] derived from the French word refroidasant

bon (interstitial solid solution) or other alloying elements such as silicon, chromium, manganese and nickel (substitutional solid solution) [Krauss 05]. Ferrite is a phase, whereas other products such as pearlite and bainite are microconstituents. Martensite is a low-temperature transformation product that is a metastable phase and, as such, does not appear on the Fe-C phase diagram. The various transformation products that can be observed in microalloyed steels will be discussed in the following sections.

Pearlite

Pearlite is a microconstituent that contains repeating platelets of ferrite and cementite that align with the same orientation within a single grain. Under equilibrium conditions, austenite decomposes into pearlite via solid-state reaction when a steel is cooled through the eutectoid temperature (727 °C). Within one colony of pearlite, the ferrite and cementite phases have similar crystallographic orientation and, as such, pearlite can be considered to be two interpenetrating single crystals [Krauss 05]. Pearlite forms by diffusion, which is a time-dependent process and generally forms during slow cooling conditions. It is possible, however, to generate pearlite in faster cooling rates since carbon can still diffuse from ferrite regions towards cementite regions; however, this process occurs at a lower temperature than 727 °C (i.e., under non-equilibrium conditions).

Pearlitic steels have high strength, high hardness and good wear resistance due to the combination of the cementitite and ferrite phases, but the ductility and toughness of these steels are quite low. As previously mentioned, carbon is added to steel to increase the both the yield strength (YS) and ultimate tensile strength (UTS). For ferrite-pearlite steels, increasing the carbon content significantly increases the UTS but does not have a large impact on the YS [Krauss 05]. The UTS increases

with carbon content due to the increased volume fraction of pearlite which has a much higher tensile strength than ferrite due to the added cementite particles. The YS remains unaffected, however, since yielding in ferrite-pearlite steels is dictated by the ferrite phase rather than pearlite. As a result, increasing the volume fraction of pearlite does not affect the mechanism of yielding in the ferrite matrix and, thus, the YS is not significantly affected. Equations have been developed to predict the relationship between alloy content, grain size and strength for pearlitic steels; however, these relationships are discussed elsewhere [Krauss 05].

Bainite

Bainite is another microconstituent that contains ferrite and cementite. The ferrite is present as acicular entities and the iron carbides are discrete particles rather than combined in lamellae as for pearlite. At lower temperatures, the short-range carbon atom diffusion which is necessary for pearlite formation cannot occur; as a result, the transformation mechanism changes from diffusion-controlled to shear or displacement-controlled. The ferrite grains become elongated and jagged while the cementite particles are no longer lamellar but rather form sharp needles [Bramfitt 98]. There are many different morphologies of bainite; the most basic classification limits the microstructures to either upper bainite or lower bainite [Bramfitt 98]. Upper bainite is considered to be the microconstituent that forms isothermally between 400 and 550 °C, whereas lower bainite forms between 250 and 400 °C [Bramfitt 98]. The morphological difference between upper and lower bainite lies in the location of cementite particles. In upper bainite, iron carbide forms at the lath boundaries and results in a coarse structure with large carbides. Lower bainite contains iron carbide particles that form within the laths on certain crystallographic habit planes and, as such, has a finer structure than upper bainite. This classifi-

cation system is specifically related to the isothermal temperature at which bainite formed and does not consider the bainitic morphologies that form during continuous cooling. As a result, another characterization system was introduced whereby bainite was divided into the following three categories: Class 1 (B_1; acicular ferrite with intra-lath or plate-like cementite, equivalent to lower bainite), Class 2 (B_2; acicular ferrite with inter-lath particles of cementite and/or austenite films, equivalent to upper bainite) and Class 3 (B_3; acicular ferrite containing a constituent of discrete austenite and/or martensite islands) [Bramfitt 98]. Bainitic steels demonstrate high strength and good toughness through both a high dislocation density and a small effective grain size within the bainite/acicular ferrite matrix [Bramfitt 98].

Multi-phase, or dual-phase, steels are essentially composites of a fine-grained polygonal ferrite matrix (responsible for high toughness) and a second 'phase' (bainite and/or martensite islands) for strength. The polygonal ferrite phase is typically 80 to 90 volume % while the bainite or martensite islands are dispersed through the matrix at a volume fraction of 10 to 20 % of the microstructure [Bramfitt 98].

Martensite

Martensite is not a constituent but rather a metastable phase that forms in plain carbon and low alloy steel products. Martensite is a supersaturated solid solution of interstitial carbon in iron that forms at very high cooling rates (approximately 1000 °C/min depending on the presence of alloying elements) by a shear (diffusionless) transformation. Elements such as manganese, nickel, chromium and molybdenum enhance hardenability (the ability to form martensite) and promote the formation of a hard martensitic structure. A large number of atoms shear in a cooperative motion and act parallel to a fixed crystallographic plane, or habit plane, which is distorted with respect to the parent austenite phase. Martensite contains

a very high dislocation density or twins which creates a very fine needle-like structure [Bramfitt 98]. The amount of carbon in martensite is far greater than what is observed in ferrite for plain carbon steels; however, the amount of carbon in both martensite and ferrite is similar for low-alloy steels such as microalloyed steels. In plain carbon steel martensite, the bcc lattice of ferrite is distorted to accommodate the extra carbon atoms and becomes body centered tetragonal (bct). The combined effect of the extra carbon atoms squished into the lattice and the very fine and highly dislocated structure leads to the high strength and corresponding low ductility of martensite. Similar to bainite, there are various morphologies of martensite depending on the carbon content of the alloy. Lath martensite forms in low- and medium-carbon steels, and consists of highly dislocated parallel lath-shaped needles with retained austenite located between the laths. Plate martensite, which is observed in high-carbon steels, has a large amount of retained austenite with very fine martensite plates that contain transformation twins. Martensite begins to form at a distinct temperature, termed the martensite start temperature (M_s), and ends at another critical temperature (martensite finish temperature, denoted by M_f). The M_s temperature is highly dependent on the steel chemistry. Carbon substantially suppresses the M_s temperature whereas other alloying elements only slightly lower the M_s temperature.

Martensite-Austenite (M-A)

Another important constituent present in steel products is martensite-austenite, or M-A. Carbon diffusion out of ferrite into adjacent austenite grains causes subsequent martensite formation with retained austenite upon cooling. Increasing the solute content (i.e., richer steel chemistries) causes an increase in M-A islands [Krauss 05]. M-A may also form in carbon-enriched austenite regions that

have become locally entrapped between regions of ferrite [Cizek 01].

M-A is typically associated with a loss in toughness since it is a very hard and brittle constituent and therefore initiates brittle fracture [Mitsuhiro 08]. The morphology of the M-A particles is actually found to play a more important role than the presence of M-A in the microstructure. Granular M-A particles do not initiate brittle fracture whereas elongated M-A regions (typically observed in the heat-affected zone of welded structures) are detrimental to toughness. The amount of alloying additions (more specifically, carbon, silicon and aluminium) must be limited in order to suppress M-A formation to prevent weld toughness degradation. If M-A is used as a second constituent (the hard constituent in a soft matrix in dual-phase steels), it is important to maintain a fine and equiaxed morphology of M-A particles to minimize the toughness degradation that is associated with the M-A microconstituent [Shikanai 08].

M-A commonly takes one of two morphologies: small, globular islands or thin, stringy shapes. An example of the globular M-A islands is shown in Figure 2.3 [Han 12]. Figure 2.3 shows two scanning electron microscopy (SEM) secondary electron (SE) images of two different X80 steels with similar chemical composition but slightly different processing parameters. The microstructures shown in Figure 2.3a and b consist of M-A islands (denoted by MA), acicular ferrite (AF) and granular bainite (GB) [Han 12]. The M-A particles are small (approximately 2 - 5 μm) and have a slightly elongated shape. Furthermore, the M-A islands are typically observed along grain boundaries.

An example of stringy M-A particles is shown in Figure 2.4 [Lan 12]. The author describes the M-A islands as having a "conspicuous character of slender shape" with a high aspect ratio (the length to width ratio for elongated structures) [Lan 12].

As previously mentioned, the morphology of M-A particles is more significant

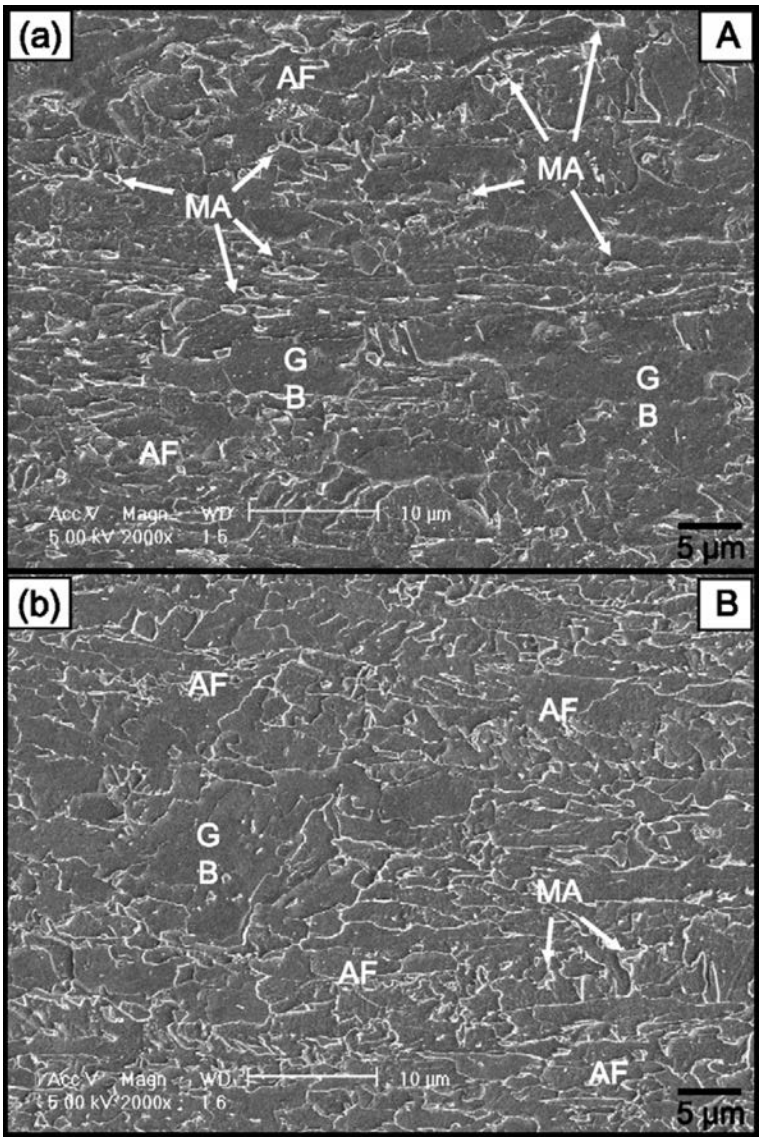

Figure 2.3: SEM SE images showing M-A islands (MA), acicular ferrite (AF) and granular bainite (GB) [Han 12].

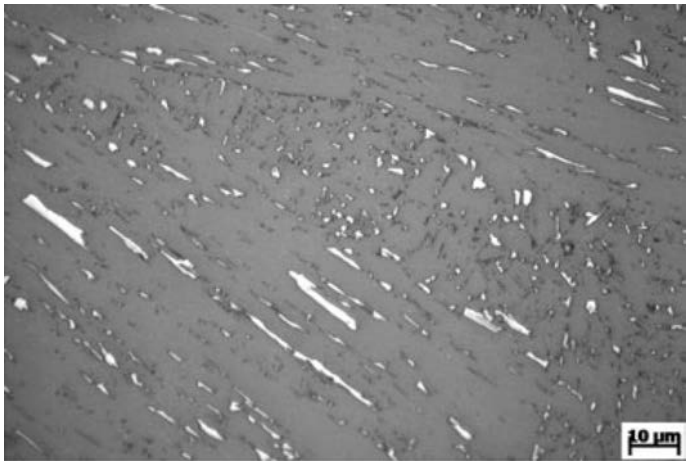

Figure 2.4: SEM SE images showing M-A islands (MA), acicular ferrite (AF) and granular bainite (GB) [Lan 12].

than the presence of M-A in a microstructure for toughness considerations. The stringy M-A particles (such as those shown in Figure 2.4) degrade toughness whereas the globular M-A islands shown in Figure 2.3 do not.

Mechanical Behaviour of Steel Microconstituents

The mechanical properties of steel are closely linked to chemical composition, processing techniques and final microstructure. In general, the "performance of steels depends on the properties associated with their microstructures, that is, on the arrangements, volume fractions, sizes and morphologies of the various phases constituting a macroscopic section of steel with a given composition in a given processed condition" [Krauss 05]. The mechanical properties that depend on microstructure include hardness, UTS and YS [Bramfitt 98]. Hardness is the measure of a material's ability to resist permanent indentation or deformation under loading conditions [Revankar 00]. The YS is an important parameter for structural applications and is defined as a material's resistance to plastic deformation (i.e., the onset

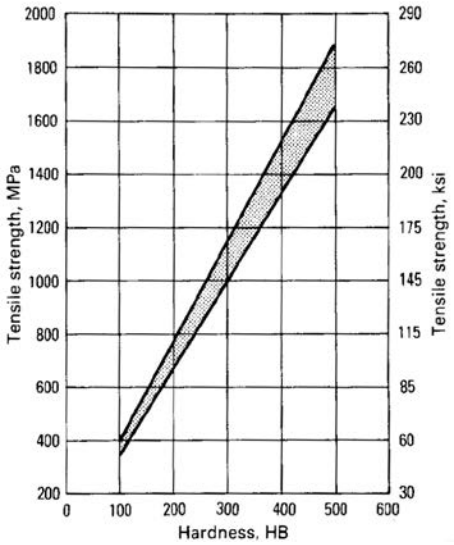

Figure 2.5: General trend illustrating tensile strength as a function of hardness [Krauss 05].

of dislocation motion) [Gladman 97]. The UTS of a material is the maximum force per unit area that can be withstood without fracture [Gladman 97]. It includes factors that affect the yield strength as well as work hardening factors and the onset of plastic instability. Work hardening is the process whereby a metal becomes both harder and stronger as it is plastically deformed [Callister 03]. The work hardening coefficient, n, is used to quantify the amount of work hardening that is capable for a given material.

The UTS is closely related to hardness, as shown in Figure 2.5, which depicts the relationship for carbon and low-alloy steels [Krauss 05]. The tensile strength increases uniformly as hardness increases.

The empirical relationship between hardness and UTS has been explored in other steel systems and the same trend has been reported [Gasko 11]. A general correlation between hardness and strength for most steels is shown in Equation 2.1, where hardness is provided in HB (Hardness Brinell) [Callister 03].

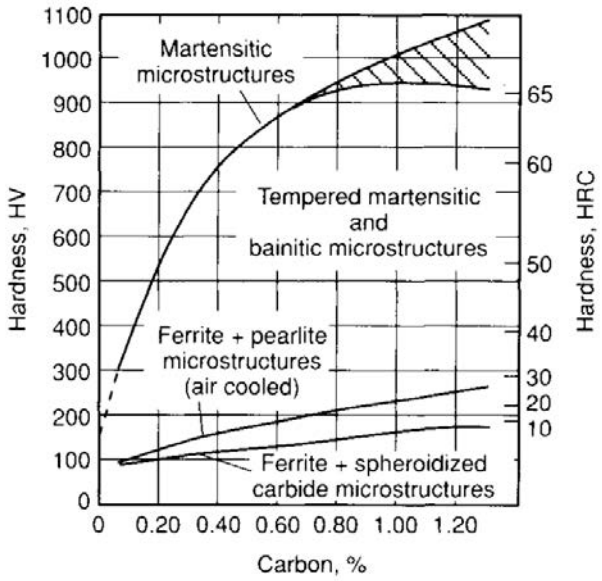

Figure 2.6: Hardness (HV) as a function of carbon content for various microconstituents [Krauss 05].

$$UTS = 3.45 \cdot HB \tag{2.1}$$

Hardness (and therefore UTS) also are influenced by carbon content, as shown in Figure 2.6. The increasing trend in hardness as a function of carbon content is shown for various microstructures, including martensite, tempered martensite (martensite after heat treatment at an elevated temperature), bainite, a mixture of ferrite and pearlite and a combined ferrite and spheroidized microstructure (spheroidized refers to the process whereby cementite particles become globular as a result of heat treatment at elevated temperatures) [Krauss 05].

Increasing the carbon content causes a simultaneous increase in both the UTS and the hardness for every constituent. According to Figure 2.6, martensite is the hardest constituent, followed by tempered martensite and bainitic microstructures

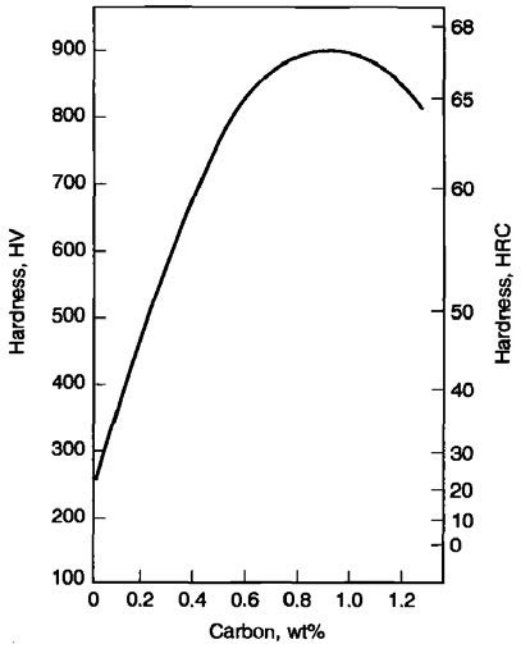

Figure 2.7: Hardness (HV) as a function of carbon content for martensite [Bramfitt 98].

and a mixed ferrite and pearlite microstructure. A ferrite and spheroidized microstructure has the lowest hardness value [Krauss 05].

As mentioned in Section 2.1.2, the hardness of martensite depends on the amount of carbon that is 'shoved' into the center of the bcc ferrite lattice, thus creating a distorted bct structure. The relationship between hardness and carbon content has been quantified for martensite as is shown in Figure 2.7 [Bramfitt 98]. For a typical microalloyed steel with a carbon content of 0.5 wt %, the hardness of a fully martensitic structure is approximately 310 HV. However, it is not practical to achieve a fully martensitic structure in microalloyed steels due to processing limitations, as themo-mechanical controlled processing (TMCP) cannot produce adequate cooling rates required for martensite formation, as will be discussed in the following section.

When considering dual-phase steels, the volume fraction and nature of the second

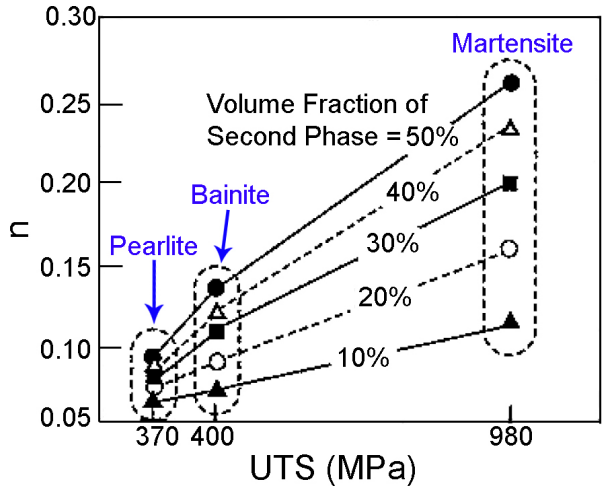

Figure 2.8: Effect of microconstituents on the n value for dual-phase steels containing pearlite, bainite and martensite as the second 'phase' [Mitsuhiro 08].

constituent greatly affects the mechanical properties. Figure 2.8 shows the effect of volume fraction (from 10 % to 50 %) on the work hardening coefficient (n) of a ferrite matrix dual-phase steel with either pearlite, bainite or martensite as the second 'phase' [Mitsuhiro 08].

The n value increases as the volume fraction of the second 'phase' increases, regardless of which second 'phase' is used. The volume fraction of martensite had the most dramatic impact on n: a phase fraction of 10 % resulted in an n value of 0.12 whereas 50 % martensite corresponded to an n value of 0.27. The ferrite-bainite dual-phase steel also showed a significant relationship between phase fraction and n; the n value doubled from a volume fraction of 10 % to a volume fraction of 50 %. The effect of volume fraction on n value for the ferrite-pearlite steel was not significant, as an increase in volume fraction from 10 % to 50 % caused an increase in n from 0.06 to approximately 0.09. For a consistent volume fraction, the ferrite-martensite steels had the highest n value and the ferrite-pearlite steels had the lowest n value.

According to Figure 2.8, the UTS (and, hence, hardness) was independent of

phase fraction and was only dependent on the nature of the second 'phase'. The ferrite-pearlite dual-phase steels had the lowest UTS/hardness while the ferrite-martensite dual-phase steels had the highest UTS/hardness. This indicates that steels with a harder second phase such as martensite have higher work hardening coefficients, and as a result, are more resistant to buckling.

This study shows that the highest work hardening coefficient can be obtained by using martensite as a second 'phase'. When using another constituent (such as bainite or pearlite), the highest work hardening coefficient is achieved when using the highest volume fraction (i.e., 50 %). In terms of UTS (and, as a result, hardness), the highest UTS was achieved with ferrite-martensite dual phase steels. The UTS of the ferrite-pearlite and ferrite-bainite steels was very similar (within 30 MPa) and, similar to the ferrite-martensite steels, the UTS was independent of volume fraction. Dual-phase steels with a harder second 'phase' are more resistant to buckling than those with a softer second 'phase'.

2.1.3 Thermo-mechanical Controlled Processing (TMCP)

Thermo-mechanical controlled processing (TMCP) is a common steel processing technique that is used to create products with excellent toughness, weldability and high strength [Shikanai 08]. The two most important techniques to achieve a fine-grained microstructure are controlled rolling (also referred to as TMCP) and microalloying. A general schematic of TMCP is shown in Figure 2.9, which is a generic example of TMCP including the casting process, a reheat furnace (roller hearth furnace in Figure 2.9), the roughing mill, controlled rolling stands and a run-out table (referred to as the Waterwall Cooling System in Figure 2.9) [Carboni 08].

Before discussing the full TMCP process, it is important to explain the first step in thermal treatments - austenitization. Austenitization involves creating a homo-

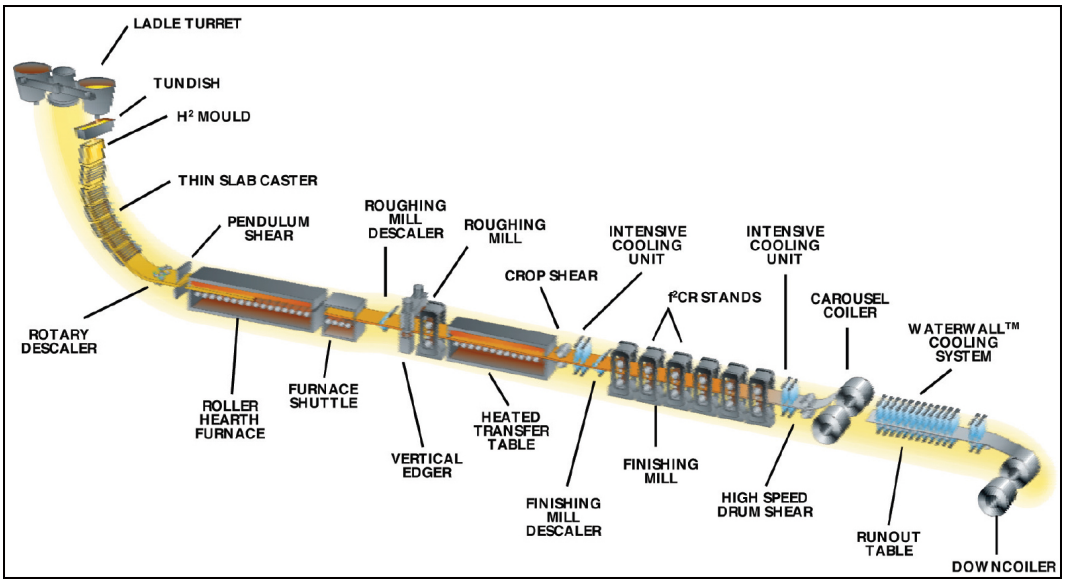

Figure 2.9: A generic schematic of TMCP [Carboni 08].

geneous austenite structure before subsequently subjecting the steel plate to various cooling rates and temperatures. Normalizing treatments, on the other hand, involve heating transformable steel to a temperature above the austenitization temperature (typically A_{c3} + 30 °C) and soaking the steel at this temperature for a certain amount of time before air cooling to a lower temperature [Gladman 97]. Normalizing is performed to eliminate variability in microstructural and mechanical properties that result from the TMCP conditions. More specifically, normalizing treatments are conducted to reduce micro- and macrosegregation caused by continuous casting. During normalizing treatments, austenite grains nucleate and grow through the temperature range of A_{c1} to A_{c3} and nucleate preferentially at ferrite-cementite interfaces or ferrite-ferrite grain boundaries in low-carbon steels. The driving force for the ferrite to austenite transformation increases with increasing temperature and, as such, the transformation will occur at higher temperatures during non-equilibrium heating. After the steel is completely austenitized, the austenite grains will rapidly

grow to undesirable grain sizes at the high temperatures unless grain growth inhibitors are added. The general grain growth equation is shown in Equation 2.2 where d is the mean grain diameter at time t, d_0 is the initial mean grain diameter and K is the rate constant. Equation 2.3 quantifies the factors that influence the rate constant K; more specifically, the activation energy for grain growth (Q_G), temperature (T), the ideal gas constant (R) and a constant (K_0).

$$d^n - d_0 = K \cdot t \tag{2.2}$$

$$K = K_0 \cdot e^{(-Q_G/R \cdot T)} \tag{2.3}$$

Equations 2.2 and 2.3 show that grain size increases with time at a constant temperature. Furthermore, grain sizes increase exponentially as the normalizing temperature increases according to Equation 2.3. One example of grain growth inhibitors is microalloy elements that form microalloyed carbonitrides which inhibit grain growth through grain boundary pinning [Gladman 97]. Precipitates are able to pin grain boundaries when the pinning force of the particle is equal to the driving force for grain growth. When particles grow larger than this critical particle size, however, grain growth occurs.

As previously mentioned, the two main techniques to achieve a fine-grained structure are controlled rolling and microalloying. Since these techniques are interrelated, they will be discussed simultaneously. Controlled rolling is a hot-rolling process whereby steel plates are rolled at controlled temperatures below the austenite recrystallization temperature in order to generate elongated or pancaked austenite grains. During controlled rolling of microalloyed steels, the vanadium, titanium and niobium carbonitrides precipitate out and act as grain growth inhibitors, thereby controlling

the austenite grain size and recrystallization [Krauss 05]. Controlled rolling is used to increase the strain in the pancaked austenite grains which increases the number of nucleation sites for ferrite and, in turn, results in a fine ferrite structure upon cooling. It is important to note that the pancaked austenite structure can only be achieved in the situation where austenite is not recrystallized, however. In the case of microalloyed steels, the precipitation of microalloying carbonitrides retards recrystallization, therefore, the pancaked austenite structure is obtained. Controlled rolling has led to great improvements in both yield strength and fracture toughness due to the significant grain refinement of the ferrite phase [Shikanai 08,Nobuyuki 06].

2.1.4 History of Microalloyed Steel Development

Steel is a very broad and general category that contains numerous subsets of steels that each have common and unique properties. One such group is microalloyed steels, which are HSLA steels containing small amounts (less than 0.10 wt% each) of niobium, vanadium and/or titanium. HSLA steels are intended to have improved mechanical properties as compared with plain carbon steels and are designed to meet specific requirements for mechanical properties rather than achieving chemistry specifications. As a general definition, microalloyed steels refer to "steels containing small additions of an alloying element that will produce grain refinement and/or precipitation strengthening by the formation of relatively stable carbides or nitrides" [Gladman 97]. Microalloying can be applied to various steel systems including structural steel, steel forgings, dual phase steels and interstitial free steels of high formability. Microalloyed steels constitute approximately 10 % of global steel production and, as such, are an important category of steel to investigate [Gladman 97]. Since microalloyed steels are named based on their mechanical properties rather than based on chemistry requirements, the nomenclature system reflects certain strength

Table 2.1: API Mechanical Performance Specifications for X52, X60 and X70 [API 12].

API Grade	Yield Strength (MPa/ksi)	Ultimate Tensile Strength (MPa/ksi)
X52	360/52.2	460/66.7
X60	415/60.2	520/75.4
X70	485/70.3	570/82.7

requirements for that particular grade of steel. For example, Grade XX is used for plate steel, where the "XX" refers to the specified minimum yield strength in ksi (e.g., Grade 80 indicates a specified minimum yield strength of 80 ksi, or approximately 550 MPa). The equivalent grade of steel used for pipelines is X80. Table 2.1 shows the material performance specifications designated by API 5L [API 12] for grades X52, X60 and X70. The chemical specifications are identical for the three grades: more specifically, carbon must be less than 0.28 wt% for welded structures and 0.26 wt% for seamless pipe, manganese cannot exceed 1.40 wt% (however, the manganese can exceed this amount if the carbon content is lower than the specified maximum), the maximum sulphur and phosphorous contents are 0.03 wt% and the maximum allowable combined percentage of vanadium, niobium and titanium is 0.15 wt%.

The developments in microalloyed steel grades from X60 to X90 have been achieved by changing the microstructure from a ferrite-pearlite structure (X60 and X70) to a ferrite-bainite (X80) or completely bainite microstructure (X90). This change in microstructure has caused a tremendous change in properties; most notably, a decrease in grain size and transformation temperature which leads to improved toughness. Figure 2.10 schematically shows the trend in toughness as a result of increasing API grade and microstructural shifts from the traditional ferrite-pearlite steels to higher strength and higher toughness constituents (such as bainite) [Garcia 12].

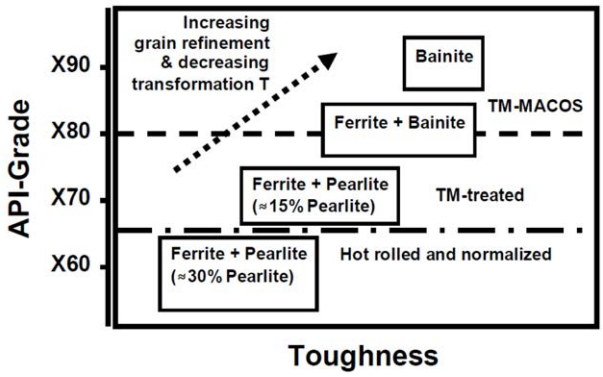

Figure 2.10: The relationship between toughness and microstructure for increasing API grades of microalloyed steels [Garcia 12].

Microalloyed steel were first developed in the 1950s when a large niobium ore body was discovered in both Canada and Brazil [Gladman 97]. The effect of niobium on steel properties was studied and the first discoveries were published in the late 1950s while the commercial development of these steels erupted in the early 1960s. The driving force to develop microalloyed steels was purely economics-based as niobium additions could be made to semi-killed steels which had much higher yields (98-99 % yield) than fully-killed steels (75 % yield), which therefore led to the creation of high-strength steels at lower cost. These steels were first used in the construction industry (reduced material costs for building projects since the cost per unit strength decreased as the strength increased), the automotive industry (reduced vehicle weight resulting in an increased payload) and the petrochemical industry (larger diameter pipelines and higher pressure transmission could be used with higher strength steels). Although microalloyed steels using niobium, titanium and vanadium were developed in the 1950s, these elements had been used in higher carbon steel products for numerous years for other purposes [Gladman 97]. Furthermore, the high cost of molybdenum in the 1970s spurred research into alternative elements; namely, microadditions of vanadium and titanium, to achieve hardenabil-

ity. The titanium was added to consume the nitrogen through the formation of titanium nitrides while vanadium acted as a hardening agent [Krauss 05].

The creation of microalloyed steels coincided with several important advances in technology including changes in fabrication methods and steel processing techniques. The transition in fabrication methods from traditional riveting and bolting to fusion welding processes occurred in the 1960s. Microalloyed steels were directly applicable to the new fusion welding procedure, since they were easier to weld than other existing steel products due to their reduced carbon content compared with traditional steel grades. Another processing development that occurred simultaneously to the development of microalloyed steel products was hot rolling practices, or controlled rolling. In the 1960s, controlled rolling practices were developed that were capable of lower temperatures during hot rolling, which created finer austenite grains that in turn produced finer grains in the final transformed product (typically ferrite). The end result was high strength and fine grained steel products that could be obtained with controlled rolling and small amounts of niobium - these advancements led to a further decrease in carbon content as it was no longer required as a strengthening agent. As a result, the drive to reduce carbon continued with the goal of further improving weldability [Gladman 97].

Microalloyed steel research in the 1960s and 1970s focused on increasing strength and concurrently decreasing cost due to compositional and processing refinements. From 1960-1965, research and experimentation centered around strengthening mechanisms in order to replace heat-treated steels. In the second half of the 1960s, research focused on improving toughness through grain refinement and desulphurization techniques [Krauss 05]. The motivation for these goals came from developments in the petrochemical industry; more specifically, oil deposits discovered in Alaska, Siberia and the North Sea created the need for higher strength steels capable of with-

standing harsh arctic conditions. Furthermore, the oil crisis in 1973 spurred further development into lightweight fuel transport vehicles and reduced material costs. The 1970s also spurred the creation of dual-phase steels, which are steel products that consist of both ferrite and martensite and, as a result, have very high strengths and work hardening capabilities with moderate ductility as compared with traditional pearlitic steels. These steels were created in conjunction with further developments in steel processing techniques such as accelerated cooling practices [Gladman 97]. Research topics in the 1970s also focused on weldability and formability. Further decreases in carbon and carbon equivalent levels were sought and inclusion shape control was also prioritized. The development of HSLA microalloyed steels has allowed larger diameter pipes to transport petrochemical products over longer distances in remote areas. Increasing the strength of the line pipe steel allows for a reduction in wall thickness, which then permits greater pumping pressures which result in increased throughput. Furthermore, smaller wall thicknesses reduce shipping costs and welding times.

The focus of research and development from the 1980s to present has been on a variety of mechanical properties including work hardening characteristics, fracture control in pipelines, fatigue, yielding behaviour and resistance to H_2S corrosion attack [Krauss 05]. Alloying additions have also been the center of recent developments as the price and availability of alloying elements fluctuates with the global market conditions and alternative strengthening mechanisms must be utilized. Microalloyed steels in the 1990s had very high strength and good weldability which increased safety in numerous applications, most notably in the shipbuilding industry [Fujibayashi 05].

Recent research focuses on improved weldability through microstructure refinement via adjustments to TMCP and cooling rates rather than the traditional de-

crease in carbon content [Nastich 07, Nobuyuki 06, Mitsuhiro 08, Hiroshi 08]. Arctic pipeline and offshore developments continue to expand and the demand is increasing for high strength and high toughness steels that can withstand extreme thermal stresses and strains due to ground movements while simultaneously satisfying the criteria for successful welding on location in these remote and environmentally severe areas. Furthermore, developments into isolated areas require longer pipelines which must have high strength and low-temperature toughness to account for reduced wall thicknesses that allow for increased operation pressures over the long travel distances [Hiroshi 08]. Another area of research that is being investigated involves the size and volume fraction of microalloy precipitates [Wiskel 08, Lu 12], which will be discussed shortly.

Low-temperature toughness and high deformability can be improved through metallurgical control techniques. One such technique is through increased cooling rates during the accelerated cooling process, which results in a fine-grained structure containing high strength constituents. Another technique involves the introduction of an on-line heat treatment system to interrupt phase transformation at a critical temperature to form a second phase after re-heating [Nobuyuki 06, Nobuyuki 08]. This heat-treatment online process, referred to as HOP, was developed by JFE Steel. According to JFE Steels' technical reports, the HOP is able to simultaneously control transformation, carbide precipitation and second phase formation while reducing the amount of scatter in mechanical properties through the thickness of the steel plate [Nobuyuki 06, Mitsuhiro 08].

The HOP involves rapidly heating the plate with induction coils directly after accelerated cooling to an interrupt temperature. The induction heating unit is placed on the production line directly after the hot leveler, so the sensible heat from the plate is utilized to minimize the amount of energy required to power the

induction coils and heat the plate. The plate then cools slowly to room temperature after reaching the re-heat temperature from the HOP. A schematic illustration of a HOP is shown in Figure 2.11 [Shikanai 08]. The steel plate is rapidly cooled using accelerated cooling to an intermediate temperature below the bainite start temperature, at which point the microstructure consists of bainite and retained austenite. The plate is then re-heated at a rate of 2 °C/s to 20 °C/s using induction heating during HOP to a re-heat temperature below A_{c1}, which allows carbon to diffuse from the bainite to the retained austenite grains. The retained austenite has high hardenability due to the high carbon content and therefore transforms to M-A upon subsequent cooling from the re-heat temperature to room temperature. The final microstructure at room temperature consists of M-A islands in a tempered bainite matrix [Shikanai 08]. The combination of a hard component (M-A constituent) in a relatively soft matrix (tempered bainite) is responsible for the excellent balance between high strength, good toughness and high hardenability.

These improvements in mechanical properties are due to TMCP conditions involving a very high cooling rate during accelerated cooling and an in-situ heat treatment process to interrupt the transformation from austenite to the first product (bainite) and subsequent and selective formation of the second phase (ferrite) upon cooling from the re-heat temperature. A mixed structure containing bainite and M-A can also be obtained if sufficient carbon is diffused out of the primary bainite phase and into the remaining austenite at the interrupt temperature directly after accelerated cooling and before the re-heat operation. The enriched austenite will transform to M-A upon cooling and will be dispersed in the bainite matrix, as shown in Figure 2.11. Accelerated cooling is stopped at a temperature between the bainite start and finish temperatures, so that the structure after accelerated cooling consists of bainite and retained austenite. The HOP process is then immediately applied to

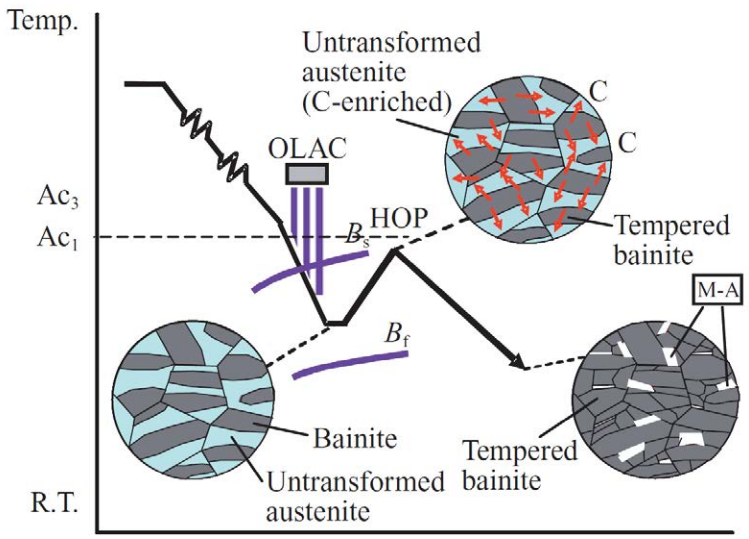

Figure 2.11: JFE Steel's Heat-Treatment Online Process (HOP): the steel is cooled to an intermediate temperature between the bainite start and finish temperatures, then is reheated to a temperature close to the A_{c1} temperature to promote carbon diffusion from the bainite to the untransformed austenite. Upon subsequent cooling, the untransformed bainite will form M-A [Shikanai 08].

diffuse carbon out of the bainite and into the remaining austenite.

Another JFE report argues that a single phase microstructure of bainitic ferrite in an ultra-low carbon steel results in high toughness [Hiroshi 08]. The results from this study show that the absorbed energy stays above 300 J at temperatures from 10 °C to -60 °C for the base material, and the absorbed energy is above 200 J for the welded seam for the same temperature range [Hiroshi 08]. One study performed by JFE Steel has suggested that a dual-phase steel of bainite and M-A results in a high strain hardenability [Mitsuhiro 08], whereas another JFE report claims that a dual-phase structure consisting of ferrite and bainite exhibits high strain hardenability and deformability [Nobuyuki 08]. Considering that several JFE reports claim that different microconstituents all provide the "best" mechanical behaviour, this area of research is important to pursue to clarify the effect of each microconstituent on

mechanical behaviour.

Other areas of research have centered around alternative steel microstructures containing ferrite and bainite as opposed to the traditional ferrite-pearlite steels [Matlock 01,Bhadeshia 98] and, more specifically, the creation of nanobainitic steels [Bhadeshia 10]. These nanostructured bainitic steels have been reported to have excellent combinations of strength (2.3 GPa), toughness (30 MPa $m^1/2$) and ductility (30 %) and, as such, are exceptional candidates for arctic pipeline developments as well as defence applications and offshore industries [Beladi08]. Another major focus of microalloyed steel research is the development of higher strength grades, including the successful production and implementation of X100 in 2002 [Nobuyuki 06] and research into even higher grades such as X120 [Nobuyuki 08].

A recent important area of research that has been explored in the past decade is the analysis of precipitate size distribution in commercially processed steels. Wiskel et al [Wiskel 08] investigated precipitate characteristics as a function of TMCP parameters, namely the finish rolling temperature and cooling interrupt temperature. Their work focuses on two different precipitate types, precipitates in the size range of 0.8 - 1.2 nm (referred to as small precipitates) and those that were 2.0 - 3.5 nm in size (referred to as larger precipitates) that are present in a wide variety of microalloyed steels including X70, X80, Grade 80 and Grade 100. The larger precipitates had a strong correlation with finish rolling temperature whereas the cooling interrupt temperature had a minimal effect on precipitate size and volume fraction. More specifically, the precipitate size increased as the finish rolling temperature increased, which can be attributed to precipitate coarsening at higher temperature. The lack of correlation between size and volume fraction with cooling interrupt temperature indicates that the larger precipitates nucleate and grow during finish rolling. The effect of cooling interrupt temperature on the smallest precipitates was also inves-

tigated. Both the precipitate size and volume fraction decreased with decreasing cooling interrupt temperature, which is not beneficial for precipitation strengthening as a large volume fraction of very fine precipitates is required for precipitation strengthening. The ratio of cooling interrupt temperature to finish rolling temperature was calculated as a single parameter to determine the effect on precipitate size and volume fraction. This new parameter provided a strong correlation with precipitation: a low ratio (i.e., a low cooling interrupt temperature and a high finish rolling temperature) resulted in a small radius and a small volume fraction. The precipitation of small precipitates is therefore dependent on both cooling interrupt temperature and finish rolling temperature [Wiskel 08].

2.1.5 Strengthening Mechanisms

There are several strengthening mechanisms that can be employed to increase the yield strength of a metallic material. Strengthening requires dislocation motion to be impeded which in turn increases the stress required for plastic deformation to occur. The four main strengthening techniques that will be discussed in the following sections are: 1) solid solution strengthening, 2) grain refinement, 3) precipitation and second phase strengthening and 4) work hardening.

Solid Solution Strengthening

Solid solution strengthening is a process whereby a metal is hardened and strengthened through alloying additions which restrict dislocation mobility within the crystal lattice [Callister 03]. Both substitutional and interstitial atoms provide obstacles for dislocation motion. Impurity atoms impose lattice strains on the neighboring host atoms and create interactions with dislocations which must be overcome in order for dislocation motion to occur. Substitutional atoms can be either larger

or smaller than the matrix atoms. If the substitutional atoms are larger than the matrix atoms, a compressive field is created; on the other hand, substitutional atoms that are smaller than the matrix atoms create a tensile field. Interstitial atoms are always larger than the interstitial sites and, therefore, produce a compressive stress field. The lattice strain interactions between the impurity atoms and the matrix are observed between the impurity atoms and mobile dislocations during plastic deformation. As a result, a higher stress is required to initiate plastic deformation, and any further plastic deformation requires the creation of new dislocations [Callister 03].

Grain Refinement

Grain refinement is another important strengthening mechanism. Grain boundaries act as barriers to dislocation motion due to discontinuity of the slip plane and slip direction between neighboring grains. The number of dislocations that pile up at a grain boundary and subsequently induce slip in a neighboring grain is directly related to the length of the dislocation slip band, which is also associated with the grain "diameter". As a result, larger grains allow for more dislocations to pile up at the grain boundaries which decreases the critical shear stress required to induce slip in a neighboring grain [Gladman 97]. Dislocations themselves also contribute to strengthening through cold working, which is a process whereby a steel product is plastically deformed at a temperature lower than the recrystallization temperature [Callister 03]. During cold working, the dislocation density increases and thus increases the YS. Dislocation arrangements (forest, cell structures, sub-grains, etc.) also strengthen the material.

The high cooling rates achievable in accelerated cooling processes are able to produce both high strength through transformation strengthening and high toughness

through grain refinement of the transformed structure [Nobuyuki 06]. The grain refinement obtained through controlled rolling has improved the YS and fracture toughness. YS is inversely proportional to the square root of the mean grain size, as shown in the Hall-Petch relationship (Equation 2.4). The YS of the polycrystal is given by σ_y in units of MPa, σ_0 is the yield strength of a single crystal of the same purity (MPa), k_y is the grain boundary strengthening coefficient (MPa $mm^{1/2}$), d is the mean grain size (mm) and T is the temperature (K) [Bramfitt 98].

$$\sigma_y = \sigma_0 + k_y \cdot d^{-1/2} \tag{2.4}$$

Elements such as manganese, nickel, chromium and molybdenum contribute to grain refinement through the suppression of the transformation temperature, which increases the nucleation rate of ferrite while simultaneously reducing the ferrite growth rate, thus generating a very fine-grained structure. As mentioned in Section 2.1.3, microalloying elements such as niobium, vanadium and titanium contribute to grain refinement by suppressing the austenite grain size through both increasing the austenite recrystallization temperature and pinning the austenite grain boundaries with very fine microalloy precipitates. Grain size strengthening can account for up to 70 % of the strengthening contributions for microalloyed steels such as X70, X80 and X100 [Lu 12]. Grain refinement via precipitation pinning is also related to precipitation and second phase strengthening, which will be discussed in the next section.

Precipitation and Second Phase Strengthening

Second phase strengthening is another important strengthening mechanism utilized in microalloyed steel processing. The precipitates that can be produced in microalloyed steels include titanium carbonitrides, niobium carbonitrides, vanadium

carbonitrides and other complex precipitates depending on the chemistry of the steel product. Chemical composition is an important factor in precipitation strengthening; however, processing conditions such as casting, the re-heat process, rough rolling, finish rolling and final cooling conditions also affect precipitation. Furthermore, the temperature and applied strain during rolling also affect the precipitation of nano-sized particles [Wiskel 08].

Microalloy precipitates can be categorized based on the TMCP step during which they form; for example, large precipitates (typically titanium nitride precipitates that are larger than 0.5 μm) form during solidification in the casting process, medium-sized precipitates (niobium and titanium carbonitrides on the order of 50 - 500 nm) form during hot rolling and fine precipitates (niobium and titanium carbonitrides that are less than 10 nm in diameter) form during and after the laminar cooling stage in TMCP [Wiskel 08]. The medium-sized precipitates can be further classified into two categories based on the stage in TMCP in which they precipitate. More specifically, precipitates with a diameter of 100 - 500 nm form during rough rolling, whereas smaller precipitates (30 - 50 nm) form during finish rolling. The fine microalloy precipitates primarily form at the interface between austenite and ferrite during transformation or in the ferrite that has already transformed. During hot rolling, precipitates nucleate on the dislocations that are introduced to the austenite grains as a result of the high strain imposed on the material [Krauss 05]. As a result, the precipitates that form in austenite during rolling act as austenite grain refiners [Lu 12].

The small precipitates (less than 20 nm) that form during hot rolling are largely responsible for precipitation strengthening. Studies performed by Wiskel et al. [Wiskel 08] and Lu [Lu 12] argue that precipitates on the order of 5 nm are the most effective for strengthening. Precipitation strengthening is closely related to precipitate size

and volume fraction; therefore, a high volume fraction of very small precipitates is required in order to maximize precipitation strengthening [Lu 12]. Since the fine precipitates form during laminar cooling on the run-out table, the most important parameters that affect precipitate size and volume fraction are the finish rolling temperature and the cooling interrupt temperature [Wiskel 08]. More specifically, the cooling interrupt temperature has a significant influence on the precipitation of fine carbonitrides since the nucleation and growth of these precipitates is highly temperature dependent in the ferrite phase.

Niobium is a crucial component in the development of fine grained and high strength steel as it has three key roles: 1) grain refiner (through retardation of austenite recrystallization during finish rolling, which effectively pins the austenite grain boundaries and therefore refines the ferrite grain size), 2) suppressor of the austenite to ferrite transformation, and 3) precipitation hardener (niobium carbonitride precipitation in the ferrite phase occurs after coiling and provides precipitation strengthening) [Collins 01]. Niobium is particularly effective when precipitates are formed above the transformation temperature, which retards the recrystallization of austenite during controlled rolling. The low solubility of niobium in austenite causes the formation of very stable precipitates which pin austenite grain boundaries and inhibit grain growth. The end result is a more refined ferrite microstructure, which subsequently results in high strength and toughness [Krauss 05].

Work Hardening

Work hardening, or strain hardening, is another technique to improve strength in a steel product. As mentioned in Section 2.1.2, work hardening is the process whereby a metal becomes both harder and stronger as it is plastically deformed [Callister 03]. In order to achieve good work hardening characteristics for steel products,

there must be a balance between a low yield strength phase (such as ferrite) and a strong second constituent (such as bainite) [Collins 09]. Studies performed by JFE steel showed that a higher work hardening coefficient can be obtained by increasing the strength or the volume fraction of the second phase in dual-phase steels, as shown in Figure 2.8 [Nobuyuki 06, Mitsuhiro 08].

The engineering stress-engineering strain curve is an indication of the amount of work hardening that is possible for a specific steel product. A low YS/UTS ratio corresponds to high work hardening, as the material increases both strength and hardness as it plastically deforms before reaching the point of plastic instability. A study performed by JFE claims that the engineering stress-engineering strain curve is more round for steels containing a higher percentage of bainite than steels with a lower percentage of bainite, as shown in Figure 2.12 [Nobuyuki 06]. A bainite volume fraction of 30 % results in the highest YS and UTS values for a fixed bainite aspect ratio of 2.0 for all three volume fractions of bainite (10, 20 and 30 %). The stress-strain curve for the ferrite sample exhibits Luders bands, or discontinuous yielding, which is undesirable in most steel products.

2.2 Experimental Techniques

The experimental techniques used in this project will be outlined in this section. Section 2.3 will describe the techniques, such as optical and electron microscopy, used to investigate and identify the microconstituents. Techniques that were utilized to quantify the microstructural constituents including imaging processing and grain size determination will be discussed in Section 2.4. Section 2.5 will outline the mechanical testing techniques; more specifically, hardness and tensile tests.

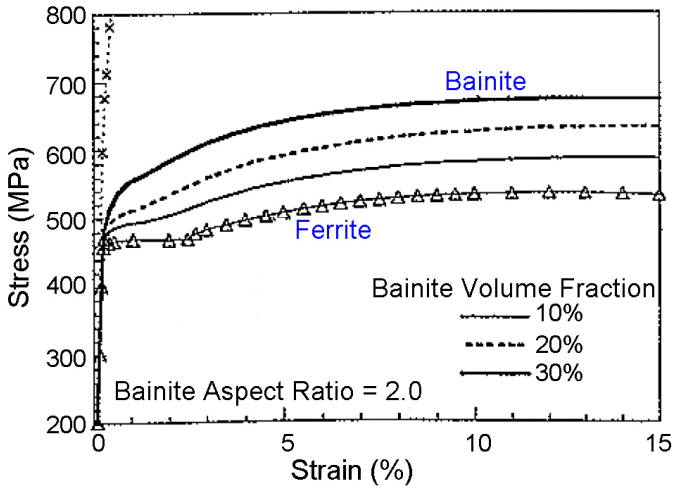

Figure 2.12: The effect of bainite volume fraction on the stress-strain curve for ferritic and bainitic dual-phase steels [Nobuyuki 06]

2.3 Microstructure Characterization

In order to determine the effect of thermal history on microstructure development, the microstructure must first be characterized and identified. Common imaging techniques used to resolve microstructural features include optical microscopy and electron microscopy, which use an incident beam (either light or electron) to image the samples.

2.3.1 Optical Microscopy

Optical microscopy is an important technique used to study general microstructures at low magnifications. Optical micrographs can be used to identify the microstructure, calculate the overall grain size and determine the phase fraction of easily distinguishable constituents. There are many types of optical microscopes including reflected light microscopes and transmitted light microscopes which are used for metals and polymers, respectively; however, the optical microscopy work

performed in this project was limited to reflected light microscopes. As a result, transmitted light microscopes will not be discussed. There are also various imaging modes such as bright-field illumination, dark-field illumination and polarized light techniques, which are explained elsewhere.

Optical microscopes use a light source to illuminate and observe the sample. Typically, a low-voltage tungsten filament lamp is used as the light source and can be adjusted to control the light intensity [Vander Voort 92]. A condenser lens is placed in front of the light source to focus the light and an aperture diaphragm is placed after the condenser lens to adjust the amount of light that enters the objective lens. The optimal setting of the aperture diaphragm is a balance between image contrast, image sharpness and depth of field. A wide aperture allows a lot of light to reach the objective lens, thereby increasing the brightness. The objective lens collects light from the sample and forms the image of the sample. The ability of the objective lens to collect light is measured by the numerical aperture (NA), as shown in Equation 2.5 where n_i is the minimum refraction index of the material between the specimen and the lens (typically air or oil) and α_i is the half-angle of the oblique light rays that enter the front lens of the objective lens [Vander Voort 92].

$$NA = n_i \cdot sin\alpha_i \tag{2.5}$$

In order to observe the microstructure with adequate detail, there must be sufficient resolution and image contrast. The resolution for optical microscopes depends on the wavelength of the incident light, λ, and the NA of the objective lens. The depth of field is another important parameter that affects optical microscopy imaging and depends on the same parameters as resolution but in the opposite sense. Increasing the NA decreases the depth of field while improving the resolution. Similarly, increasing the wavelength of incident light degrades the resolution but increases

the depth of field. As a result, a balance must be met between these two competing factors.

Optical microscopy is often inadequate to accurately distinguish very small microstructural features and, instead, is only used to gather general information about the microstructure at low magnifications. To observe sample features that are less than 10 μm, electron microscopy may be utilized.

2.3.2 Scanning Electron Microscopy (SEM)

Instead of using light to observe the sample through a series of optical lenses, SEM instruments form images by collecting secondary electrons (SEs) that have been produced due to an interaction with the primary beam (SEM).

A SEM instrument can be divided into four different parts to understand its operation: 1) the electron source, 2) the electron optics, 3) beam/sample interaction and 4) signal detection. The two common electron sources used in electron microscopy are thermionic and field emission (FE) sources. Thermionic emission (using a tungsten filament or LaB_6 crystal) occurs by elevating the surface temperature of the electron source, thus allowing electrons to more readily escape from the surface. When comparing thermionic sources, LaB_6 cathodes allow more electron current to be concentrated into a smaller beam spot, which improves the image resolution and increases the brightness by 5 to 10 times as compared with the original tungsten cathode.

FE filaments use a high electric field (rather than a thermal source) to lower the energy required for electrons to be extracted from an atomically sharp tungsten tip. FE sources provide even more brightness than the LaB_6 electrodes. A typical FE probe is on the order of nanometers, which allows for a very high current density (105 A/cm^2 as compared with 3 A/cm^2 for a thermionic source) [Goldstein 03].

FE SEM instruments require the sources to be in an ultra high vacuum (UHV) environment due to the high electric fields. Stray atoms may cause arcing and may result in irreversible damage to the machine.

For both thermionic and FE sources, the stream of electrons must be conditioned after it is removed from the source in order to ensure a controlled interaction between the electron beam and the sample surface. Beam conditioning is achieved by using lenses; however, the lenses in an electron microscope use magnetic fields whereas lenses in an optical microscope focus the incident light beam. The SEM lenses are used to demagnify, columnate and manipulate the stream of electrons as it passes through the beam column. Further beam control is achieved with physical apertures in order to accomplish a specified current with a specific spot size. The electron beam diameter ranges from less than 1 nm to hundreds of nm depending on the machine conditions. The resolving power of an SEM instrument is significantly better than for optical microscopes. The ultimate resolution is not only determined by the machine conditions such as spot size, current and energy of the primary beam, but also depends on the interaction between the primary electron beam and the sample based on composition and morphology.

There are several interactions that can occur between the incident electron beam and the sample surface. Electrons can pass through the sample (transmitted), be elastically scattered by the unit cells near the sample surface or be inelastically scattered as a result of interactions with the sample, as shown in Figure 2.13. Signal generation is not limited to the surface of the sample, however. As the beam enters the sample, multiple scattering events can occur and can produce SEs that can be collected by the SE detectors. Back scattered electrons (BSEs) are high energy electrons close to that of the primary electron beam. A BSE signal can offer comparative information as heavier elements reflect more of the incident beam then lighter

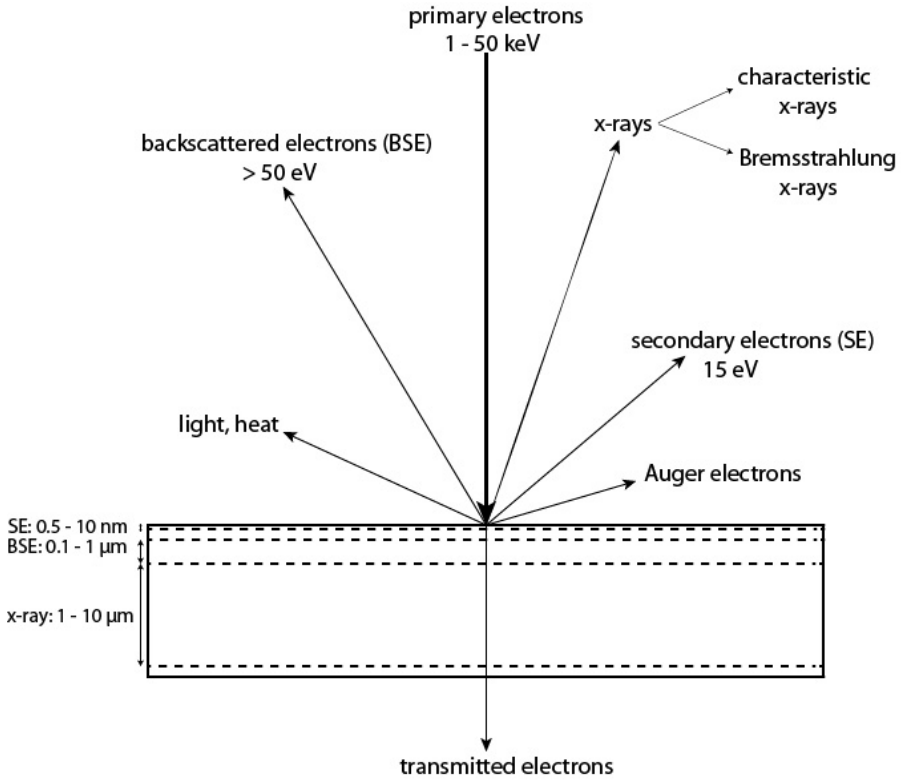

Figure 2.13: Interactions between the incident electron beam and the specimen in SE.

elements. SEs have energies that are under 50 eV and are released as a by-product of the primary beam causing the atoms in the sample to release an electron. SEs offer morphological information as they have a escape depth of 0.5 nm to 10 nm, depending on the instrument and sample.

Composition information is obtained by collecting X-rays and auger electrons. X-rays are the result of the relaxation of core shell electrons after the primary beam imparts some of it's energy onto the atom. This X-ray is a characteristic x-ray with a specific energy; by collecting and counting the amount of these X-rays it is possible to form a spectrum identifying the elements that are present in the sample. Auger electrons also reveal compositional information since they have characteristic

energies when released from their atoms.

The crystal structure and grain orientation of the top-layer crystals on the sample surface can be determined using electron back-scattering diffraction (EBSD). The sample surface is typically tilted from the horizontal in order to collect a majority of the diffracted BSE. The BSE are then collected with a specific detector to produce a diffraction pattern to identify phases and show misorientations between grains in the area of interest [Goldstein 03].

Detectors in an SEM allow electrons to be collected to extract quantitative and qualitative data about the region they were obtained from. Although beam currents can be on the order of tens of pA, collection efficiency is typically low and therefore detectors must be sensitive to small currents. This is typically achieved through amplification of the original signal [Goldstein 03]. Higher accelerating voltages allow for more scattering events thus leading to higher interaction volumes which affects the practical resolution. Using higher beam currents may achieve higher counts at the expense of beam spot size and thus resolution. To form an image of the sample, the focused electron beam is rastered across the surface and generates a stream of electrons unique to that site that is then collected.

2.3.3 Transmission Electron Microscopy (TEM)

TEM images are generated by collecting the electrons that have passed through the electron transparent sample. Sample preparation is crucial to successful TEM investigations as the sample must be electron transparent at the specified voltage. Thicknesses of 10 - 100 nm yield electron transparency suitable for TEM analysis. Samples can be prepared by electrochemical polishing, extraction replicas, dimpling/ion milling, microtoming or focused ion beam (FIB). TEM samples in this work were prepared using a FIB machine. A FIB operates using similar principles

to an SEM, except ions are used as the primary beam rather than electrons to interact with the sample, and will be discussed in Section 2.3.4.

Similar concepts found in the operation of an SEM can be used to explain the operation of a TEM. Electron sources and optics are similar in concept but are designed to accommodate higher accelerating voltage operation in the TEM (100 kV to 300 kV versus 0.1 kV to 30 kV for SEM instruments). A benefit of using higher accelerating voltages is that smaller spot size diameters are possible, thus improving resolving power [Vander Voort 92]. Current TEM instruments are able to resolve features that are 0.5 Angstroms in size [Freitag 08]. Different imaging modes are enabled by manipulating the beam through different optics or apertures.

Techniques offered by a TEM include, but are not limited to: bright field (BF) and dark field (DF) imaging, phase contrast imaging, selected area diffraction (SAD) and EDX. Defects including individual dislocations, dislocation clusters, grain boundaries, point defects, stacking faults and twins can be imaged in BF and DF mode. Twins and stacking faults will be evident in images that are collected at different tilt angles, since the twins and faults will appear in and out of contrast as the tilt angle is changed at the same location. A phase contrast or lattice image is generated by a minimum of two beams that interact and cause interference in the image plane of the objective lens [Vander Voort 92]. Precipitates are characterized using EDX analysis, similar to the process in SEM, and diffraction analysis. Furthermore, the crystal structure can be identified using selected area diffraction (SAD) patterns, which can be solved and compared with a known database to identify the crystal structure and lattice parameters. More specifically, the TEM SAD pattern can be indexed to include the planes of atoms corresponding to SAD spots and the zone axis can also be identified if the SAD pattern was obtained close to the zone axis. The full procedure on solving SAD patterns is detailed elsewhere [Beeston 72]

and will not be discussed further here.

2.3.4 Focused Ion Beam (FIB)

A focused ion beam (FIB) microscope operates in a very similar fashion to a SEM instrument, but instead of electrons to interact with the sample, a fine beam of gallium ions (Ga^+) is used. Since Ga^+ ions have a mass that is 5 orders of magnitude larger than an electron, they are capable of producing higher SE emission per interaction. As the primary ion beam hits the sample surface, a small amount of material is sputtered and generates SEs as the beam is rastered across the sample surface. As a result, a low current Ga^+ beam is used when imaging to minimize beam damage. The SEs are collected in a similar fashion to an SEM to form an image. Ion imaging also allows for grains of varying orientation to produce different contrasts due to channel effects. Increasing the ion beam currents will increase the sputtering rate of sample material, thus changing the mode from imaging to milling suitable for micromachining, serial sectioning, and polishing. Pairing an SEM with a FIB creates a powerful instrument cable of observing and locating areas of interest on a sample and simultaneously isolating and preparing the region of interest to a thickness less than 100 nm, which is suitable for observation and analysis in TEM.

Preparation of an electron transparent sample is a complicated process. A detailed explanation for producing a TEM sample using the FIB is provided by Mayer et. al [Mayer 07]. A visual representation the processes on one of the heat treated steel samples is provided in Figure 2.14. For the initial milling and tungsten deposition, high accelerating voltages and beam currents were used to achieve high sputter/deposition rates. Lower currents and lower accelerating voltages were used in the thinning and polishing stage to have finer control and minimize beam damage.

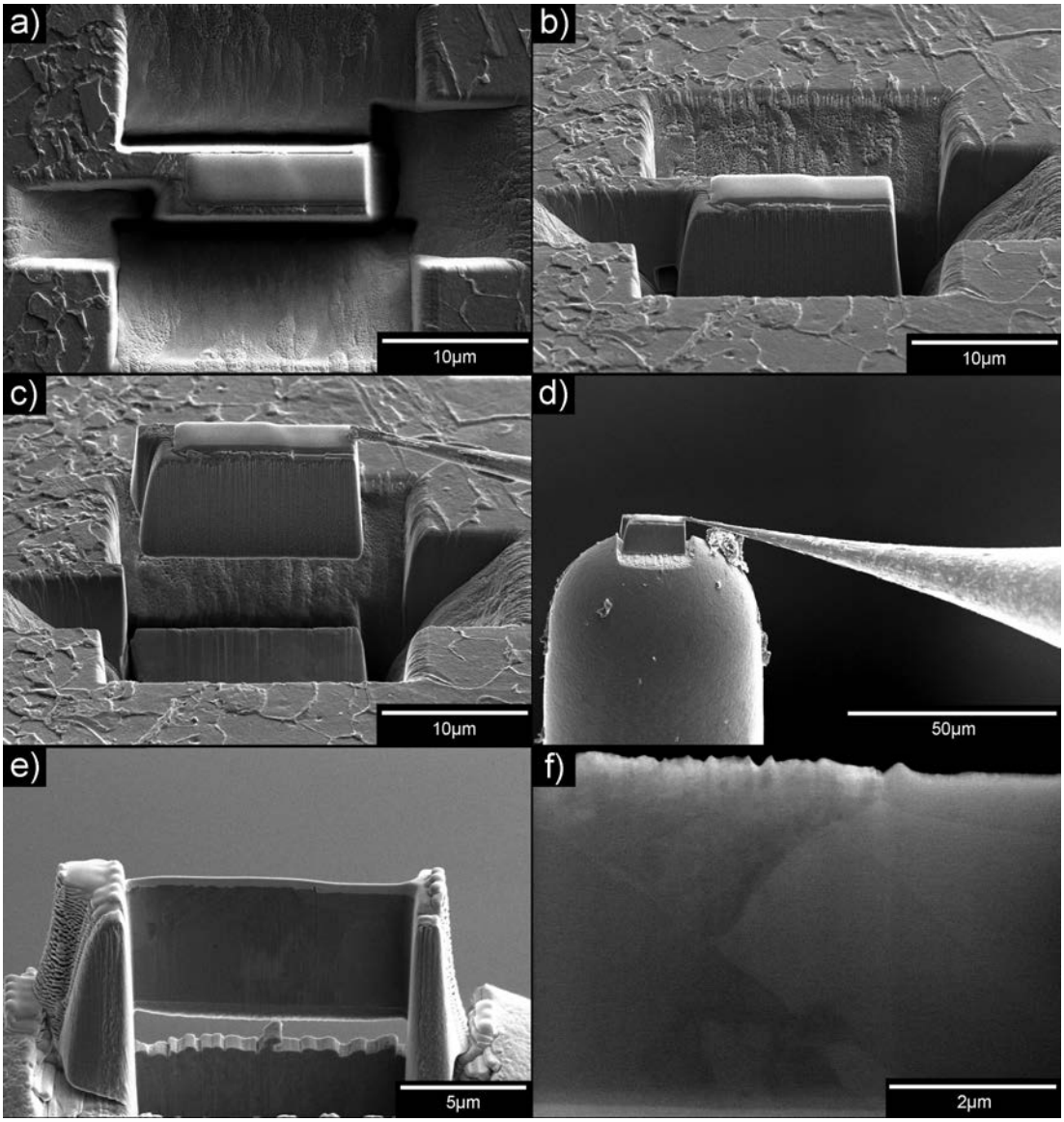

Figure 2.14: TEM sample preparation using a FIB: a) top view and b) oblique view of a region of interest; c) FIB probe tip welded to the lamella in b; d) placing the lamella on the tip of a copper TEM grid finger; e) low magnification and f) high magnification images after ion milling to a thickness of approximately 100 nm.

2.4 Microstructure Quantification

The experimental techniques used to observe the microstructure were described in the previous sections. A qualitative description of the microstructure is not sufficient to directly compare the effect of one parameter on the microstructure development; rather, phase quantification must be conducted using image processing techniques. It is important to quantitatively describe not only the amount of each constituent present in the microstructure, but also the size and morphology of the grains. The following sections will describe two important techniques used to quantify microstructures; namely, phase quantification through image processing and grain size determination.

2.4.1 Phase Quantification

There are several open-source programs that facilitate image processing, including Photoshop, GIMP, Inkscape as well as more scientific software such as ImageJ and FIJI (which is an acronym for 'Fiji Is Just ImageJ'). Quantitative image analysis requires certain steps to improve the visual appearance of the objects and to prepare the image for measurements. Image enhancement is performed in order to eliminate surface roughness and defects, enhance edges, identify points, optimize texture and improve contrast [Oberholzer 96]. Uniformity of illumination throughout the entire image is also important in image analysis as background "noise" interferes with the discrimination process between various objects. Surface roughness, defects and texture can be addressed by performing several pixel-based or neighbourhood-based operations, such as histogram equalization and filters.

Filters are used in order to either accentuate or suppress specific features in the image. There are two main types of filters; averaging and ranking. In averaging filters, each pixel is replaced with the average value of its own grey value and the

grey value of its neighbours through the use of "kernels", which are two-dimensional arrays of integers that correspond to weights based on the grey count associated with each pixel. As as result, each pixel in the image is multiplied by its weight as defined by the kernel before it is averaged. Gaussian filters are one of the most common averaging filters. The set of kernels used in a Gaussian filter simulate the profile of a Gaussian histogram using the original pixel as the peak value in the histogram. As a result, Gaussian filters are used to smooth the image or correct noise (defects) through this balancing of local differences in brightness. The Laplace filter is a different averaging filter that is used to sharpen and detect edges, improve contrast and correct noise.

The second type of filter is a ranking filter, whereby each pixel value is replaced with the median value of the neighboring grey values. The most important ranking filter is the median filter, which has two significant advantages over averaging filters: 1) median filters do not reduce brightness across steps; 2) edges remain well-defined and are not shifted during the filter process [Oberholzer 96]. Since the edges are not affected during the application of a median filter, it can be repeated several times to reduce the grey value count in the image while maintaining the original edges.

Another aspect of image analysis is image arithmetic, whereby two images can be added, subtracted, multiplied or divided pixel by pixel. These arithmetic operations are performed in order to remove unwanted background pixels or to isolate features of interest in the original image. Furthermore, image arithmetic (more specifically, image subtraction) can help determine whether previous image analysis steps have successfully identified the objects of interest in the original image.

Segmentation is another important step in image analysis and involves the selection and separation of objects of interest from all other objects which henceforth constitute the background. Segmentation is traditionally performed using threshold

values and results in a binary image (black and white) when the process is complete. Thresholding involves selecting a grey value that corresponds to the value when the region of interest is completely selected. The binary images obtained from segmentation can be used for Boolean operations (image arithmetic as previously described) or to generate masks that can be overlayed on the original image to select regions of interest in the image. Since the binary image consists only of pixels with a value of 0 or 1 (0 corresponding to the background and 1 representing the foreground in the binary image), the mask restricts which pixels in the original image are used for subsequent quantification evaluation and those pixels which are completely eliminated. It is important to note, however, that the thresholding process in segmentation is a source of significant error. Manual selection of a thresholding value is not consistent between users, nor is it consistent for a single user over a period of time. Thresholding can also lead to bias, as some operators may select a threshold value that is just outside or inside the actual region boundary which makes the dimensions larger or smaller than they actually are. To compensate for this bias, there are morphological operations that can be performed on the binary images to account for the enlarging or shrinking of the actual feature. Erosion and dilation are two ranking neighbor operations that shrink or expand the features, respectively [Oberholzer 96].

As previously mentioned, image analysis is performed to obtain quantitative information about the features in an image. For the scope of this project, image analysis refers to enhancing, segmenting and quantitatively evaluating the various microconstituents present in the microstructures by calculating the area fraction of each microconstituent. Microstructure quantification incorporates more than just the area fraction of each microconstituent; however; the grain size is another important factor which will be discussed in the next section.

2.4.2 Grain Size Determination

There are several ways to measure grain size, including, but not limited to, the comparison procedure, the intercept method (such as Heyn) and the planimetric method (or Jeffrie's) as described in ASTM E112 [AST 10]. These methods can be used to determine the average size of a single phase microstructure or the average size of a particular grain structure in a multiconstituent system. Furthermore, these tests methods outline procedures for determining the average grain size for metals consisting principally of a single phase; samples with duplex or bimodal grain size distribution are outlined in ASTM E1181 [AST 0]. The comparison procedure involves comparing the structure to a series of images with a known grain size and, as such, introduces a significant amount of bias to the results since the grain size is not actually measured but visually compared. The intercept and planimetric procedures involve counting the grains or grain intercepts within a known area. The precision of both techniques relies on the number of grains or grain intercepts counted, and results are reproducible within 0.5 grain size units. The intercept method, however, has the same amount of precision as the planimetric method but requires less time and is more convenient. Furthermore, ASTM E112 recommends intercept methods for specimens that "depart from the uniform equiaxed form"; i.e., for aniosotropic structures [AST 10]. As a result, the intercept method was chosen as the grain measurement technique and will be discussed further.

There are two different intercept procedures; more specifically, the Heyn lineal intercept procedure or circular intercept procedures. The Heyn intercept method involves counting the number of grain boundaries that are intersected by a straight line of a given length, from which the mean intercept length of the grains can be calculated. An intercept is defined as "a segment of text line overlaying one grain", whereas an intersection is "a point where a test line is cut by a grain bound-

ary" [AST 10]. Either intercepts or intersections can be counted and yield identical results. The effect of orientation on non-equiaxed structures can be accounted for and eliminated by making intercept/intersection counts on line segments with four or more orientations; for example, two diagonal lines, one vertical line and one horizontal line can be used as line segments to count the number of intersepts/intersections. ASTM E112 states that at least 50 grains must be intersected per micrograph, usually corresponding to a combined intercept length of 500 mm [AST 10].

Circular intercept methods can also be used to determine the average grain size of a particular structure and are commonly used in order to overcome the issue of elongated grains and non-equiaxed structures. In this method, concentric circles are drawn across the metallographic plane. Any circle of a known circumference can be used, but circumferences of 100, 200 or 250 mm are most commonly used [AST 10]. Circular intercepts produce an average intercept length that can be used to predict the grain boundary area per unit volume, regardless of orientation or textural effects in the microstructure [Gladman 97].

For each field of count, the mean lineal intercept value is calculated according to Equation 2.6, where N_i is the number of intercepts/intersections counted on the field, L is the total length of the test lines (mm) and M is the magnification [AST 10].

$$l_i = \frac{L/M}{N_i} \tag{2.6}$$

The mean linear intercept for the entire sample based on several field counts, $\bar{l}$, is then calculated by dividing the sum of the lineal intercepts for each area, l_i, by the number of areas that were measured, n_g, as shown in Equation 2.7 [AST 10].

$$\bar{l} = \frac{\sum_{i=1}^{n_g} l_i}{n_g} \tag{2.7}$$

The standard deviation of the individual measurements can be calculated using the traditional statistical relationship as shown in Equation 2.8, where s is the standard deviation.

$$s = [\frac{\sum(l_i - \bar{l})^2}{n_g - 1}]^{1/2} \tag{2.8}$$

The mean lineal intercept length, $\bar{l}$, can then be converted to an ASTM grain size, which is detailed in ASTM E122 and hence will not be described here. The calculated linear intercept length was was a sufficient estimate of the average grain size for the constituents investigated in this project.

For dual-phase microstructures containing a substantial amount of each phase, ASTM E1181 can be used [AST 0]. ASTM E1181 recommends calculating the area fraction of each 'phase', rather than the grain diameter. Using the area fraction technique, the total area of each 'phase' is determined and divided by the total number of grains represented by the total area, as shown in Equation 2.9 [AST 0]. In Equation 2.9, the average grain area is denoted by A_{ave}, the total grain area is represented by A_{tot} and n_{tot} corresponds to the number of grains represented by the total area.

$$A_{ave} = \frac{A_{tot}}{n_{tot}} \tag{2.9}$$

2.5 Mechanical Testing

The term "mechanical behaviour" includes deformation and fracture characteristics under tensile, compressive or multiaxial stresses [Dieter 00]. There are many properties that fall under this category, including hardness, YS, UTS, percent elongation (% EL or ductility), work hardening coefficient (n) and Young's Modulus of

elasticity (E). The focus of this project was to assess the mechanical behaviour in terms of hardness and uniaxial tensile behaviour and, as such, only these two testing techniques will be described in the following sections.

2.5.1 Hardness Testing

Hardness is the ability of a material to resist deformation during indentation. Hardness tests involve pressing an indenter of known geometry and material type into the test specimen, followed by quantifying the resulting hardness of the specimen using the correct scale for the corresponding indenter. There are several classifications of hardness tests based on the type of measurement (indentation dimensions or depth of indentation), magnitude of the indentation load (macrohardness, microhardness or nanoindentation) and load conditions (static or dynamic). There are various indenters that can be used to measure hardness, including Brinell (spherical balls), Rockwell (conical-shaped indenters), Vickers or Knoop (pyramidal) indenters. Rockwell hardness tests involve determining the depth of the indentation at a prescribed load and converting this value to a dimensionless hardness value which is inversely related to indent depth. There are several different Rockwell indenters that are available based on the type of material being investigated; for example, a diamond indenter is used for steel, hard cast irons and titanium whereas a steel ball is used for softer steel, aluminium alloys and copper alloys. The different indenter tips correspond to different Rockwell scales, ranging from Rockwell A to Rockwell V, although the A, B and C scales are most common. Brinell, Vickers and Knoop hardness tests record hardness as the indenter load (kgf) supported by the area of indentation (mm^2) which is measured using a microscope with a built-in scale.

Macrohardness tests involve indenter loads greater than 1 kgf; more specifically, Vickers tests can use loads up to 120 kgf, Rockwell tests use indenter loads from

15 to 150 kgf and Brinell tests use indenter loads in the range of 500 to 300 kgf. Microhardness tests use indenter loads of 1 gf to 1000 gf and are performed using Vickers and Knoop indenters.

Nanoindentation tests use a range of indenter loads that may be as small as 0.1 mN with indenter depths of approximately 20 nm [Revankar 00]. More specifically, a Berkovich diamond indenter tip is used for nanoindentation and microindentation tests. The configuration of the Berkovich indenter is such that the surface areas of the indents are identical to those made by a Vickers indenter for the same penetration depth [Yovanovich 06]. Rather than measuring the direct size of the resulting indents, the contact area for each indent is calculated using the depth measurement and the shape of the indenter; however, the comprehensive explanation of nanoindentation tests is presented elsewhere [Yovanovich 06] and will not be discussed further here.

There are several international standards (ASTM A 384, ASTM E 18, BS EN ISO 6508-1, and JIS B 7726 for example) that detail the specific operating conditions for the various hardness tests, as well as provide conversion tables that list equivalent hardness values in various units so that multiple hardness tests using different indenter tips are not required. Furthermore, correlations between the various hardness tests can be found in graphical form as a fast comparison [Revankar 00].

Hardness values can be correlated with grain size according to a Hall-Petch relationship shown in Equation 2.10, where H_0 and K_H are constants and d is the average grain size (same as the 'd' parameter used in the Hall-Petch relationship for yield strength, shown in Equation 2.4). The hardness values can be plotted as a function of grain size (more specifically, by plotting the inverse of the square root of d) to determine whether the experimental hardness values follow the Hall-Petch relationship.

$$H = H_0 + K_H \cdot d^{-1/2} \tag{2.10}$$

Hardness tests are commonly performed on metallic and non-metallic materials as they are fast, simple, inexpensive and provide valuable information about the nature of the sample without performing detailed and time-consuming in-depth experiments such as electron microscopy. Hardness tests give a quick indication of the mechanical properties of the specimen without substantial sample preparation; however, hardness is only one of the important properties that are used to describe a material's mechanical performance.

2.5.2 Tensile Testing

Tensile tests are performed on metallic materials in order to identify the deformation behaviour of a sample including the YS, UTS, %EL and E. Uniaxial tension tests involve gripping a specimen of known and standard geometry from opposite ends in a load frame of a tensile test machine. The sample is then subjected to continually increasing uniaxial loads while observing and measuring the resulting sample elongation using an extensometer. Data is collected and recorded as load (kg) and extension (mm). The load, or force, is commonly converted to engineering stress via Equation 2.11, where engineering stress is denoted by σ_{eng}, A_0 is the original cross section area and F is the instantaneous load [Dieter 00]. Similarly, engineering strain is calculated from extension using Equation 2.12, where l is the measured extension and l_0 is the original gauge length of the specimen. There are several international standards describing the sample geometry and testing procedure, as described in ASTM E 8M-04 [AST 04].

$$\sigma_{eng} = F/A_0 \tag{2.11}$$

$$\epsilon_{eng} = l - l_0/l_0 \tag{2.12}$$

A typical engineering stress-engineering strain curve is shown below in Figure 2.15. This type of curve is called a "round-house" engineering stress-engineering strain curve as the stress exhibits a circular pattern after the initial linear region. Region A corresponds to the elastic regime whereby stress linearly increases as a function of strain until the yield point is reached, denoted by Point 1 in Figure 2.15. If the load was removed in this region, the stress value would follow the linear path to the origin since no permanent deformation would have occurred, but rather only the elastic stretching of bonds would be experienced. For this type of stress-strain curve, the yield strength is determined by superimposing a tangent line with an equivalent slope to the elastic region noted by region A at an x-axis (strain) value of 0.02 % [Dieter 00]. After the yield strength is reached, dislocations begin to move and plastic deformation ensues (section B) until plastic instability (Point 2 in Figure 2.15). Point 2 corresponds to the ultimate tensile strength of the material and also signifies the beginning of necking, which is a process in which the load applied to the sample is concentrated in a reduced cross section rather than the entire sample. Section C in Figure 2.15 corresponds to the necking region, during which the engineering stress decreases as engineering strain increases. This occurs since engineering stress is calculated using the instantaneous force and the initial cross sectional area, rather than the instantaneous area. The instantaneous area is accounted for in true stress-strain curves.

Engineering stress-engineering strain curves do not reflect the actual load conditions from the point of necking to the point of fracture as the engineering stress is calculated based on initial cross sectional area. Furthermore, no information is provided about the work hardening coefficient, which represents the amount of work

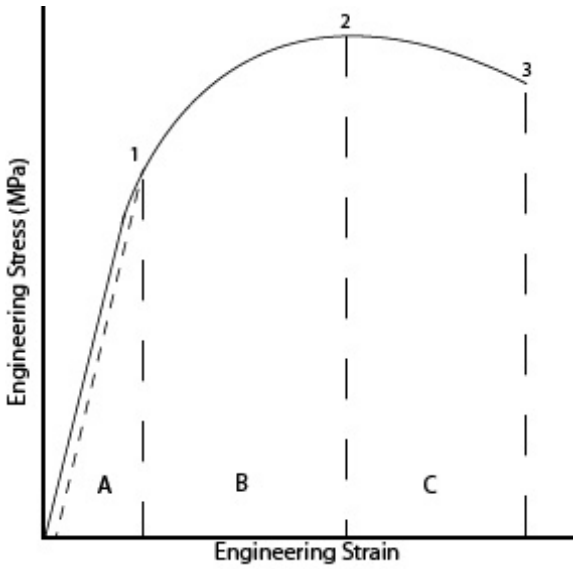

Figure 2.15: Typical engineering stress-strain curve with "round-house" behaviour.

hardening that can be achieved during plastic deformation of a sample from the YS to the UTS value. In order to determine the work hardening coefficient, the experimental load and elongation values must be converted to true stress and true strain values according to Equations 2.13 to 2.15 [Abbaschian 94]. The true stress is given by σ_{true}, the engineering strain is given by ϵ_{eng} and the true strain is given by ϵ_{true}. The work hardening coefficient, n, is determined by plotting $\ln\sigma_{true}$ against $\ln\epsilon_{true}$ in Equation 2.15 with the slope value corresponding to the work hardening coefficient. These equations are only valid up to the onset of necking and cannot be used at stress values above the UTS value.

$$\sigma_{true} = \sigma_{eng}(1 + \epsilon_{eng}) \tag{2.13}$$

$$\epsilon_{true} = ln(1 + \epsilon_{eng}) \tag{2.14}$$

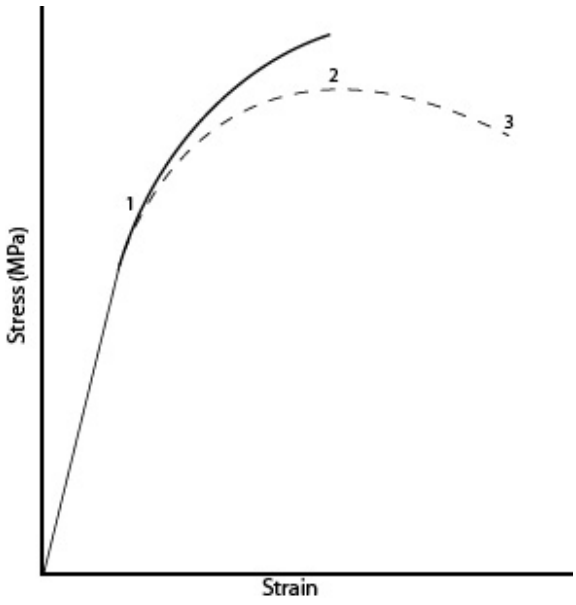

Figure 2.16: True stress-strain curve corresponding to the engineering stress-strain values in Figure 2.15.

$$ln\sigma_{true} = n \cdot ln\epsilon_{true} + k \tag{2.15}$$

A schematic illustration of a true stress-strain curve is shown in Figure 2.16. The true stress-true strain curve is superimposed on the round-house engineering stress-engineering strain curve shown in Figure 2.15 for comparison. The engineering stress-engineering strain curve in Figure 2.16 is the dotted line with points 1, 2 and 3 corresponding to the YS, UTS and final fracture.

2.6 Project Goals

Microalloyed steels are used in a wide variety of applications such as truck frame rails, transmission pipelines, structural steels, crane booms, bridges and ship plates [Collins 01, Vander Voort 92]. This project will focus specifically on X80

steel intended for use in Arctic pipeline applications such as the MacKenzie Valley pipeline which is scheduled for installation in North America. These pipelines are intended to transport natural gas from the Arctic (MacKenzie Delta or Prudhoe Bay) to the United States of America at distances in excess of 3000 km and operating at pressures up to 17 MPa (2500 psi) [Collins 01]. Alliance Pipeline successfully constructed a high strength, steel line pipe that transports natural gas from Fort St. John, British Columbia to Chicago, Illinois at an operating pressure of 1750 psi (12 MPa). The metallurgical properties that were required for the Alliance Pipeline include a YS of 540 MPa, a UTS of 634 MPa, 42 % EL and a Charpy impact energy value of 347 J at -5 °C [Collins 01]. The Mackenzie Gas Project pipeline demands a minimum yield strength of 550 MPa (Grade 550 or API X80), an outer diameter of 762 mm and and a wall thickness of 16.2 mm [Collins 09].

Pipeline steels are required to have high YS and UTS values while simultaneously exhibiting good weldability, good toughness at low temperatures, excellent corrosion resistance and a high n value. Microalloyed steels are therefore excellent candidates for pipelines due to the low carbon levels (translating to good weldability) and microalloying additions (which contribute to strengthening through both precipitation strengthening and grain refinement). Microalloyed steels also have high toughness due to TMCP which prevents austenite recrystallization during rolling and incorporate accelerated cooling practices which promote a fine-grained structure upon cooling. A high degree of work hardening is desirable for steels to be employed in strain-based pipeline designs due to the high levels of compressive and tensile stresses. More specifically, Arctic pipelines require steels with high buckling resistance since the ground movements in permafrost regions induce large plastic strains on the pipelines [Mitsuhiro 08]. Buckling resistance is achieved with a high work hardening coefficient and a round engineering stress-engineering strain curve

and, as a result, is highly dependent on microstructure.

The goal of this research project was to determine the effect of thermal treatment on microstructure development and the subsequent relationship between microstructure and mechanical behaviour of high strength microalloyed line pipe steel in an effort to enhance work hardening characteristics. The relationship between thermal history and microstructure development was determined by applying different thermal schedules to X80 steel specimens under zero strain conditions; as a result, the effect of deformation (including strain-induced precipitation and phase transformation) was not studied. The aim of this study was to investigate the possibilities of manipulating the microstructures of X80 steel products without the influence of deformation. The microstructures obtained from the thermal treatments were characterized using optical and electron microscopy and the amounts and morphology of the constituents were determined using image analysis techniques. The relationship between microstructure and mechanical properties was obtained by subjecting the samples to mechanical testing and comparing the mechanical behaviour with the quantified microstructures and the corresponding heat treatment. Although the mechanical behaviour of materials includes deformation and fracture characteristics under tensile, compressive or multiaxial stresses [Dieter 00], this research project focused on the mechanical behaviour in terms of hardness and uniaxial tensile characteristics. The final desired goal was to determine the thermal treatment parameters that resulted in the highest work hardening coefficient.

Chapter 3

Continuous Cooling Transformation (CCT)

A continuous cooling transformation (CCT) diagram is useful to predict the final microstructure that will result from a particular continuous cooling rate. The A_{c1} and A_{c3} transformation temperatures and the phase transformation temperatures are included on the CCT curve along with the corresponding constituents. The CCT diagram constructed for the X80 steel used in this project was generated under no-strain conditions (i.e., no deformation was applied to the sample during heat treatment). As a result, strain-induced precipitation and strain-induced phase transformation were not studied and the resulting CCT curve only reflects the microstructure and transformation temperatures that correspond to an X80 microalloyed steel under no strain conditions.

This chapter will outline the operating conditions and the experimental results used to generate the CCT diagram. General experimental techniques were described in Section 2.2, but the specific equipment models and experimental parameters for the CCT curve tests will be discussed in Section 3.1. The dilation results and final

CCT diagram will be presented in Section 3.3. The thermal expansion coefficients (TECs) for both the austenite and ferrite phases were determined and are included in Section 3.3.4.

3.1 Experimental Methods

3.1.1 Thermal Cycling - Gleeble Thermomechanical Simulator

A Gleeble thermomechanical simulator was used to apply various thermal treatments and create various microstructures in the X80 samples. A Gleeble machine is capable of applying both tensile and compressive stresses on a metallic sample at high temperatures. Various process parameters can be measured including force, stroke, temperature and dilation [Inc. 12]. Metallic specimens are heated using resistive heating between the grips (typically copper to provide high current to the sample while minimizing losses to the grips) and cooling rates are controlled using either the controlled resistive heating or through a water quenching unit that can achieve cooling rates up to 150 °C/s.

The Gleeble simulator is connected to a control tower where heating and cooling rates as well as force/stroke restrictions can be programmed. A dilatometer is used to record changes in length which correspond to changes in TEC values of the various phases present in the sample. For circular samples, the change in length recorded by the dilatometer corresponds to a change in diameter. The uniform expansion or contraction detected by the dilatometer is indicative of the expansion and contraction due to the combined effect of phase transformation and thermal effects.

The thermomechanical simulator used to thermally treat the CCT specimens was a Gleeble 3800, located at the EVRAZ Inc. NA research facility. The steel

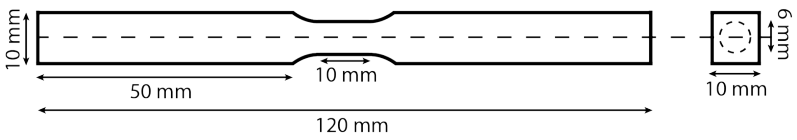

Figure 3.1: Sample dimensions for CCT curve specimens.

samples used to create the CCT diagram were obtained from as-rolled plate that was subjected to standard TMCP techniques according to the designated operating conditions (plate width, casting speed, number of passes in the rolling mill, cooling rate on the run-out table, etc.) for the desired end product. The samples were machined into 10 mm square-ended bars with a 6 mm diameter reduced cross section as shown in Figure 3.1. The rolling direction was not indicated in any of the samples.

3.1.2 Sample Preparation

Once the Gleeble samples were successfully heat treated, they were cut using a horizontal band saw into smaller pieces (approximately 30 mm in length), ensuring that the center of the original specimen was contained in the cut section as this section corresponds to the most representative microstructure. The 30 mm pieces were then sectioned in half lengthwise using a diamond blade in order to expose the centerline. The samples were then mounted in a 1 1/4" bakelite mount using a hot press and the back edges were rounded using a belt grinder. The samples were then ground using progressively finer silicon carbide grit papers; more specifically, 60, 120, 320, 400, 600, 800 and 1200 grit size. Final polishing was conducted with 1 μm diamond paste followed by 0.05 μm alumina slurry. In between each grinding step, the samples were rinsed thoroughly with water. Between the polishing stages, the samples were washed with water, rinsed with ethanol and dried with air to prevent contamination between polishing steps.

After the samples were polished to a flat, shiny and scratch-free surface, they were chemically etched to reveal certain microstructural features. A simple solution of 2 % Nital (2 mL of nitric acid in 98 mL ethanol) was used as a general etch to observe the overall microstructure. This etch is performed to preferentially corrode ferrite grain boundaries in low carbon steels and also enhances the interface between carbides and the matrix [Benscoter 02, Vander Voort 01]. The dissolution of ferrite is a function of crystal orientation and, as such, ferrite grains with a preferential orientation will corrode at a faster rate than those with a different orientation [Vander Voort 01]. One major disadvantage of the conventional Nital etch is that specimens must be over-etched in order to develop significant contrast and, as a result, bainite and martensite may appear the same "shade" as the grain boundaries [LePera 79]. The fact that grain boundaries are preferentially etched with Nital is beneficial for grain size measurements but images that are used for phase quantification require some post-image processing to remove the grain boundary area from the calculated phase fraction values.

3.2 Microscopy

The sample preparation techniques described in Section 3.1.2 are specific to microscopy analysis and hardness testing. Microscopy analysis was conducted using both optical and electron sources, which will be detailed in the following sections.

Optical Microscopy

The microstructures of the X80 steel samples investigated in this project were evaluated in two different optical microscopes. A Nikon Epiphot TME-017 optical microscope was used at the EVRAZ Inc. NA research facility in order to image the CCT curve specimens before SEM analysis. The images were analyzed using

Clemex Vision Professional Edition 5.0 software, version 014-5.0.014z, that used a Sony XC-ST50CE camera to collect the images from the microscope.

High resolution color images were obtained at the University of Alberta using a ZEISS AxioImager.M2M optical microscope equipped with an AxioCam HRc camera. This optical microscope was used primarily for the samples that were etched for color metallography since the polishing and etching equipment and chemicals were available at the University of Alberta.

Scanning Electron Microscopy (SEM)

SEM was used in order to view the microstructure at higher resolution than was capable with optical microscopy. The samples were polished and etched in the same manner as that for optical microscopy using the 2 % Nital etchant to reveal the grain boundaries within the microstructure. The SEM instrument used was a Philips XL Series DX4-i XL-30 equipped with a thermionic tungsten gun and an oil diffusion pump. This microscope is also equipped with an EDX detector although it was not used in this work. Images were obtained at 10 kV in SE imaging mode at 0° tilt. SEM SE images were collected to view the microstructure at high magnification (most commonly at 5 000x but occasionally at 20 000x magnification) and to help quantify the microstructure.

Transmission Electron Microscopy (TEM)

The TEM samples were investigated using an operating voltage of 200 kV in a JEOL JEM-2010 TEM equipped with a CCD camera and EDX detector.

Focused Ion Beam (FIB)

The TEM samples investigated in this project were prepared using a Hitachi NB5000 joint FIB-SEM located at the National Research Council in the National Institute of Nanotechnology located at the University of Alberta. The NB5000 was used to prepare electron transparent sections for TEM analysis by using the microsampler/liftout method detailed by Mayer et. al [Mayer 07]. Section 2.3.4 detailed the preparation method and, as such, it will not be discussed further here. For bulk milling and material removal, an accelerating voltage of 40 kV was used with currents between 20 nA and 64 nA. Currents ranged between 3 nA to 1 nA with an accelerating voltage of 40 kV during sample thinning. Final polishing was accomplished using accelerating voltage of 10 kV and currents of 80 pA and less.

3.2.1 Mechanical Testing

The only mechanical test that was performed on the CCT specimens was macrohardness indents, which will be discussed in the following section.

Hardness Testing

Section 2.5.1 described some of the various hardness tests that are commercially available. Vickers macrohardness tests were conducted on the CCT specimens using a Mitutoya AVK-C1 Hardness Testing Machine with a 10 kg indent load. Five indents were made per sample to obtain average hardness values and the standard deviation for each specimen.

3.3 CCT Curve Development

3.3.1 A_{c1} and A_{c3} Transformation Temperatures

The first step in generating a CCT diagram is determining the transformation temperatures corresponding to the onset and completion of the ferrite to austenite transformation during heating; more specifically, A_{c1} and A_{c3} temperatures, respectively. Since only the heating procedure is important for determining the A_{c1} and A_{c3} transformation temperatures, a very slow cooling rate of 2 °C/min was chosen to mimic near-equilibrium conditions. The test performed to determine the A_{c1} and A_{c3} transformation temperatures involved heating the test coupon to 1100 °C at 2 °C/min followed by continuously cooling the sample to room temperature at 10 °C/s. As mentioned in Section 3.1.1, a dilatometer measures linear changes in sample length due to the combined effects of phase transformation and thermal expansion/contraction. As a steel sample is heated, it will expand due to the increased thermal energy but will also contract due to changes in the cubic structure between ferrite and austenite. As discussed in Section 2.1.1, fcc austenite is a closer packed structure than α-ferrite; therefore, the transformation from α-ferrite to austenite corresponds to a volume decrease. The volume change associated with transformation is much more significant than the thermal expansion and, as such, the thermal expansion is excluded from the overall analysis. As a result, the onset of austenite transformation on cooling is easily detected as the thermal contraction of austenite is counteracted and overpowered by the volume expansion due to phase transformation [Eldis 78]. For circular specimens, such as were used for the A_{c1} and A_{c3} test (Figure 3.1), the linear values recorded by the dilatometer are changes in diameter, which correspond to volumetric changes.

The corresponding dilation curve obtained during heating is shown in Figure 3.2

for the A_{c1} and A_{c3} test. The A_{c1} and A_{c3} data is plotted as dilation versus temperature; therefore, the slope at any given point can be calculated by calculating the change in y value (dilation) divided by the change in x value (temperature) for two points on the curve. The slope is given in units of mm/°C and is a function of the thermal expansion coefficient (given in units of 1/°C). In order to calculate the thermal expansion coefficient for each phase, the slope can be determined for the region corresponding to each phase and subsequently divided by the diameter of the sample (for circular specimens). Changes in slope correspond to phase transformation: the ferrite to austenite transformation is associated with a volume decrease and, therefore, the resulting dilation curve should show a distinct decrease in slope. Dilation studies define the transformation temperature as the exact temperature at which the dilation data changes slope; or rather, the point at which a tangent line (drawn using a significant portion of data with a uniform slope) deviates from the dilation curve [Eldis 78]. More specifically, the ferrite to austenite transformation temperature (A_{c1}) can be determined by drawing a tangent line to the linear section of the curve corresponding to the ferrite region and noting the exact point at which the tangent line deviates from the original curve. Similarly, the A_{c3} temperature is obtained by drawing a tangent line to the austenite region and identifying the temperature at which the tangent deflects away from the experimental dilation data.

Since the tangent line is a straight line, it is governed by an equation of the form $y = mx + b$. The tangent line can be drawn manually and the linear regression equation can be calculated using two data points; however, this method is more susceptible to a subjective line of best fit as it introduces significant human error and a lack of consistency. As a result, various techniques and "guidelines" to hand-draw the tangent lines will not be discussed further. Computational methods can also

be used to calculate the equation of the linear regression line as well as determine the amount of error associated with the line. Computational methods are much simpler and more efficient than hand calculations, as the equations governing the quantification of linear regression error (which are described elsewhere [Chapra 02]) are cumbersome and tedious when evaluating several hundreds (or thousands) of data points.

The coefficient of determination, also referred to as the R^2 value, can be determined using computational methods and is an indication of how well an equation fits the data. An R^2 value of 1 means that the equation explains 100 % of the variability in the data, whereas an R^2 value of 0 indicates that the equation does not represent any of the data. An R^2 value close to 1 therefore means that there is a high probability that the data points will be actual solutions to the proposed equation; in other words, the equation fits the data very well [Chapra 02]. In order to calculate the linear regression equation for the tangent line using computational methods, a range of data is selected that accurately represents the linear section of interest (i.e., the section with constant slope) and the governing linear regression equation for the tangent line can be determined from that set of data.

The tangent lines that were calculated to determine both the A_{c1} and A_{c3} temperatures were obtained by maximizing the R^2 value to a minimum value of 0.990. Based on the shape of the dilation curve in the lower temperature region, two tangent lines were drawn for the A_{c1} temperature. The lower tangent line, A, represents the linear region of the dilation curve from 625 °C to 700°C and had an R^2 value of 0.999. The A_{c1} temperature predicted using this lower tangent was 700 °C. Although this temperature seems reasonable based on the methodology used to determine the temperature, it does not makes sense when considering the chemical composition of these steel samples. According to Figure 2.1, the A_1 temperature for a eutectoid

steel with 0.77 wt% carbon is 727 °C, and the A_1 temperature increases as carbon content decreases. The A_1 temperature therefore had to should be greater than 727 °C, thus the proposed value of 700 °C was considered incorrect. Although the equilibrium transformation temperatures shown in the Fe-Fe_3C phase diagram shift with the addition of alloying elements, the alloying contributions for this system are minimal and are therefore irrelevant. Based on these considerations, a second tangent line (B) was calculated from the linear region of 710 °C to 740 °C. Tangent line B had an R^2 value of 0.994 and provided a transformation temperature of 740 °C. This value was more reasonable based on the Fe-Fe_3C phase diagram; thus, the A_{c1} temperature was determined to be 740 °C. The A_{c3} temperature was investigated using the same procedure and was determined to be to be 895 °C.

The dilation changes slope above 950 °C which could be due to slippage in the dilatometer; however, this phenomenon was not investigated further. The values for the two A_{c1} temperatures and the A_{c3} temperature are included in Figure 3.2 for clarification. The lower A_{c1} temperature is labeled as A_{c1A} and corresponds to the first tangent line (A) drawn from the dilation data, whereas the higher transformation temperature (A_{c1B}) represents the second tangent line (B) that was modified from the first tangent line based on the comparison with the expected A_1 value from literature. The A_{c1} and A_{c3} temperatures determined using dilatometry can include errors of ± 35 °C [Eldis 78].

3.3.2 Austenitization Investigation

The Gleeble 3800 thermomechanical simulator used for both the CCT and ITT specimens had two different jaw configurations to hold a sample. The first type of jaw is used when force on the sample is programmed to a value of zero and the stroke is allowed to fluctuate to compensate for the programmed constraint on the

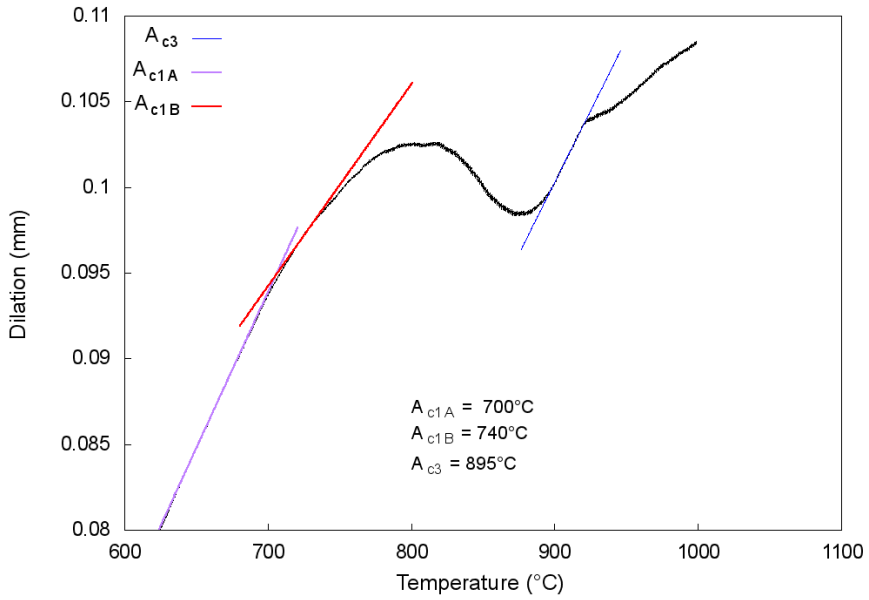

Figure 3.2: Dilation curve corresponding to the determination of A_{c1} and A_{c3} transformation temperatures.

force parameter. The second type of jaw configuration is a low-force jaw, which provides free movement within the chamber to allow for expansion and contraction of the sample during heating and cooling; i.e., no force is applied to the sample as it experiences volume changes due to thermal and phase transformation effects. The first set of jaws was used for all the CCT curve specimens. Tests performed with the first set of jaws resulted in a consistent contraction during the austenitization process (the isothermal hold at 945 °C). Since the low-force jaws allow the sample to expand and contract freely, the dilation data should not show a contraction during the isothermal hold at 945 °C. If this is the case, the sample contraction during austenitization observed with the first jaw configuration would contribute to stress relaxation.

Figure 3.3 shows the dilation data during austenitization for all CCT curve specimens. The beginning portion of the curve (section a in Figure 3.3) corresponds to

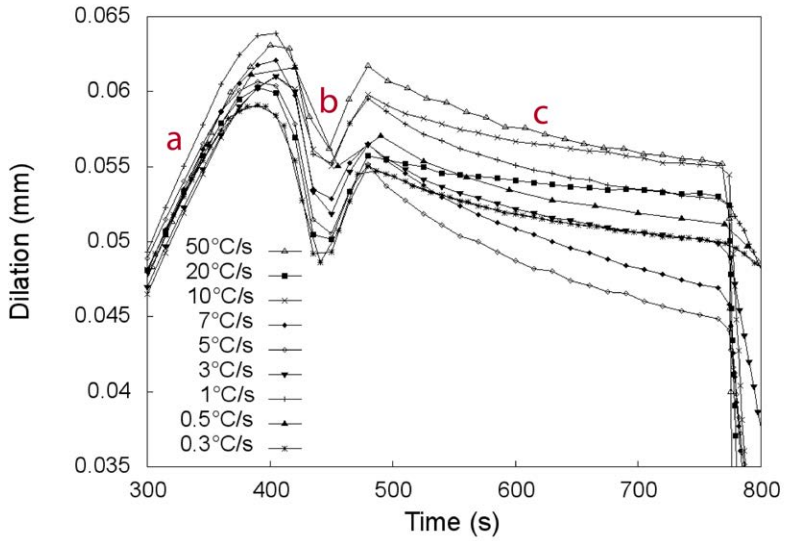

Figure 3.3: Dilation data for CCT specimens during austenitization at 945 °C for 5 minutes using regular jaws.

ferrite expansion. The middle portion of the curve, labeled as b in Figure 3.3, illustrates the transformation from ferrite to austenite as evidenced by the sample contraction and subsequent expansion. Section c in Figure 3.3 represents the 5 minute isothermal hold at the austenitization temperature of 945 °C. The dilation data from each CCT curve specimen is included in Figure 3.3 to demonstrate the reproducibility of this effect regardless of thermal history.

The contraction observed in Figure 3.3 was tentatively attributed to stress relaxation as the sample showed a decrease in length (more specifically, diameter for circular specimens) as time at a constant temperature increased, but the phase transformation from ferrite to austenite was already complete. Ideally, the dilation curve should be horizontal during an isothermal hold since the transformation to austenite has already occurred (therefore, no change in dilation from phase transformation is expected) and the temperature was not changing (similarly, no change in dilation due to thermal expansion is expected). However, the dilation values showed

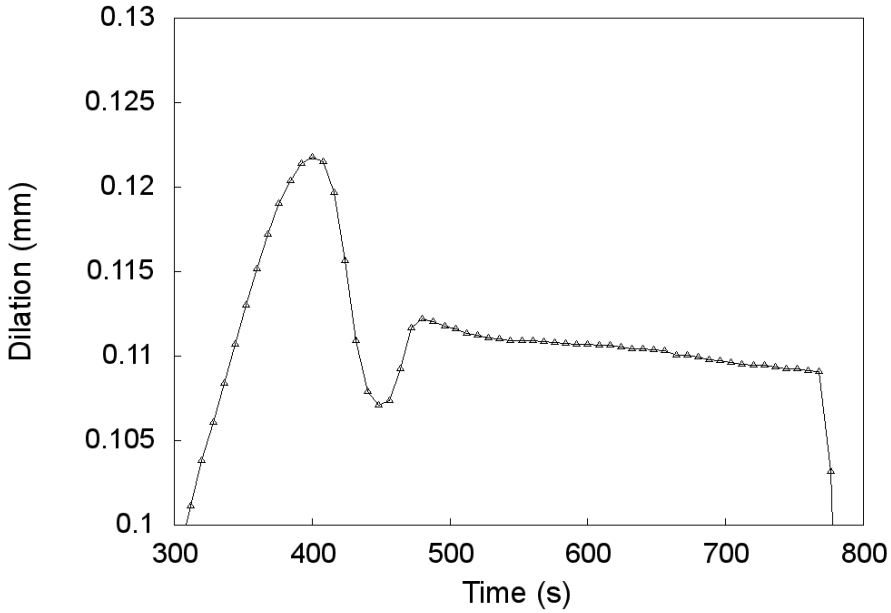

Figure 3.4: Dilation data during austenitization at 945 °C for 5 minutes using the low-force jaws.

evidence of contraction as a function of time, indicating that the sample was relaxing or releasing stored energy during the heat treatment at 945 °C. In order to confirm this hypothesis, isothermal hold tests were repeated using the low-force jaws to allow the sample to expand and contract freely without constraint from the sample grips. Figure 3.4 shows the dilation curve during austenitization at 945 °C for 5 minutes using low-force jaws.

The contraction during the isothermal hold at 945 °C is less severe in Figure 3.4 than in Figure 3.3; however, contraction was still observed with the low force jaws. The contraction observed for the CCT samples in Figure 3.3 was 0.006 to 0.012 mm, whereas the contraction observed in Figure 3.4 using the low-force jaws was 0.003 mm. As a result, the effect noticed in Figure 3.3 cannot be attributed to stress relaxation and the cause of this effect was not determined.

Table 3.1: Detailed thermal schedule for all CCT samples.

Sample	Austenitization Temperature (°C)	Austenitization Time (min)	Cooling Rate (°C/s)
D3	945	5	50
D4	945	5	20
D6	945	5	10
D7	945	5	7
D8	945	5	5
D9	945	5	3
D12	945	5	1
D10	945	5	0.5
D11	945	5	0.3

3.3.3 Transformation Temperatures during Continuous Cooling

After the A_{c1} and A_{c3} temperatures were determined, the temperature required for austenitizing the samples was determined for all the subsequent CCT tests. The austenitizing temperature was chosen to be the A_{c3} temperature plus 50 °C to ensure complete transformation from the starting microstructure (a mixture of various microconstituents) to austenite.

The CCT curve was developed by applying nine different cooling rates to the CCT specimens, ranging from fast (50 °C/s) to slow (0.3 °C/s). The samples were first heated to the austenitizing temperature of 945 °C at a slow heating rate of 2 °C/s to ensure near-equilibrium heating conditions [Eldis 78]. The samples were held at 945 °C for 5 minutes to ensure a homogeneous austenite structure before the various cooling rates were applied. The full heat treatment schedule and sample description for all CCT specimens are shown in Table 3.1.

As mentioned in the previous section, the location of the tangent line on the dilation curve is very subjective and can have a significant impact on the final transformation temperature that is interpreted from the data. This presents a significant problem when creating a full CCT diagram; therefore, a consistent approach

was necessary to prevent human bias and to ensure that each dilation curve was analyzed in an identical manner. Two different approaches were taken to determine the transition temperatures from the dilation data based on different criteria for the data range that was used to calculate the tangent line. The first method selected the data range for the tangent curve based on the dilation curve for the slowest cooling rate (0.3 °C/s for sample D11). The high and low temperature ranges were optimized to a minimum R^2 value of 0.999 and these temperature ranges were applied to all dilation curves regardless of the cooling rate. This method will be referred to as CT for simplicity. The slowest cooling rate was chosen as the model since this cooling rate can be approximated to near-equilibrium conditions and, as such, the temperature ranges should provide the most accurate transition temperatures for both the high and low tangents. The optimized temperature ranges determined from the 0.3 °C/s cooling rate were 920 °C to 840 °C (with an R^2 value of 0.9995) for the high tangent and 465 °C to 220 °C (corresponding to an R^2 value of 0.9999) for the low tangent. As mentioned, the CT method applied the same temperature range for the high and low tangents to all dilation curves, resulting in various R^2 values for the tangent equations.

The second approach that was employed in this study was to optimize the R^2 value for both high and low tangents for every individual cooling rate. The temperature ranges were varied to achieve a minimum R^2 value of 0.98 (most R^2 values were optimized to 0.999 but some tangent data could only be optimized to 0.98 based on scatter in the dilation data). This second method is referred to as R^2 and the results can be directly compared with the CT method.

An example of the two different methods is illustrated in Figure 3.5. Figure 3.5a shows the 50 °C/s dilation data with both the CT and R^2 method tangents included on the lower temperature linear region. Figure 3.5b shows the dilation data used to

calculate the CT tangent and Figure 3.5c shows the dilation data used to generate the R^2 tangent. Although the coefficients of determination are similar for the two methods (0.998 versus 0.999), the R^2 method fits the entire dilation curve better than the CT method, as shown in Figure 3.5. The CT tangent line intersects the dilation data rather than remaining tangential to it, whereas the R^2 method generates a true tangent line to the original data. As a result, the R^2 method was chosen as the better method to determine transformation temperatures for each cooling rate.

The dilation curves with the corresponding high and low tangents for both the CT method and R^2 methods are shown in Figures 3.6 to 3.14. The results from the CT method are shown on the left (a) of the figures, whereas the tangents and transformation temperatures for the R^2 method are shown on the right of each figure (b). The upper and lower transition temperatures correspond to the transition start and finish temperatures, T_{start} and T_{finish}, respectively. These temperatures were determined by locating the temperature at which the tangent line deviates from the dilation curve, as previously described. More specifically, the T_{start} and T_{finish} temperatures represent the temperature at 0 % and 99 % completion, respectively. The transition temperatures are included with the dilation curves as a direct comparison in addition to comparing the fit of the tangent line to the dilation data through visual inspection.

The results from the CT and R^2 methods shown in Figures 3.6 to 3.14 are similar for the slower cooling rates; however, the higher cooling rates revealed a larger difference between the two methods. The transformation finish temperatures agree quite well for the two methods (within 5 °C) for all cooling rates except 50 °C/s, which had a 40 °C discrepancy between the CT and R^2 methods. There was a larger discrepancy between the CT and R^2 methods for the transformation start temperature. Cooling rates of 5 °C/s and higher resulted in a minimum 30 °C difference

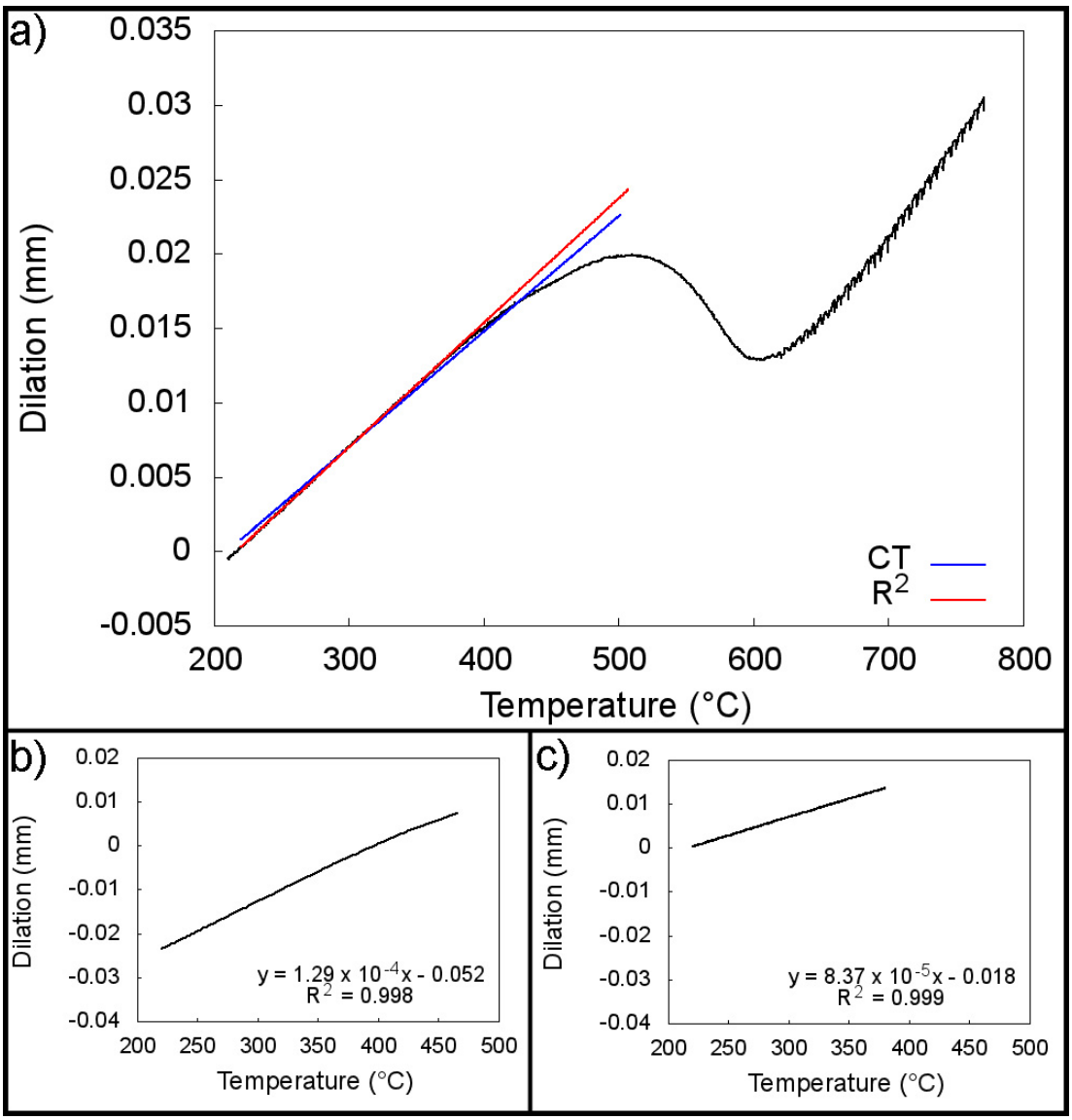

Figure 3.5: Demonstration of the CT and R^2 methods to determine the lower transformation temperature for the 50 °C/s cooling rate: a) dilation data with both the CT and R^2 tangents included on the lower linear region; b) the range of data used to calculate the CT tangent line; c) the range of data used to calculate the R^2 tangent line.

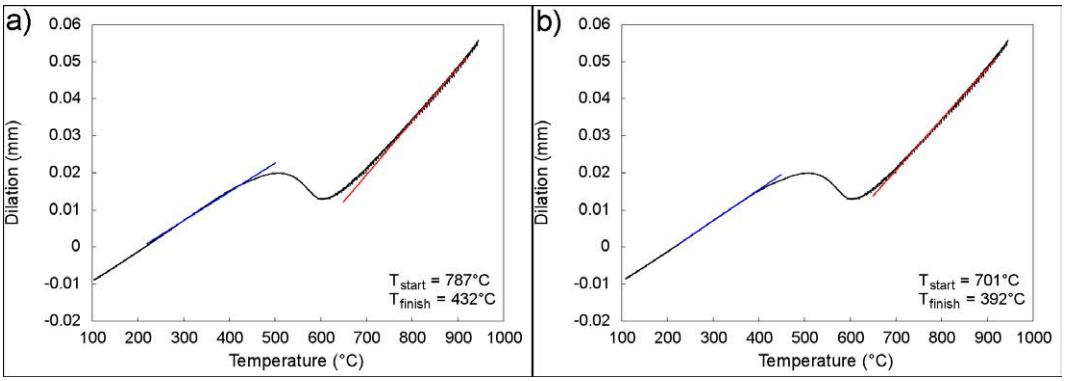

Figure 3.6: Methods to determine the transformation start and finish temperatures for CCT specimen D3 (50 °C/s): a) CT, b) R^2.

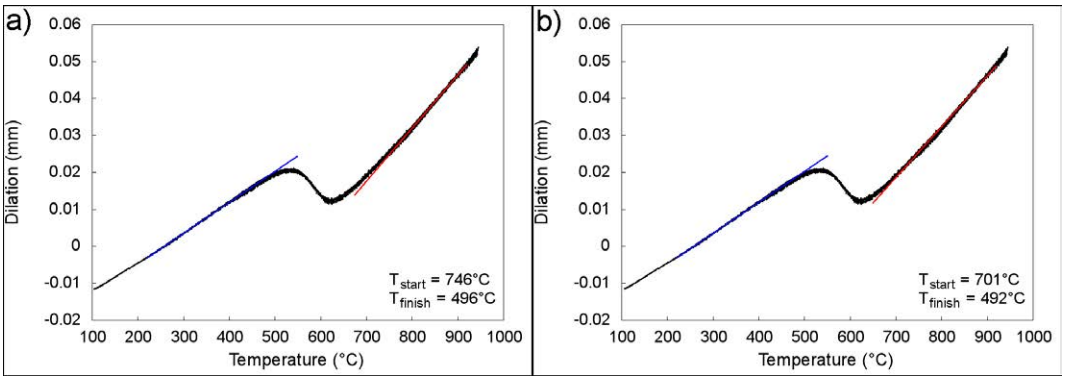

Figure 3.7: Methods to determine the transformation start and finish temperatures for CCT specimen D4 (20 °C/s): a) CT, b) R^2.

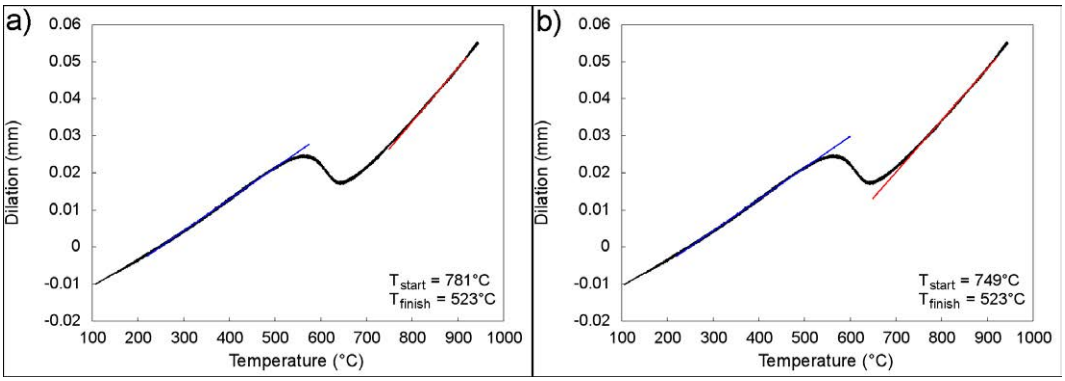

Figure 3.8: Methods to determine the transformation start and finish temperatures for CCT specimen D6 (10 °C/s): a) CT, b) R^2.

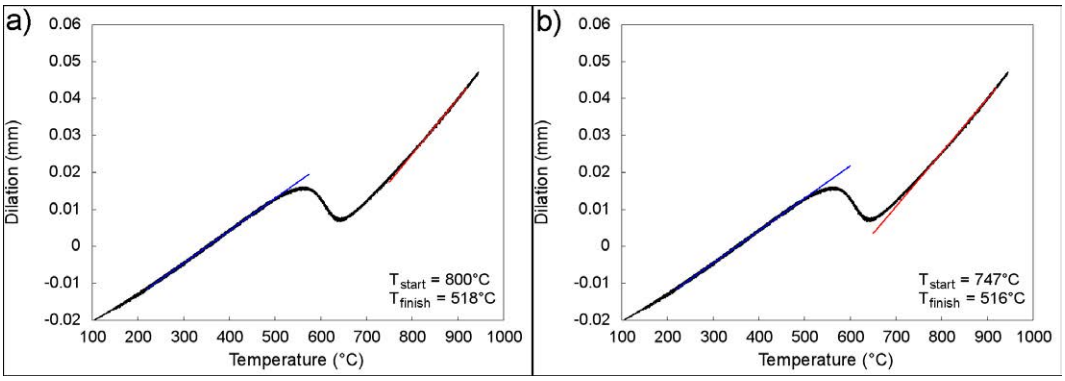

Figure 3.9: Methods to determine the transformation start and finish temperatures for CCT specimen D7 (7 °C/s): a) CT, b) R^2.

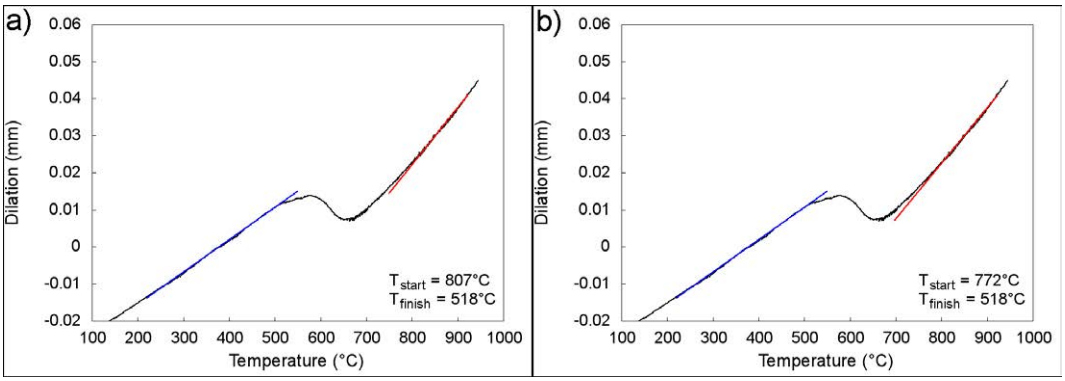

Figure 3.10: Methods to determine the transformation start and finish temperatures for CCT specimen D8 (5 °C/s): a) CT, b) R^2.

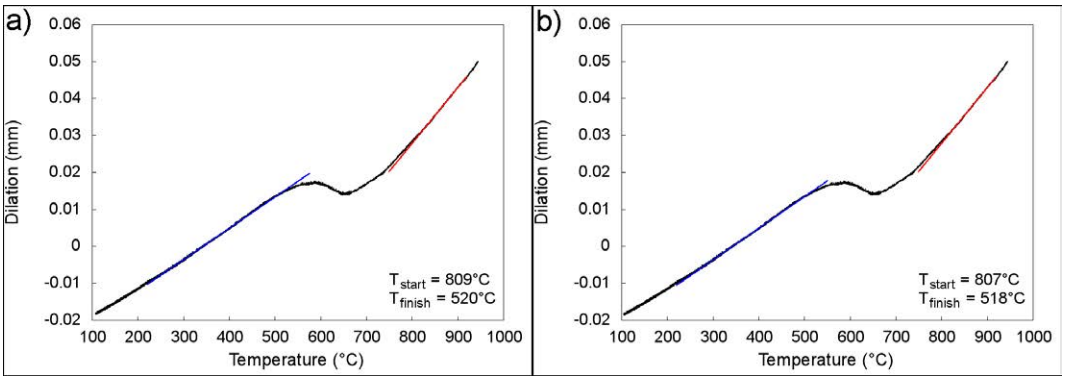

Figure 3.11: Methods to determine the transformation start and finish temperatures for CCT specimen D9 (3 °C/s): a) CT, b) R^2.

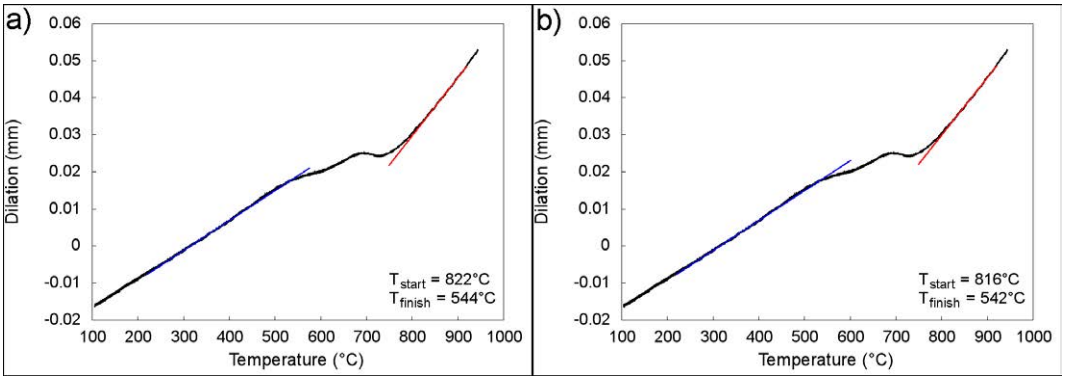

Figure 3.12: Methods to determine the transformation start and finish temperatures for CCT specimen D12 (1 °C/s): a) CT, b) R^2.

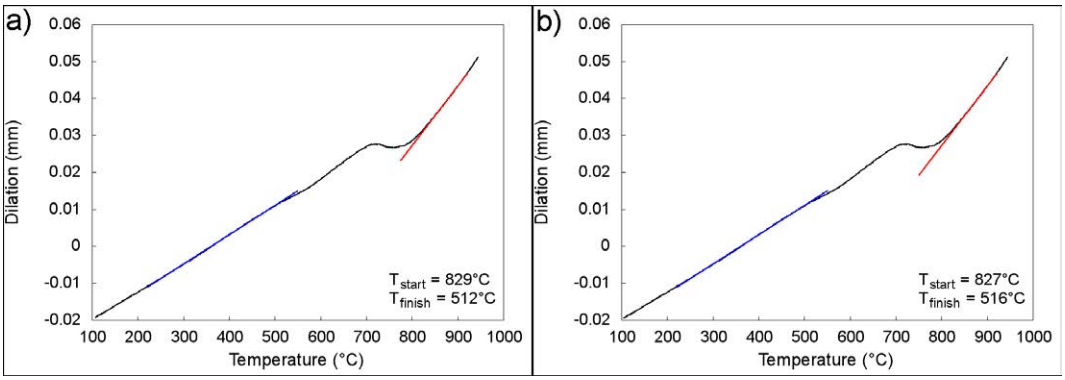

Figure 3.13: Methods to determine the transformation start and finish temperatures for CCT specimen D10 (0.5 °C/s): a) CT, b) R^2.

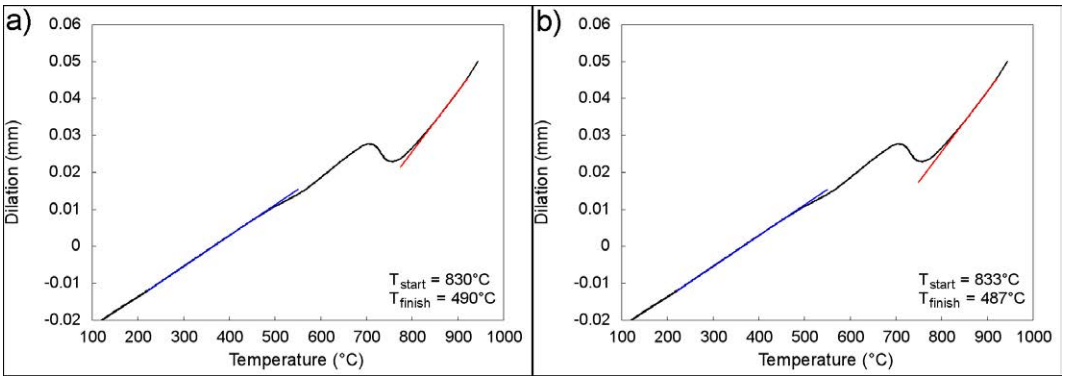

Figure 3.14: Methods to determine the transformation start and finish temperatures for CCT specimen D11 (0.3 °C/s): a) CT, b) R^2.

between the CT method and the R^2 methods, with the CT approach predicting a higher transition temperature. The 50 °C/s cooling rate had the highest difference between the two methods, with the CT method predicting a transformation start temperature that was 85 °C higher than the R^2 predicted temperature.

The tabulated results from the two different methods are shown in Table 3.2. The start and finish transformation temperatures are labeled for each method for direct comparison. There was good conformance between the two methods, which indicates that either method can be used to determine the transformation temperatures with reasonable accuracy. It is important to note, however, that the same method must be applied to all dilation curves to ensure a consistent analysis.

Table 3.2 shows only the transformation temperatures for the beginning and end of total transformation for the different cooling schedules utilized to develop the CCT curve. The fast cooling rates represented a single transformation from austenite to a lower temperature product and, as such, only the upper and lower transformation temperatures were required for the CCT curve. The dilation curves for the slower cooling rates of 1 °C/s, 0.5 °C/s and 0.3 °C/s, however, represented more than one transformation as evident by a "hump" in the dilation data as shown in Figures 3.12,

Table 3.2: Start and finish transition temperatures obtained for both the CT and R^2 methods.

Sample ID	Cooling Rate (°C/s)	CT finish (°C)	R^2 finish (°C)	CT start (°C)	R^2 start (°C)
D3	50	432	392	787	701
D4	20	496	492	746	701
D6	10	523	523	781	749
D7	7	518	516	800	747
D8	5	518	518	807	772
D9	3	520	518	809	807
D12	1	544	542	822	816
D10	0.5	512	516	829	827
D11	0.3	490	487	830	833

3.13 and 3.14. This "hump" corresponds to a second phase or microconstituent that forms and, as such, the intermediate transformation temperature corresponding to this second transformation had to be determined. The second "hump" is illustrated in Figure 3.15, which plots the dilation data for sample D12 in the specific region where the double "hump" occurs.

As previously mentioned, the accuracy of the transformation temperatures is subjective. The thermal expansion curves for austenite and the austenite transformation products are not always linear and can in fact exhibit significant curvature. As G. Eldis explains, "when pronounced curvature is obtained, estimation of isotransformation contours and volume fraction transformation product from the length vs temperature record becomes increasingly inaccurate. These estimates are based on extrapolations of the thermal expansion (contraction) curves for both the austenite and the transformation product aggregate, and the greater the curvature, the more uncertain the extrapolation" [Eldis 78]. Furthermore, Eldis suggests that the temperature at which the austenite begins to transform (i.e., the transformation start temperature) is most accurate to determine. The transformation start tem-

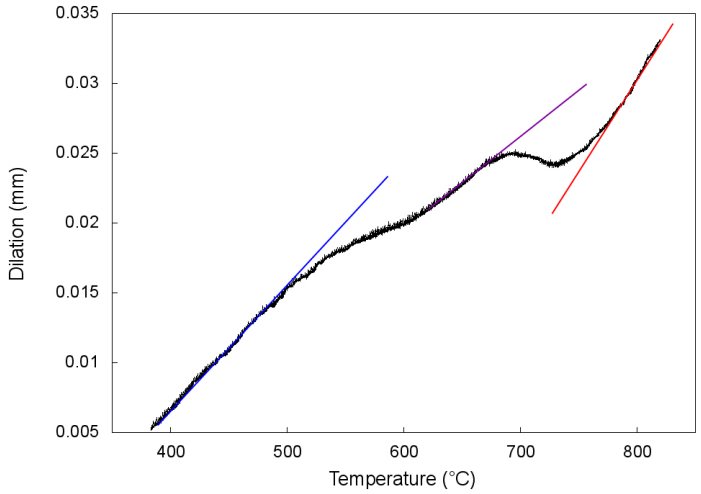

Figure 3.15: Dilation data for sample D12 (1 °C/s) to illustrate the double "hump" indicating a second transformation.

perature has an accuracy of ± 5 °C/s, whereas uncertainties as high as ± 35 °C/s have been noted for lower transformation temperatures [Eldis 78].

Figures 3.12 to 3.14 were re-investigated to determine the intermediate transformation temperatures based on the "double humps" noted above. Figures 3.16, 3.17 and 3.18 show the dilation data and intermediate transformation temperatures for the 1 °C/s, 0.5 °C/s and 0.3 °C/s cooling rates, respectively. The intermediate transformation temperatures were determined using the same procedure outlined above; namely that the transformation temperatures were determined by identifying the exact point at which the tangent line deviates from the dilation curve. There are two intermediate temperatures included in Figures 3.16 to 3.18, T_{inter1} and T_{inter2}, respectively, which correspond to the start and finish temperatures of the intermediate transformation product.

The amount of inaccuracy associated with transformation temperature determination has been discussed and each dilation curve was analyzed in the same way.

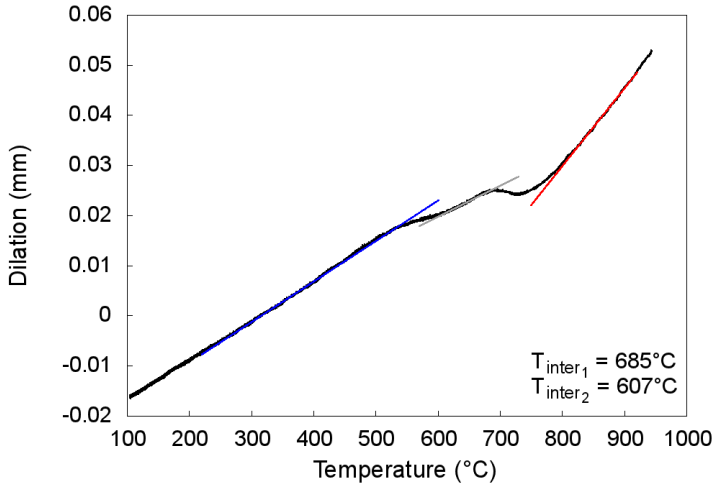

Figure 3.16: Intermediate transformation temperatures for CCT specimen D12 (1 °C/s) using the R^2 method.

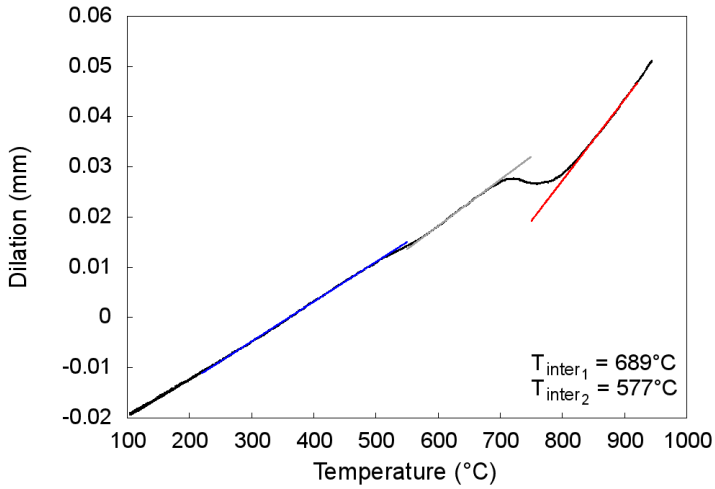

Figure 3.17: Intermediate transformation temperatures for CCT specimen D10 (0.5 °C/s) using the R^2 method.

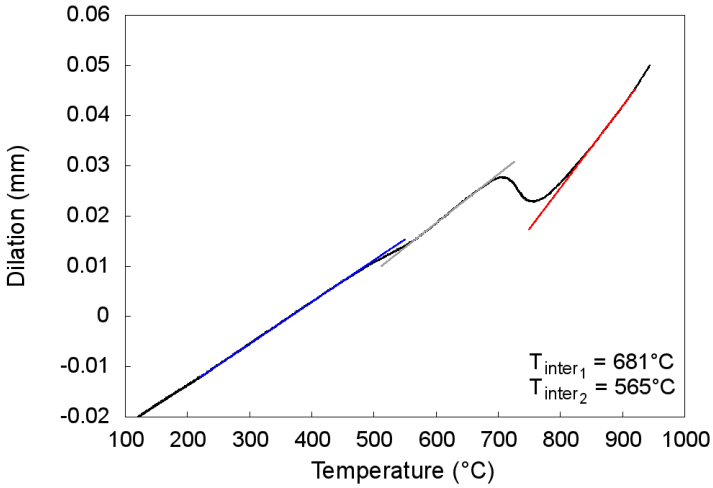

Figure 3.18: Intermediate transformation temperatures for CCT specimen D11 (0.3 °C/s) using the R^2 method.

The discrepancy that arises from the dilatometer method was considered when the transformation temperatures were determined, and the final results are presented based on a consistent methodology that was chosen to reduce the discrepancies as much as possible. As previously mentioned, the final transformation temperatures for each cooling rate were determined using the R^2 method. The transformation temperatures were superimposed on the continuous cooling plots to generate the CCT diagram shown in Figure 3.19. The major regions that were identified using the dilatometry results were martensite, bainite, ferrite and pearlite. The pearlite section of the CCT diagram corresponds to the "double-hump" curves that were discussed previously.

The CCT diagram shown in Figure 3.19 has four distinct regions: ferrite, bainitic ferrite, pearlite and martensite. The location of the phase boundaries were determined using dilatometry, whereas the nature of each constituent was confirmed with microscopy, as will be discussed in Sections 3.4.1, 3.4.2 and 3.4.3. A similar

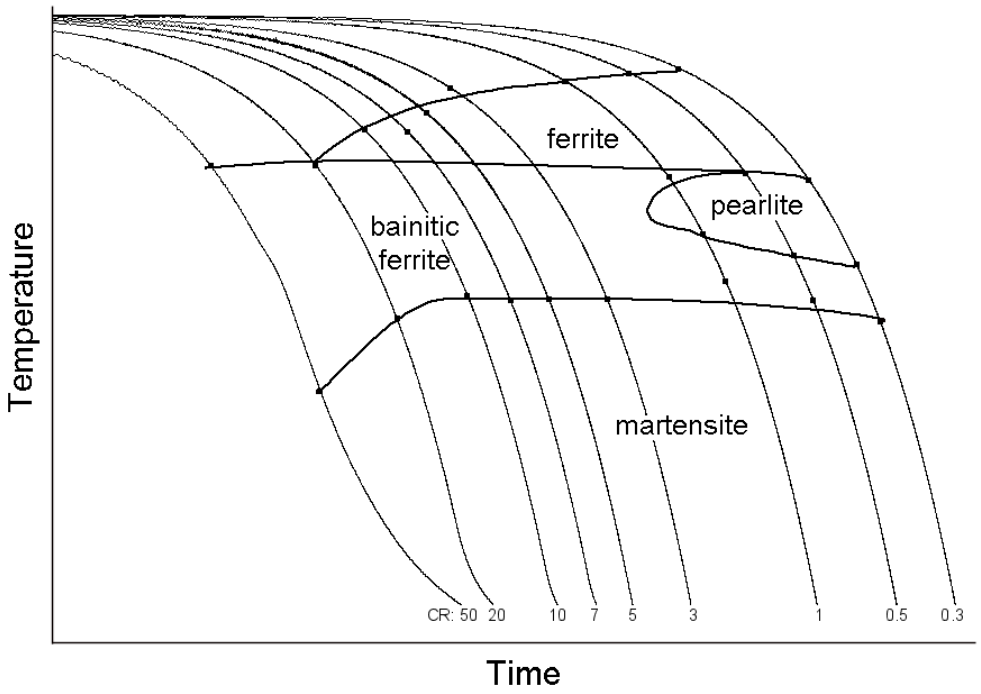

Figure 3.19: Experimentally developed CCT curve for X80 microalloyed steel under no strain conditions. The individual points represent transformation start and finish temperatures for each cooling rate.

CCT diagram was constructed by Cizek for a steel with the following composition: 0.065 mass % carbon, 0.29 mass % silicon, 1.55 mass % manganese, 0.28 mass % molybdenum, 0.076 mass % niobium, 0.020 mass % titanium, 0.018 mass % phosphorous and 0.003 mass % sulphur [Cizek 01]. The CCT diagram included regions of polygonal ferrite, granular ferrite and quasi-polygonal ferrite, bainite, bainitic ferrite, martensite and a region of bainite, pearlite and degenerate pearlite [Cizek 01].

3.3.4 Thermal Expansion Coefficients (TECs)

During construction of the CCT curve, the thermal expansion coefficient (TEC) values were determined for both the austenite phase and combined lower-temperature phases (i.e., ferrite, bainitic ferrite, pearlite and M-A). As mentioned in Section 3.3.1, the TEC can be calculated using the equation of the tangent line for both the upper and lower linear portions of the curve. The slope of the tangent line is divided by the diameter of the circular specimen that was thermally treated in the Gleeble instrument to obtain the TEC. For the CCT curve specimens, the diameter of the sample was 6 mm.

The TECs for austenite (γ) and the mixed lower temperature microconstituents (referred to as α^1) were calculated from the dilation data that was used to generate the CCT diagram; more specifically, the data upon cooling from 945°C to room temperature. In addition, the TEC of γ and α^1 were also determined for one sample (D3) during heating from room temperature to the austenitization temperature of 945°C. The heating curve was analyzed in order to verify whether that the TEC values on cooling were similar to the TEC values during heating. Since all samples had identical starting microstructures and were subjected to the same heating process, only one heating curve was required to verify the cooling TEC values. Since the R^2 method was used to generate the CCT diagram, the linear regression lines

Table 3.3: TEC values for γ and α^1 during cooling from 945 °C to room temperature. The TEC values obtained during heating from room temperature to 945 °C are included in the first row. The final row contains literature values for γ and α^1 [Onsien 09, Caballero 05]

Cooling Rate (°C/s)	γ TEC (1/°C x 10^{-5})	α^1 TEC (1/°C x 10^{-5})
50* (heating)	1.87	1.53
50	2.29	1.39
20	2.29	1.40
10	2.33	1.42
7	2.43	1.46
5	2.50	1.45
3	2.52	1.43
1	2.59	1.35
0.5	2.68	1.32
0.3	2.72	1.39
Literature	2.09	1.22 or 1.29

from this method were used to determine the TEC values.

The results from the TEC investigation are shown in Table 3.3. The cooling rate, γ TEC value and α^1 TEC value are shown for the cooling dilation data. The TEC values obtained from the heating dilation data are included in the first row (marked by an asterisk) for comparison. Furthermore, the literature TEC values for austenite and bainite are included as a reference [Onsien 09]. The TEC value of bainite is very close to that of ferrite (1.29 x 10^{-5} 1/(°C) versus 1.22 x 10^{-5} 1/(°C)); therefore, either value could be used as the reference value for the lower temperature constituents [Caballero 05].

The α^1 TEC values are fairly consistent for the heating and cooling curve results, ranging from 1.32 to 1.53 x 10^{-5} 1/°C. The TEC values are comparable with the literature values of 1.22 or 1.29 x 10^{-5} 1/°C; therefore, the lower temperature TEC values show good agreement with literature and good reproducibility. The γ values, however, vary from 2.29 to 2.72 x 10^{-5} 1/°C for the cooling dilation data values.

This is a substantial spread (16 %), indicating that the γ TEC value is sensitive to cooling rate. Furthermore, the γ TEC value obtained from the heating dilation data is not consistent with the cooling dilation data values. The γ TEC values differ by up to 0.9 x 10^{-5} 1/°C, with the TEC value during heating having the lower TEC than the value obtained from the cooling data. Every γ TEC value is above the literature value of 2.09 x 10^{-5} 1/°C. The variation in the γ TEC values shows that these values are more subjective than the α^1 TEC values.

3.3.5 Percent Transformation during Continuous Cooling

If austenite has completely transformed to a lower temperature product during continuous cooling, the amount of transformation as a function of temperature can be determined directly from the dilatometer data. A linear relationship between the tangent lines and the experimental dilation data can be determined, and the amount of transformation at a particular temperature can be calculated. The experimental dilation data is plotted on the ordinate with temperature plotted on the abscissa, similar to the dilation curves shown in Figures 3.6 to 3.14. Equation 3.1 defines the simple equation governing the amount of transformation as a function of temperature, where f is the fraction transformed, y_T is the experimental dilation value at a given temperature T, $y_{1(T)}$ is the dilation value of the low tangent (ferrite region) at temperature T and $y_{2(T)}$ is the dilation value of the high tangent (austenite region) at temperature T [L.Collins].

$$f = (y_{(T)} - y_{2(T)})/(y_{1(T)} - y_{2(T)}) \tag{3.1}$$

Figure 3.20 schematically demonstrates this concept, where region A corresponds to the numerator in Equation 3.1 (i.e., $y_{(T)}$ - $y_{2(T)}$) and region B represents the denominator ($y_{1(T)}$ - $y_{2(T)}$) in Equation 3.1. The fraction transformed is therefore a

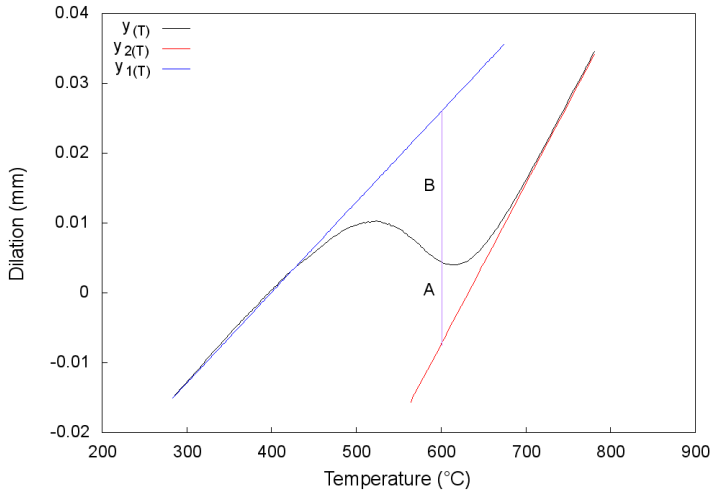

Figure 3.20: Hypothetical dilation curve including upper and lower tangents in order to demonstrate the calculation procedure for the amount of transformation at a given temperature.

simple calculation of the dilation change in region A divided by the dilation change in region B [L.Collins].

Equation 3.1 was applied to each CCT curve specimen listed in Table 3.1 to calculate the amount of transformation from austenite to the lower temperature product; however, the fraction transformed for the slower cooling rates of 1, 0.5 and 0.3 °C/s were not determined due to the multiple phase transformations corresponding to the double "humps" shown in Figures 3.16 to 3.18. Figures 3.21 to 3.26 show the fraction transformed as a function of temperature for samples D3 through D9 (50 °C/s to 3 °C/s).

Figures 3.21 to 3.26 are useful to determine the amount of transformation that has occurred at a specific temperature when cooling from austenite. For example, the temperature at which 80 % of the austenite has transformed to a lower temperature product during continuous cooling at 10 °C/s is approximately 585 °C. For a cooling rate of 20 °C/s, the temperature corresponding to 80 % transformation is

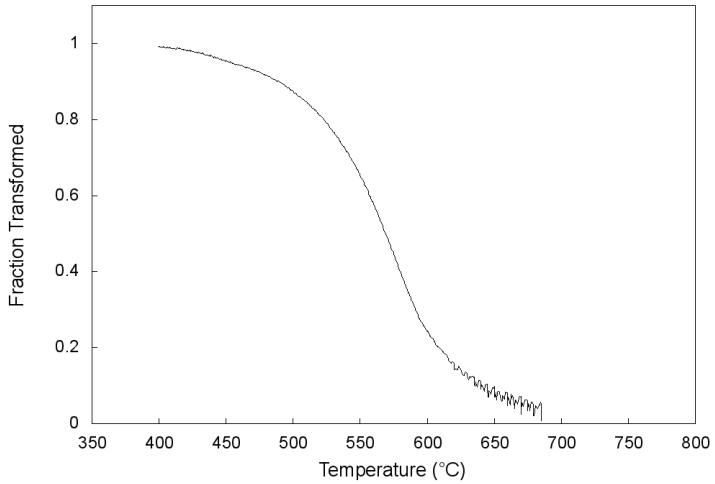

Figure 3.21: Fraction transformed as a function of temperature for sample D3 (50 °C/s).

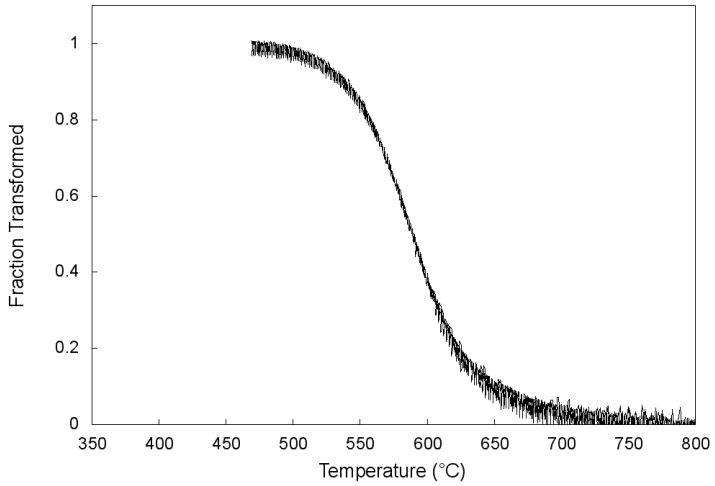

Figure 3.22: Fraction transformed as a function of temperature for sample D4 (20 °C/s).

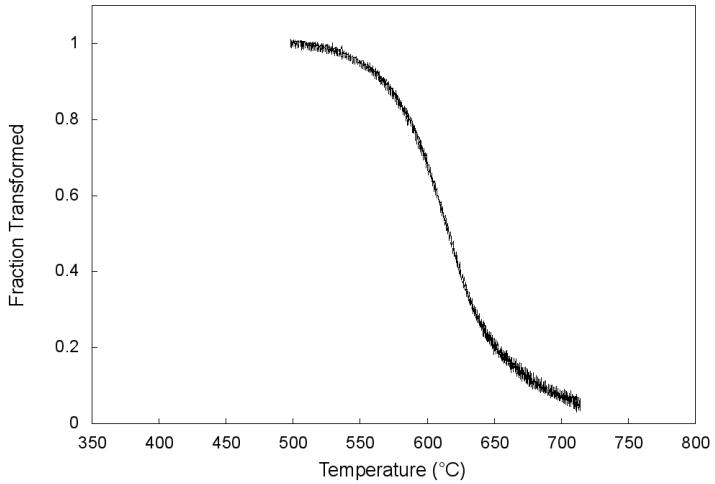

Figure 3.23: Fraction transformed as a function of temperature for sample D6 (10 °C/s).

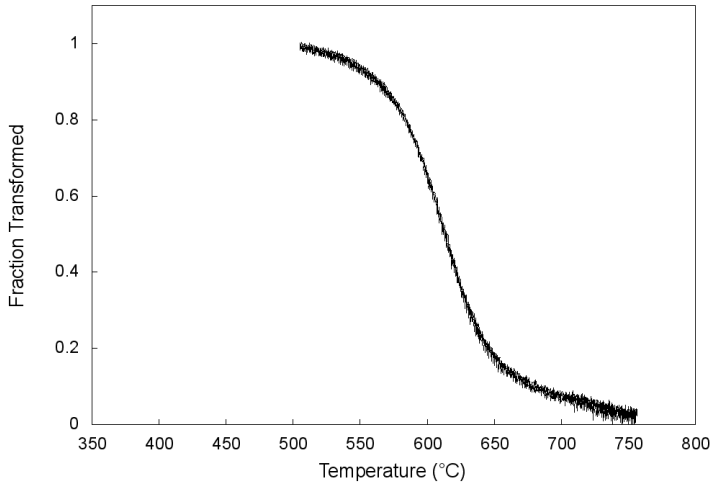

Figure 3.24: Fraction transformed as a function of temperature for sample D7 (7 °C/s).

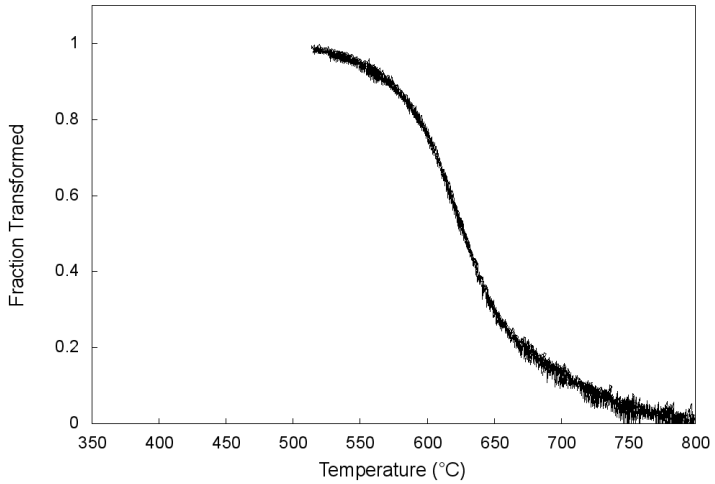

Figure 3.25: Fraction transformed as a function of temperature for sample D8 (5 °C/s).

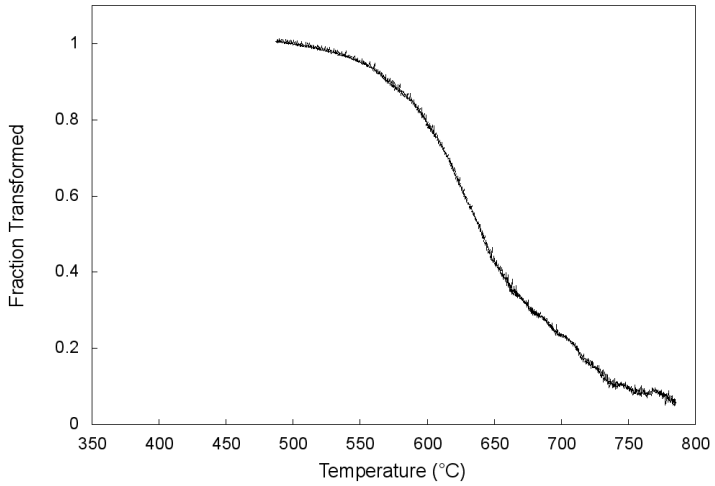

Figure 3.26: Fraction transformed as a function of temperature for sample D9 (3 °C/s).

565°C.

3.4 Microstructure Characterization of CCT Curve Specimens

In order to verify the CCT curve, the microstructures had to be investigated to confirm the nature and quantify of microconstituents present for each cooling rate. The microstructural investigation included optical, scanning electron and transmission electron microscopy which will be detailed in the following sections.

3.4.1 Optical Micrographs of CCT Specimens

A metallographic sample for each CCT curve specimen was prepared according to Section 3.1.2. The mounted and polished samples were etched with 2 % Nital and subsequently imaged using the optical microscope described in Section 3.2. A representative micrograph from each specimen is shown in Figure 3.27. Since Nital was used as an etchant, martensite and the ferrite grain boundaries are well etched. In Figure 3.27, the dark regions are classified as either martensite or bainite, the elongated white grains with black dots/streaks are either bainite and/or pearlite and the white equiaxed grains represent ferrite. It is difficult to distinguish between martensite and bainite in optical images, as both constituents have lath-like features and bainite may appear dark in optical images depending on the orientation of the grain relative to the light source. Furthermore, it is difficult to differentiate between bainite and pearlite in the optical images as both bainite and pearlite consist of ferrite and carbides - the difference lies in the location of the carbides within the structure.

Individual constituents (martensite, bainite and ferrite) are identified in Fig-

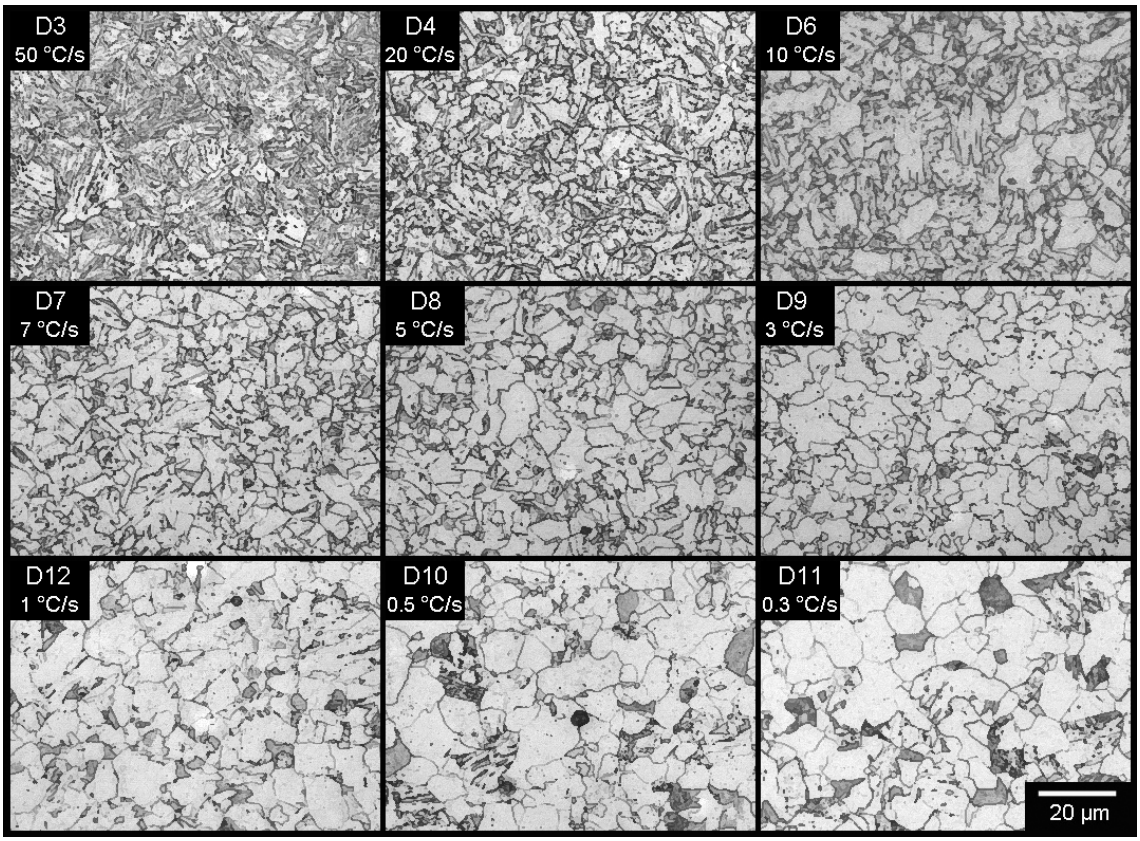

Figure 3.27: Optical micrographs for CCT curve specimens listed in Table 3.1. The samples were mounted, polished and etched with 2 % Nital before optical imaging.

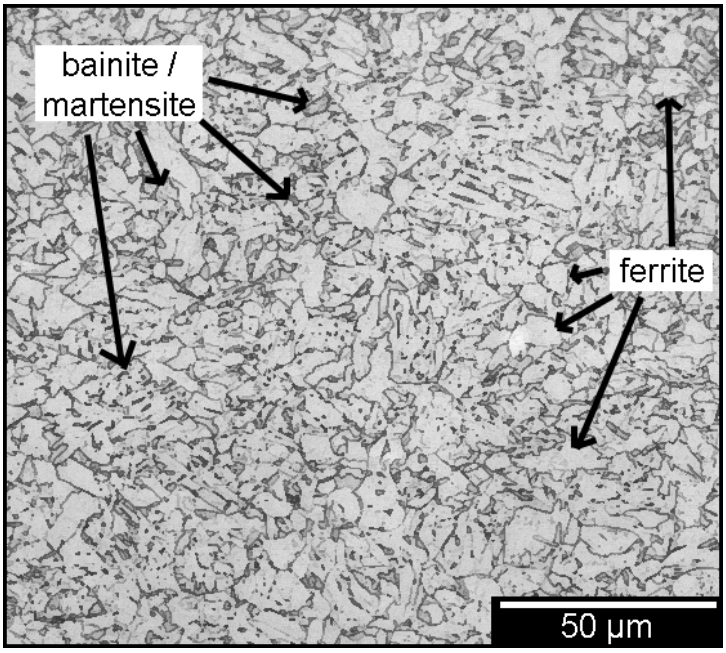

Figure 3.28: Optical micrograph of sample D6 (10 °C/s) with martensite, bainite and ferrite labeled.

ure 3.28 for clarification, which is an optical micrograph of the 10 °C/s specimen.

Sample D3 (50 °C/s cooling rate) contains a significant amount of martensite which is characterized by the large and lath-like structures. The optical micrograph for sample D4 (20 °C/s) in Figure 3.27 contains a lot of elongated white grains that have black features in the grain interiors (which could either correspond to bainite or pearlite, but are indistinguishable in these images). Samples D6 and D7 (10 °C/s and 7 °C/s) consist of dark grains (martensite or bainite) with a small percentage of ferrite (the globular white grains). The slower cooling rates of 5 °C/s (D8) and 3 °C/s (D9) contain more ferrite than samples D6 and D7 but have dark grains as well. Samples D12, D10 and D11 (the slowest cooling rates of 1 °C/s, 0.5 °C/s and 0.3 °C/s, respectively) are mostly dominated by large, globular ferrite grains with small isolated dark grains. As the dark regions could not be identified using optical

microscopy, the need became apparent for electron microscopy to view and image the samples at both higher magnification and higher resolution. The results from electron microscopy will be discussed in the next section.

3.4.2 SEM SE Micrographs of CCT Specimens

SEM imaging was chosen over optical images due to the higher resolution attainable and, as a result, the potential to better identify specific constituents which are indistinguishable in optical microscopy. In SEM, the contrast of the grains is opposite to that for optical microscopy; therefore, martensite, bainite, M-A and pearlite grains appear white whereas ferrite appears darker in SEM SE images. The difference in contrast between the various phases and constituents is due to the nature of the electrons used to collect the image. More specifically, SEs reveal the topography of the sample. Since ferrite etches faster than martensite and bainite, ferrite appears recessed in the microstructure while the harder regions appear higher. Grains/regions that are positioned higher are closer to the SE detector and therefore the SEs that are generated during imaging travel a shorter distance to the SE detector than grains/regions that are recessed. As a result, higher features (such as martensite or bainite) appear brighter in SEM SE images.

Figure 3.29 is an SEM SE micrograph for sample D6 (10 °C/s) with martensite, bainite, ferrite and M-A labeled for clarification. The martensite and bainite regions are almost identical, as the internal substructure is not easily seen in the SEM SE image. M-A appears as white globular or stringy particles, and ferrite is classified as the dark, equiaxed and recessed grains.

A representative SEM SE micrograph for each CCT specimen is shown in Figure 3.30 where the sample number and cooling rate are indicated in the top left corner of each micrograph.

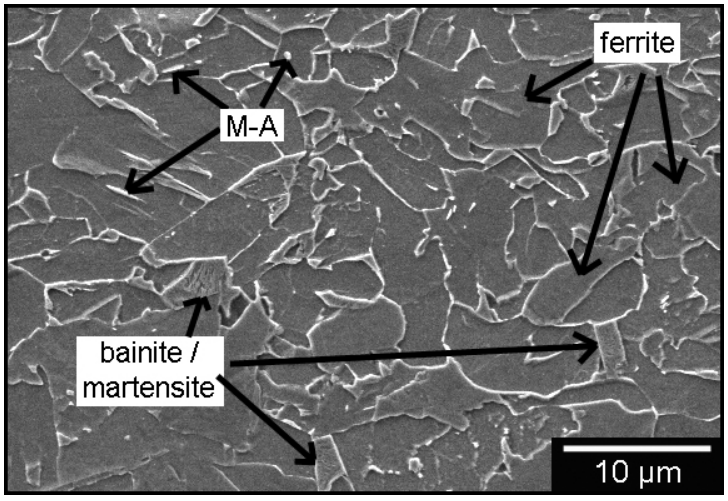

Figure 3.29: SEM SE micrograph of sample D6 (3 °C/s) with martensite , bainite and ferrite labeled.

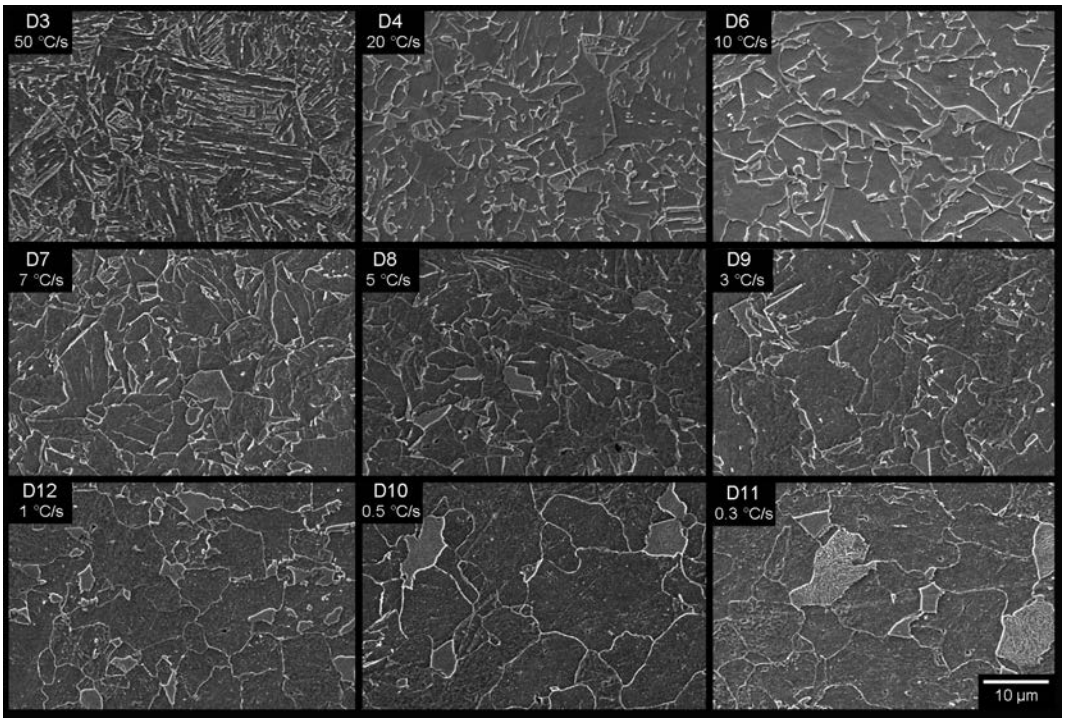

Figure 3.30: SEM SE micrographs of the CCT specimens labeled according to the sample ID and cooling rate indicated in Table 3.1.

Similar to the optical micrographs, Figure 3.30 shows that a decrease in cooling rate causes a significant increase in the amount of ferrite and a corresponding decrease in the amount of martensite and/or bainite. Sample D3 (continuously cooled at 50 °C/s) contains a substantial amount of martensite, while sample D4 (20 °C/s) shows a significant amount of ferrite and a smaller fraction of what could be bainite or martensite. Not only does the amount of ferrite increase as cooling rate decreases, but the grain size increases as well. The grain size of each sample was determined according to the procedure outlined in Section 2.4.2, and will be discussed in further detail in Section 3.5. Ten representative SEM SE images were obtained for each sample, which are included in Appendix D; however, only one representative image is shown in Figure 3.30.

The difference between martensite and bainite grains was difficult to determine in the SEM SE images as both structures appear bright and any internal morphology is hard to observe. A TEM study was undertaken in order to determine the nature of the grains for correct and accurate characterization of the microconstituents. The increased resolution capability of TEM allows for individual regions to be analyzed and identified based on several important characteristics including the presence of iron carbides (indicating a pearlitic or bainitic structure), laths without iron carbides (bainitic ferrite) or microtwins (present in martensite structures).

3.4.3 TEM Analysis of CCT Specimens

The previous sections presented the optical and scanning electron images that were obtained for the CCT specimens in order to observe and characterize the microconstituents. As mentioned, the nature of some grains was very difficult to ascertain in the SEM SE images and, as a result, a more in-depth investigation was pursued to correctly identify specific grains that were undistinguishable in the SEM

SE micrographs. The goal of the TEM analysis was to generate a 'microconstituent characterization database' of grains that were conclusively identified with TEM and could subsequently be used as known examples for comparison with unknown grains with similar morphology and features in other SEM SE images. As a result, microconstituents could be characterized accurately and confidently by comparing known grains to unknown grains of similar appearance; thus, the need for TEM on every single grain would not be necessary in order to confidently state its nature. The regions in the 'microconstituent characterization database' would serve as templates to expedite grain characterization and, hence, quantification for microstructures that are difficult to interpret using SEM alone.

The micrograph that initiated the TEM investigation was taken from the CCT curve specimen cooled at 0.3 °C/s (sample D11), as shown in Figure 3.31. This sample was chosen because the nature of the two regions, indicated by 1 and 2 in Figure 3.31, was difficult to determine with accuracy. The complicated internal structure evident in region 1 suggested that the sample could be either martensite or bainite, but the difference between these two constituents is difficult to make conclusively without confirming the presence of microtwins (martensite) or iron carbides located either between or within the laths (bainite). Similarly, region 2 was initially labeled as bainite; however, this was a questionable proposition that needed to be confirmed or refuted. As such, FIB samples were prepared from the regions of interest and these were characterized using TEM.

Sample D11 was imaged in the FIB-SEM instrument and appropriate regions of interest were selected to represent the two different regions identified in Figure 3.31. The regions of interest are shown in Figure 3.32, Figure 3.33 and Figure 3.34. The regions of interest shown in Figure 3.32 and Figure 3.33 were selected to mimic region 1 in Figure 3.31 and Figure 3.34 shows the region of interest that was chosen

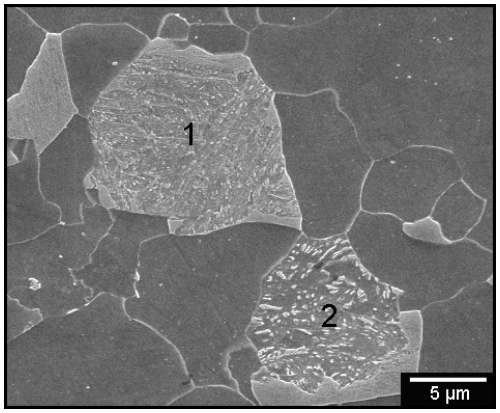

Figure 3.31: SEM SE micrograph of sample D12: two particular regions (indicated by points 1 and 2) were difficult to interpret in the SEM SE micrograph and hence provoked further investigation through TEM analysis.

to represent region 2 in Figure 3.31. The FIB TEM samples were prepared according to Section 3.2 and were imaged in the TEM as detailed in Section 3.2.

Figure 3.35a shows a low magnification TEM bright field (BF) micrograph with a box indicating the region from which a higher magnification image was obtained (shown in Figure 3.35b). Figure 3.35c is the same region as Figure 3.35d and was taken at a tilt angle of 1.8 ° relative to Figure 3.35d to illustrate that the microstructural features (in this case, microtwins) go in and out of contrast based on tilt angle. The box shown in in Figure 3.35d corresponds to the area where the selected area diffraction (SAD) pattern was collected. The SAD pattern is shown in Figure 3.35e and can be indexed to ferrite with a zone axis (ZA) close to a $[51\overline{3}]$ orientation. Since the c/a ratio for martensite will be very close to 1 for steels with this low carbon content, this pattern can also represent martensite. It is the presence of the microtwins that confirms that this region is, in fact, martensite.

Another region of the TEM sample close to the region observed in Figure 3.35 was investigated. Another set of microtwins was observed, as shown in Figure 3.36. In this region, the diffraction pattern shows both primary and twin spots as well

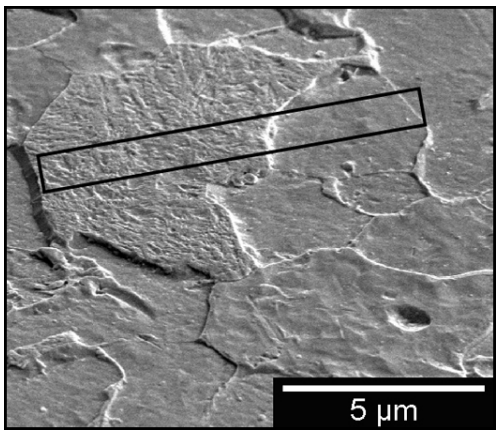

Figure 3.32: SEM SE micrograph of the first region of interest in CCT sample D11, chosen to mimic region 1 in Figure 3.31.

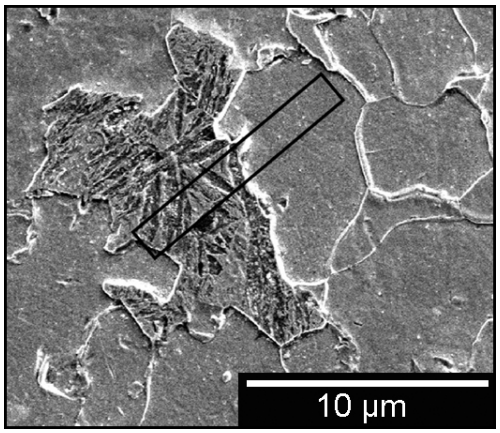

Figure 3.33: SEM SE micrograph of the second region of interest in CCT sample D11, chosen to mimic region 1 in Figure 3.31.

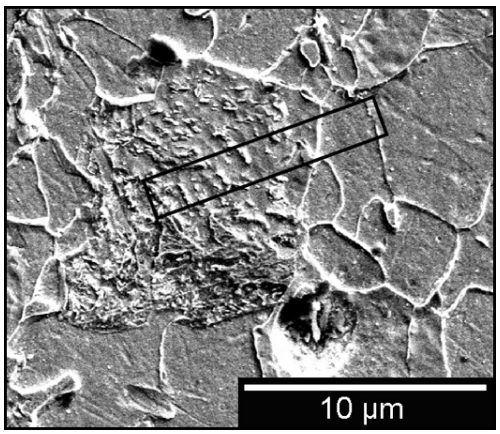

Figure 3.34: SEM SE micrograph of the third region of interest in CCT sample D11, chosen to mimic region 2 in Figure 3.31.

as double diffraction spots. The primary diffraction spots are outlined with a dark black circle, whereas the twin diffraction spots are identified by the red dotted circles and the double diffraction spots are circled with a thin blue line. Double diffraction occurs when electrons that are diffracted from one set of lattice planes act as the primary electron beam for a second set of planes, rather than the incident beam providing the electrons for diffraction. The second set of planes can be the same set of planes as the first diffraction or they can be a different set of planes within the same crystal or in a second phase [Beeston 72]. Twin diffraction spots, on the other hand, are extra reflections that occur in a specimen containing both a matrix and a twinned structure [Beeston 72]. In this sample, the twin diffraction spots result from the martensite, as do the regular diffraction spots. The diffraction pattern shown in Figure 3.36b was indexed to ferrite with a zone axis close to the $[1\overline{1}\overline{3}]$ direction; however, as discussed above, the presence of the microtwins verifies that this region is martensite.

Figure 3.37 shows the TEM results from the second region of interest in Figure 3.33. Figure 3.37a is a low magnification TEM BF image of the region, with

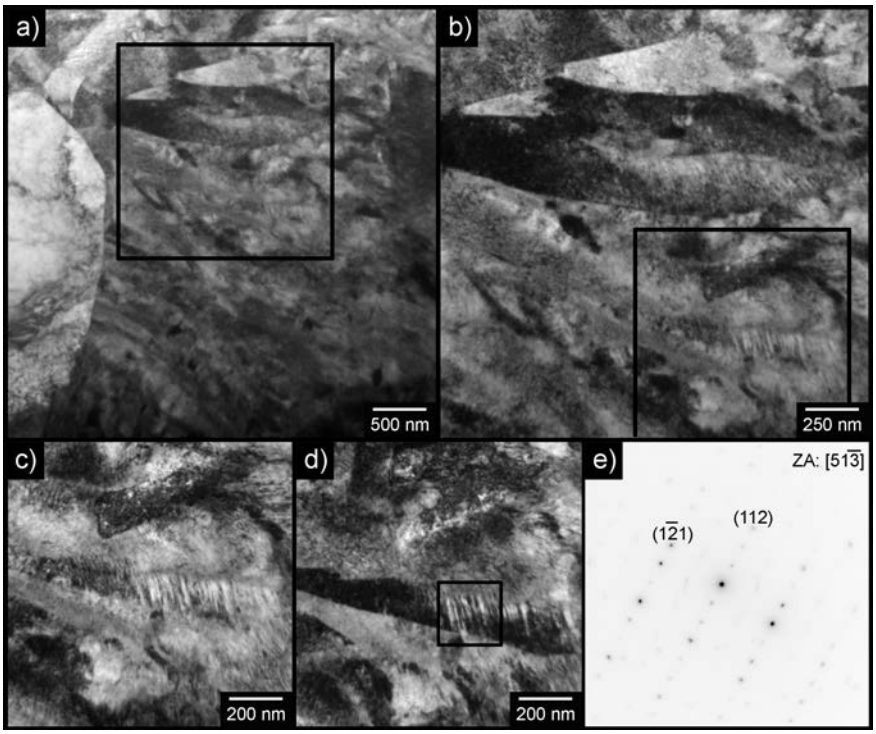

Figure 3.35: TEM results for the region indicated in Figure 3.32: a) low magnification TEM BF micrograph; b) high magnification TEM BF micrograph from the region identified in a); c) high magnification TEM BF image from the region identified in c); d) high magnification TEM BF image from the region identified in b) taken at a tilt angle of 1.8 ° relative to c); e) SAD pattern from the region identified in d).

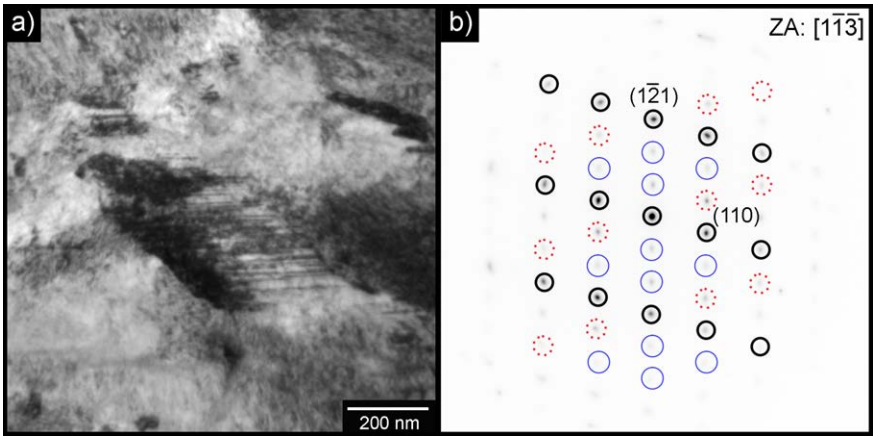

Figure 3.36: TEM results from the region of interest indicated in Figure 3.32: a) high magnification TEM BF image showing fine microtwins; b) SAD pattern from the microtwins in a). The dark black circles correspond to primary diffraction spots whereas the red dotted circles identify the twin diffraction spots and the blue circle marks the double diffraction spots.

the box indicating the section that was further magnified in b and c. Figure 3.37b and 3.37c were taken at the same magnification but at a tilt angle of 7.3 ° relative to each other to show the features of interest (in this case, laths) that go in and out of contrast depending on the tilt angle. The laths that are clearly visible in Figure 3.37c are not observed in Figure 3.37b; however, they are, in fact, part of the sample and not simply artifacts.

Figure 3.38 shows further TEM results from the region of interest shown in Figure 3.33 at higher magnification. Figure 3.38a is the same image as shown in Figure 3.37c with the addition of a black box which identifies the section that was further magnified in Figure 3.38b. Figure 3.38b has three numbers included (1, 2, 3) which correspond to the areas where SAD patterns were obtained and are shown in Figures 3.38c, 3.38d and 3.38e. The diffraction spots are labeled in Figure 3.38c, d and e and follow the rules governing a bcc crystal structure; however, since the sample orientation was not directly on the zone axis, the diffraction pattern could

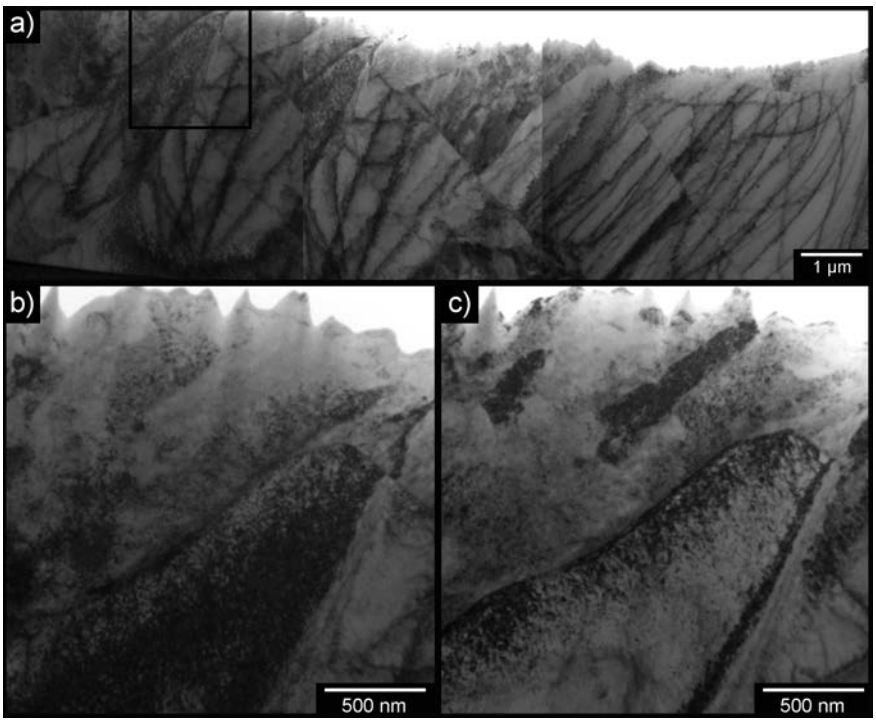

Figure 3.37: TEM results from the region of interest indicated in Figure 3.33: a) low magnification TEM BF image; b) high magnification TEM BF image of the region identified in a); c) high magnification TEM BF image of the region identified in a) taken at a 7.3 ° tilt angle relative to b).

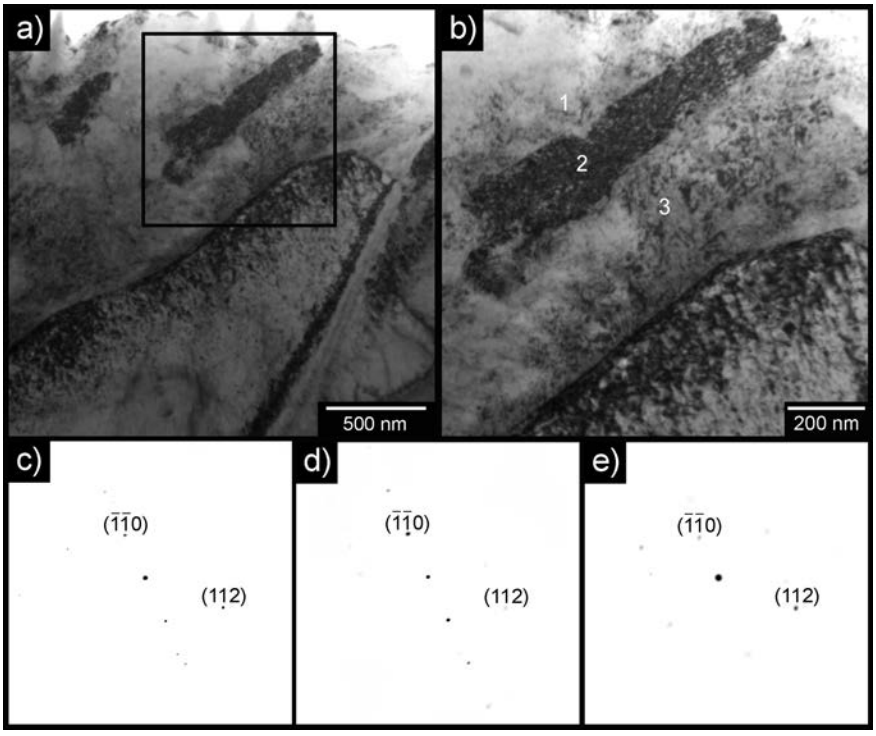

Figure 3.38: Additional TEM results from the region of interest indicated in Figure 3.33: a) low magnification TEM BF image of the laths identified in Figure 3.37c, b) high magnification TEM BF image of the region identified in a) with three spots labeled 1, 2 and 3; c) SAD pattern corresponding to label 1 in b); d) SAD pattern corresponding to label 2 in b); e) SAD pattern corresponding to label 3 in b).

not be fully indexed (i.e., the ZA was not determined as the sample was not directly on the ZA). Regardless of the ZA direction, Figures 3.38c, d and e are similar patterns that differ only in the spot brightness due to slightly different orientations relative to one another. The lath that appears darker (spot 2 in Figure 3.38b) is oriented closest to the Bragg condition and diffracts more strongly than the laths that are oriented farther from the Bragg condition (spots 1 and 3 in Figure 3.38). The region of interest contained parallel laths that are slightly misoriented relative to each other; however, no iron carbides were observed in the region of interest. As a result, the region of interest shown in Figure 3.33 is classified as bainitic ferrite.

The third region from CCT curve specimen D11 is shown in Figure 3.34 and the TEM results are presented in Figure 3.39. Figure 3.39a shows a low magnification TEM BF micrograph of the TEM sample. The box in Figure 3.39a is magnified in Figure 3.39b. The box in Figure 3.39b is further magnified in Figure 3.39c. The number 1 shown in Figure 3.39c represents the location where an EDX spectrum was obtained as shown in Figure 3.39d. The EDX spectrum in Figure 3.39d shows that the main elemental peak is iron with no microalloy elements appearing; thus, the particle was determined to be an iron-rich carbide, or more specifically, Fe_3C. The SAD pattern shown in Figure 3.39e was indexed to be ferrite with a zone axis close to the $[1\bar{1}0]$ direction. The presence of ferrite with cementite particles proves that the region of interest was pearlite ; however, this is not classical pearlite. Classical pearlite contains alternating lamellae of ferrite and Fe_3C. In this region, the lamellae have degenerated so that the remaining structure contains carbides that are not aligned into lamellar plates. A study performed by Cizek also presented evidence of degenerate pearlite grains in a microalloyed steel that was continuously cooled at 0.3 °C/s [Cizek 01].

Three regions from CCT specimen D11 (0.3 °C/s) were correctly identified through TEM and formed the beginning of the 'microconstituent characterization database', which will be presented and discussed in Section 4.3.2. The first region that was investigated with TEM is shown in Figure 3.32 and was originally thought to be bainite or martensite. The presence of microtwins in two separate regions in the sample confirmed that the region of interest was martensite. The second region shown in Figure 3.33 was originally classified as bainite or martensite but was confirmed as bainite based on the existence of laths that had similar DPs at slightly different orientations. The third region of interest obtained from sample D11 is shown in Figure 3.34. This region was determined to be pearlite due to the

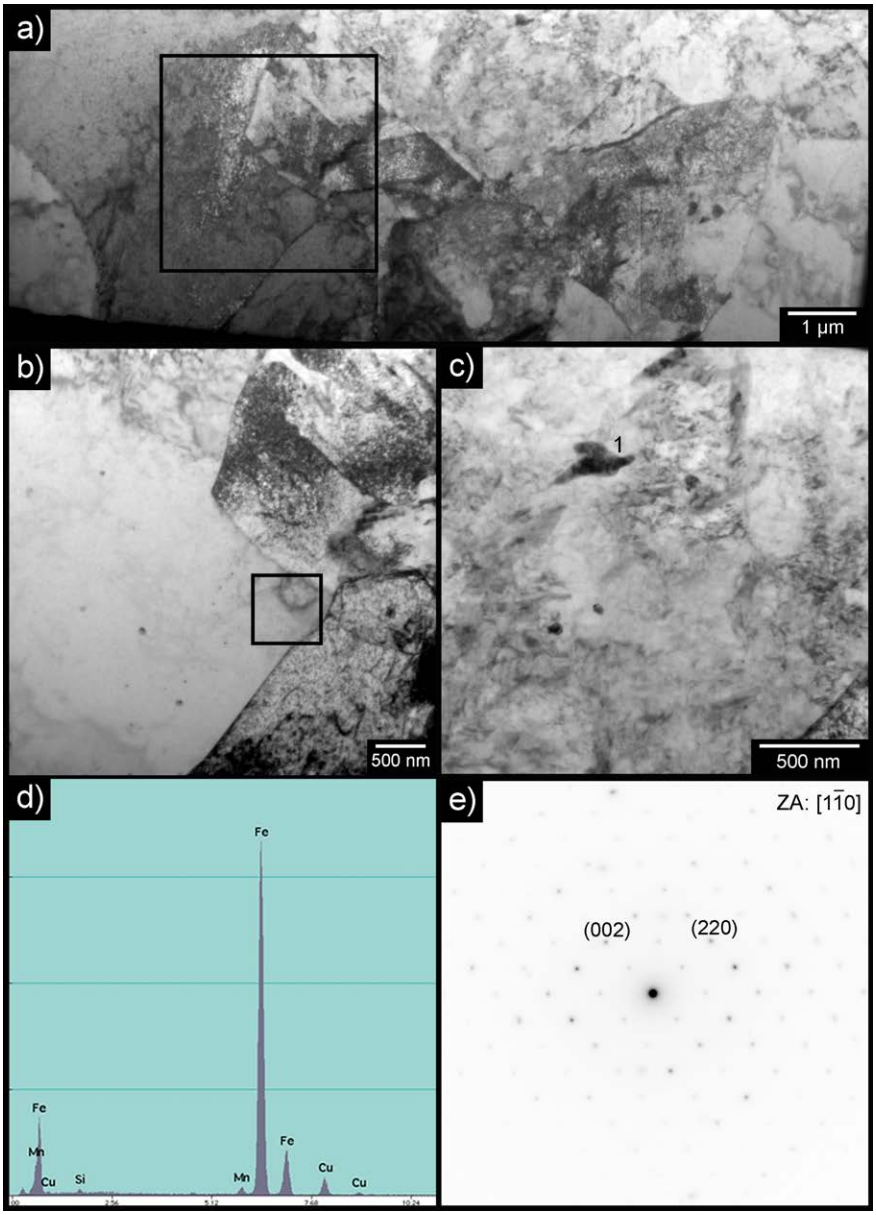

Figure 3.39: TEM results from the region of interest in Figure 3.34: a) low magnification TEM BF image; b) high magnification TEM BF image of the region identified in a); c) high magnification TEM BF image of the region identified in b) with label 1 corresponding to the location where an EDX spectrum shown in d) and a SAD pattern shown in e) were obtained.

confirmation of Fe_3C precipitates within a ferrite matrix.

3.5 Microstructure Quantification for CCT Curve Specimens

As previously mentioned, it is important to quantify microstructures to directly compare them. The following sections will outline the quantification of the CCT curve specimens in terms of phase fraction (Section 3.5.1) and grain size (Section 3.5.2).

3.5.1 Phase Fractions for CCT Curve Specimens

The TEM investigation detailed in Section 3.4.3 led to the correct identification of certain regions that were indistinguishable in SEM. Although these grains and regions were successfully characterized, it was still very difficult to differentiate between martensite and bainitic ferrite in SEM SE images. The difference between ferrite and bainitic ferrite/martensite, however, was much easier to make. Five representative SEM SE micrographs for each sample were investigated using FIJI and the constituents were quantified according to the following four categories: ferrite, bainite/martensite, M-A and pearlite. Since the micrographs were largely dominated by ferrite grains, the image analysis procedure involved identifying and individually coloring grains of martensite/bainite, M-A or pearlite; i.e., everything that was not ferrite was marked. The amount of each constituent was then determined by calculating the area (in μm^2) occupied by each constituent and dividing that value by the total image area. The results from the phase quantification are shown in Table 3.4.

The SEM images verify the CCT curve which predicts pearlite grains in the slow-

Table 3.4: Microstructure distribution for the various constituents observed in the CCT specimens, including ferrite, bainitic ferrite, martensite, M-A and pearlite.

Sample ID	Cooling Rate (°C/s)	Ferrite (%)	Bainitic Ferrite/Martensite (%)	M-A (%)	Pearlite (%)
D3	50	0	100	0	-
D4	20	87.4 ± 1.3	6.8 ± 1.2	5.8 ± 0.4	-
D6	10	88.3 ± 3.5	8.0 ± 2.6	3.7 ± 1.7	-
D7	7	94.3 ± 1.5	2.7 ± 1.4	3.0 ± 0.5	-
D8	5	93.5 ± 2.3	3.9 ± 1.8	2.7 ± 0.8	-
D9	3	93.9 ± 1.2	2.7 ± 0.6	3.5 ± 0.8	-
D12	1	92.1 ± 0.7	5.1 ± 0.5	2.9 ± 0.4	trace
D10	0.5	95.5 ± 1.4	3.1 ± 1.3	0.9 ± 0.2	0.5 ± 0.4
D10	0.3	92.6 ± 1.8	5.3 ± 1.9	0.8 ± 0.3	1.3 ± 0.7

est cooling rates (i.e., less than 1 °C/s). Furthermore, the CCT diagram predicts that every sample will have martensite, bainite and ferrite in various proportions. Each sample consisted of a mixture of the first three constituents, with the exception of sample D3 (50 °C/s) which contained 100 % bainitic ferrite/martensite and samples D12 (1 °C/s), D10 (0.5 °C/s) and D11 (0.3 °C/s) which were the only samples that contained pearlite. There is no clear trend in the phase quantification, other than the amount of M-A decreases as the cooling rate decreases. Samples D4 (20 °C/s) and D6 (10 °C/s) have roughly the same phase composition within appreciable error. Similarly, the remaining samples (D7 (7 °C/s) through D12 (1 °C/s)) are approximately identical in composition, with the exception of pearlite noted for samples D10, D11 and D12. Sample D12 had trace amounts of pearlite that were not quantified due to the extremely low count of grains in the micrographs; however, a few pearlite grains were observed in the micrographs which was in agreement with the CCT diagram.

Figure 3.40 shows the relationship between ferrite phase fraction (F), martensite/bainitic ferrite phase fraction (M/BF) and cooling rate for the CCT specimens,

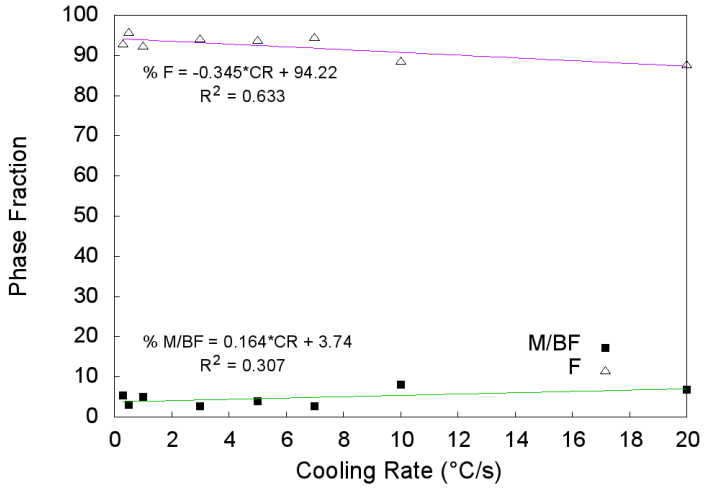

Figure 3.40: Phase fraction of ferrite and martensite/bainite as a function of cooling rate for CCT specimens (excluding D3 (50 °C/s)).

excluding sample D3, which contains 100 % martensite/bainitic ferrite. There is a good correlation between the cooling rate and the amount of each constituent. It was expected that faster cooling rates would yield higher fractions of martensite/bainitic ferrite whereas slower cooling rates would generate microstructures that were largely dominated by ferrite grains. This trend is generally followed for ferrite, but not followed as well for martensite/bainite as shown in Figure 3.40. The coefficient of determination for the martensite/bainitic ferrite data was 0.307, indicating that roughly 30 % of the the data fits a linear curve. The R^2 value for the ferrite data was 0.63, which reflects a better fit between the data and the linear equation. The relationship between cooling rate and M-A is not included in this figure but is shown in Figure 3.41. According to Figure 3.41, the equation governing the amount of M-A as a function of cooling rate fits 76 % of the data, which is a very strong correlation.

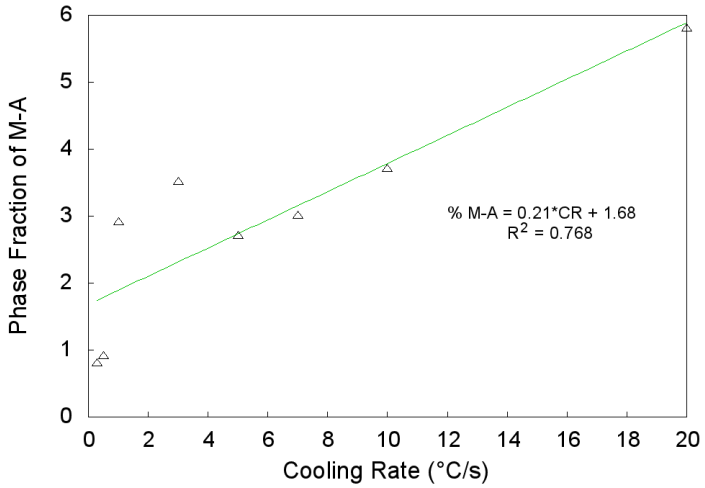

Figure 3.41: Phase fraction of M-A as a function of cooling rate for CCT specimens (excluding D3 (50 °C/s)).

3.5.2 Grain Size Analysis of CCT Curve Specimens

The overall grain size of the microstructures present in the CCT curve specimens was investigated using optical micrographs. Table 3.4 shows that each sample is largely dominated by a single phase; as a result, the overall grain size can be calculated rather than the grain size for specific constituents. Optical micrographs were chosen for grain size determination due to the very clear grain boundaries and the large sample area that could be measured. Section 2.4.2 describes the Heyn lineal intercept method that was used to determine grain size according to ASTM E112 [AST 10]. The average grain size for each sample is shown in Table 3.5. The grain size for samples D3, D4 and D6 (50 °C/s, 20 °C/s and 10 °C/s, respectively) is approximately equal. Samples D12, D10 and D11 (1 °C/s, 0.5 °C/s and 0.3 °C/s cooling rates) also have similar grain sizes.

The grain size was plotted as a function of cooling rate, as shown in Figure 3.42. The grain size increases as cooling rate decreases. The R^2 value for this curve is

Table 3.5: Average grain size for CCT specimens.

Sample ID	Cooling Rate (°C/s)	Average Grain Size (μm)
D3	50	6.7 ± 0.2
D4	20	6.6 ± 0.2
D6	10	6.5 ± 0.4
D7	7	7.9 ± 0.3
D8	5	8.1 ± 0.4
D9	3	9.5 ± 0.1
D12	1	10.2 ± 0.4
D10	0.5	10.3 ± 0.3
D11	0.3	10.4 ± 0.2

0.802, which shows a very good correlation between the data and the equation. The trend shown in Figure 3.42 agrees with first principles governing grain growth as a function of time and temperature.

3.6 Mechanical Testing

The only mechanical test that was performed on the CCT curve specimens was hardness testing, which will be discussed in the following section.

3.6.1 Hardness Testing

Hardness tests were performed on the mounted metallographic samples according to the procedure outlined in Section 3.2.1. Five indents were made on each sample and the average and standard deviation were calculated. Table 3.6 summarizes the results of the hardness tests performed on the CCT curve specimens. The hardness decreases as cooling rate decreases; the samples cooled at the fastest cooling rates had the highest hardness whereas the slow-cooled specimens had the lowest hardness.

The trend between hardness and cooling rate is shown in Figure 3.43. The trend

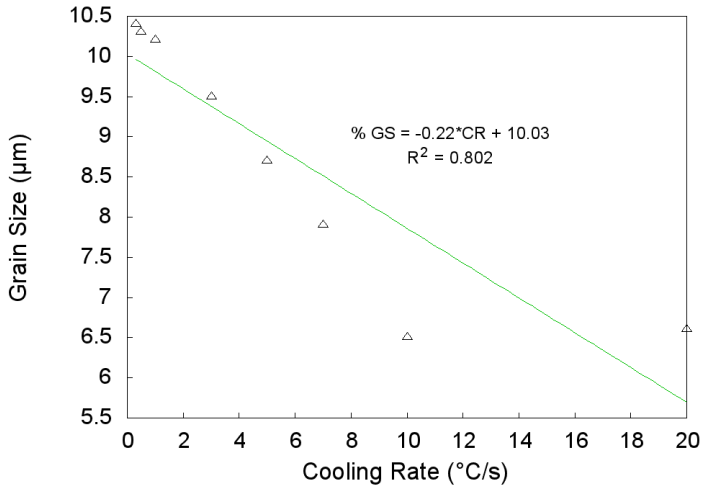

Figure 3.42: Average grain size as a function of cooling rate for CCT specimens (excluding D3 (50 °C/s)).

Table 3.6: Hardness values (HV) for CCT specimens.

Sample ID	Cooling Rate (°C/s)	Average Hardness (HV)
D3	50	262 ± 7.3
D4	20	236 ± 2.8
D6	10	223 ± 3.0
D7	7	216 ± 2.9
D8	5	207 ± 3.9
D9	3	202 ± 6.3
D12	1	183 ± 2.8
D10	0.5	182 ± 4.3
D11	0.3	178 ± 1.6

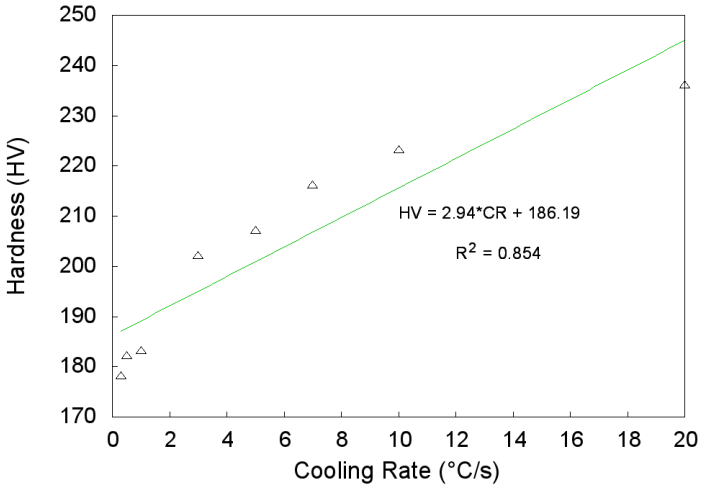

Figure 3.43: Hardness as a function of cooling rate for the CCT specimens (excluding D3 (50 °C/s)).

agrees well with the predicted result; more specifically, that the hardness would decrease as cooling rate decreased. Samples with a faster cooling rate have a higher hardness, which could be related to phase fraction, grain size, or both phenomena. The relationship between hardness and microstructure was investigated and is shown in Figure 3.44. When comparing the hardness values to the percentage of phases present in each sample from Table 3.4, the trend in hardness is not obvious. There is a weak correlation between phase fraction and hardness, as shown in Figure 3.44. The hardness increases as the phase fraction of martensite/bainitic ferrite increases; however, this trend is not consistent with cooling rate as shown in Figure 3.40. Similarly, the hardness increases as the ferrite content decreases. Since the samples are largely comprised of ferrite, the hardness is not expected to change much as a function of phase fraction, which is illustrated in Figure 3.44.

As there is no significant trend between hardness and phase fraction, the critical factor that is determining the trend in hardness must be the grain size. The hardness

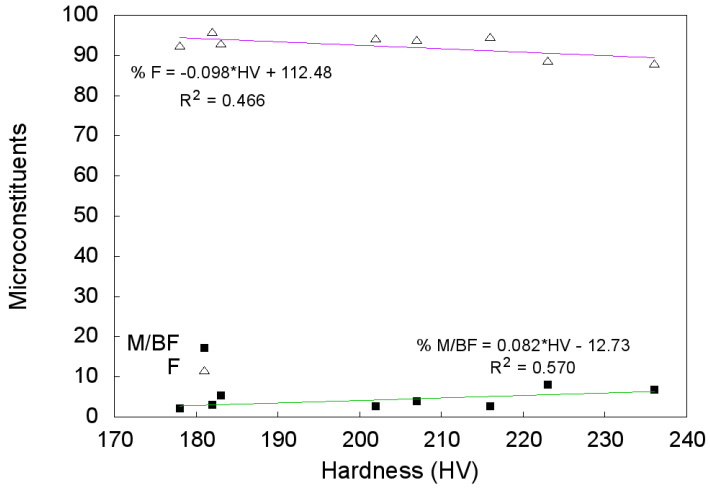

Figure 3.44: Hardness as a function of phase fraction for CCT specimens (excluding D3 (50 °C/s)).

values shown in Table 3.6 were plotted as a function of the average grain size listed in Table 3.5. As mentioned in Section 2.5.1, hardness values should follow a Hall-Petch relationship according to Equation 2.10. In order to verify the Hall-Petch equation for this data, the hardness was plotted against the inverse of the square root of the average grain size based on Equation 2.10. The resulting graph is shown in Figure 3.45.

The hardness values agree fairly well with grain size as the coefficient of determination was 0.82 for this set of data. As a result, it can be concluded that the grain size follows a Hall-Petch relationship for the CCT curve specimens.

3.7 Summary

This chapter detailed the experimental techniques, conditions and results for the CCT curve. The CCT curve was developed by applying nine cooling rates (varying from 50 to 0.3 °C/s) to round specimens using a Gleeble 3800 thermomechanical sim-

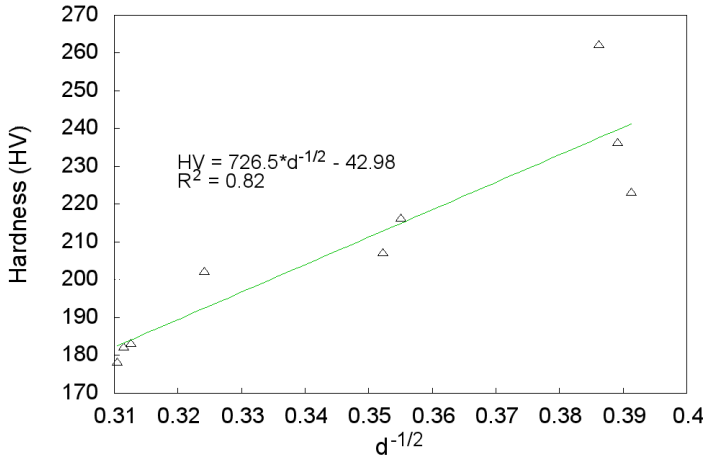

Figure 3.45: Experimental hardness and grain size values plotted according to the Hall-Petch relationship.

ulator. The transformation temperatures were determined from dilatometry results using two independent methods. The first method used a consistent temperature range to generate a tangent line to the dilation data and was termed the CT method. The second method was termed the R^2 method. The R^2 method was an iterative process whereby the coefficient of determination was maximized for each tangent curve; i.e., the temperature range from which the tangent line was calculated was optimized based on the R^2 value. The start and finish transformation temperatures were similar for both the CT and R^2 methods with the exception of the transformation start temperatures for the higher cooling rates of 7 °C/s, 10 °C/s, 20 °C/s and 50 °C/s. The R^2 method utilized data corresponding to a higher coefficient of determination and, as such, the CCT curve was constructed using the transformation temperatures determined with this method.

The thermal expansion coefficients for austenite and the combined lower temperature products were calculated during continuous cooling. The TEC values were

also determined for one sample during heating for comparison with the cooling TEC values. The austenite TEC values ranged from 2.29 x 10^{-5} 1/°C to 2.72 x 10^{-5} 1/°C during cooling as compared with the reference value of 2.09 x 10^{-5} 1/°C. The austenite TEC value during heating was 1.87 x 10^{-5} 1/°C, which is substantially lower than the heating values. The TEC values for the combined lower temperature products ranged from 1.32 x 10^{-5} 1/°C to 1.46 x 10^{-5} 1/°C on cooling, whereas the TEC value during heating was 1.53 x 10^{-5} 1/°C. The reference value for bainite was listed as 1.29 x 10^{-5} 1/°C and the TEC value for ferrite is 1.22 x 10^{-5} 1/°C.

The amount of transformation as a function of temperature was determined for all cooling rates (except 1 °C/s, 0.5 °C/s and 0.3 °C/s which exhibited multiple phase transformations and, hence, could not be analyzed for the fraction transformed). The fraction transformed curves can be used to estimate the amount of transformation at a particular temperature.

The CCT diagram was confirmed by investigating the microstructures through both optical and electron microscopy. The difference between martensite and bainitic ferrite in SEM SE images was difficult to ascertain as both structures had dark and light regions with complicated internal substructures. A TEM study was performed on three regions of interest in order to accurately determine the nature of the regions that were difficult to distinguish in the SEM SE images. The results from the TEM investigation were used to characterize and quantify the phase fractions of each constituent the SEM SE images. The difference between martensite and bainitic ferrite was still unclear after the TEM investigation; however, the difference between bainitic ferrite/martensite and ferrite was easily distinguishable. As a result, bainitic ferrite and martensite were considered as one entity during phase quantification.

The microstructure for the highest cooling rate (50 °C/s) consisted primarily

of martensite/bainitic ferrite, whereas the other cooling rates resulted in mixed microstructures. The amount of ferrite increased as cooling rate decreased. The combined fraction of bainitic ferrite and martensite generally decreased as cooling rate decreased, and the phase fraction of M-A decreased with decreasing cooling rate. For the samples that contained pearlite (1 °C/s, 0.5 °C/s and 0.3 °C/s), the slower cooling rates had higher phase fractions of pearlite.

The grain size was measured according to ASTM E112 using optical micrographs. The grain size increased as cooling rate decreased, which agrees with the expected trend. The average grain size went from 6.7 μm for 50 °C/s to 10.4 μm for the slowest cooling rate of 0.3 °C/s.

Macrohardness values were obtained for each specimen and a positive linear relationship was observed between hardness and cooling rate. The hardness was plotted as a function of microstructure (both phase fraction and grain size). Hardness increased as the fraction of martensite/bainitic ferrite increased and the ferrite phase fraction simultaneously decreased. Furthermore, the hardness values showed a strong correlation with the amount of M-A present in the sample: higher M-A fractions corresponded to higher hardness values. Hardness was also plotted as a function of grain size to determine whether the Hall-Petch relationship was obeyed. There was good agreement between grain size and hardness; smaller grain sizes resulted in higher hardness values than large grain sizes.

The CCT experiments provided the foundation for the ITT trials. Once the transformation temperatures were determined, the ITT test parameters were selected based on the fraction transformed. The ITT trial experiments will be detailed in the next chapter.

This page was intentionally left blank

Chapter 4

Interrupted Thermal Treatment (ITT)

As described in Chapter 3, the CCT curve was developed to determine the important transformation temperatures that are relevant for the X80 steel used in this project. After the CCT curve was generated and the microstructures were successfully characterized and quantified, a set of experiments was designed to determine the effect of thermal history on microstructure development and the subsequent relationship between microstructure and mechanical properties (most notably, work hardening behaviour) through the introduction of an interrupted thermal treatment, or ITT, process. This chapter will outline the experimental conditions and results for the ITT samples. Excerpts from this chapter have been modified from published works at MS&T 2011[1], IPC 2012[2] and an invited publication in AIST Iron and Steel Technology journal[3]. General experimental techniques were described in

[1] "The Effect of Microstructure on the Mechanical Properties of X80 Microalloyed Steel, Jonsson et al, MS&T 2011.

[2] "The Effect of Microstructure on Tensile Behaviour of X80 Microalloyed Steel, Jonsson et al, IPC 2012.

[3] "The Effect of Microstructure on the Mechanical Properties of X80 Microalloyed Steel, Jonsson et al, AIST 2012.

Section 2.2 and the specific equipment models and experimental parameters were discussed in Section 3.1; however, different operating conditions between the CCT and ITT samples will be addressed in Section 4.1. The ITT transformation kinetics will be discussed in Section A. The microstructure characterization is detailed in Sections 4.3.1 and 4.3.2. The results from microstructural quantification (through both phase fraction analysis and grain size) are presented in Sections 4.4.1 and 4.4.2. Section 4.5 includes the mechanical behaviour and relates the mechanical properties to both phase fraction and grain size.

A second set of ITT trials was conducted based on the results from the first ITT experiments. The results from the second ITT trial experiments will be presented and discussed in Section 4.6.

4.1 Experimental Methods

4.1.1 Thermal Cycling - Gleeble Thermomechanical Simulator

The Gleeble 3800 described in Section 3.1.1 was used to thermally treat both the CCT curve specimens and the ITT specimens; however, the geometry for the ITT samples was slightly different from the CCT samples as shown in Figure 4.1. The tests on the Gleeble 3800 were conducted as preliminary experiments to investigate the microstructural development as a function of thermal history using the same thermomechanical simulator as the CCT curve specimens. The microstructural investigation of the Gleeble 3800 specimens will be presented in Section 4.3.1.

Metallographic sample preparation for microstructural investigation and hardness testing. In order to obtain tensile properties for the ITT trials, however, a different sample geometry and Gleeble thermomechanical simulator were required. The Gleeble 3800 grips and chamber were not compatible with the ASTM sample

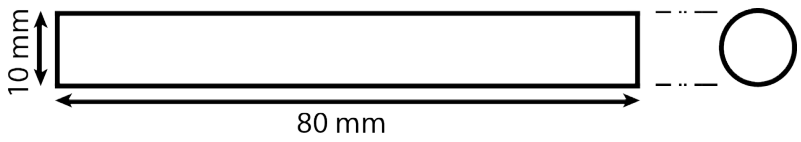

Figure 4.1: Geometry used for the ITT trial specimens.

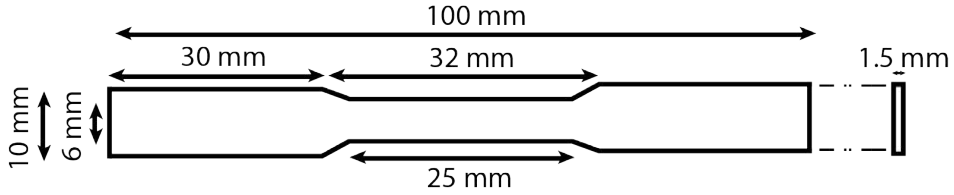

Figure 4.2: ASTM E 8M-04 specification for sub-size sample geometry [AST 04].

geometry, shown in Figure 4.2 [AST 04]. As a result, the Gleeble 3500 located at the University of British Columbia was used to thermally treat X80 strip specimens that were subsequently machined into sub-size tensile specimens. Figure 4.3 shows the Gleeble 3500 with its control tower in Figure 4.3a and the sample chamber in Figure 4.3b. In this machine, the strip samples were placed in the grips (copper grips embedded in a stainless steel block) and the sample spanned the distance between the grips as illustrated in Figure 4.3b.

Sub-size tensile specimens were chosen, as the standard size specimens did not fit the geometry of the grips in either the Gleeble 3500 or the Gleeble 3800. As a result, a larger flat specimen had to be used to thermally treat a piece of steel that was subsequently machined into three sub-size specimens according to ASTM E 8M-04, as shown in Figure 4.2 [AST 04]. The sub-size specimens had a gauge length of 25 mm and a reduced cross-section of 6 mm. There are no thickness requirements for sub-size tensile specimens; therefore, the thickness of the sub-size specimens was the same as that of the strip samples that were thermally tested in the Gleeble 3500 (i.e., 1.5 mm).

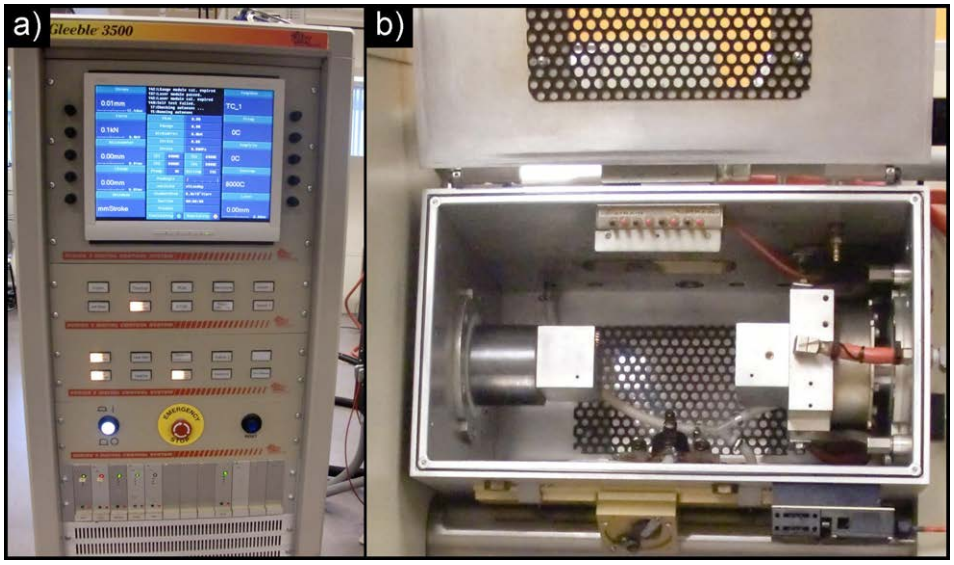

Figure 4.3: Gleeble 3500 thermomechanical simulator: a) Control tower; b) sample chamber.

The large samples tested in the Gleeble 3500 had the dimensions indicated in Figure 4.4. The dimensions were provided by the University of British Columbia based on the geometric constraints of the Gleeble machine.

The thermal schedule applied to the strip specimens was identical to the ITT trials conducted on smaller samples in the Gleeble 3800, as shown in Table 4.3. Before the ITT trial tests were conducted, two experiments were performed to de-

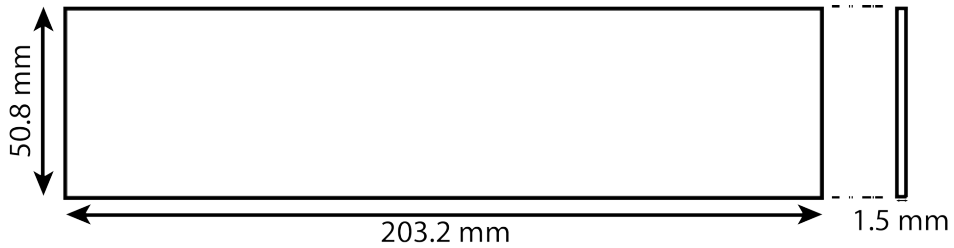

Figure 4.4: Sample geometry for strip specimens intended for subsequent tensile testing.

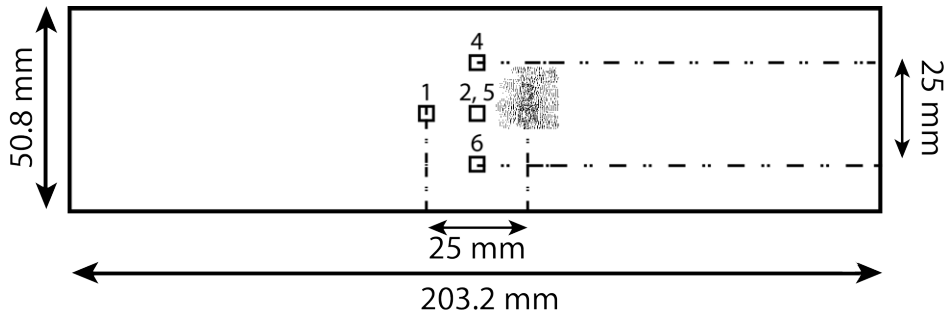

Figure 4.5: Sample geometry for strip specimens intended for subsequent tensile testing. Points 1, 2 and 3 correspond to thermocouples 1, 2 and 3 used to assess horizontal temperature conformance and Points 4, 5 and 6 correspond to the thermocouple placements when testing for thermal homogeneity in the vertical direction.

termine the thermal homogeneity across the horizontal and vertical sections of the strip sample. Since sub-size tensile specimens were removed from the strip samples, it was important to verify thermal agreement in the area that would be subjected to tensile stresses. More specifically, it was critical to maintain a uniform temperature across a horizontal span of 25 mm which corresponds to the gauge length of the sub-size tensile specimen as indicated in Figure 4.2. Furthermore, it was important to ensure agreement with temperature in the vertical direction so that all three sub-size tensile specimens would receive the same thermal treatment and therefore be suitable duplicate samples for statistical analysis.

Three thermocouples were attached to the strip in the horizontal direction (points 1, 2 and 3 in Figure 4.5) with thermocouples 1 and 3 placed 25 mm apart. The center thermocouple (2) was therefore placed 12.5 mm from the outer thermocouples. The next test incorporated three thermocouples in the vertical direction (4, 5 and 5 in Figure 4.5). The vertical thermocouples were also placed 12.5 mm apart for a total span of 25 mm with point 4 representing the top thermocouple and point 6 in Figure 4.5 corresponding to the position of the bottom thermocouple.

Table 4.1: Thermocouple readings during temperature homogeneity experiments on strip samples; thermocouples are labeled according to Figure 4.5.

Thermocouple	Temperature at 468 s (°C)	Temperature at 768 s (°C)	Temperature at 803 s (°C)
1	938.71	937.55	633.01
2	945.21	944.00	585.00
3	945.06	939.55	594.61
4	961.92	946.00	609.23
5	945.73	945.00	585.00
6	940.63	943.56	585.46

Table 4.1 shows the combined results from the temperature homogeneity tests. The temperature values are shown for all six thermocouples at three distinct times during the experiment: 1) when the sample first reaches 945 °C (468 s), 2) the end of the 5 minute hold at 945 °C (768 s) and 3) when the sample reached 585 °C at a continuous cooling rate of 10 °C/s (803 s). The center thermocouples (2 and 5) are the thermocouples that the Gleeble 3500 was programmed to control; therefore, these temperatures should be the most accurate.

The thermocouple readings for the first point of interest (after 468 s when the sample is programmed to reach 945 °C) show that the temperature difference between the vertical thermocouples is quite significant: thermocouple 4 (top thermocouple in Figure 4.5 is 16 °C hotter than the center thermocouple (5), whereas thermocouple 6 is 5 °C cooler than the center thermocouple. The horizontal thermocouples have better performance at this temperature: the left thermocouple (1) is only 7 °C cooler than the center thermocouple, and thermocouple 3 is almost exactly the correct temperature. At the second distinct point during the experiment (at 768 s, signifying the end of the 5 minute hold at the austenitization temperature), the thermocouples are within a good tolerance of the expected value. The vertical thermocouples have a maximum deviation of 1.5 °C; however, the horizontal thermocouples are approximately 8 °C cooler than the specified temperature. Ther-

mocouple 1 was consistent at approximately 938 °C, while thermocouple 3 actually cooled from 945 °C to 939 °C during the austenitization process. The temperature conformance at 585 °C (after 803 sec) was very poor - the top thermocouple (4) was almost 25 °C hotter than the reference thermocouple (5), and the left thermocouple (1) is almost 50 °C hotter than the center thermocouple (2). This quick analysis was unfortunately not replicated and verified due to time and sample constraints, as these experiments actually required six specimens in order to obtain results.

After the temperature homogeneity tests were performed, the ITT thermal treatments were conducted using horizontal thermocouples (1, 2, and 3). The thermal schedules that were applied to the strip specimens followed the conditions outlined in Table 4.3 but the experiments were not conducted in sequential order. The cooling gas used for all experiments was helium and was supplied to the sample chamber through one, two or three nozzles. Most experiments used one helium nozzle; however, sample 3 in Table 4.3 used two nozzles and sample 8 used three helium nozzles. The temperature readings that resulted from using multiple helium nozzles did not improve the temperature homogeneity; therefore, a single nozzle was used for the remainder of the experiments.

The thermal profiles for each sample are shown in Figures 4.6 to 4.15. The labels T1, T2 and T3 correspond to the thermocouples that were placed vertically as described above for the Gleeble 3500 experiments performed at UBC. The data series T0 corresponds to the thermocouple data from the EVRAZ Gleeble 3800 simulation experiments.

The temperature plots showed good agreement for the three thermocouples on the strip specimens and the intended cooling schedule performed on the round ITT specimens tested in the Gleeble 3800. The recorded temperatures from the thermocouples are almost identical upon heating from room temperature to 945 °C; how-

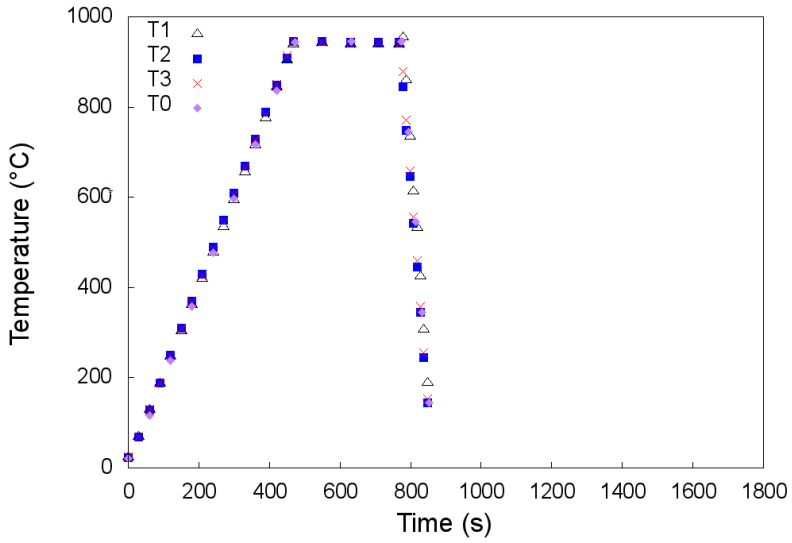

Figure 4.6: Thermal profile of the reference sample, CCT D6, continuously cooled at 10 °C/s.

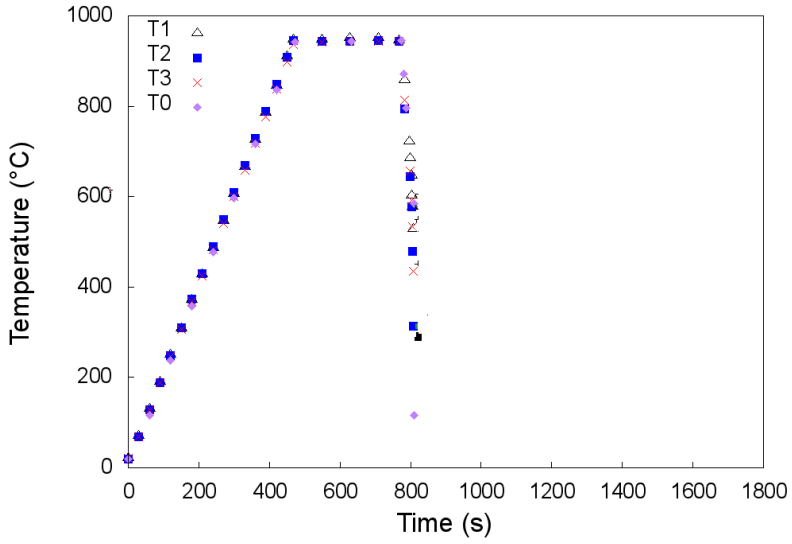

Figure 4.7: Thermal profiles for ITT sample 1.

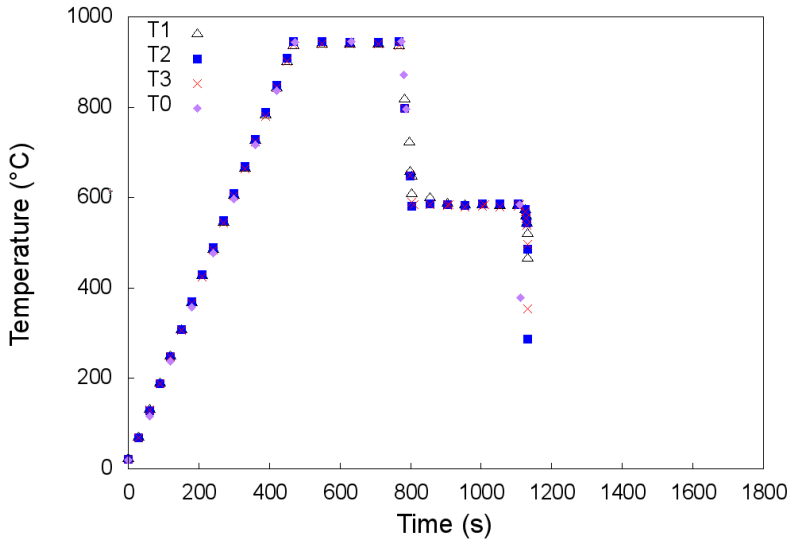

Figure 4.8: Thermal profiles for ITT sample 2.

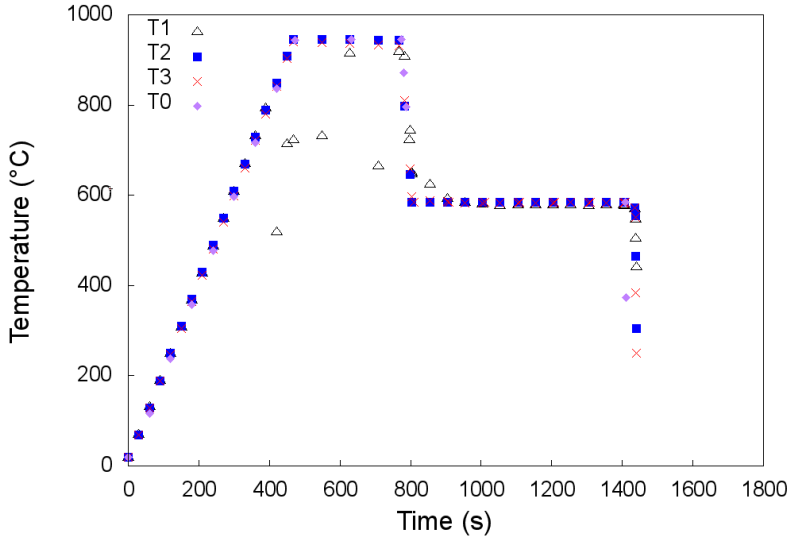

Figure 4.9: Thermal profiles for ITT sample 3.

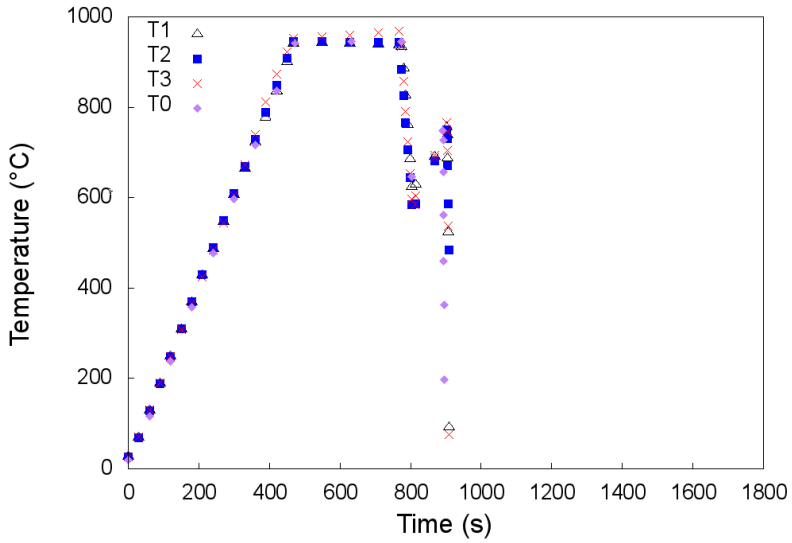

Figure 4.10: Thermal profiles for ITT sample 4.

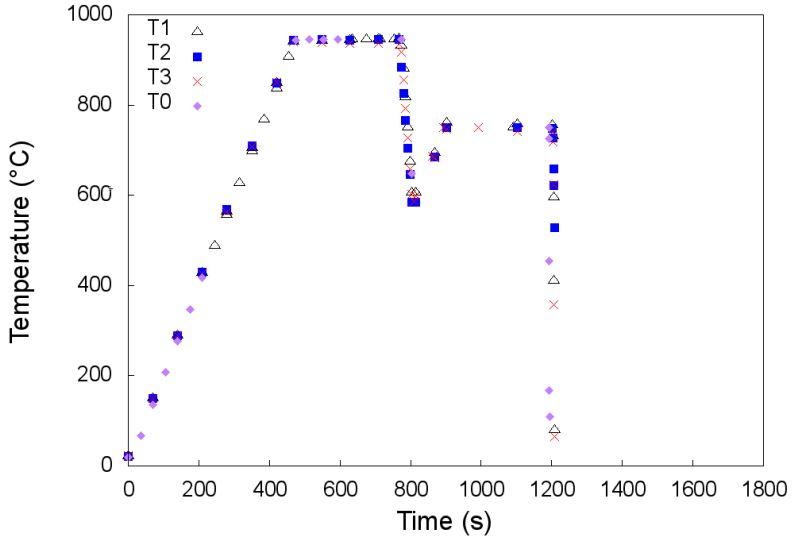

Figure 4.11: Thermal profiles for ITT sample 5.

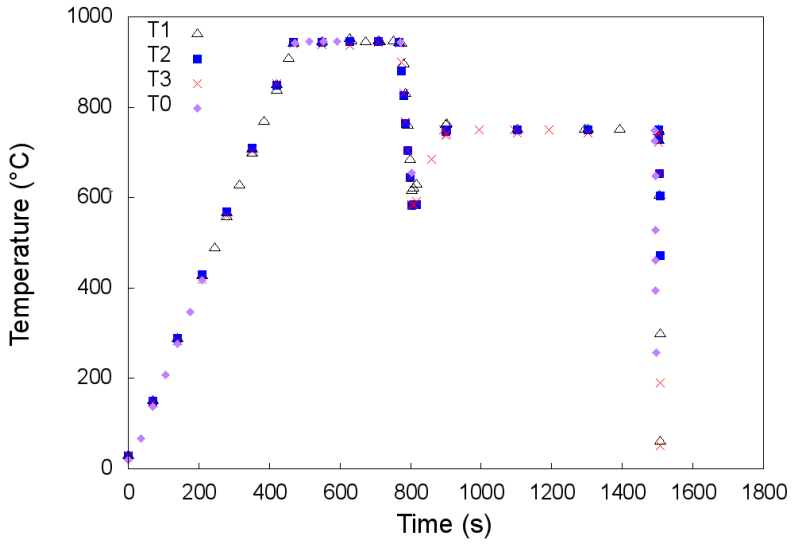

Figure 4.12: Thermal profiles for ITT sample 6.

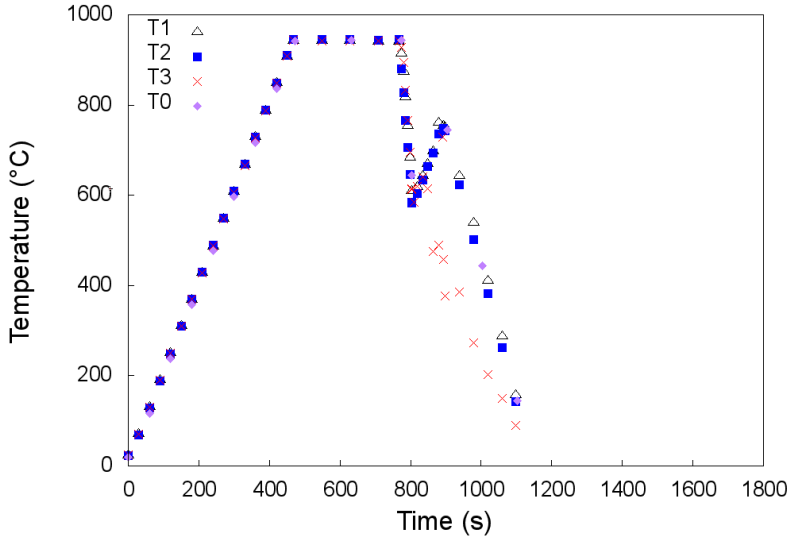

Figure 4.13: Thermal profiles for ITT sample 7.

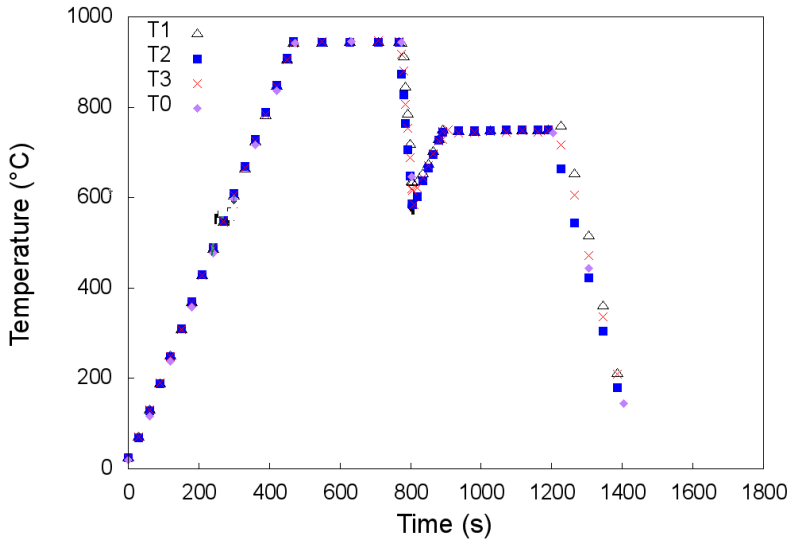

Figure 4.14: Thermal profiles for ITT sample 8.

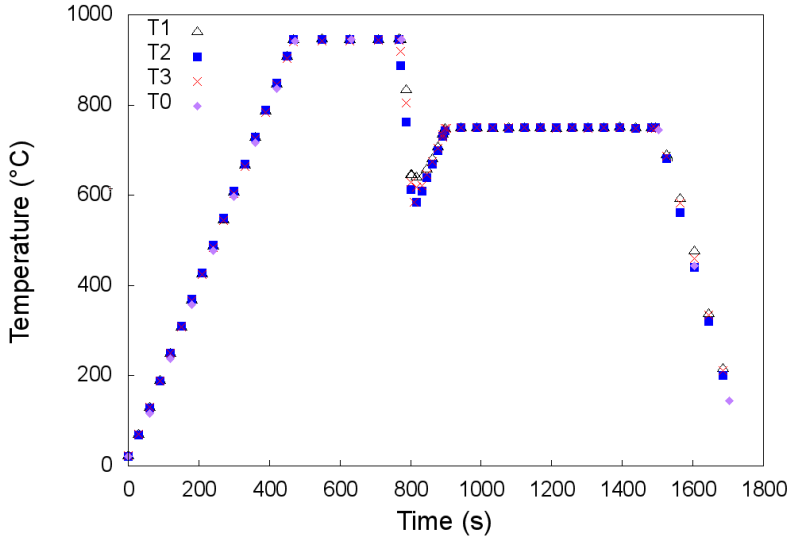

Figure 4.15: Thermal profiles for ITT sample 9.

ever, there are two experiments during which the temperatures deviate significantly from the center thermocouple after austenitization. In Figure 4.9, for example, thermocouple 3 (on the right of the center thermocouple) shows a scattered trend after austenitization and subsequent cooling to 585 °C. As previously mentioned, this experiment was conducted using three helium nozzles to attempt homogeneous cooling across the sample surface; as a result, the cooling rate between 945 °C and 585 °C was not controlled well and the thermal profile reflected this instability. Figure 4.8 shows another interesting trend. The temperatures for the left thermocouple (1) are scattered only at the hold temperature of 945 °C and then they stabilize. This trend cannot be explained by an experimental anomaly; however, the test can be considered a success if one assumes inaccurate readings for thermocouple 1 but that the correct heat treatment was applied as uniformly as possible throughout the sample.

The thermal performance for both the EVRAZ Gleeble 3800 samples and the UBC Gleeble 3500 strip samples verified that the sample geometry did not affect the thermal treatment nor, more importantly, the final microstructure which will be discussed in Section 4.3.1.

4.1.2 Sample Preparation

The sample preparation techniques for the ITT trial specimens were identical as for the CCT curve specimens, which were described in Section 3.1.2. One additional technique was used for the ITT specimens but not for the CCT curve specimens. Color metallography was attempted in order to both identify and quantify the phase fractions of each constituent. Color metallography is a process whereby certain phases and microconstituents are tinted different colors based on their different structures. One such etch is the LePera's etch, which uses picric acid, sodium

Table 4.2: LePera's etch for color metallography [LePera 79]

Solution Symbol	Chemical Solution	Solution Preparation
A	10 % HCl	10 mL HCl diluted in 90 mL ethanol
B	4 % picric acid	4 g picric acid dissolved in 100 mL ethanol
C	1 % sodium metabisulphite, 1 % EDTA	1 g sodium metabisulphite and 1 g EDTA dissolved in 100 mL water

metabisulphite and EDTA to stain bainite colonies black, M-A islands white and ferrite grains a tan color. A modified version of LePera's etch was used for color metallography and is detailed in Table 4.2 [LePera 79]. The major modification included a preliminary etch in a diluted hydrochloric acid (HCl) solution (solution A in Table 4.2). In order to correctly etch a sample with the modified LePera's etch, the sample must be vigorously cleaned between each grinding and polishing step using cold water and cold air only. The sample is first etched with solution A listed in Table 4.2 for approximately 15 seconds or until the sample surface appears slightly "pitted". Equal parts of solutions B and C are then mixed together and the sample is etched with this mixture until a black film forms on the entire sample surface [LePera 79]. This etching step can take anywhere from 5 to 20 minutes at room temperature [L.Goode]. As there is little or no consistency between experiments, color metallography using LePera's etch was a significant challenge.

4.1.3 Microscopy

The sample preparation techniques for the ITT trial specimens were identical to the techniques described for the CCT curve specimens in Section 3.2. The optical, SEM, FIB-SEM and TEM instruments and operating conditions were the same for the ITT samples as for the CCT specimens described previously.

4.1.4 Mechanical Testing

The mechanical tests that were performed on the ITT trials included hardness and tensile tests, which will be discussed in the following sections. Three types of hardness tests were performed: macrohardness, microhardness and nanoindentation. The experimental procedure used for the hardness and tensile tests will be discussed in the next sections.

Hardness Testing

The equipment and operating conditions for the microhardness tests for the ITT specimens were the same as for the CCT samples, and are described in Section 3.2.1. Microhardness tests were performed using a 1 kg load on a Mitutoya MVK-H1 Hardness Testing Machine. Five indents were made per sample to obtain average hardness values and the standard deviation for each specimen. Nanoindentation experiments were performed using a Hysitron TriboIndenter using a maximum load of 4000 μN. Several indents were made across one grain which was first located in the NB5000 FIB-SEM and then identified by milling a region around the grain of interest so that the region was easily located in the TriboIndenter. The full experimental procedure and results of the nanoindentation experiments are detailed in Appendix C.

Tensile Testing

As mentioned in the previous section, tensile tests were conducted on sub-size tensile specimens according to the geometry specified in ASTM E 8M-04, shown in Figure 4.2 [AST 04]. The sub-size tensile specimens were machined from the large strip samples thermally treated in the Gleeble 3500. Figure 4.16 shows the position of the sub-size tensile specimens within the larger strip specimen as well as the

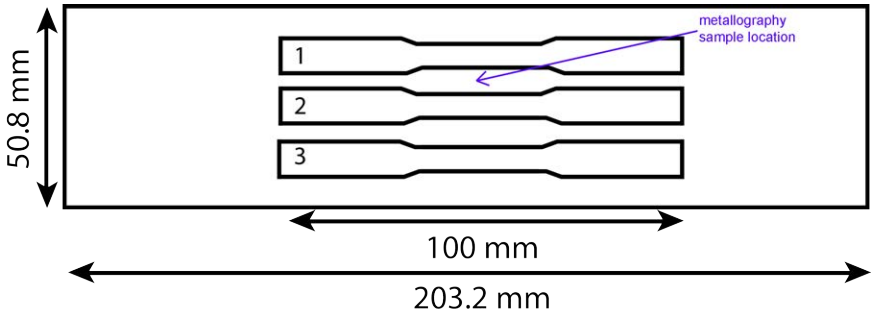

Figure 4.16: Sub-size tensile specimens removed from strip samples (Figure 4.4) that were thermally treated in the Gleeble 3500. The metallographic sample used for hardness and microstructure investigation was removed from the area shown by the arrow.

location of the metallography sample. Three tensile specimens were removed from each strip to ensure that there would be triplicate tensile experiments for each heat treatment condition. The metallography samples were obtained from the region identified in Figure 4.16.

An Instron 8800 servohydraulic actuator tensile tester with a maximum load cell of 100 kN was used to test the specimens under uniaxial loading conditions. Figure 4.17a shows the Instron 8800 tensile machine and a loaded sub-size tensile specimen is shown in Figure 4.17b. The sample dimensions (width and thickness) were measured and recorded before the sample was loaded in the machine. An extensometer was attached to the center of the gauge length on the sub-size specimen as indicated by the center mark in Figure 4.17b. A uniform elongation rate of 2 mm/s was used to mechanically deform the sample to failure. The parameters recorded during the experiment included displacement from the extensometer and instantaneous load recorded from the load cell.

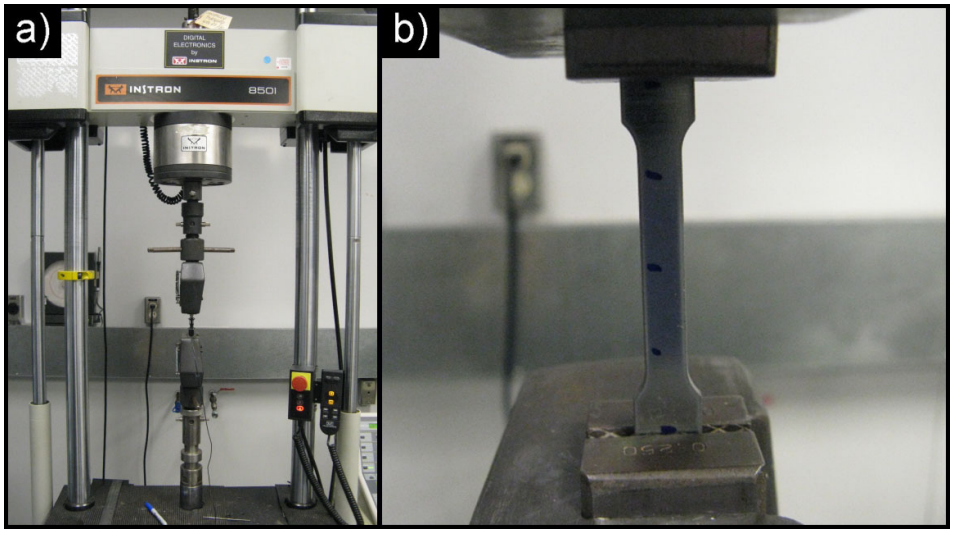

Figure 4.17: Instron 8800 tensile testing instrument.

4.2 Interrupted Thermal Treatment (ITT)

As mentioned in Section 2.6, the purpose of this research project was to first determine the effect of thermal treatment on microstructure development and secondly to identify the relationship between microstructure and mechanical properties. More specifically, the goal was to assess the conjecture put forward by the Japanese researchers that reheating and subsequent cooling could cause carbon to diffuse to austenite regions which subsequently forms M-A upon cooling. The thermal treatments that were chosen for the ITT tests were performed under no-strain conditions. As a result, the ITT trials were intended to strictly evaluate the effect of thermal history on microstructure development without considering the effect of deformation on phase transformation, grain refinement and precipitation; hence, the effect of deformation on strengthening mechanisms. The ITT trials are therefore not complete representations of traditional TMCP products since deformation during rolling is a very important component in microalloyed steel processing that affects the relevant

strengthening mechanisms.

There are six major parameters that can be varied in order to affect microstructure development in an intermediate heat treatment process: 1) initial cooling rate, 2) interrupt temperature after accelerated cooling, 3) hold time at the interrupt temperature, 4) re-heat temperature, 5) hold time at the re-heat temperature and 6) final cooling rate. The original proposed test matrix evaluated each variable at a high and low condition, which would require 64 individual experiments (or 192 experiments to account for triplicates of each test condition).

The first set of ITT trial tests had an initial cooling rate of 10 °C/s as this cooling rate is easily achievable in most steel mills. The interrupt temperature was chosen based on dual-phase steel considerations. More specifically, dual phase steels are created to efficiently and effectively combine the best mechanical properties of the two individual microconstituents. The optimized composition of dual phase steels consists of 80 % of the tough and ductile matrix microconstituent with the remaining 20 % providing the strength and work hardening characteristics, as mentioned in Section 2.1.4 and Section 2.1.2 [Nobuyuki 06, Krauss 05]. According to the fraction transformed results presented in Section 3.3.5 for a continuous cooling rate of 10 °C/s, the interrupt temperature that corresponds to 80 % transformation to the primary product is 585 °C. These two parameters (initial cooling rate and interrupt temperature) should ensure that 80 % of the available austenite will transform to the primary structure, leaving 20 % of the austenite to become enriched in carbon during subsequent thermal treatments and thus form M-A upon final cooling. The next parameter that was chosen for the ITT trials was the hold time at the interrupt temperature: hold times of 0, 5 and 10 minutes were investigated at the interrupt temperature of 585 °C. These three hold times were chosen to represent immediate, intermediate and long term conditions to assess the formation of bainite at a

critical isothermal temperature. The re-heat temperature of 750 °C was selected to promote carbon diffusion out of the primary bainite structure into the 20 % remaining austenite. The A_{c1} was determined to be 740 °C as discussed in Section 3.3.1; however, this value is subject to experimental variation and may in fact be within ± 5 °C to ± 35 °C of the determined value [Eldis 78]. The re-heat temperature was chosen to maximize carbon diffusion from the primary structure (anticipated to be bainite); as a result, a temperature close to the A_{c1} temperature was required. However, the temperature had to be selected to prevent reaustenitization; i.e., less than A_{c1}. Based on the error associated with the A_{c1} temperature determination (more specifically, that the A_{c1} temperature could range from 705 °C to 780 °C), a re-heat temperature of 750 °C was chosen to balance maximum carbon diffusion with the prevention of reaustenitization. The hold times at the re-heat temperature were chosen to be 0, 5 and 10 minutes to maintain consistency with the hold times at the interrupt temperature. The final cooling rate was selected as 3 °C/s.

Figure 4.18 schematically depicts the ITT schedule performed for ten samples (one reference sample and nine ITT trial samples).

The reference sample was continuously cooled at 10 °C/s after austenitization (equivalent to sample D6 of the CCT curve specimens). Each sample was heated to 945 °C at 2 °C/s and held at this temperature for 5 minutes before the thermal schedule was applied. Samples 1, 2 and 3 were continuously cooled from 945 °C to 585 °C at 10 °C/s before quenching to room temperature after 0, 5 and 10 minutes, respectively. Based on a preliminary microstructural investigation of samples 1, 2 and 3, it was determined that the hold time at 585 °C was optimized for a 0 minute hold; as a result, all subsequent ITT samples were re-heated to an intermediate temperature after a 0 minute hold at the interrupt temperature. Samples 4, 5 and 6 were continuously cooled from 945 °C to 585 °C at 10 °C/s, immediately re-heated to

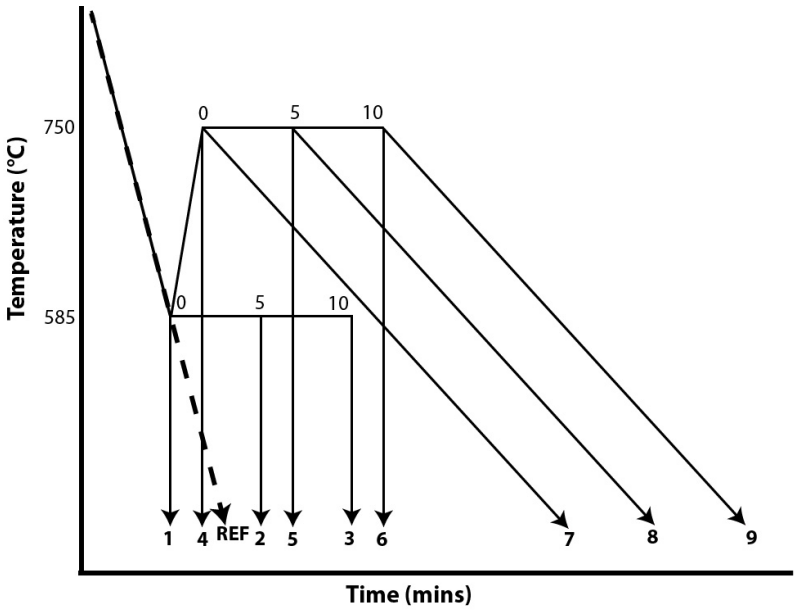

Figure 4.18: Schematic diagram for ITT trial samples.

750 °C at a rate of 2 °C/s and held at 750 °C for 0, 5 and 10 minutes, respectively, before quenching to room temperature. Samples 7, 8 and 9 followed the same thermal treatment as 4, 5 and 6 with the exception of the final cooling rate, which was 3 °C/s. It is important to note that all the ITT tests were performed without a dilatometer, as the dilatometer is very delicate and could have been damaged by the water jet during the quench operations. Even though samples 7, 8 and 9 did not require the quench unit, the dilatometer was not attached to these specimens. Table 4.3 summarizes the specific thermal treatments performed on each of the ITT specimens studied.

Table 4.3: Detailed thermal schedule for all ITT samples.

Sample ID	Primary Cooling Rate (°C/s)	Interrupt Temperature (°C)	Hold Time (min)	Re-heat Temperature (°C)	Hold Time (min)	Secondary Cooling Rate (°C/s)
REF	10	-	-	-	-	-
1	10	585	0	-	-	quench
2	10	585	5	-	-	quench
3	10	585	10	-	-	quench
4	10	585	0	750	0	quench
5	10	585	0	750	5	quench
6	10	585	0	750	10	quench
7	10	585	0	750	0	3
8	10	585	0	750	5	3
9	10	585	0	750	10	3

4.3 Microstructure Characterization of ITT Curve Specimens

Section 2.6 presents the goals of this thesis; more specifically, to determine the effect of thermal history on microstructural development in relation to modified thermal treatments and then to correlate the microstructure to mechanical performance. In order to identify the relationship between thermal history and microstructure, the microstructures of the ITT specimens first had to be characterized and quantified. This was performed using optical, scanning electron and transmission electron microscopy which will be presented and discussed in the following sections.

4.3.1 SEM SE Micrographs of ITT Specimens

The ITT specimens from both Gleeble experiments were cut, mounted, polished and etched for microstructural investigation according to Section 3.1.2. As mentioned, the EVRAZ Gleeble 3800 specimens were thermally treated to provide preliminary insight into the microstructures present as a result of interrupted heat-

ing and cooling schedules. Color metallography was attempted on these samples to determine the phase fraction of martensite, bainite and M-A based on the preferential etching of the constituents [LePera 79]. Unfortunately, color metallography was not a viable technique for these steel samples as the polishing and etching procedure resulted in varying success. Color metallography was attempted for several months before one sample yielded positive results, which were only obtained once and were unfortunately not reproducible. The color metallography experiments and results are detailed in Appendix B and will not be discussed further here.

SEM SE images were obtained for the UBC ITT trial samples according to the techniques and operating conditions described in Section 3.2. The compilation of ITT samples 1 through 9 is shown in Figure 4.19 based on the numbering system shown in Table 4.3. These micrographs were obtained from the strip specimens that were heat treated in the Gleeble 3500 for direct comparison of the microstructure with the final mechanical properties. The average sample size that was removed from the strip specimen was approximately a 4 mm by 4 mm square section that was removed from the center of the strip (between sub-size specimens 1 and 2, as shown in Figure 4.16). After mounting and polishing, the samples were etched with 2 % Nital to reveal the grain boundaries and structures. Ten micrographs were obtained for each sample: one representative image for each specimen is shown in Figure 4.19 and the other nine micrographs are shown in Appendix D. All ten images were used for microstructure quantification, which will be discussed in Section 4.4.

Similar to the CCT curve micrographs shown in Figure 3.30, the brighter regions in Figure 4.19 can be classified as martensite, bainite and/or pearlite since these constituents do not etch quickly in Nital and therefore appear "raised" in SEM SE images. Ferrite etches very easily with Nital and therefore is present as the dark regions in Figure 4.19. Furthermore, ferrite is characterized by relatively equiaxed

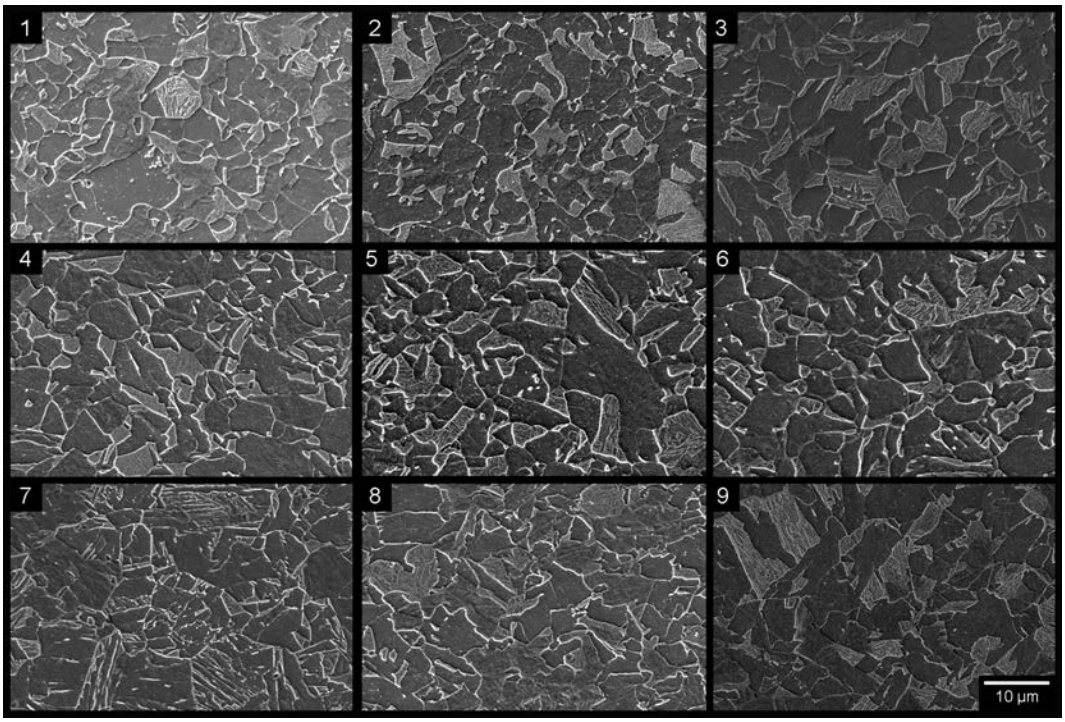

Figure 4.19: SEM micrographs of the ITT specimens labeled 1 through 9.

grains that appear lower than the martensite, bainite and/or pearlite grains. The M-A constituent appears as very small round or "stringy" features that are situated along grain boundaries or at triple points.

The TEM study conducted on CCT specimen D11 was presented and explained in Section 3.4.3. Three regions (shown in Figures 3.32, 3.33 and 3.34 were positively identified as martensite, bainitic ferrite and pearlite, respectively. However, the 'microconstituent characterization database' at this stage consisted of three grains; thus, further investigation was required to expand the database to include multiple examples of each confirmed grain before the ITT microstructures could be quantified. More specifically, it was necessary to attempt the differentiation between martensite and bainitic ferrite grains in the SEM SE images in order to quantify each constituent independently. As a result, two ITT samples were selected for TEM analysis, which will be discussed in the following section.

4.3.2 TEM Analysis of ITT Specimens

The TEM analysis on the ITT specimens adds to the 'microconstituent characterization database' that was initiated with the CCT curve samples, as discussed in Section 3.4.3.

Two TEM samples were fabricated using the FIB technique that was described in Section 3.2. The first sample that was investigated was sample 1 in Table 4.3. This sample was chosen because of the high percentage of bright grains (either martensite or bainite/bainitic ferrite) observed in the SEM SE micrographs and TEM analysis was performed to accurately characterize the nature of the bright grains.

The first region of interest selected from this specimen was originally thought to be pearlite due to the lamellar-like internal structure, as shown in Figure 4.20. The TEM results from the FIB sample (represented by the box in Figure 4.20) are

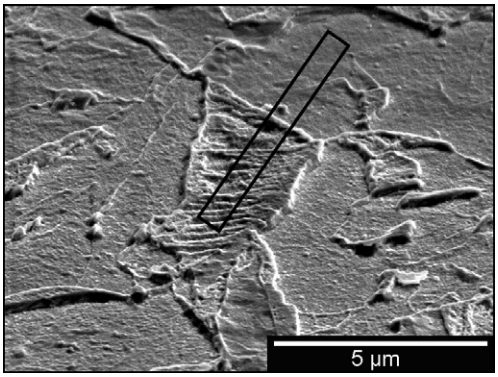

Figure 4.20: SEM SE micrograph showing a region of interest from ITT sample 1.

shown in Figure 4.21. Figure 4.21a is a low magnification TEM BF image of the TEM sample with the box indicating a particular region that is further magnified in Figure 4.21b. The numbers (1, 2 and 3) in Figure 4.21b correspond to the regions from which SAD patterns were taken, which are shown in Figures 4.21c, d and e. As described in Section 3.4.3, laths that appear darker (spots 1 and 2 in Figure 4.21b) are oriented closest to the Bragg condition and diffract more strongly than the laths that are oriented farther from the Bragg condition (spot 3 in Figure 4.21b). The SAD patterns for spots 1, 2 and 3 were similar with the only main difference being in the diffraction spot brightness. The SAD patterns were solved according to the procedure outlined in Section 2.3.3 and were indexed to ferrite with zone axes close to a [012] orientation. The slight misorientation between the laths is characteristic of a bainitic structure containing laths at slight misorientations relative to the Bragg condition; however, no iron carbide precipitates were observed which would have been present either between or within the bainite laths. As a result, the region of interest shown in Figure 4.20 was classified as bainitic ferrite.

The second region of interest taken from ITT sample 1 is shown in Figure 4.22. The TEM sample that was prepared using the FIB technique is represented by

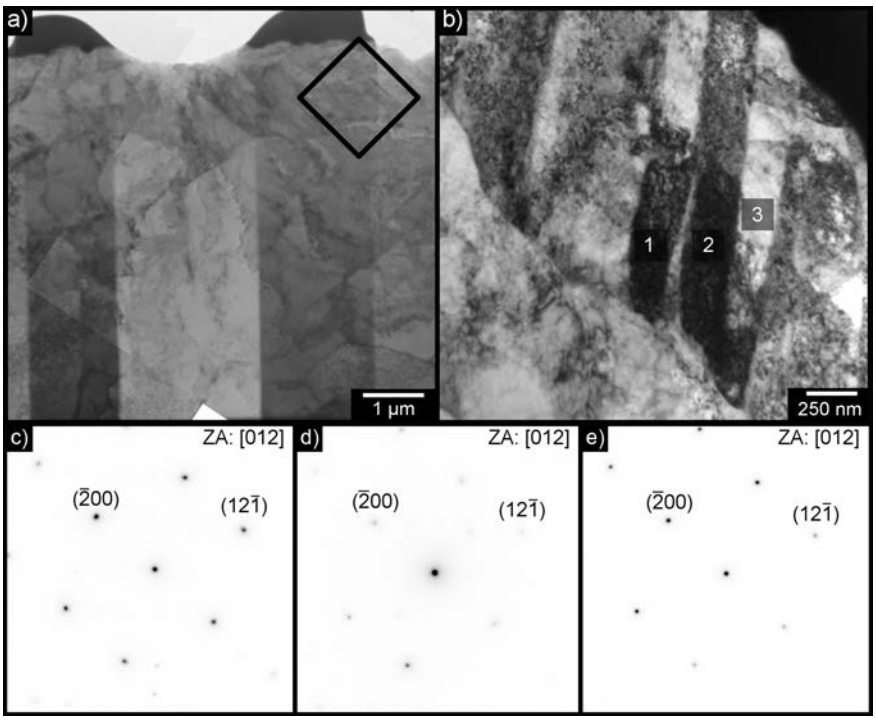

Figure 4.21: TEM results from the region of interest indicated in Figure 4.20: a) low magnification and b) high magnification TEM BF micrographs; SAD patterns (c, d e) corresponding to numbers 1, 2 and 3 in Figure 4.21b.

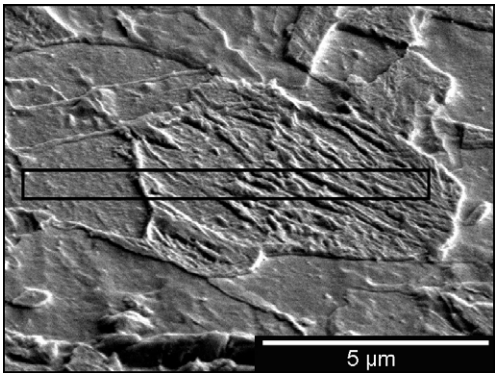

Figure 4.22: SEM SE micrograph showing a second region of interest from ITT sample 1.

the box in Figure 4.22, and the TEM micrographs are presented in Figure 4.23. Figure 4.23a is a low magnification TEM micrograph of the FIB sample shown in Figure 4.22, where the black box represents an area further magnified in Figure 4.23b and the white box indicates the region that was further magnified in Figure 4.23d. The box in Figure 4.23b represents the region where a SAD pattern was obtained, which is shown in Figure 4.23c. The diffraction pattern was solved and indexed to ferrite with a zone axis close to a $[\bar{3}13]$ direction. As mentioned in Section 3.4.3, the diffraction pattern in Figure 4.23c can also represent martensite as the c/a ratio for this grade of steel is very close to 1 and, as such, martensite can be indexed with the same pattern as ferrite. Figure 4.23d is a magnified image of the white box in Figure 4.23a and shows parallel microtwins. The box around the microtwins in Figure 4.23d represents the area from which the SAD pattern, shown in Figure 4.23e, was obtained. The SAD pattern in Figure 4.23e was indexed to ferrite with a zone axis close to a $[\bar{1}10]$ orientation; however, the presence of microtwins confirms that this region is martensite.

A third region of interest was obtained from ITT specimen 1 as shown in Figure 4.24. The TEM results are shown in Figure 4.25. A low magnification TEM BF

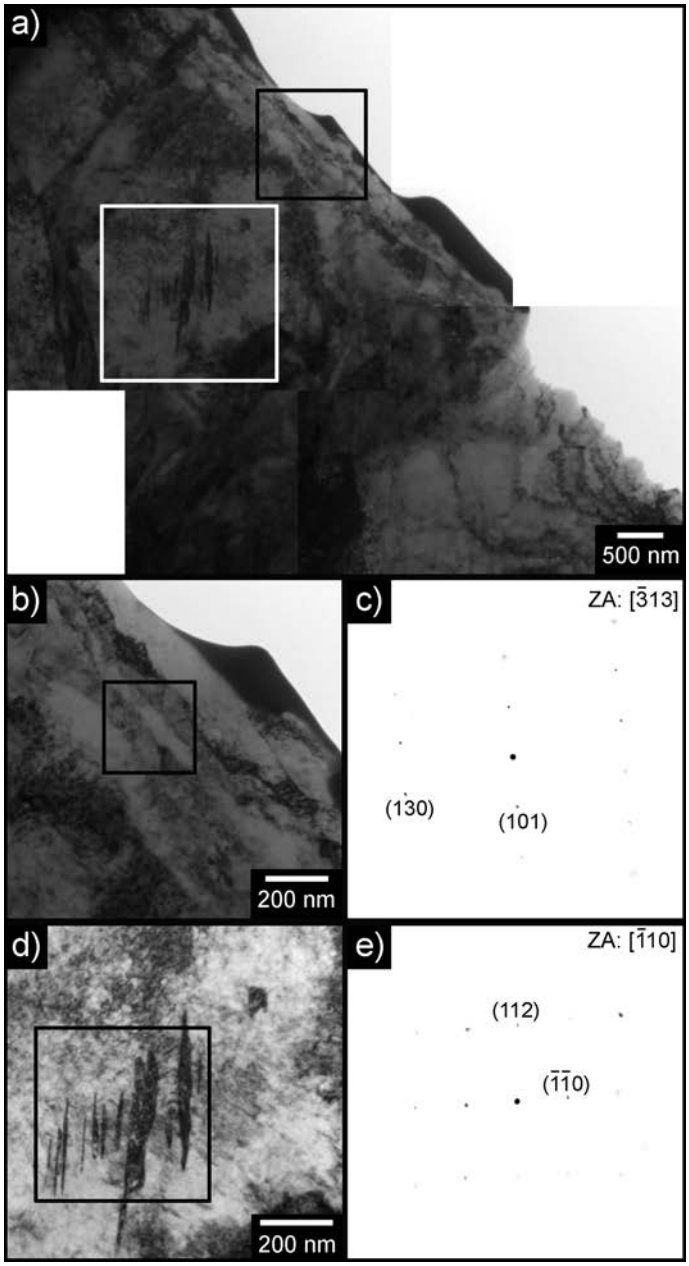

Figure 4.23: TEM results from the region of interest indicated in Figure 4.22: a) low magnification TEM BF micrograph; b) high magnification TEM BF micrograph of the region indicated by the black box in Figure 4.23a); c) SAD patterns corresponding to the region identified by the black box in Figure 4.23b); d) high magnification TEM BF micrograph of the region marked by the white box in Figure 4.23a); e) SAD pattern corresponding to the black box in Figure 4.23d).

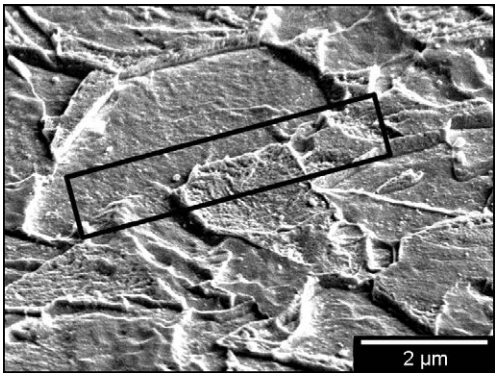

Figure 4.24: SEM SE micrograph showing a third region of interest from ITT sample 1.

image is shown in Figure 4.25a with the box in Figure 4.25a representing the region from which a higher magnification TEM BF image was collected (Figure 4.25b). Numbers 1, 2 and 3 in Figure 4.25b correspond to the individual areas from which SAD patterns were obtained, as shown in Figure 4.25c - e, respectively. The position of the spots in the SAD patterns are identical, only the brightness of each pattern was different. As previously described, the darker laths (spots 1 and 3 in Figure 4.25b) are closer to the Bragg condition than spot 2; therefore they diffract more strongly and the patterns appear brighter. The SAD patterns were indexed to ferrite with zone axes close to the [113] orientation. Since this region contained parallel laths but no iron carbides were observed, the region was characterized as bainitic ferrite.

Another TEM sample was prepared; this time a region of interest was selected from sample 2. This sample was chosen based on preliminary SEM SE micrographs that showed extraordinarily large and odd-shaped grains which were tentatively labeled as bainite grains. The specific region of interest that was removed from the sample is shown in Figure 4.26 and the relevant TEM results are shown in Figure 4.27. Figure 4.27a shows a low magnification TEM BF micrograph with the box

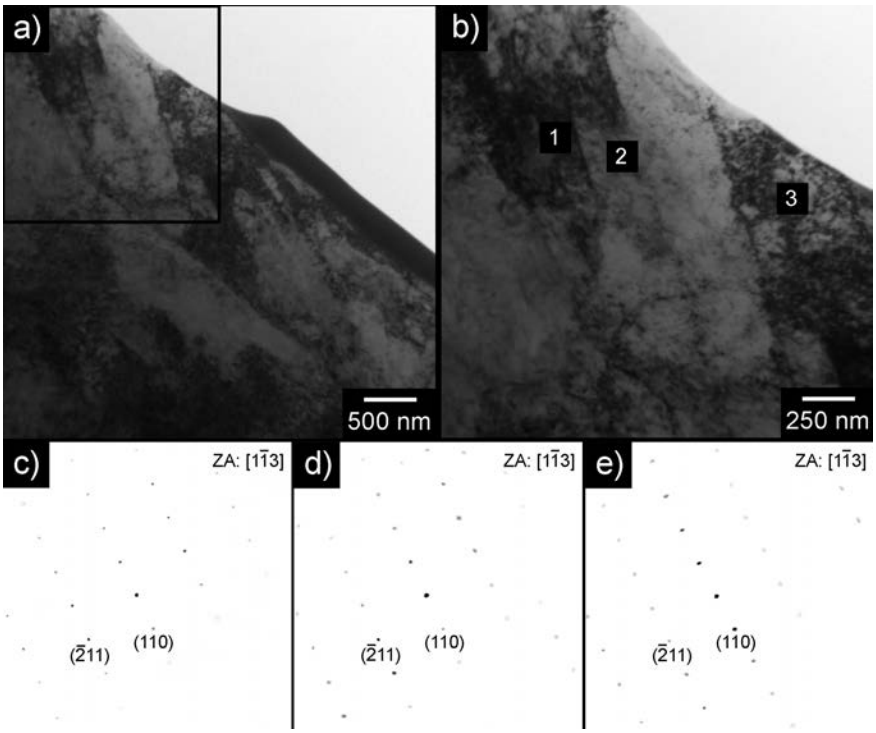

Figure 4.25: TEM results from the region of interest indicated in Figure 4.24: a) low magnification and b) high magnification TEM BF micrographs; SAD patterns (c, d e) corresponding to numbers 1, 2 and 3 in Figure 4.25b).

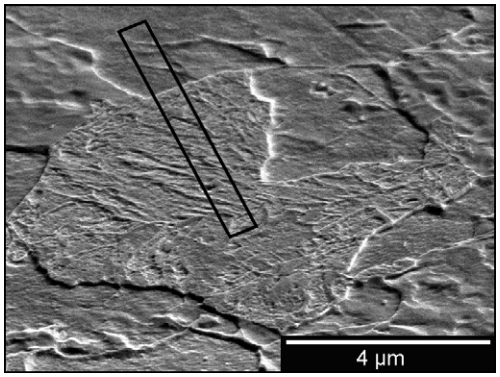

Figure 4.26: SEM SE micrograph showing a region of interest from ITT sample 2.

representing a higher magnification BF image shown in Figure 4.27b. Figure 4.27c shows the same region as Figure 4.27b, but the image was taken at a different tilt angle to illustrate that the microstructural features (in this case, microtwins) observed go in and out of contrast based on tilt angle. Figure 4.27b was taken at a tilt angle of 13.4 ° relative to Figure 4.27c. The microtwins that are present in Figure 4.27b are not observed in Figure 4.27c; however, different microtwins are observed in Figure 4.27c than in Figure 4.27b. The SAD pattern shown in Figure 4.27d was obtained from the boxed region in Figure 4.27c and was indexed to ferrite with a zone axis close to a $[1\bar{3}6]$ orientation. Since the c/a ratio for martensite will be very close to 1 for steels with this low carbon content, the presence of the microtwins confirms that the phase is, in fact, martensite.

The four regions that were investigated in the TEM from ITT trial samples 1 and 2 (according to Table 4.3) were successfully identified using TEM. Figures 4.20 and 4.24 show regions that were correctly identified as bainitic ferrite based on the observation of adjacent laths that were absent of iron carbides. Figures 4.22 and 4.26 represent the regions of interest that were classified as martensite based on the presence of microtwins in high magnification TEM images.

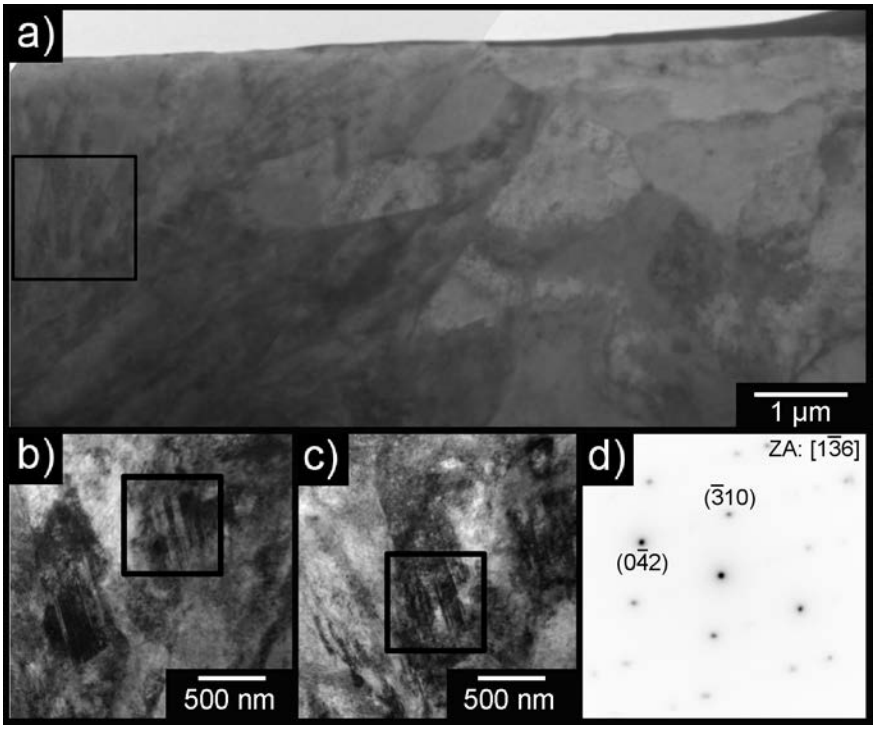

Figure 4.27: TEM results from the region of interest indicated in Figure 4.26: a) low magnification TEM BF micrograph; b) high magnification TEM BF micrograph of the region in Figure 4.27a); c) high magnification TEM BF micrograph of the region in Figure 4.27a) at a different title angle than Figure 4.27b); d) SAD pattern from the black box indicated in Figures 4.27b) and c).

After the TEM investigation of the ITT samples, the 'microconstituent characterization database' was compiled using the results from both the ITT grains detailed above and the CCT regions presented in Section 3.4.3. The 'microconstituent characterization database' is shown in Figure 4.28, where the black boxes indicate the FIB TEM sections. The FIB sections each contain a portion of the grain of interest and a portion of a neighboring ferrite grain. The ferrite grains are the flat, light grey regions with no evidence of carbides, lamellar structures or raised features. Thus, the regions that were confirmed using TEM correspond to the section of the boxes in Figure 4.28 that are not ferrite. Figure 4.28a, d and e represent martensite regions, Figure 4.28b, f and g correspond to bainitic ferrite regions and Figure 4.28c is a region that was solved to be pearlite.

The 'microconstituent characterization database' shown in Figure 4.28 was subsequently used as a template to compare grains of a known structure with unknown regions that were observed in the SEM SE images in order to correctly identify their structure. Although the specific regions shown in Figure 4.28 were correctly identified through individual TEM analysis, it was still difficult to distinguish between martensite and bainitic ferrite in the SEM SE images. For example, Figure 4.28d and Figure 4.28e have similar internal structures; both appear to have a somewhat ordered lath-like morphology but Figure 4.28d was determined to be martensite whereas Figure 4.28e was classified as bainitic ferrite. Similarly, the region in Figure 4.28g has a similar structure to that of Figure 4.28a (although the regions are different sizes); the results from the TEM investigation showed that the region in Figure 4.28a was martensite while Figure 4.28e was bainitic ferrite. As such, there was no clear trait or characteristic that could be used to correctly and consistently differentiate between martensite and bainitic ferrite in the SEM SE images.

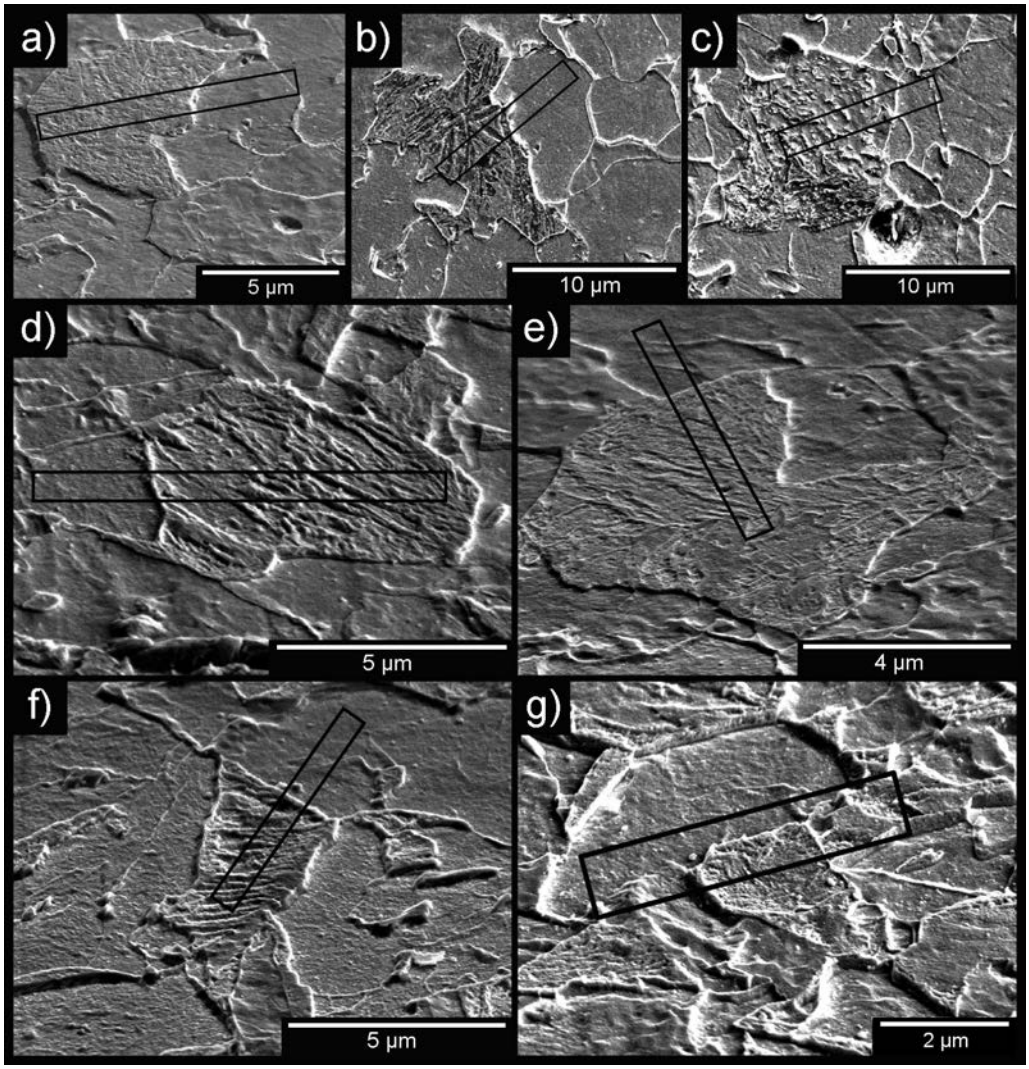

Figure 4.28: Microconstituent characterization database showing the regions of interest from: a) CCT specimen D3 (martensite); b) CCT specimen D3 (bainitic ferrite); c) CCT specimen D3 (pearlite); d) ITT trial 1 martensite); e) ITT trial 1 (martensite); f) ITT trial 1 (bainitic ferrite); g) ITT trial 2 (bainitic ferrite).

4.4 Microstructure Quantification for ITT Specimens

After the TEM investigation was performed and the nature of some indistinguishable regions was determined, the SEM SE micrographs were quantified using FIJI image analysis software. The phase fractions and grain size of each constituent were determined for each sample and will be discussed in the following sections.

4.4.1 Phase Fractions for ITT Specimens

The SEM SE micrographs for the ITT specimens are shown in Section 4.3.1. The constituents that were identified in the micrographs included ferrite, bainitic ferrite, martensite and M-A. As previously mentioned, the TEM investigation detailed in Section 3.4.3 and Section 4.3.2 was performed in order to determine the nature of certain grains and, more specifically, to identify the difference between martensite and bainite grains in SEM SE micrographs. The TEM study successfully identified the difference between martensite and bainitic ferrite; however, there were no distinct traits that could be used to differentiate between martensite and bainitic ferrite in SEM SE micrographs. The martensite and bainitic ferrite grains have similar morphology in the SEM SE images and were only differentiated using TEM. Since it was very difficult to correctly discerning the various microconstituents in the SEM SE micrographs, bainitic ferrite and martensite were considered a single entity in the phase quantification analysis. As a result, the phase fractions for each sample include ferrite, bainitic ferrite/martensite and M-A islands. This group structure was chosen since the differences between ferrite and the other constituents were obvious in the SEM SE images. Furthermore, the mechanical properties of bainitic ferrite and martensite are similar and thus, grouping these two constituents together in phase quantification provides a basis for comparison with mechanical performance. Figure 4.28 was used as a guide to identify the regions that could

either be martensite or bainitic ferrite, but the distinction between the two structures was not made for the purpose of phase quantification. It is important to note that this was an exploratory technique: no publications were found which correlated TEM results with SEM microconstituent quantification; thus, the results presented in this section were not verified by literature results for similar materials.

In order to determine the phase fractions present in the microstructures for each sample, five micrographs from each sample were subjected to a similar image analysis procedure and the results were averaged. The full procedure is demonstrated in Figure 4.29, where the full image analysis process is performed on a sample micrograph. The specific settings (i.e., the values used for the dark/bright outliers, contrast enhancement and the median blur radius) used for image processing are detailed in Appendix F.

The first step in image analysis was to remove the dark and bright outliers that were evident in the image. For example, very small specks such as dust particles on the sample surface are not microconstituents; therefore, they must be removed prior to image calculation. After the dark and bright outliers were removed, the contrast was enhanced. This was performed in order to enhance the grain boundaries and internal structures within the grains. A median blur was then applied in order to average the grey value of the image within a 5 pixel radius. As mentioned in Section 2.4.1, a median blur is the most powerful ranking filter because the brightness and edges are not affected by the filter operation and, as such, the median filter in this application did not affect the grain boundary shape but rather enhanced the grain boundaries. After the median blur was applied, the threshold was adjusted and applied to the image to isolate the bright regions from the dark regions. The image after the threshold was applied contained only black regions (corresponding to the dark regions of ferrite in the original micrograph) and regions of white (cor-

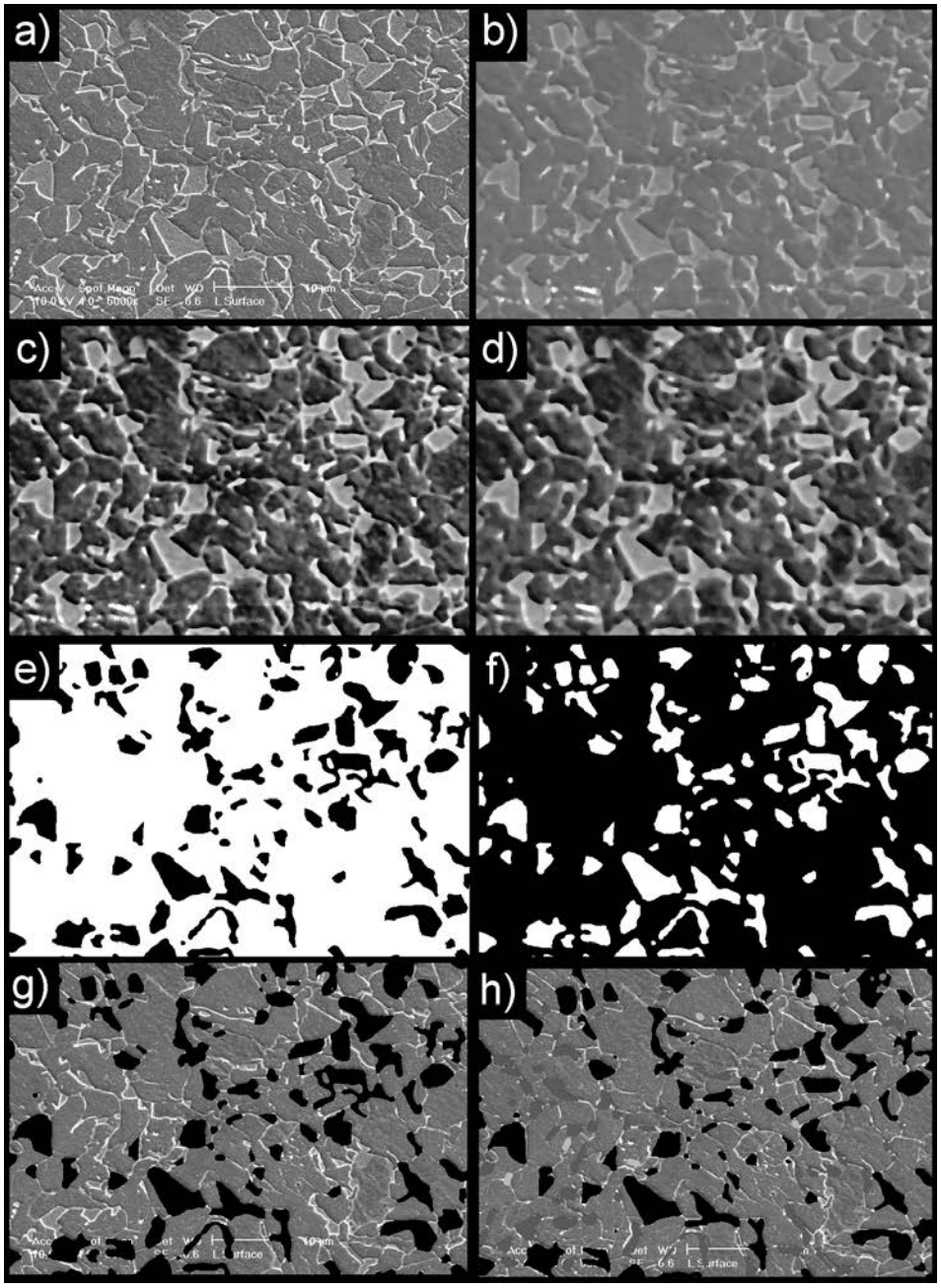

Figure 4.29: Image analysis procedure for determining the phase fractions of the ITT specimens using SEM SE micrographs: a) original image, b) dark and white outliers are removed, c) contrast is enhanced, d) median filter is applied, e) threshold is adjusted, f) threshold image is inverted and phase fractions of white (ferrite) and dark (bainite and martensite) are calculated, g) inverted image is subtracted from original micrograph, h) M-A islands are manually isolated and marked in both the ferrite and bainite/martensite regions.

responding to the brighter regions of bainitic ferrite and martensite in the original micrograph). The image was then inverted and the area fraction of white and black regions was calculated to reveal the percentage of ferrite (white regions) and the combined fraction of bainitic ferrite and martensite (black regions). The inverted image was then subtracted from the original image so that the bainitic ferrite and martensite grains appeared black in the original image and the ferrite grains were unaffected. This was performed in order to assess the accuracy of the image processing procedure and to compare the original image with the marked image. After subtracting the inverted image from the original image, it was apparent that the small M-A islands were neglected from analysis.

Due to the segmentation steps performed during image analysis, a binary image was created. Although this was the goal of image processing, the median blur affected the original grain size and, in some cases, evidence of certain grains. More specifically, some M-A islands were not eliminated during the median blur and hence were considered as bainitic ferrite/martensite in some processed images. Other M-A regions were erased during image processing and were therefore considered in the ferrite phase fraction. The incorrectly quantified M-A regions were noticed when the final inverted image was subtracted from the original image, as shown in Figure 4.29g. As a result, regions of M-A were identified and marked individually for each micrograph. In these micrographs, M-A was identified by its appearance and location: either the islands were small and globular or they were elongated and 'stringy'; however, both geometries of M-A were located on prior austenite grain boundaries [Han 12, Lan 12]. This selection criteria was applied to each micrograph and the M-A islands were manually marked on the final image. The area fraction of M-A was then calculated from the image and the values were subtracted from either the ferrite or bainitic ferrite/martensite phase fraction (depending on which

Table 4.4: Microstructure distribution for the constituents observed in the ITT specimens, namely ferrite, bainitic ferrite, martensite and M-A.

Sample ID	Ferrite (%)	Bainitic Ferrite/Martensite (%)	M-A (%)
REF	88.3 ± 3.5	8.0 ± 2.6	3.7 ± 1.7
1	77.4 ± 1.8	20.9 ± 1.9	1.7 ± 0.7
2	76.6 ± 1.2	21.5 ± 1.3	1.8 ± 0.3
3	70.7 ± 1.8	28.0 ± 1.8	1.3 ± 0.3
4	79.4 ± 1.3	19.9 ± 1.4	0.7 ± 0.1
5	72.6 ± 2.9	26.4 ± 3.2	1.0 ± 0.4
6	67.5 ± 2.3	32.1 ± 2.3	0.4 ± 0.1
7	71.4 ± 1.6	26.6 ± 1.7	2.0 ± 0.2
8	74.5 ± 2.5	22.6 ± 2.6	2.9 ± 0.5
9	71.4 ± 1.1	28.6 ± 1.1	0.0

category the M-A island fell into during image analysis).

After the image processing was completed, the micrographs were quantified according to ferrite, bainitic ferrite/martensite and M-A content. Table 4.4 includes the final phase fractions for the nine ITT samples as well as the reference sample (CCT specimen D6, which was continuously cooled at 10 °C/s).

The reference sample had the highest percentage of ferrite and M-A and the lowest amount of martensite/bainitic ferrite of all the ITT trial samples. The effect of hold time at the interrupt temperature of 585 °C can be determined by comparing samples 1, 2 and 3 as shown in Figure 4.30. The amount of ferrite decreases as the hold time at 585 °C increases and, simultaneously, the combined fraction of bainitic ferrite/martensite increases as the hold time increases. This indicates that the phase transformation from austenite to bainitic ferrite/martensite continues at the expense of ferrite formation as the hold time at 585 °C increases. The decrease in ferrite content is consistent with this conclusion. There is no significant trend between the amount of M-A and the hold time, as evidenced by the near-horizontal linear regression line in Figure 4.30. The formation of M-A is therefore independent of

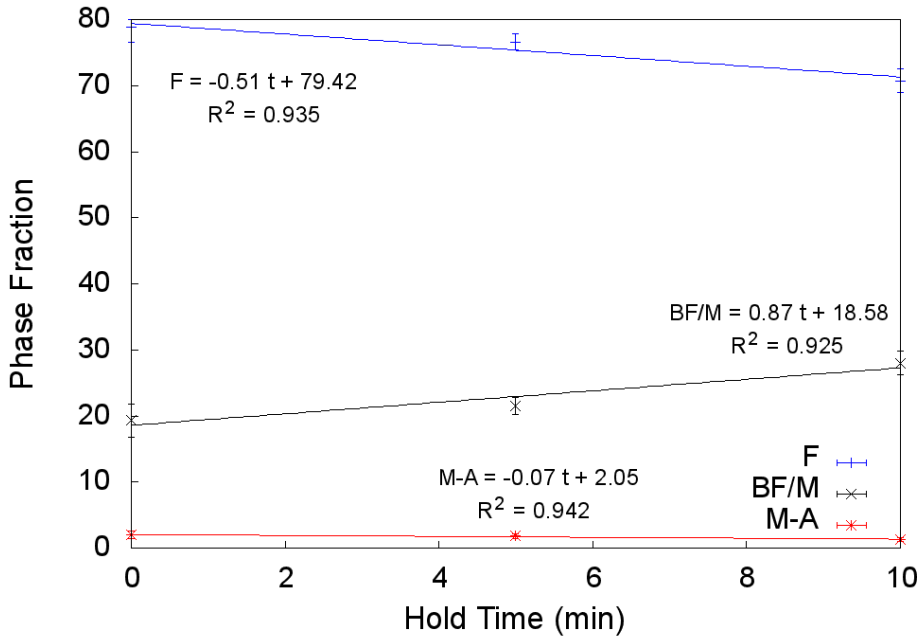

Figure 4.30: Effect of hold time at 585 °C on the phase fractions of ferrite (F), bainitic ferrite (BF/M) and M-A for ITT samples 1, 2 and 3.

hold time at 585 °C.

The effect of hold time at 750 °C can be determined by comparing samples 4, 5 and 6 as shown in Figure 4.31. As for samples 1, 2 and 3, the ferrite content decreases and the combined fraction of martensite/bainitic ferrite simultaneously increases as hold time at 750 °C increases for samples 4, 5 and 6. Furthermore, there is little correlation between M-A fraction and hold time shown by the horizontal linear regression line in Figure 4.31. This could be attributed to potential reaustenitization at 750 °C: the primary ferrite may transform back to austenite during the isothermal hold at 750 °C and subsequently form martensite/bainitic ferrite upon quenching. As a result, the amount of ferrite in the final microstructure would decrease as it is transformed to austenite and, subsequently, the amount of bainitic ferrite/martensite in the final microstructure would increase due to the

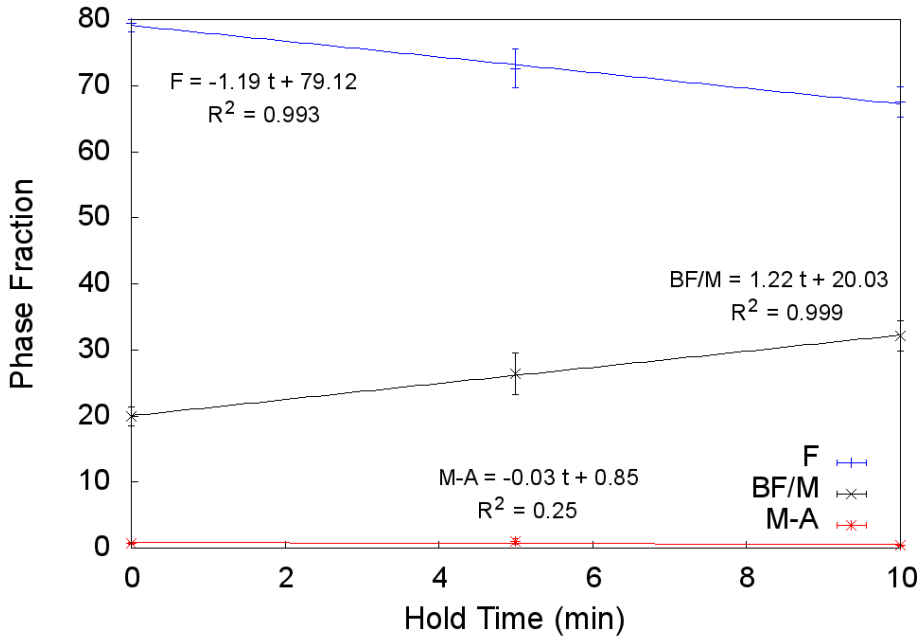

Figure 4.31: Effect of hold time at 750 °C on the phase fractions of ferrite (F), bainitic ferrite (BF/M) and M-A for ITT samples 4, 5 and 6.

additional grains from the new austenite that is quenched from 750 °C.

The full ITT process was conducted for samples 7, 8 and 9. The relationship between microstructure and hold time at 750 °C is shown in Figure 4.32. The phase fraction of each constituent remains fairly constant as hold time increases from 0 to 10 minutes. The trend between hold time and M-A content is consistent with samples 1 through 6, as shown in Figures 4.30 and 4.31. There appears to be no trend between thermal history and M-A development. If the ferrite in fact reaustenitizes during the hold at 750 °C, as was suggested for samples 4, 5 and 6, the new austenite should transform to ferrite during slow cooling (3 °C/s) from 750 °C in samples 7, 8 and 9. This trend is not observed, however, as both the ferrite and martensite/bainitic ferrite contents are approximately equal as shown in Figure 4.32.

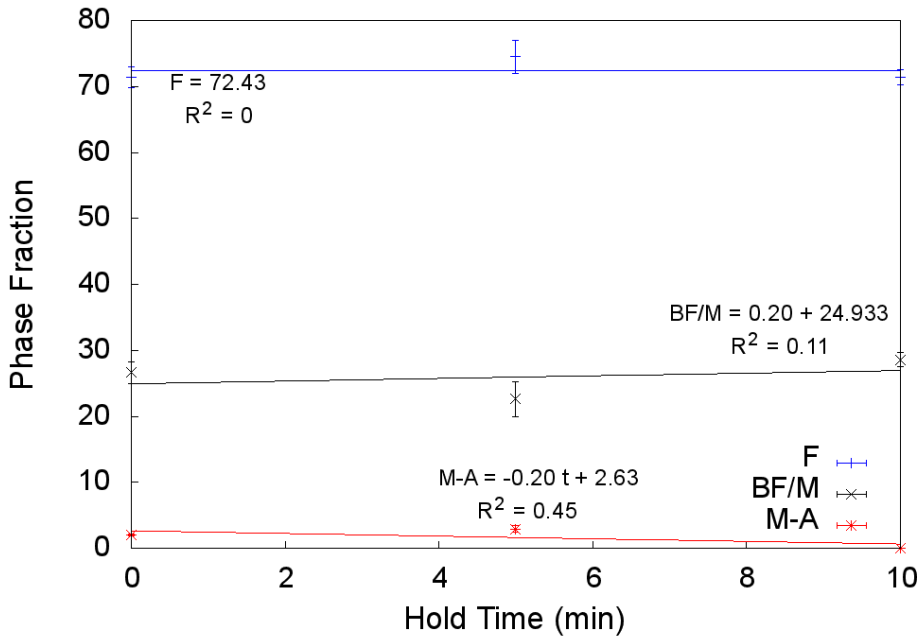

Figure 4.32: Effect of hold time at 750 °C on the phase fractions of ferrite (F), bainitic ferrite (BF/M) and M-A for ITT samples 7, 8 and 9.

The phase fractions of each microconstituent for the ITT trials provided a partial correlation between thermal history and microstructure development. As mentioned in Section 2.4.2, phase fractions are not the only factor that affects microstructure development, especially when comparing the microstructures to mechanical properties. Grain size strengthening is an important strengthening mechanism, as described in Section 2.1.5, and must be investigated. As a result, the grain size of each constituent was determined and will be presented in the next section.

4.4.2 Grain Size Analysis of ITT Specimens

The final processed images that resulted from image analysis described in Section 4.4.1 were used for grain size determination. For the ITT samples, the microstructures comprised two major components: ferrite and bainitic ferrite/martensite. Furthermore, the grains had jagged and unequiaxed shapes; therefore, a grain diameter would not provide an accurate parameter for grain size. As a result, ASTM E 1382 was used to determine the representative grain dimension as grain area rather than grain size [AST 0]. The results from the grain area measurements are shown in Table 4.5. The grain size of the reference sample was determined in Section 3.5.2 to be 6.5 ± 0.4 μm; however, this value represents the overall structure rather than the individual constituents. Furthermore, the grain dimension is expressed as a grain diameter, whereas Table 4.5 presents grain area results.

The grain area for each 'group' of samples is shown in Figures 4.33, 4.34 and 4.35, similar to Figures 4.30 to 4.32. The grain area for each constituent will be compared with mechanical performance (both hardness and tensile behaviour) to determine the overall effect of microstructure on mechanical properties.

For samples 1 through 3, shown in Figure 4.33, the grain area of both ferrite and bainitic ferrite/martensite increase as hold time increases at 585 °C. This trend

Table 4.5: Grain area for ferrite and bainitic ferrite/martensite in the ITT trial samples.

Sample ID	Ferrite Grain Area (μm^2)	Bainitic Ferrite/Martensite Grain Area (μm^2)
1	43.6 ± 3.9	12.4 ± 1.9
2	44.2 ± 2.9	13.7 ± 1.0
3	45.2 ± 2.7	28.0 ± 2.8
4	37.0 ± 2.2	10.9 ± 1.0
5	32.7 ± 2.7	15.0 ± 1.4
6	40.0 ± 2.5	23.8 ± 1.57
7	45.7 ± 3.3	23.7 ± 3.3
8	39.1 ± 2.4	18.6 ± 1.9
9	39.4 ± 3.6	29.6 ± 3.0

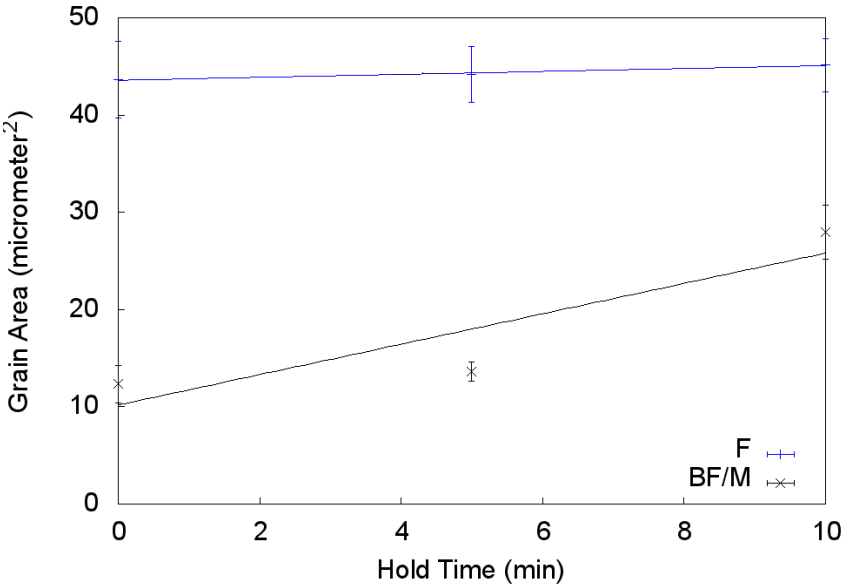

Figure 4.33: Effect of hold time at 585 °C on the grain area of ferrite (F), bainitic ferrite (BF/M) and M-A for ITT samples 1, 2 and 3.

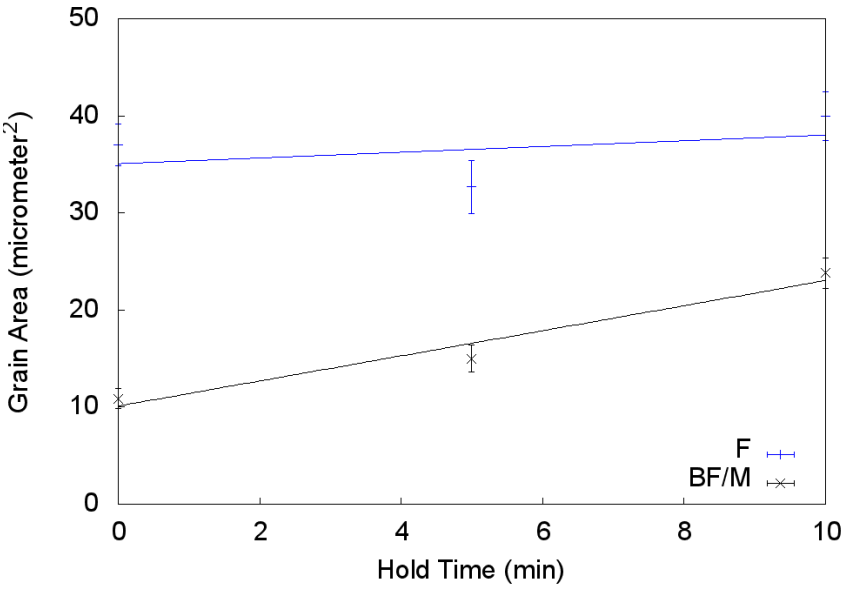

Figure 4.34: Effect of hold time at 750 °C on the grain area of ferrite (F), bainitic ferrite (BF/M) and M-A for ITT samples 4, 5 and 6.

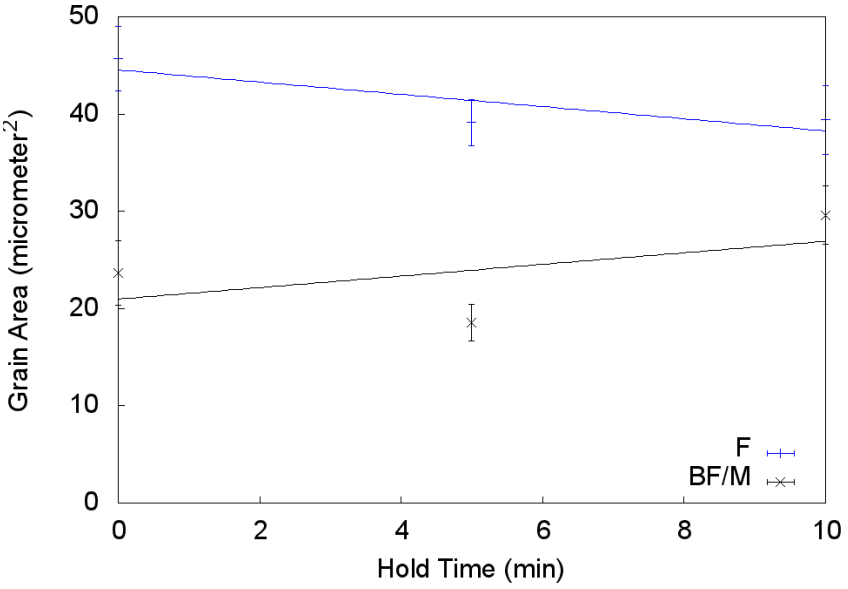

Figure 4.35: Effect of hold time at 750 °C on the grain area of ferrite (F), bainitic ferrite (BF/M) and M-A for ITT samples 7, 8 and 9.

suggests that both constituents experience grain growth at 585 °C. Figure 4.34 shows the same trend as Figure 4.33; namely, that both the ferrite and bainitic ferrite/martensite grains grow as hold time increases at 750 °C. For samples 7, 8 and 9, the grain area increases as a function of hold time only for the bainitic ferrite/martensite grains. The ferrite grains show a decrease in grain area as hold time at 750 °C increases. This may be due to reaustenitization, as discussed previously when comparing the hold times to phase fraction.

After the phase fractions and grain areas for the microconstituents were determined and compared with thermal history, the mechanical behaviour was tested. As mentioned in Section 4.1.1, the sample geometry and grips used in the Gleeble 3800 at EVRAZ Inc. were not suitable for tensile testing and, therefore, a different sample geometry and thermomechanical simulator were required. The specific equipment and sample geometry were detailed in Section 4.1.4. The mechanical performance of the ITT trials will be discussed in the following section.

4.5 Mechanical Performance of ITT Trials

Once the relationship between thermal treatment and microstructure was investigated, the correlation between microstructure and mechanical properties was required. The mechanical behaviour of the ITT test specimens was determined by hardness tests and tensile tests, which will be outlined in the following sections.

4.5.1 Hardness Tests

The mounted and polished ITT specimens were subjected to micro- and macrohardness tests according to the procedure outlined in Section 4.1.4. Furthermore, nanoindentation experiments were performed on one ITT trial specimen (sample 1 as defined in Table 4.3). Sample 1 was chosen for the same reasons as for TEM:

Table 4.6: Micro- and macrohardness results for all ITT specimens and the reference sample.

Sample ID	Microhardness (HV)	Macrohardness (HV)
REF	229.3 ± 1.4	233.2 ± 0.4
1	232.1 ± 1.4	226.6 ± 0.4
2	231.3 ± 2.8	239.4 ± 0.8
3	234.8 ± 2.0	240.2 ± 1.4
4	238.9 ± 1.6	250.0 ± 1.2
5	240.3 ± 2.3	231.5 ± 1.3
6	242.2 ± 2.9	229.9 ± 3.2
7	254.2 ± 2.2	254.2 ± 2.2
8	241.8 ± 1.3	252.6 ± 1.6
9	241.8 ± 3.4	255.0 ± 1.6

this sample exhibited a large percentage of martensite/bainitic ferrite grains and the goal of nanoindentation was to determine the hardness of a single grain relative to the surrounding matrix. The results from the nanoindentation experiments will be discussed in Appendix C.

As mentioned in Section 4.1.4, the hardness values shown in Table 4.6 represent the average and standard deviation of five indents per specimen. The results are tabulated in Table 4.6. Each macrohardness indent using a 10 kg load was approximately 200 μm by 200 μm. The microhardness indents from a 1 kg indentor load were approximately 90 μm by 90 μm in size. Since the indents from both the micro- and macrohardness tests incorporated at least 100 grains per indent, the hardness values listed in Table 4.6 are representative values of the mixed microstructure and do not reflect clusters or regions of a particular microconstituent. This may be due to insufficient sample thickness, which will be discussed later.

Hardness was plotted as a function of ferrite percentage as shown in Figures 4.36 and 4.37. The hardness plots are divided into 4 categories as follows: 1) REF; 2) Group 1 (ITT samples 1, 2, 3); 3) Group 2 (samples 4, 5, 6); and 4) Group 3 (samples

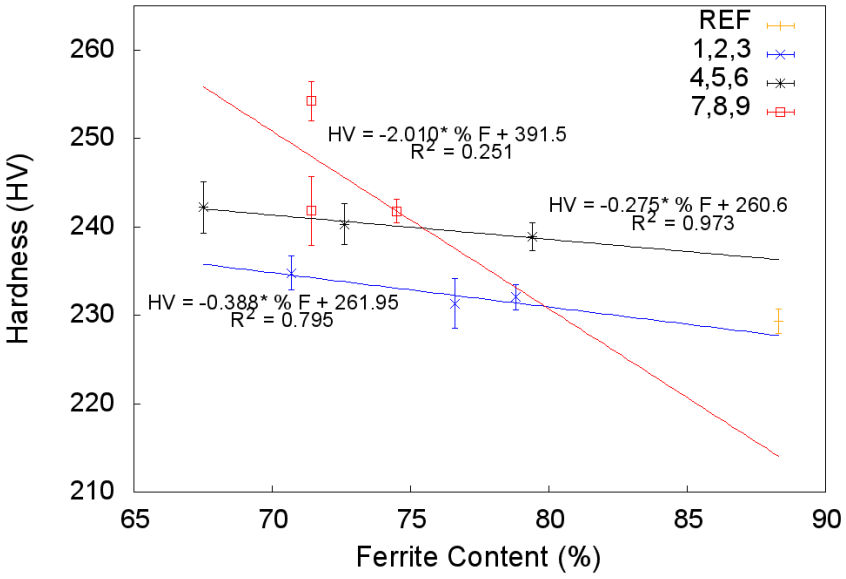

Figure 4.36: Microhardness 1 kg load as a function of ferrite content for the ITT trial specimens.

7, 8, 9). The data was separated into these categories to better identify any trend that existed for each 'group' of samples (based on hold time at the interrupt or re-heat temperature and final cooling rate).

Figure 4.37 which showed a positive relationship between hardness and ferrite content. A higher percentage of ferrite corresponds to a lower hardness since the remaining microstructure comprises bainitic ferrite, martensite and M-A. These constituents have higher hardness values than ferrite, as discussed in Section 2.1.2.

4.5.2 Tensile Tests

Section 4.1.4 describes the geometry of the ITT specimens that were thermally treated in the Gleeble 3500. The thermal schedule applied to the strip specimens was identical to the ITT trials conducted on smaller samples in the Gleeble 3800, as shown in Table 4.3. The strip samples (shown in Figure 4.4) were machined into

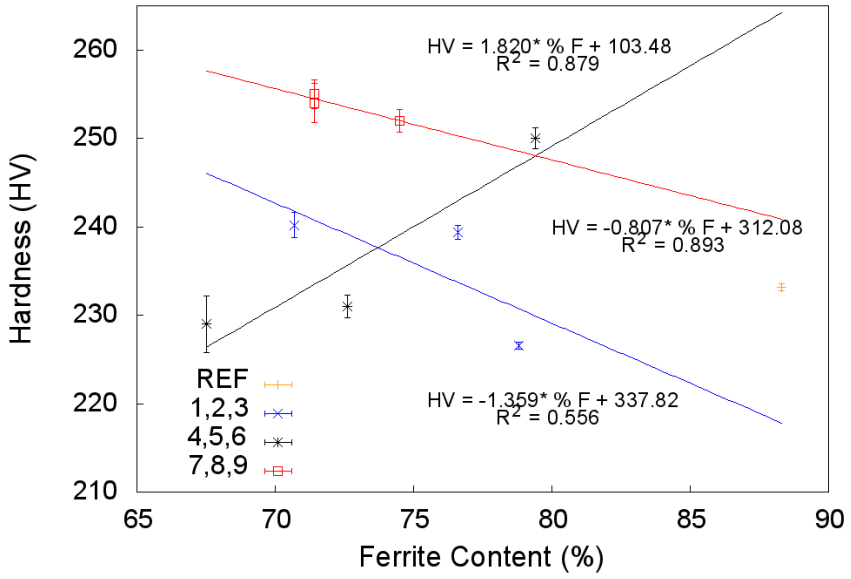

Figure 4.37: Macrohardness 10 kg load as a function of ferrite content for the ITT trial specimens.

sub-size tensile specimens according to Figure 4.2 in Section 4.1.4. As mentioned in Section 4.1.4, the sub-size specimens were loaded in an INSTRON 8800 equipped with a 100 kN load cell and a servohydraulic actuator. The initial width, final width and thickness of each specimen were manually recorded, while the instantaneous load and strain values were collected during the test duration. The procedure to generate engineering stress-strain curves was described in Section 2.5.2. The engineering stress-strain curves for the ITT samples were obtained by plotting the engineering stress (which was calculated from the instantaneous load via Equation 2.11) against the engineering strain, as determined by Equation 2.12.

The individual engineering stress-strain curves for the ITT samples listed in Table 4.3 are shown in Figures 4.38 to 4.47. The yield strength was determined using the 0.2 % offset according to ASTM E 8M-04 [AST 04]. More specifically, the yield strength was determined by calculating the equation of best fit for the linear

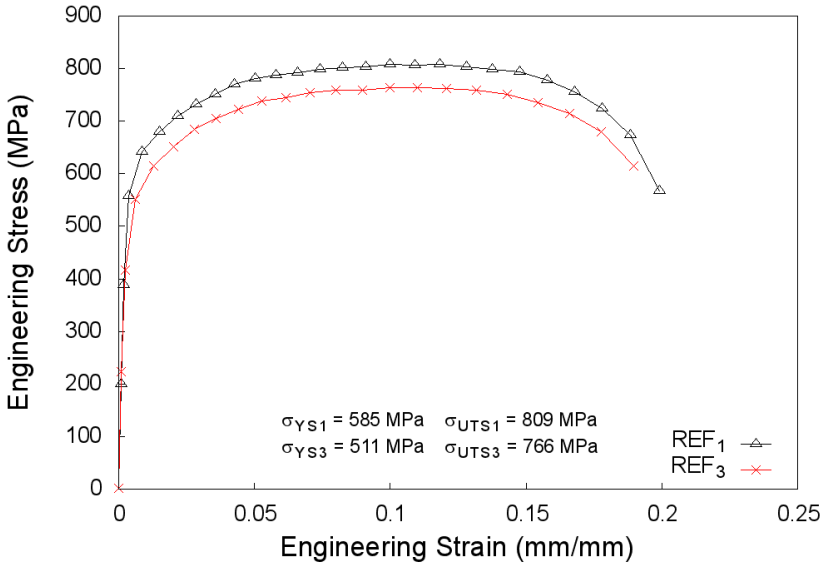

Figure 4.38: Engineering stress-strain curves for the reference sample.

portion of the stress-strain curve and maximizing the R^2 value to fit the curve to an equation of the form y = mx (i.e., forcing the y-intercept through the origin), since there is no strain at zero stress.

Figure 4.48 shows the combined engineering tensile behaviour for all ITT trial samples. The stress-strain curves shown are from the middle of the strip (the center specimen in Figure 4.16), which is where the thermocouples were placed according to Figure 4.5. The reference sample (continuously cooled at 10 °C/s) has the highest strength and the longest elongation. Sample 1, which was cooled to 585 °C and immediately quenched, has the second highest strength and very little ductility. Samples 2 and 3, which were cooled to 585 °C and held for 5 and 10 minutes respectively before quenching, have lower UTS values than 1 and considerably lower elongation.

Samples 4, 5 and 6, which were cooled to 585 °C, heated to 750 °C and held for 0, 5 or 10 minutes before quenching, exhibited very good mechanical behaviour.

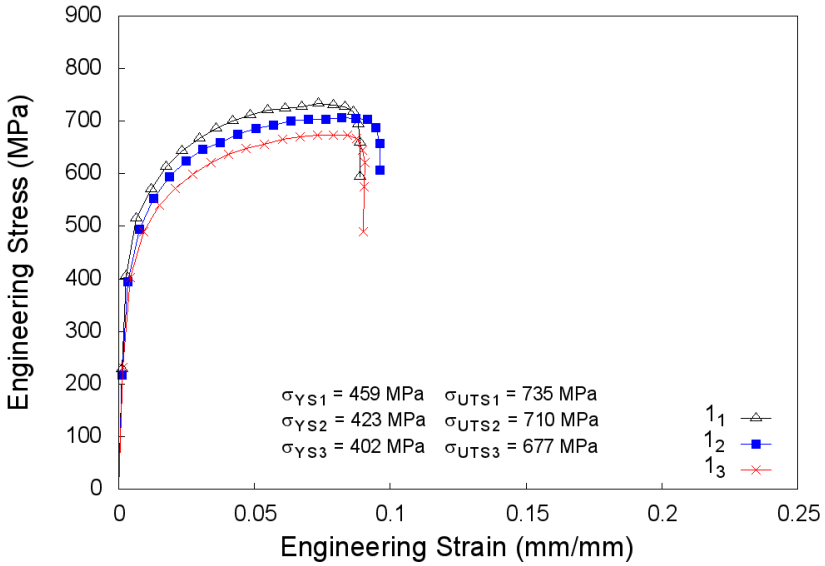

Figure 4.39: Engineering stress-strain curves for sample 1.

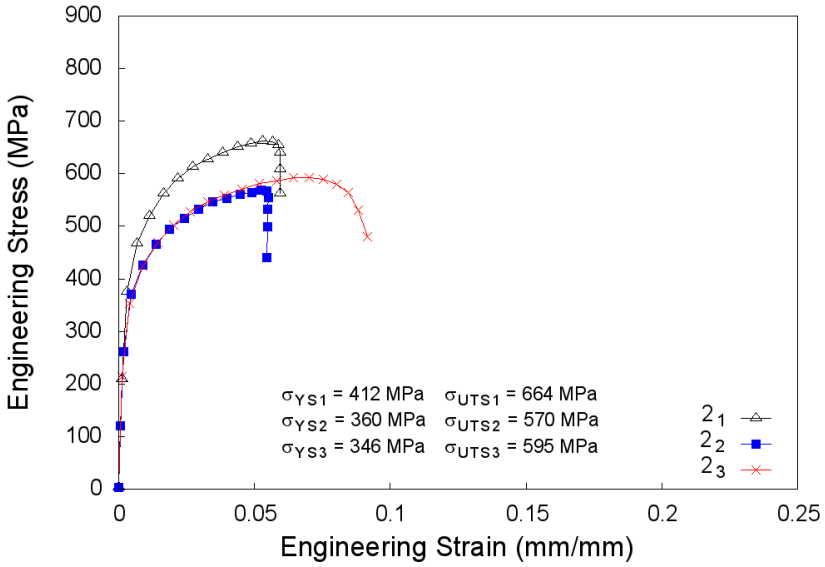

Figure 4.40: Engineering stress-strain curves for sample 2.

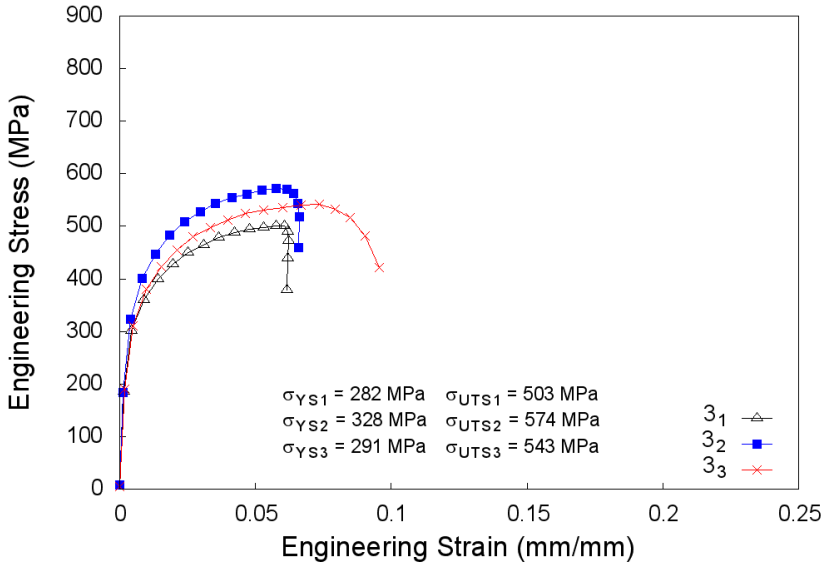

Figure 4.41: Engineering stress-strain curves for sample 3.

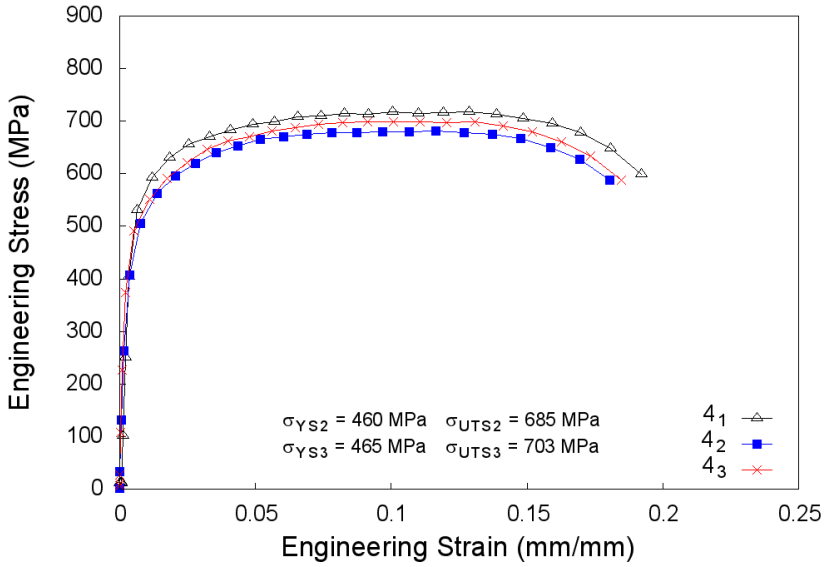

Figure 4.42: Engineering stress-strain curves for sample 4.

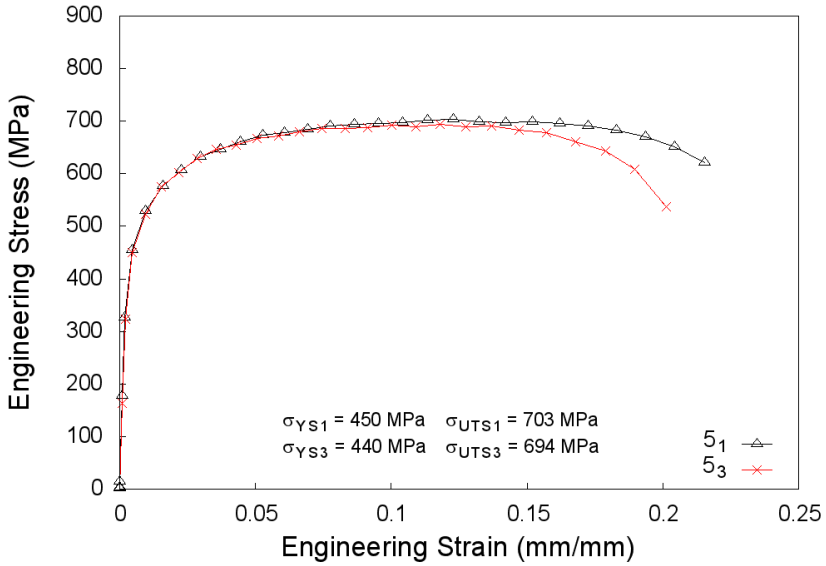

Figure 4.43: Engineering stress-strain curves for sample 5.

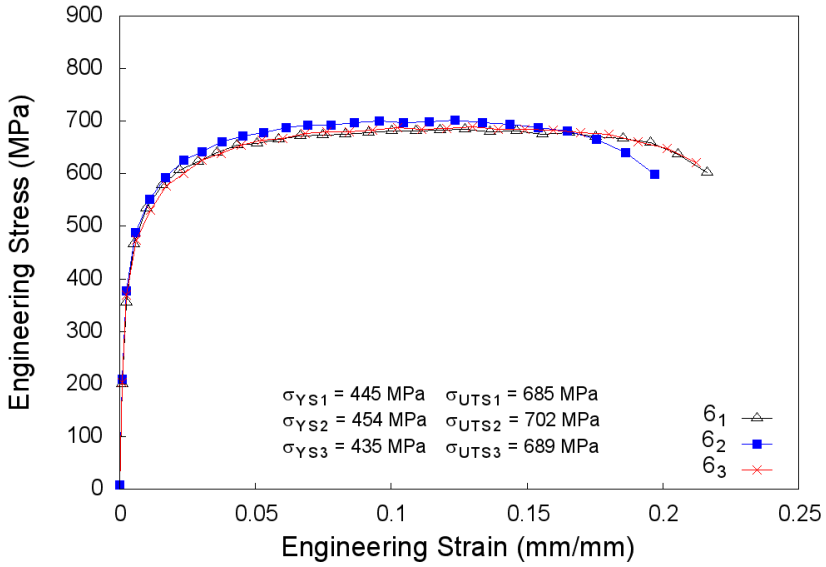

Figure 4.44: Engineering stress-strain curves for sample 6.

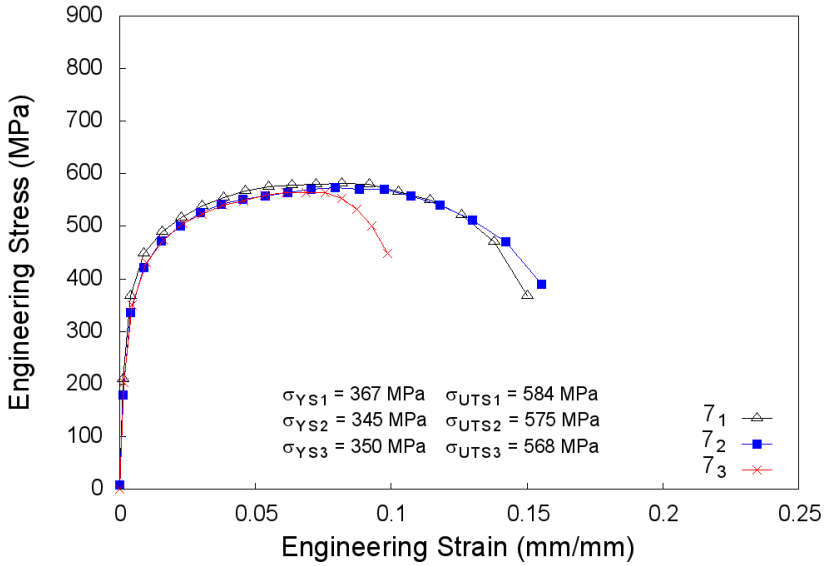

Figure 4.45: Engineering stress-strain curves for sample 7.

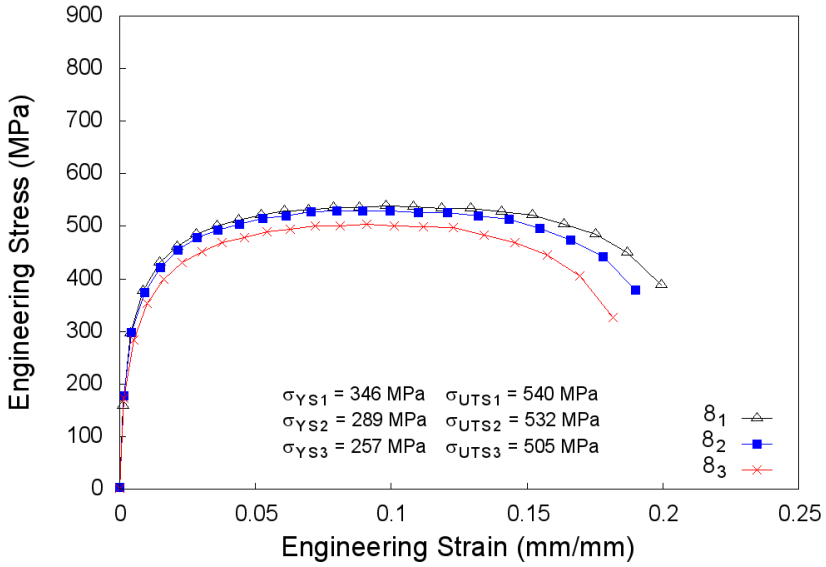

Figure 4.46: Engineering stress-strain curves for sample 8.

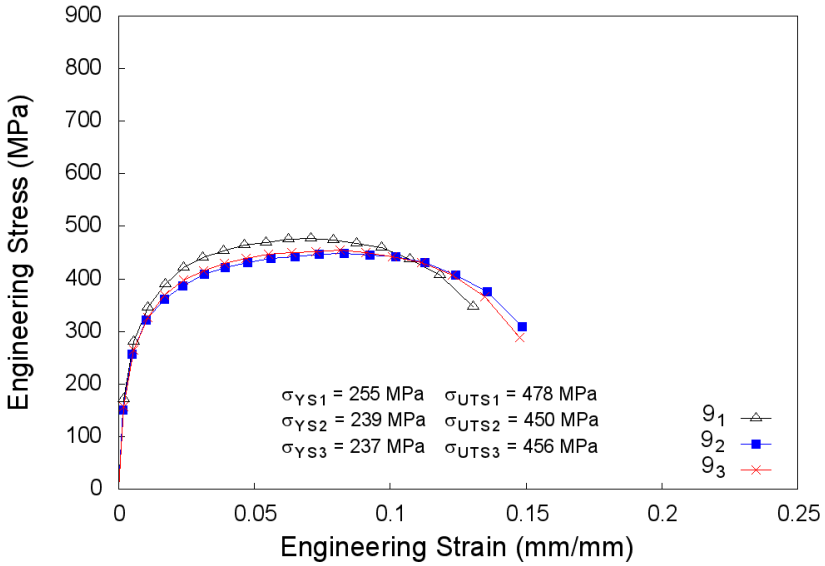

Figure 4.47: Engineering stress-strain curves for sample 9.

The engineering stress-strain curves were round and the samples had the longest percent elongation of all the ITT specimens. The UTS values for samples 4, 5 and 6 were comparable to sample 1, which was immediately quenched after reaching the interrupt temperature.

Sample 7, which is the full ITT process with no hold at the re-heat temperature of 750 °C, has the same UTS as samples 2 and 3 but with a higher percent elongation. Sample 8 (held for 5 minutes at the re-heat temperature of 750 °C) has a slightly lower UTS than 7 but more ductility. Sample 9, which was held for 10 minutes at the re-heat temperature of 750 °C, has the lowest UTS of all the ITT samples. For the full ITT process (7, 8 and 9), the hold time at 750 °C decreases the UTS.

Although engineering stress-strain curves are the most common depiction of a sample's mechanical behaviour and provides important information including strength and ductility, the work hardening coefficient cannot be determined directly from these diagrams. True stress-true strain curves provide information about the

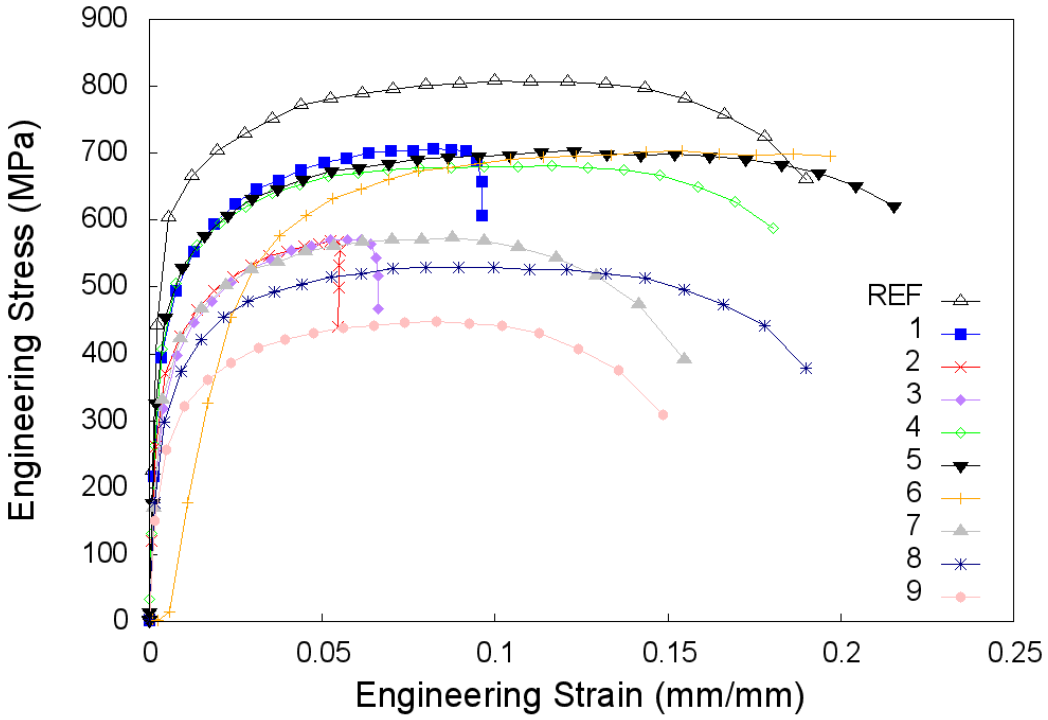

Figure 4.48: Engineering stress-strain curves for all ITT samples.

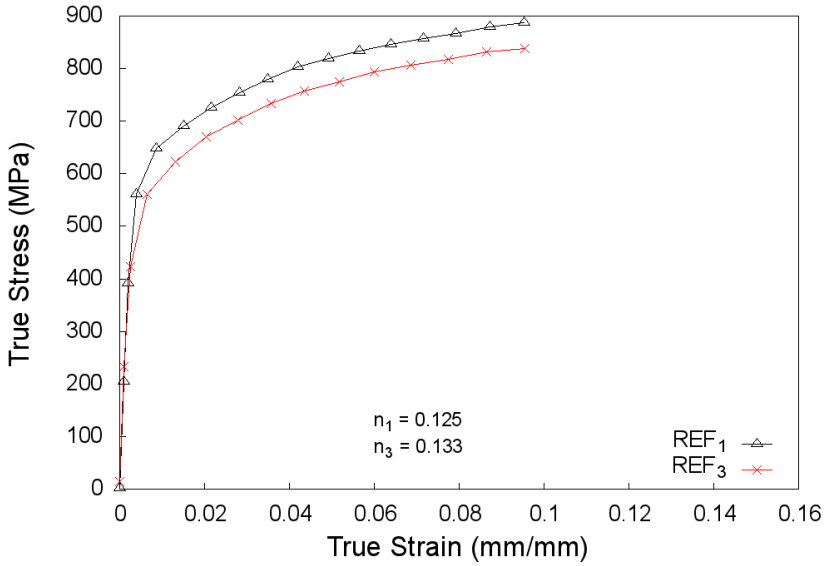

Figure 4.49: True stress-strain curves for the reference sample.

work hardening behaviour, as detailed in Section 2.5.2. Equations 2.13 to 2.15 were used to determine the work hardening coefficient for each ITT trial specimen. Since these equations are only valid to the point of necking, the true stress-strain curves are determined from the beginning of the test to the highest engineering stress value (UTS) which is where necking and plastic instability start. The true stress-strain curves for the ITT specimens are shown in Figures 4.49 to 4.58. The work hardening coefficients are included in each figure for clarification.

The highest work hardening coefficient was observed for samples 2 and 3, which were continuously cooled at 10 °C/s to 585 °C and quenched to room temperature after 5 and 10 minutes, respectively. According to the engineering stress-strain curves shown in Figures 4.51 and 4.52, samples 2 and 3 had reasonable strength but very little ductility. The sample with the lowest work hardening coefficient was sample 4, which was continuously cooled to 585 °C at 10 °C/s, immediately re-heated to 750 °C and quenched to room temperature.

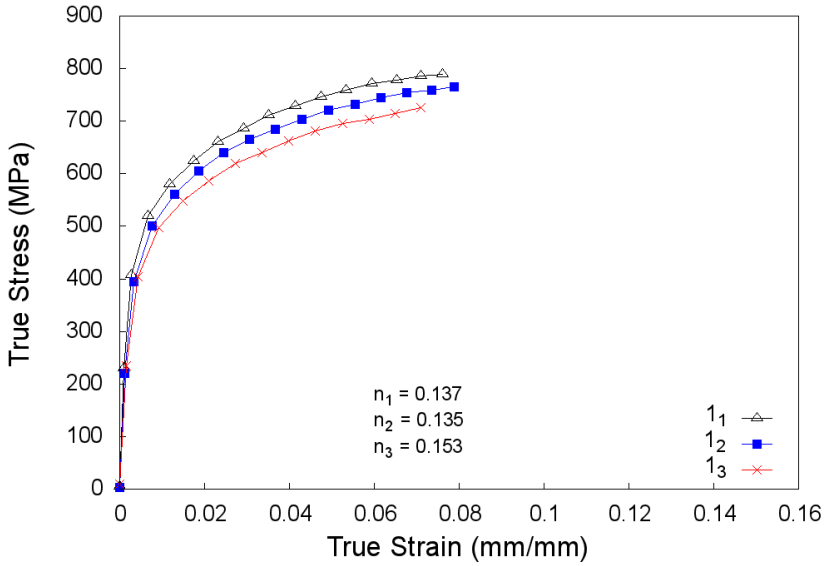

Figure 4.50: True stress-strain curves for sample 1.

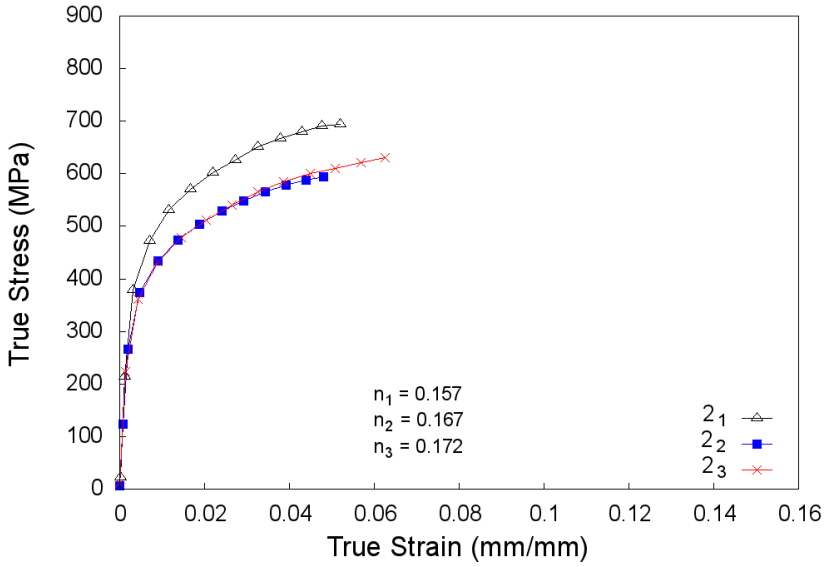

Figure 4.51: True stress-strain curves for sample 2.

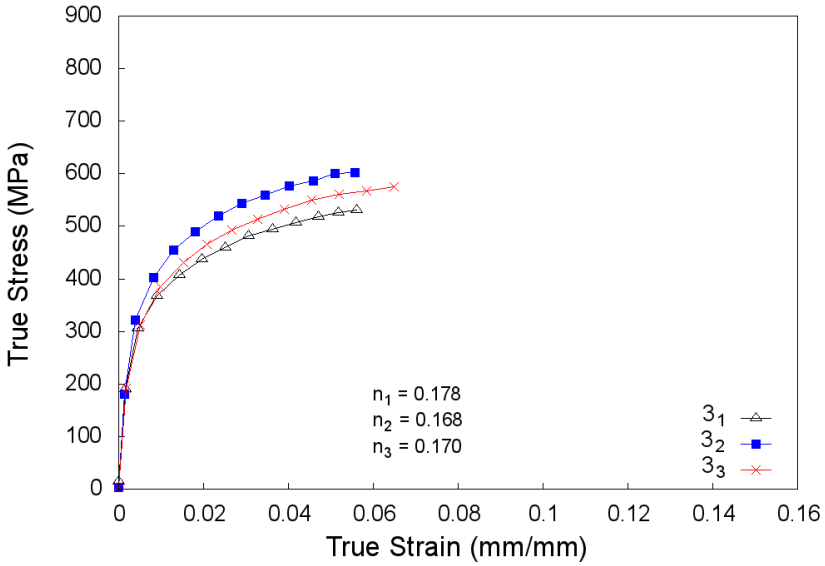

Figure 4.52: True stress-strain curves for sample 3.

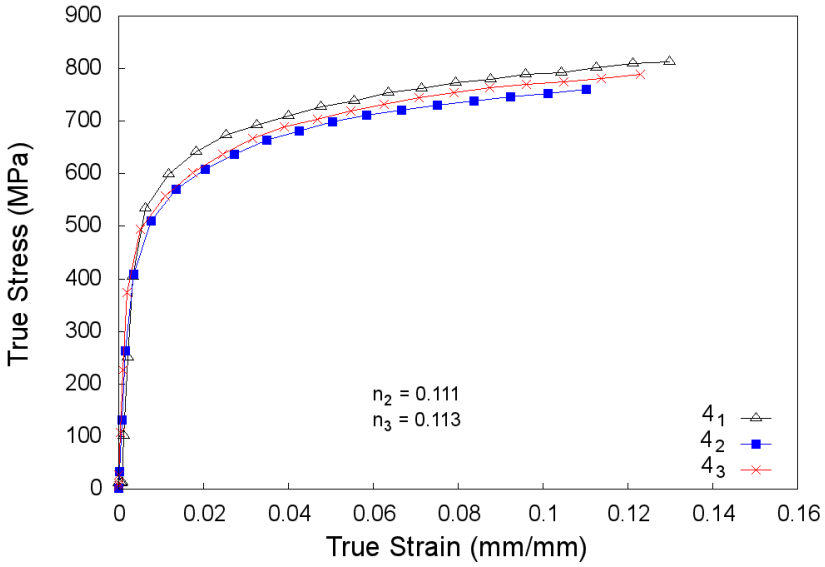

Figure 4.53: True stress-strain curves for sample 4.

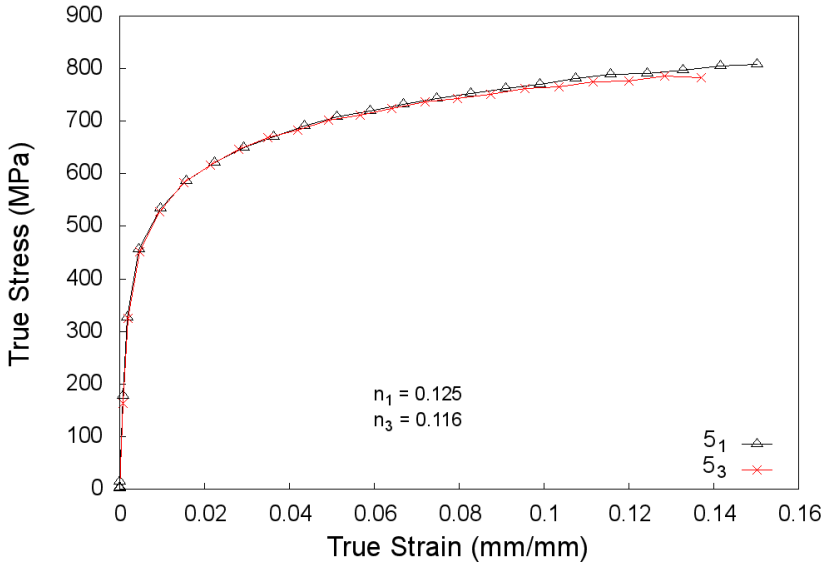

Figure 4.54: True stress-strain curves for sample 5.

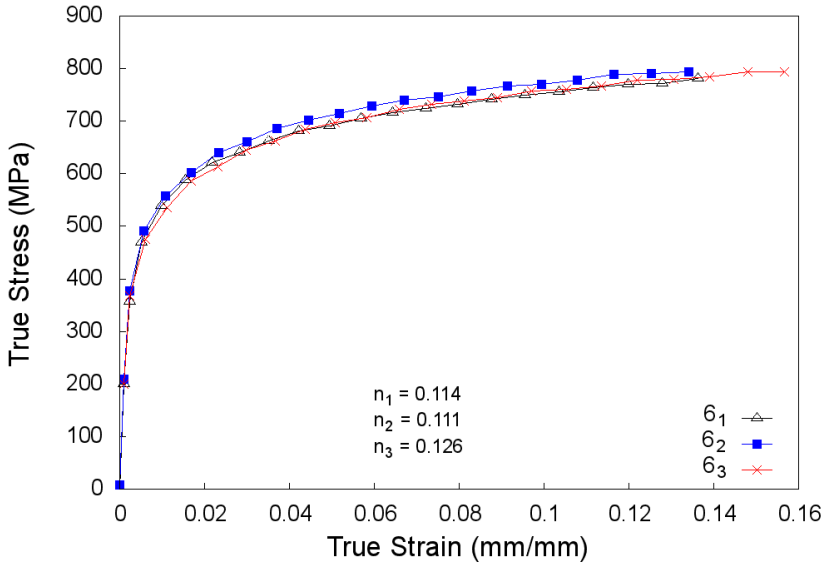

Figure 4.55: True stress-strain curves for sample 6.

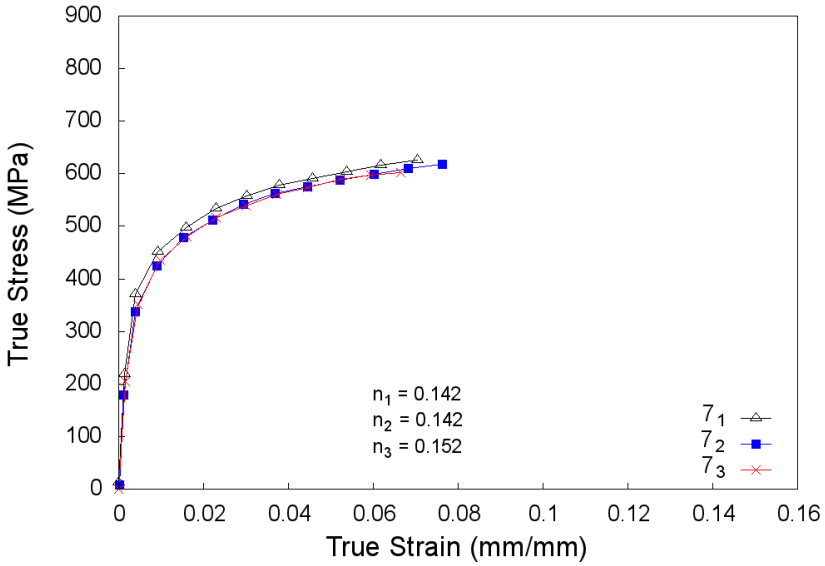

Figure 4.56: True stress-strain curves for sample 7.

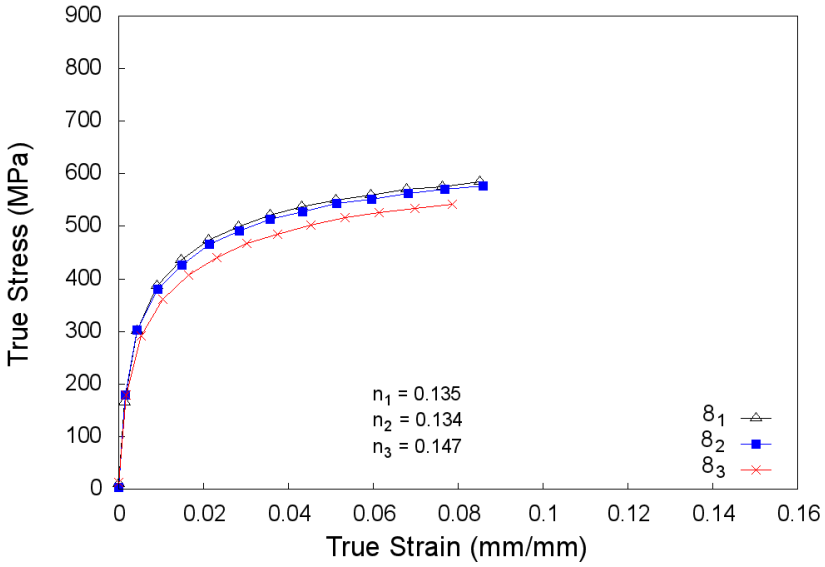

Figure 4.57: True stress-strain curves for sample 8.

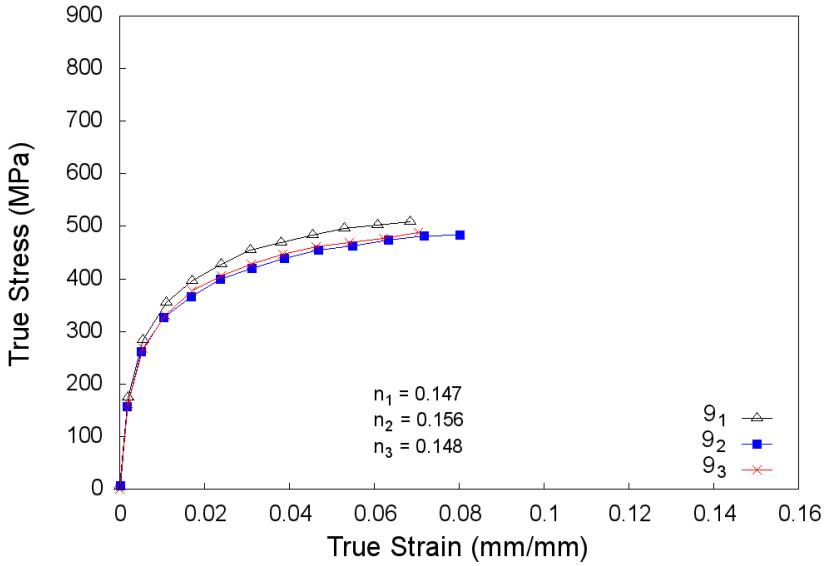

Figure 4.58: True stress-strain curves for sample 9.

The complete tensile data for the ITT trials is summarized in Table 4.7. The average UTS and YS are shown as individual numbers as well as a ratio of YS/UTS. The average work hardening coefficient and average ductility are also included in Table 4.7.

As mentioned in Section 2.6, the goal of this project was to decrease the YS/UTS ratios to increase the amount of work hardening that occurs after yielding and before plastic instability; however, this goal was supposed to be achieved by increasing the UTS while ensuring a minimum YS of 80 ksi. These ITT trials do show a decrease in YS/UTS, although it was achieved through a decrease in both the UTS and YS values rather than by the intended increase in UTS.

In order to understand and explain the trends in tensile behaviour, the relationship between mechanical performance and microstructure had to be determined. Table 4.4 in Section 4.4.1 presents the phase fractions for each ITT specimen and Table 4.6 includes the micro- and macrohardness values for the ITT trials. Hard-

Table 4.7: Tensile behaviour of ITT trial specimens.

Sample	Average UTS (MPa)	Average YS (MPa)	YS/UTS	Average n	Average Ductility (%)
REF	788	548	0.70	0.13	20
1	707	428	0.60	0.14	9
2	610	373	0.61	0.17	7
3	540	300	0.56	0.17	8
4	694	463	0.67	0.11	19
5	699	445	0.64	0.12	21
6	692	445	0.64	0.12	22
7	576	354	0.61	0.15	14
8	526	297	0.56	0.14	19
9	431	244	0.53	0.15	15

ness was plotted as a function of UTS, and the relationship between microstructure ferrite content and tensile behaviour; more specifically, YS, UTS and n was also plotted.

The relationship between hardness and UTS is shown in Figures 4.59 and 4.60. Samples 1, 2 and 3 show a negative correlation between hardness and UTS for both the micro- and macrohardness results. This trend is opposite to the expected trend: as discussed in Section 2.1.5, UTS and hardness have a positive correlation. Increasing the hardness value corresponds to a higher UTS [Gasko 11]. In Figures 4.59 and 4.60, samples 4, 5 and 6 show very little correlation between hardness and UTS as evidenced by the near-horizontal line corresponding to the linear regression results. The trend between hardness and UTS for samples 7, 8 and 9 is unclear: in Figure 4.59, the UTS increases as hardness increases; however, the UTS shows a negative correlation with hardness in Figure 4.60.

The inconsistent trends between hardness and UTS may be the result of the small sample size that was tested. As mentioned in Section 4.3.1, the samples that were mounted for microstructural investigation and hardness testing were obtained from the larger strip specimens were approximately 1.5 mm thick. After polishing,

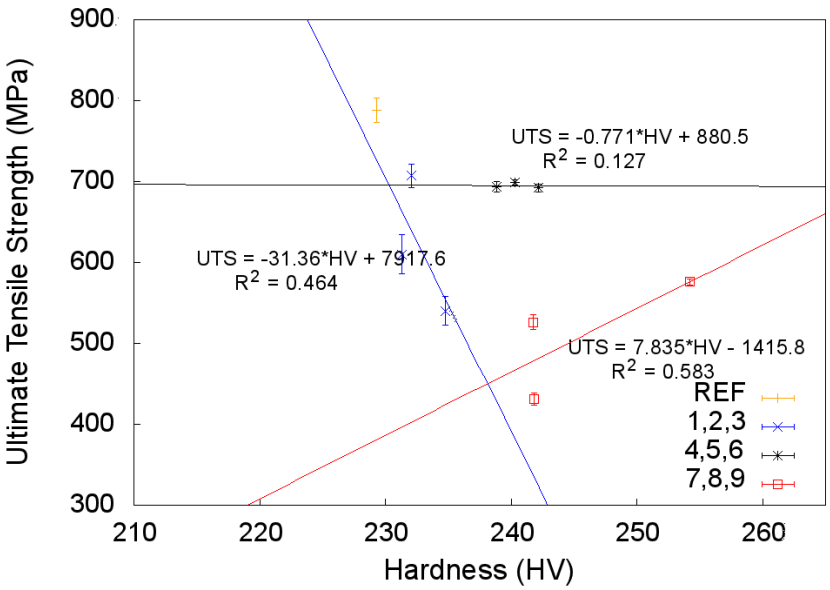

Figure 4.59: Relationship between hardness (HV 1 kg) and UTS for all ITT trial samples.

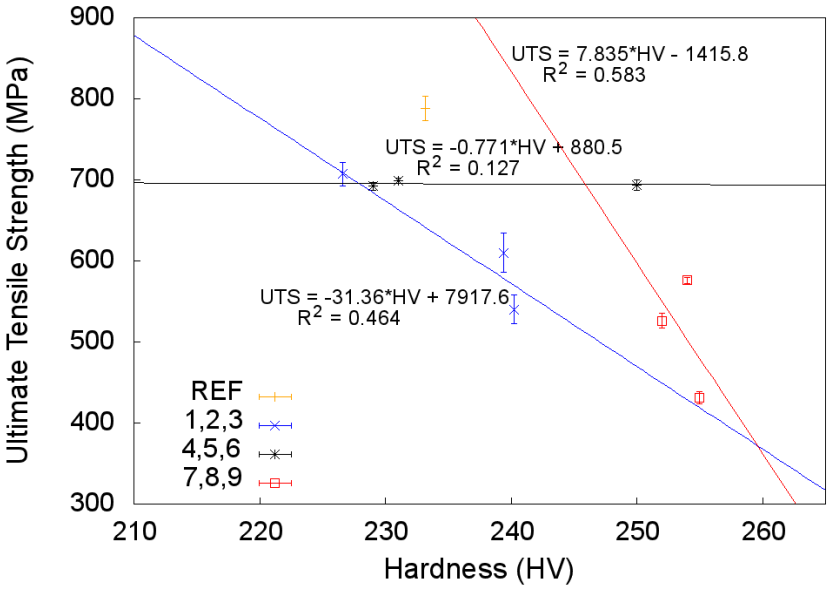

Figure 4.60: Relationship between hardness (HV 10 kg) and UTS for all ITT trial samples.

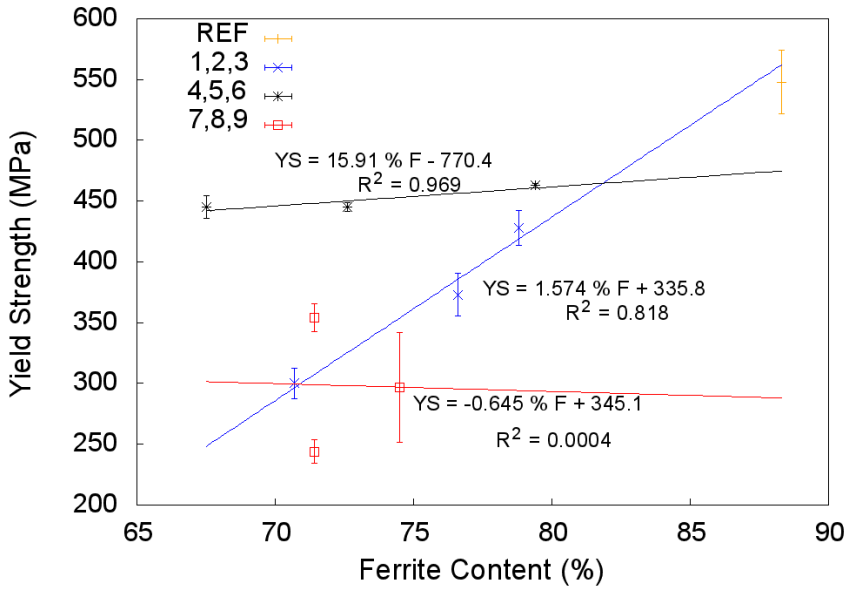

Figure 4.61: Relationship between ferrite content and YS for all ITT trial samples.

the sample thickness would be reduced to 0.5 mm - 1.0 mm and may have influenced the hardness results. Even though the hardness results reflect 5 indents, the sample thickness may have been insufficient to bear the load and the resulting hardness values may be inaccurate. Due to the error in hardness values as a result of the small sample size, the tensile results will be correlated with microstructure as the tensile specimens had sufficient thickness to determine accurate mechanical properties.

The relationship between ferrite content and YS is shown in Figure 4.61. According to Figure 4.61, the YS increases with increasing ferrite content for ITT samples 1, 2 and 3. The trend between YS and ferrite content for the ITT specimens is not as significant, although there is a positive relationship for samples 4, 5 and 6. The YS for samples 7, 8 and 9 decreases as ferrite content increases.

The trend between ferrite content and UTS is shown in Figure 4.62. Similar to Figure 4.61, the UTS increases with increasing ferrite content for samples 1, 2 and

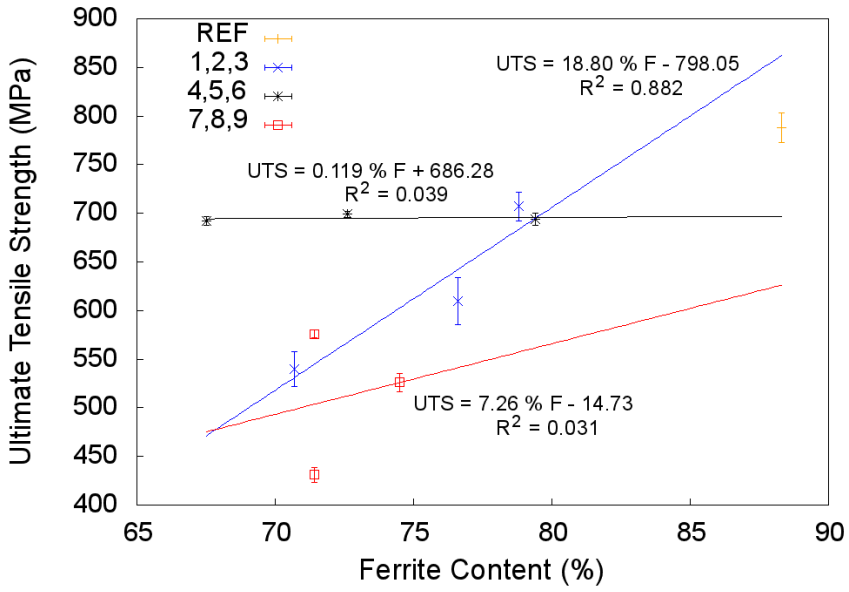

Figure 4.62: Relationship between ferrite content and UTS for all ITT trial samples.

3. Samples 4, 5 and 6, on the other hand, do not show a significant relationship between ferrite content and UTS, as evidenced by the nearly horizontal regression line. Furthermore, the UTS for samples 7, 8 and 9 increases as ferrite content increases, which is opposite to the trend between YS and ferrite content observed for these samples.

The relationship between work hardening coefficient and ferrite content is presented in Figure 4.63. All ITT samples exhibited the same trend: the work hardening coefficient decreases as ferrite content increases. This agrees with the expected results, as ferrite does not have high work hardening capabilities compared with bainitic ferrite and martensite. Work performed by JFE Steel confirmed that the work hardening coefficient increases with increasing volume fraction of bainite and martensite, whereas a higher volume fraction of ferrite does not contribute to the work hardening coefficient [Mitsuhiro 08].

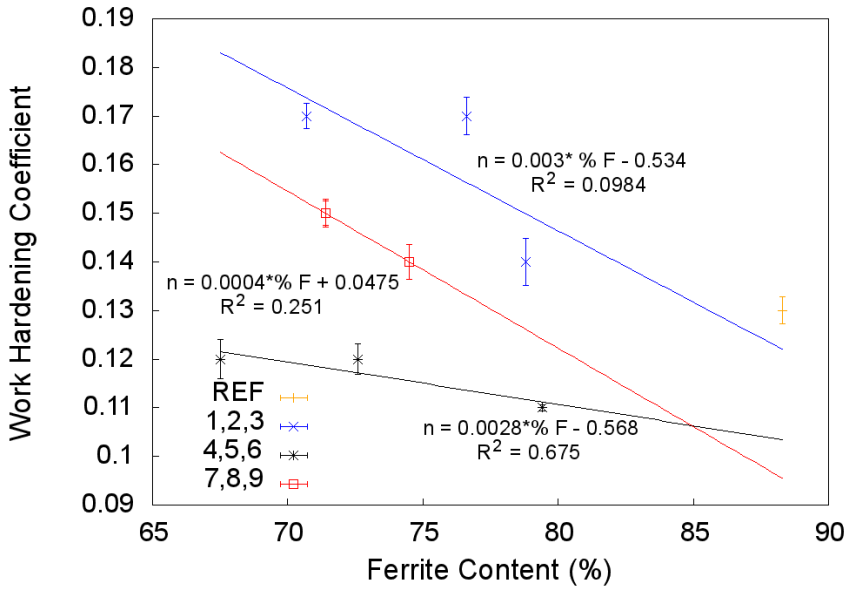

Figure 4.63: Relationship between ferrite content and work hardening coefficient for all ITT trial samples.

One explanation for the opposite trends observed in Figures 4.59 through 4.63 is related to the phase quantification technique. Grains that appeared dark, flat and slightly recessed in the SEM SE images were characterized as ferrite, whereas bright, jagged and raised features were considered to be bainitic ferrite/martensite based on the results from the TEM investigation. Some of the grains that were termed ferrite could potentially be bainitic ferrite or martensite grains that were sectioned and, hence, imaged along a different crystallographic orientation which would resemble a ferrite grain. It is important to remember that grains are three-dimensional and SEM SE images are two-dimensional; therefore, the SEM SE images could be viewing the grain along a certain plane that would appear ferritic when in fact the grain is actually martensitic. Although this observation is true, it can be applied to any SEM SE micrograph of a polished sample since it is a consequence that is inherent to all mounting, polishing and imaging situations. As a result, it

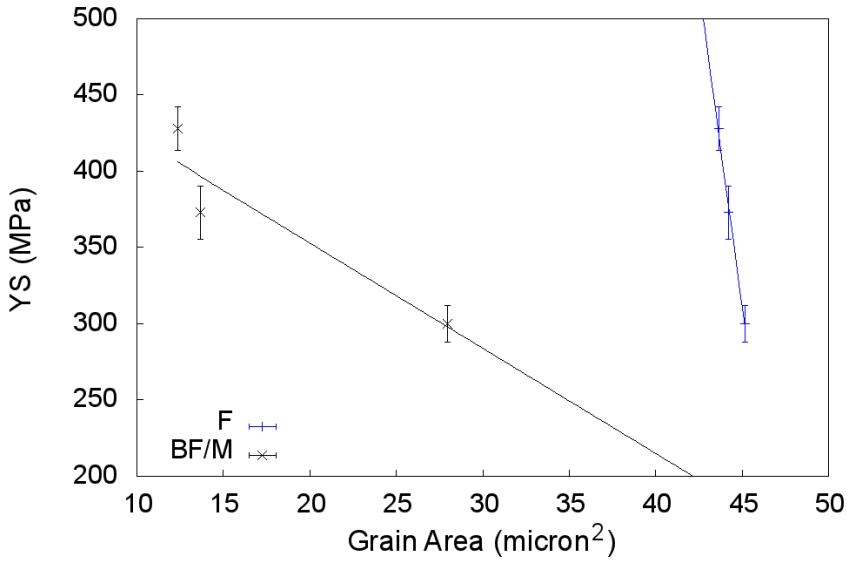

Figure 4.64: Relationship between ferrite grain area and YS for ITT trial samples 1, 2 and 3.

cannot be considered the sole reason for the variation and trends presented here.

Since the trends between phase fraction and mechanical properties did not provide a clear insight into the relationship between microstructure and mechanical performance, the mechanical data was plotted as a function of grain area for both ferrite and bainitic ferrite/martensite to determine whether a trend existed. Figure 4.64 shows the relationship between YS and area fraction of ferrite (F) and bainitic ferrite (BF/M) for ITT samples 1 through 3. For both the ferrite and bainitic ferrite/martensite, the YS decreases as grain area increases. The change in slope is more severe for the ferrite data, however, indicating that ferrite has a stronger relationship between grain area and YS than bainitic ferrite/martensite.

The YS and grain area data for samples 4 through 6 are shown in Figure 4.65. The correlation between YS and grain area is not significant for these specimens, as evidenced by the nearly horizontal lines in Figure 4.65. Furthermore, the linear

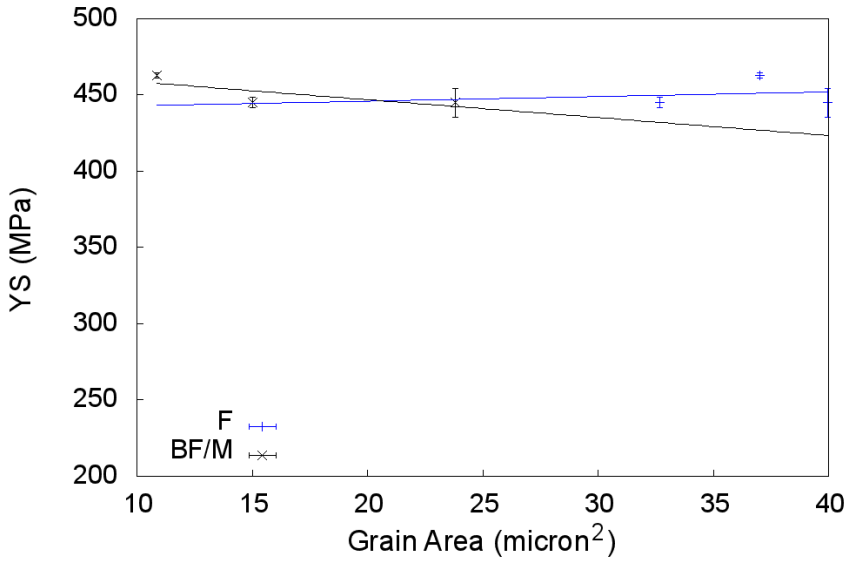

Figure 4.65: Relationship between ferrite grain area and YS for ITT trial samples 4, 5 and 6.

regression line for ferrite shows an increase in YS with increasing grain area. This correlation is opposite to the expected trend, since grain refinement is a common strengthening mechanism in steel products [Gladman 97].

Figure 4.66 shows the relationship between YS and area fraction of F and BF/M for ITT samples 7 through 9. The ferrite data shows a positive correlation with YS, whereas bainitic ferrite/martensite reveals a negative relationship with YS. As previously mentioned, the ferrite correlation with YS does not agree with the expected results.

Figures 4.67 to 4.68 show the relationship between UTS and area fraction of F and BF/M for all ITT samples. The trends are identical as for the YS versus grain area graphs shown in Figures 4.64 to 4.65. The UTS increases as grain area of ferrite decreases (with the exception of samples 7, 8 and 9). The bainitic ferrite/martensite grain area shows a consistent trend with UTS; more specifically, the UTS increases

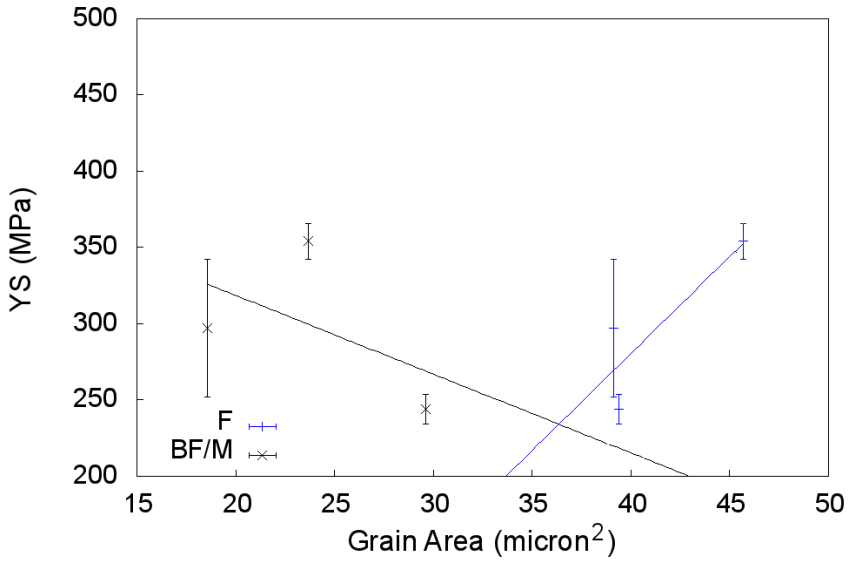

Figure 4.66: Relationship between ferrite grain area and YS for ITT trial samples 7, 8 and 9.

with decreasing grain area.

Figure 4.70 shows the relationship between work hardening coefficient and area fraction of ferrite (F) and bainitic ferrite/martensite (BF/M) for ITT samples 1 through 3. There is a strong positive correlation between ferrite grain area and work hardening coefficient, whereas the relationship between bainitic ferrite/martensite and n is not as strong (yet still positive).

For samples 4, 5 and 6, ferrite and bainitic ferrite/martensite show opposite trends. The n value increases with increasing bainitic ferrite/martensite grain area and decreasing ferrite grain area, as shown in Figure 4.70 to 4.72.

Figure 4.72 shows the relationship between n and area fraction of ferrite (F) and bainitic ferrite/martensite (BF/M) for ITT samples 7 through 9. The trends shown in Figure 4.72 echo the results for ITT samples 1, 2 and 3. However, the slope for both ferrite and bainitic ferrite/martensite is almost identical for samples 7, 8 and

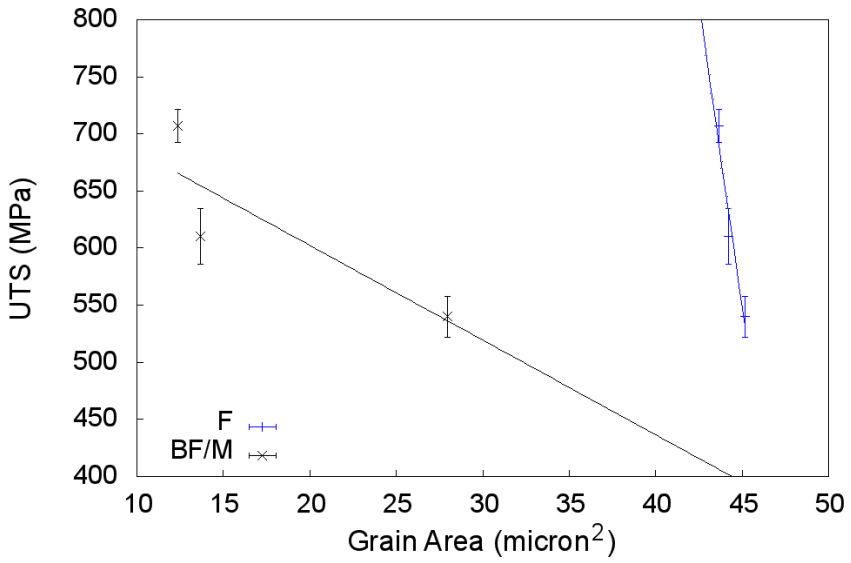

Figure 4.67: Relationship between ferrite grain area and UTS for ITT trial samples 1, 2 and 3.

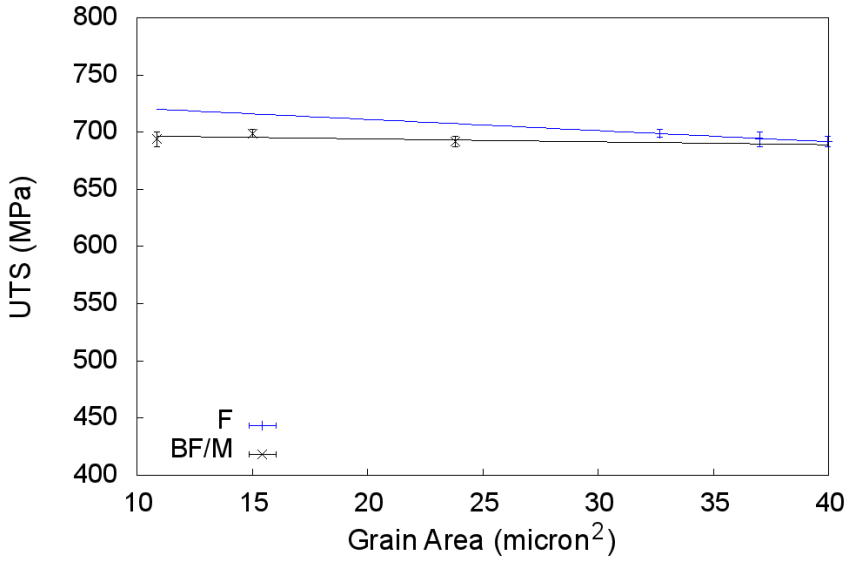

Figure 4.68: Relationship between ferrite grain area and UTS for ITT trial samples 4, 5 and 6.

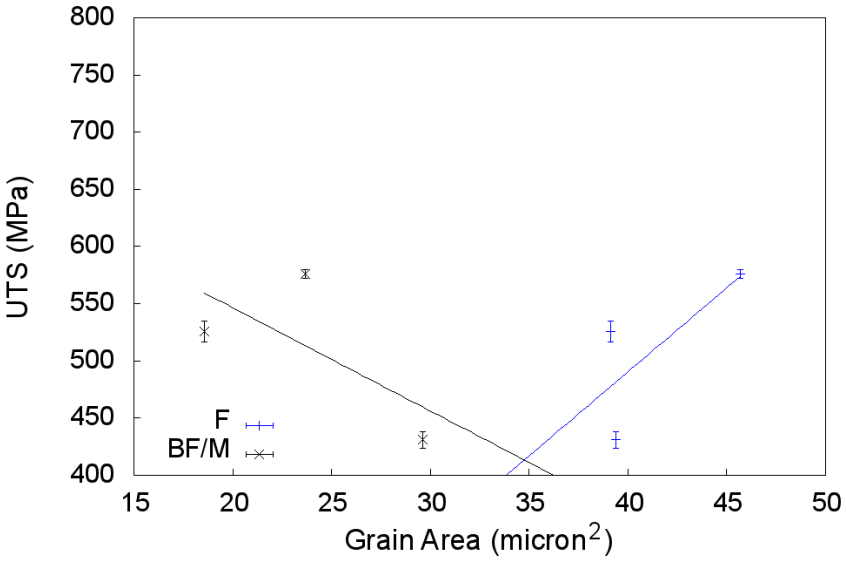

Figure 4.69: Relationship between ferrite grain area and UTS for ITT trial samples 7, 8 and 9.

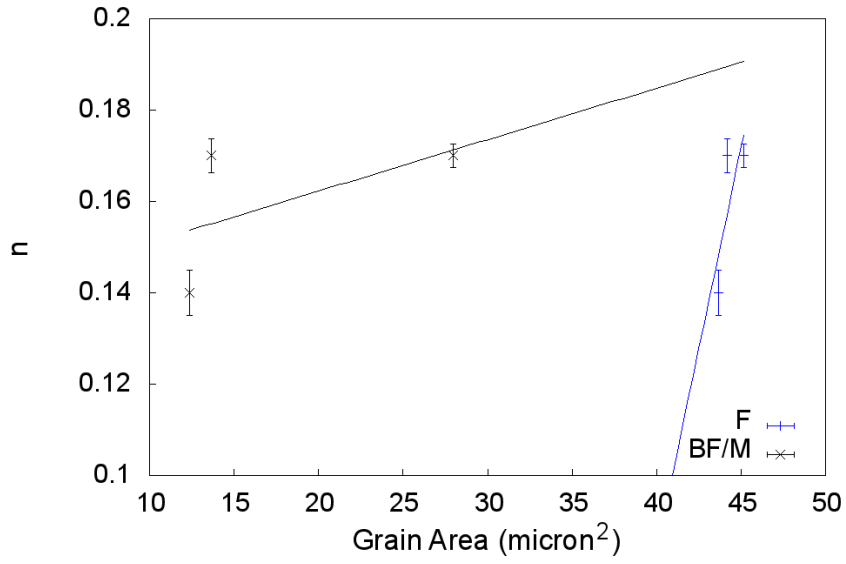

Figure 4.70: Relationship between ferrite grain area and n for ITT trial samples 1, 2 and 3.

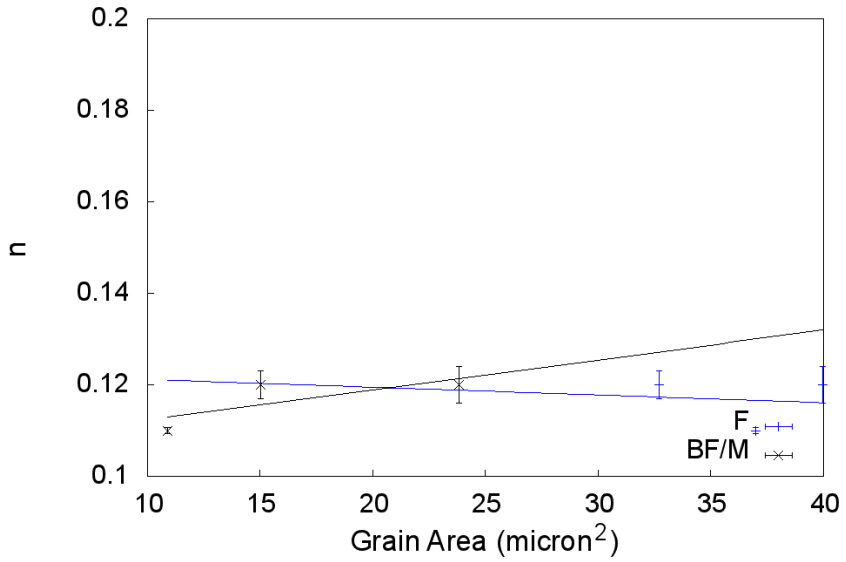

Figure 4.71: Relationship between ferrite grain area and n for ITT trial samples 4, 5 and 6.

9 whereas the slopes in Figure 4.72 are not equivalent for bainitic ferrite/martensite and ferrite.

4.6 Re-engineered ITT Trials

The mechanical results from the ITT results described in Section 4.5 indicated that the proposed thermal treatments did not successfully enhance work hardening behaviour or increase strength relative to the reference sample that was continuously cooled at 10 °C/s. As a result, a new set of experiments was designed based on the isothermal hold study shown in Section A. Three tests were performed with the goal of improving the mechanical performance. Samples with the geometry shown in Figure 4.1 were thermally tested in the Gleeble 3800 and the Gleeble 3500 was used to thermally treat the strip samples with a geometry shown in Figure 4.4.

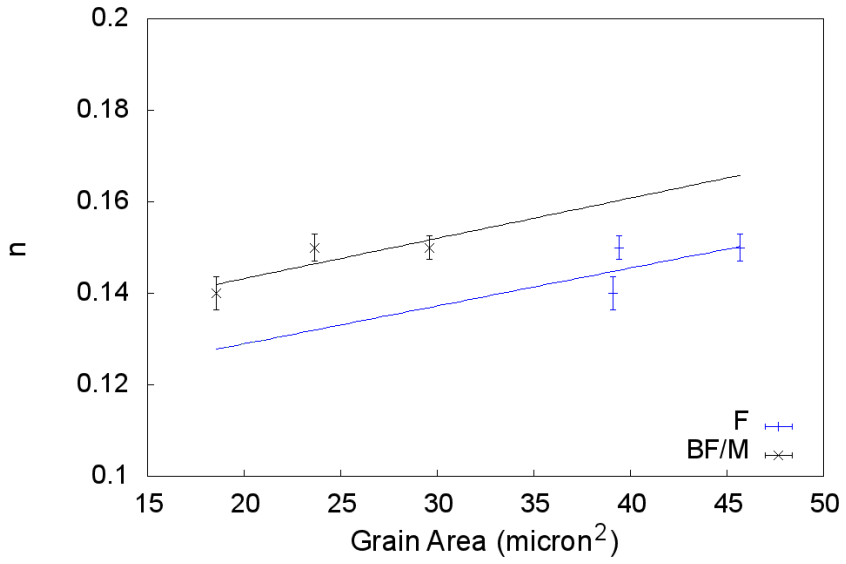

Figure 4.72: Relationship between ferrite grain area and n for ITT trial samples 7, 8 and 9.

As mentioned in Section 4.2, the six parameters that affect microstructural development and, hence, mechanical behaviour are: 1) initial cooling rate, 2) interrupt temperature after accelerated cooling, 3) hold time at the interrupt temperature, 4) re-heat temperature, 5) hold time at the re-heat temperature and 6) final cooling rate. The re-engineered ITT trials changed five of the six parameters as follows: the initial cooling rate was increased to 20 °C/s to an interrupt temperature of 560 °C (to again correspond with 80 % transformed), a re-heat temperature of 675 °C was implemented and a final cooling rate of 20 °C/s was implemented. The hold times at the re-heat temperature were kept the same at 0, 5 and 10 minutes. A faster initial cooling rate was chosen to promote the formation of bainite/bainitic ferrite over ferrite for the first constituent. Similarly, a faster second cooling rate was chosen to promote M-A formation after the isothermal hold at the re-heat temperature. The re-heat temperature was lowered to 675 °C based on the results presented in

Table 4.8: Thermal schedule for re-engineered ITT tests.

Sample ID	Primary Cooling Rate (°C/s)	Interrupt Temperature (°C)	Hold Time (min)	Re-heat Temperature (°C)	Hold Time (min)	Secondary Cooling Rate (°C/s)
N1	20	560	0	675	0	20
N2	20	560	0	675	5	20
N3	20	560	0	675	10	20

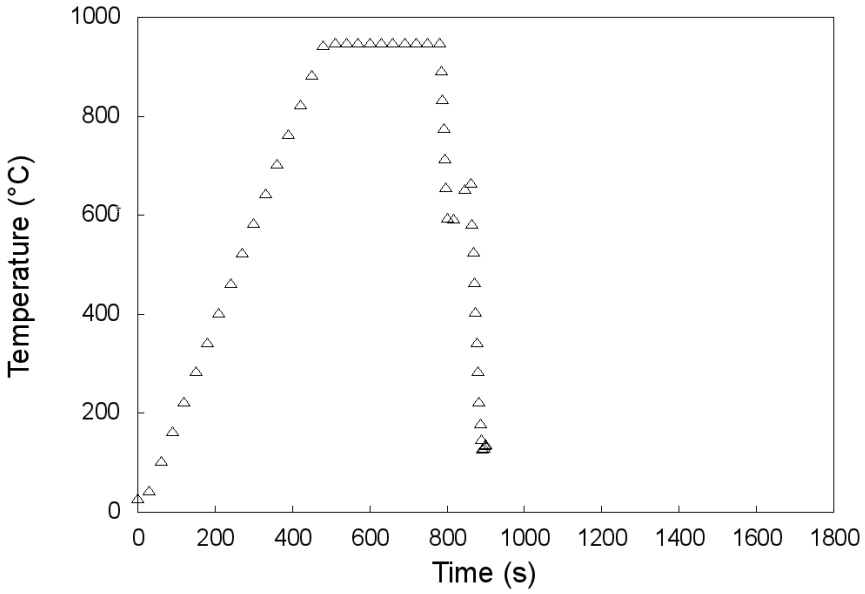

Figure 4.73: Thermal profile of sample N1.

Section A. More specifically, the re-heat temperature was reduced to prevent any re-austenitization as the initial re-heat temperature of 750 °C was very close to the A_{c1} temperature.

The thermal profiles for samples N1, N2 and N3 are shown in Figures 4.73 to 4.75. Only one thermocouple was placed on these strip specimens in a location corresponding to the horizontal and vertical center of the strip (indicated by point 2 or 5 in Figure 4.5).

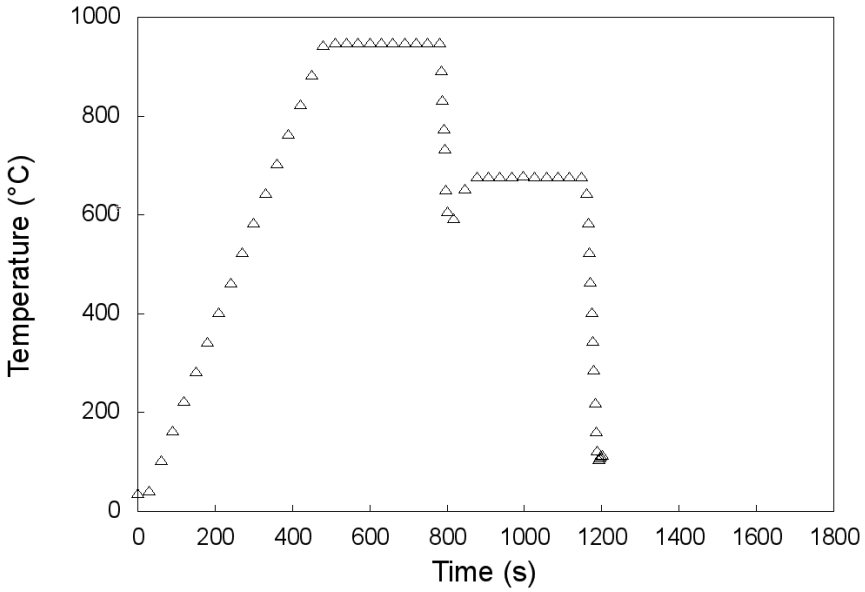

Figure 4.74: Thermal profile of sample N2.

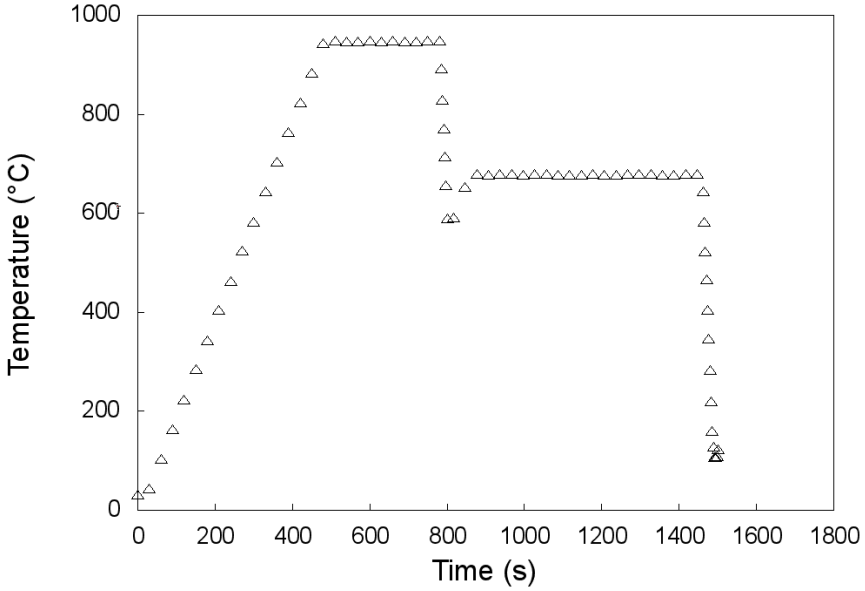

Figure 4.75: Thermal profile of sample N3.

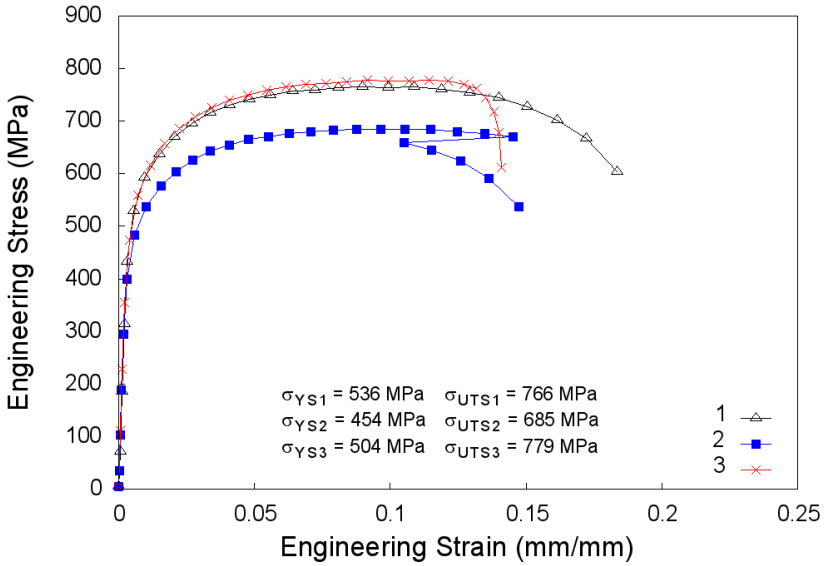

Figure 4.76: Engineering stress-strain curves for re-engineered ITT sample N1.

The samples were machined into sub-size tensile specimens according to the procedures outline for the first ITT specimens. Tensile testing was performed on the sub-size specimens according to the procedure outlined in Section 4.1.4. The engineering stress-strain curves are shown in Figures 4.76 to 4.78. The extensometer slipped during tensile testing of the center sub-size specimen (number 2) for sample N1, as shown by the squares in Figure 4.76. The extensometer slipped after the YS and UTS values had been reached; therefore, the values included in Figure 4.76 are valid.

The new mechanical data was compared against the reference sample to determine whether the new parameters improved mechanical performance. Figure 4.79 shows the comparison between the engineering stress-strain curves for samples N1, N2, N3 and the reference sample. As for the first set of ITT trials, the engineering tensile behaviour for the center specimen (sample 2) was plotted for N1, N2 and N3.

The re-engineered trials did not improve the mechanical performance as com-

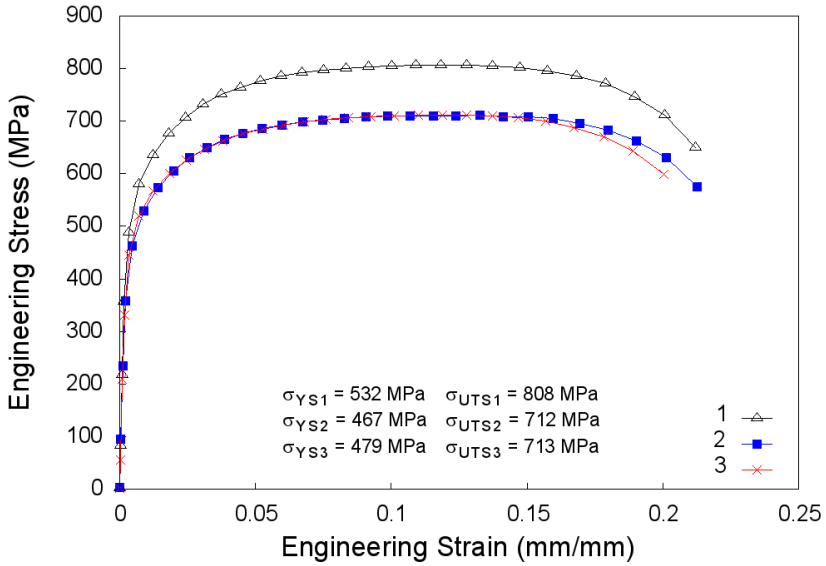

Figure 4.77: Engineering stress-strain curves for re-engineered ITT sample N2.

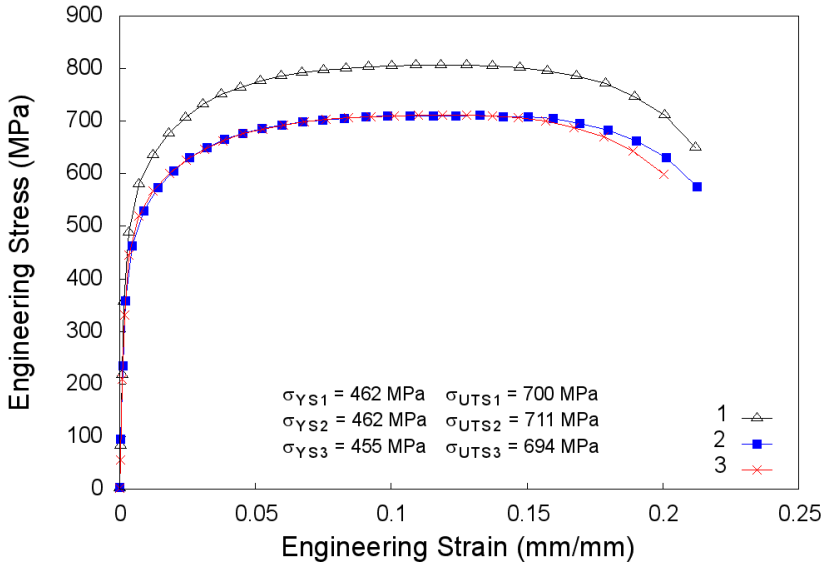

Figure 4.78: Engineering stress-strain curves for re-engineered ITT sample N3.

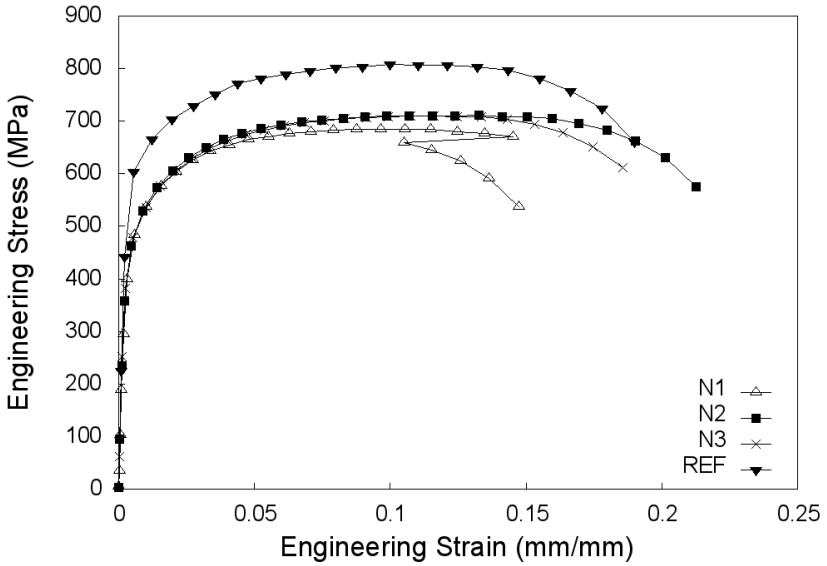

Figure 4.79: Comparison of the engineering stress-strain curves for re-engineered ITT samples N1, N2 and N3 and the reference sample.

pared with the reference sample. The UTS and YS values were similar to the ITT samples 4, 5 and 6.

The true stress-strain curves were also generated for the re-engineered samples and are included in Figures 4.80 to 4.82. The work hardening coefficients are included for each stress strain curve for comparison.

The mechanical performance of the new ITT trials is summarized in Table 4.9 which includes the reference sample for comparison. As previously mentioned, there was no improvement in mechanical performance relative to the reference sample or the previous ITT trials.

Since the re-engineered ITT trials did not improve the mechanical performance as compared with the reference sample or the first set of ITT trials, the microstructures were not investigated.

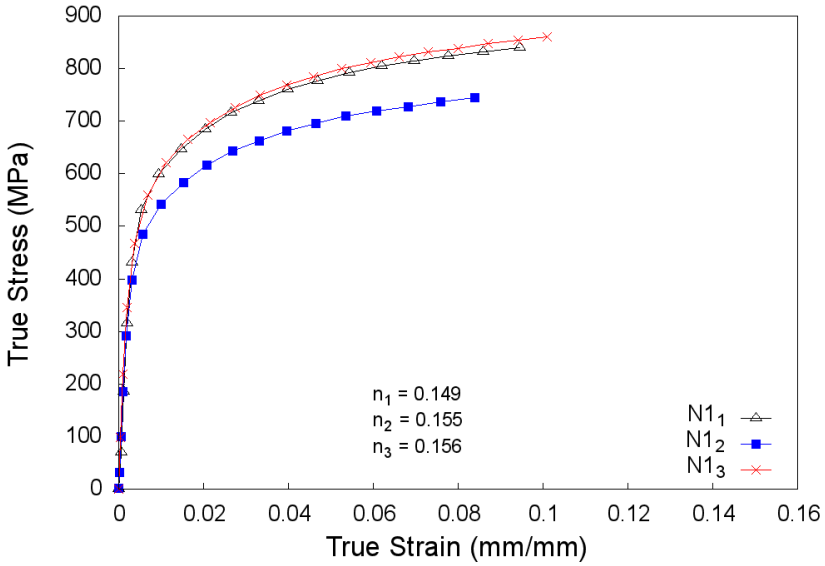

Figure 4.80: True stress-strain curves for re-engineered ITT sample N1.

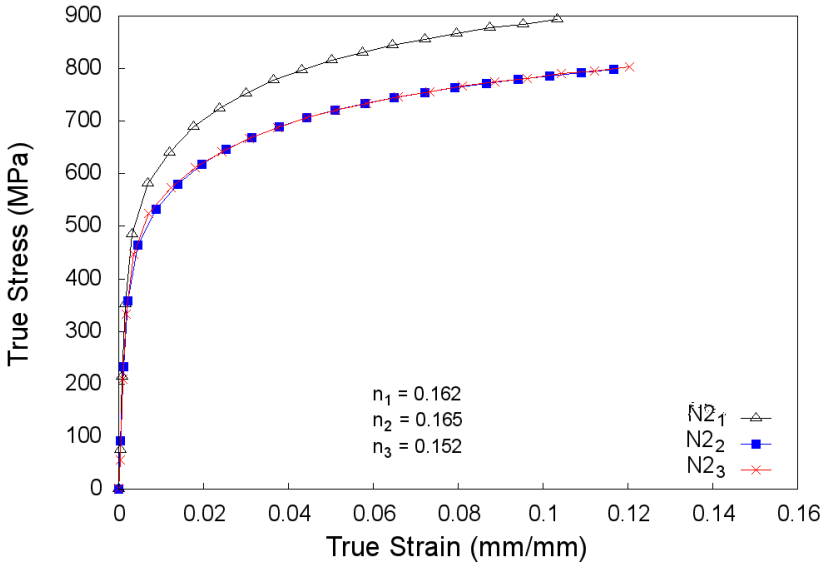

Figure 4.81: True stress-strain curves for re-engineered ITT sample N2.

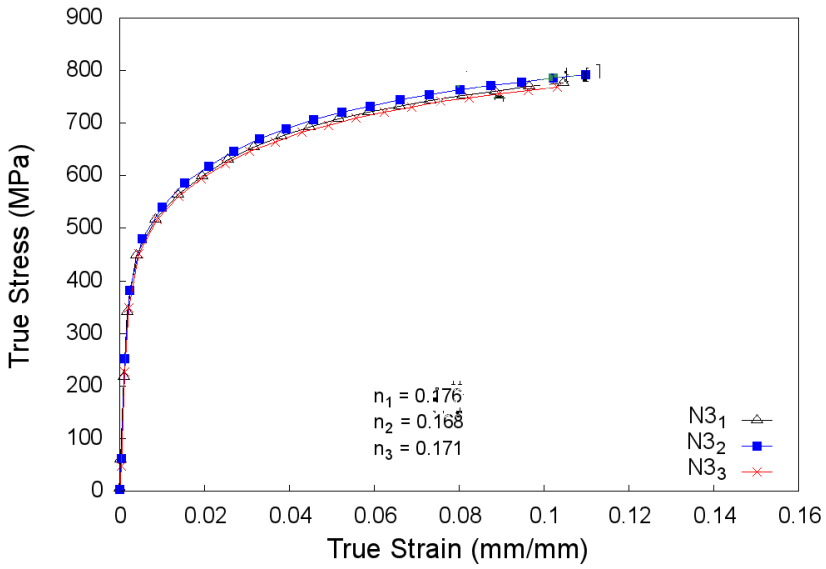

Figure 4.82: True stress-strain curves for re-engineered ITT sample N3.

Table 4.9: Tensile behaviour of the re-engineered ITT trial specimens.

Sample	Average UTS (MPa)	Average YS (MPa)	YS/UTS	Average n	Average Ductility (%)
REF	788	548	0.70	0.13	20
N1	743	498	0.67	0.15	17
N2	744	493	0.66	0.16	23
N3	701	460	0.66	0.17	22

4.7 Summary

This chapter detailed the experimental techniques, conditions and results for the ITT samples. The ITT specimens consisted of cooling to an interrupt temperature of 585 °C for 0, 5 or 10 minutes and either quenching to room temperature or re-heating to 750 °C after the 0 minute hold. After a hold time of 0, 5 or 10 minutes at the re-heat temperature of 750 °C, the samples were either quenched or slowly cooled to room temperature at 3 °C/s. It is important to note that the effect of precipitate size, volume fraction and type was not included in this study. More specifically, the role of precipitates on the size of secondary constituents was not addressed, although precipitation has a significant role on the microstructural development and mechanical performance.

The ITT specimens were cut, mounted and polished for microstructural investigation. Color metallography was performed on a few samples using LePera's etch; however, this procedure was very difficult and time consuming. Furthermore, the results from the color etch were not reproducible and did not justify the technique as a viable method to identify and quantify the microstructures. SEM SE images were obtained for each sample. Similar to the CCT curve specimens, a TEM investigation was performed to determine the nature of indistinguishable grains observed in the SEM SE images. A 'microconstituent characterization database' was generated using the results of the CCT and ITT specimens. The phase fractions were calculated for each sample using the 'microconstituent characterization database' as a guideline for grain identification. Image analysis was performed using FIJI to determine the phase fraction of each constituent. Martensite and bainitic ferrite were considered as a single constituent in terms of phase quantification; as a result, the microstructures consisted of martensite/bainitic ferrite, ferrite and M-A. No pearlite was observed in these samples as the cooling rates were too high to allow for the

diffusion-based transformation to occur.

The relationship between thermal history and microstructure development was investigated. As hold time increased at 585 °C/s, the phase fraction of bainitic ferrite/martensite increased at the expense of ferrite. This suggests that the transformation from austenite to bainitic ferrite/martensite continues at 585 °C. The same trend was observed for the hold time at 750 °C for the quenched samples: increasing the hold time at 750 °C caused an increase in bainitic ferrite/martensite phase fraction. There was no significant effect of hold time at 750 °C on the phase fraction for the slow-cooled samples, however. For both elevated temperatures, increasing the hold time caused an increase in grain area of both constituents.

The samples that were re-heated to 750 °C were heated to the intercritical region, which caused more austentite formation. As the austenite volume fraction increased during the hold, the austenite carbon content decreased and formed a softer martensite/bainitic ferrite structure with a large 'grain size' during quenching. The re-heat process may also have caused dislocation annealing in ferrite/bainitic ferrite as well as precipitate growth, which was not investigated.

The mechanical properties of the ITT specimens were determined through hardness and tensile testing. Micro- and macrohardness tests were conducted to determine the overall hardness of the specimens, and nanoindentation experiments were performed to identify the hardness of a bainitic ferrite/martensitic grain relative to the surrounding ferrite matrix. The nanoindentation tests did not yield useful results as the resulting hardness values had significant variability and the values were all within error for both the grain of interest and the surrounding ferrite matrix. As a result, nanoindentation was not considered a feasible technique to determine the hardness of the bainitic ferrite/martensite grains.

The tensile performance of the ITT trials did not meet X80 specifications for

minimum yield criterion; however, this was not the goal of the research project. The goal was to explore the possibility of creating mixed microstructures from an X80 steel under no strain conditions. The reference sample (continuously cooled at 10 °C/s) had the best mechanical performance of all the ITT samples in terms of UTS and YS. The ITT samples that came closest to the reference sample in terms of UTS and YS were samples 4, 5 and 6, which were continuously cooled to 585 °C, immediately heated to 750 °C, held for 0, 5 or 10 minutes and then quenched to room temperature. The UTS ranged from 431 MPa (for sample 9) to 788 MPa (for the reference sample) and the YS varied from 244 MPa (sample 9) to 548 MPa (for the reference sample).

The relationship between hardness and constituent phase fraction was investigated. The hardness showed good correlation with ferrite content; more specifically, the hardness decreased as ferrite content increased. The only contradictory set of samples were the quenched samples from 750 °C using the macrohardness results. Hardness was also investigated as a function of UTS. The microhardness results provided a positive relationship between hardness and UTS (with the exception of the samples quenched from 585 °C). The macrohardness results, on the other hand, showed the opposite trend. The UTS decreased with increasing hardness for all ITT samples, which did not agree with the expected results. The hardness results may be inaccurate as a result of insufficient sample thickness which will affect the hardness readings.

Both the YS and UTS increased as ferrite content increased for the ITT specimens that were cooled to 585 °C and quenched to room temperature. The YS slightly increased as ferrite increased for the samples that were re-heated to 750 °C and quenched to room temperature; however there was almost no correlation between UTS and ferrite content for these samples. For the specimens that were

slowly cooled to room temperature from 750 °C, there is a slightly negative correlation between YS and ferrite content, but the UTS increases as ferrite fraction increases. The work hardening coefficient for all ITT samples decreases as ferrite content increases, which agrees with expected results.

The mechanical properties were plotted as a function of grain area. There is a strong negative correlation between YS and grain area for the samples quenched from 585 °C, but the other samples did not show clear trends. The same was observed for UTS plotted as a function of grain area. The work hardening coefficient consistently increases as grain area of both ferrite and bainitic ferrite/martensite increased.

The results from the first ITT specimens did not provide a clear relationship between thermal history and microstructure, nor between microstructure and mechanical properties. As a result, the transformation kinetics at the interrupt and re-heat temperatures were investigated to determine whether a 0 minute hold at 585 °C was sufficient and also to investigate whether the re-heat temperature of 750 °C was causing partial transformation back to austenite. The isothermal kinetics investigation resulted in a new set of ITT trials that incorporated a faster cooling rate (20 °C/s instead of 10 °C/s), a lower re-heat temperature (675 °C as compared with 750 °C) and a faster secondary cooling rate of 20 °C/s instead of 3 °C/s. The re-engineered ITT trials did not show enhanced mechanical performance as compared with the previous ITT trials. The re-engineered trials were very similar to the first set of samples that were heated to 750 °C/s and quenched to room temperature.

This page was intentionally left blank

Chapter 5

Conclusions and Future Work

5.1 Conclusions

The goals of this research project were to: 1) identify the relationship between thermal history and microstructure development, and 2) determine the effect of microstructure on mechanical properties, most notably work hardening behaviour, for an X80 microalloyed steel. A series of Interrupted Thermal Treatments (ITT) were applied to explore the possibility of achieving multi-phase microstructures from an X80 steel under zero-strain conditions. The following parameters were varied: 1) hold time at the interrupt temperature of 585 °C, 2) hold time at the re-heat temperature of 750 °C and final cooling rate. Prior to the ITT experiments, a Continuous Cooling Transformation (CCT) diagram was constructed to identify the transformation temperatures corresponding to the various constituents in the microstructures. A microstructure development map was generated to understand the microstructure evolution at various stages in the ITT process, and the mechanical properties of the ITT trials were obtained. A second set of ITT experiments was designed to improve the mechanical performance; however, the re-engineered ITT

trials had similar performance to the original experiments.

A detailed TEM investigation revealed that the ITT microstructures consisted of ferrite, bainitic ferrite, martensite and martensite-austenite (M-A). The relationship between thermal history and microstructure was investigated by correlating the phase fractions and grain sizes with hold times at the elevated temperatures of 585 °C (interrupt temperature) and 750 °C (re-heat temperature). The hold time at 585 °C resulted in grain growth for both ferrite and bainitic ferrite/martensite. In addition, the phase fraction of ferrite decreased at the expense of bainitic ferrite/martensite as hold time increased at 585 °C. This confirmed that the reaction from austenite to bainitic ferrite/martensite was still progressing at 585 °C. Similarly, increasing the hold time at 750 °C caused an increase in bainitic ferrite/martensite with a corresponding decrease in ferrite phase fraction for the samples that were quenched from 750 °C to room temperature. No relationship was observed for the samples that were slowly cooled from 750 °C to room temperature. The grain area of ferrite and bainitic ferrite/martensite increased as hold time increased, which verifies that grain coarsening occurs at elevated temperatures.

The relationship between microstructure and mechanical properties was investigated by plotting the mechanical data as a function of phase fraction and grain size. The hardness increased as ferrite content increased, which does not agree with the expected results. The yield strength and ultimate tensile strength increase as ferrite increases for the samples that were cooled to 585 °C and quenched to room temperature. The samples that were re-heated to 750 °C and either quenched or slowly cooled to room temperature did not show a significant trend in yield strength or ultimate tensile strength as a function of ferrite content. Furthermore, the yield strength and ultimate tensile strength decreased as ferrite grain area increased, which agrees with the expected trends.

One major concern with the mechanical performance of the ITT trials was the negative correlation between hardness and ultimate tensile strength. Since both of these properties are related to a material's strength, they should exhibit a positive relationship with one another; however, this trend was not observed. A possible explanation for this observation is that the sample thickness was not sufficient for macrohardness testing, and therefore, the hardness readings were erroneous. The sample thickness was 1.5 mm; however, the sample was polished in order to reveal the microstructural features and to ensure a flat surface for hardness testing. The final sample thickness may have been reduced to 0.5 mm to 1.0 mm after repeated polishing and etching steps; as a result, the sample may have had insufficient thickness for hardness testing.

Phase quantification was another concern. The TEM study successfully confirmed the nature of regions that were indistinguishable in the SEM SE images; however, the difference between martensite and bainitic ferrite was only determined through TEM analysis. There was no clear and consistent characteristic that identified a martensite grain from a bainitic ferrite grain in the SEM SE images. As a result, image processing was conducted for each SEM SE micrograph and the phase quantification results were presented with the combined fraction of martensite/bainitic ferrite. This 'simplification' may have influenced the phase fractions reported in this work as the image analysis procedure involved a manual adjustment to threshold levels. It was not feasible to use a fully automated macro for image analysis as three different constituents were isolated simultaneously. Furthermore, the phase quantification technique presented in this work was an exploratory method using TEM results to characterize grains/constituents in SEM SE images. No other publications were available to verify the phase quantification procedure. The image analysis errors were relevant for both the phase quantification and the

grain area calculations, since the grain area measurements were obtained from the processed images that were used for phase quantification. As a result, the trends that are observed may represent incorrect image analysis techniques rather than actual material performance.

Although the ITT trials did not improve the mechanical performance relative to a continuously cooled sample, one successful outcome of this research was the creation of a multi-phase microstructure without the addition of strain during thermal processing. The ITT trials comprised mixtures of ferrite, bainitic ferrite, martensite and M-A, which is not common for typical X80 grades. This research shows that the microstructure can be successfully manipulated through thermal treatment alone and provides important groundwork for future work into interrupted thermal treatments.

5.2 Future Work

The results of this thesis provide insight into the relationship between thermal history and microstructure development and mechanical behaviour; however, this work inspired questions that require further analysis.

In order to fully understand the relationship between thermal treatment and microstructure development, additional parameters in the ITT matrix must be varied, including: 1) primary cooling rate, 2) interrupt temperature, 3) hold time at the interrupt temperature, 4) re-heat temperature, 5) hold time at the re-heat temperature and 6) final cooling rate. As mentioned in Chapter 4, the original proposed matrix involved varying these six parameters at two levels which required 64 tests. In order to assess the statistical significance and repeatability of the results, however, 192 tests should be performed to account for triplicates of each test condition. The full test matrix would provide a statistical and quantifiable indication of the

significance of each variable on the end result (percentage of each microconstituent, hardness, YS, UTS, % EL and work hardening coefficient). The large number of experiments would generate a substantial database that could be statistically analyzed to determine the significance of each variable on the final microstructure. The most significant parameters could then be varied further and optimized. In addition, the triplicate experiments for each test condition would verify the reproducibility of the results, which is something that not investigated in this work. The results from the current ITT trials were not verified with repeat experiments and, therefore, no comment can be made about the reproducibility of the results.

The re-engineered trials showed an improvement relative to the first set of ITT trials with regards to mechanical performance. Future tests could be conducted with a lower interrupt temperature corresponding to 90 - 95 % transformation to bainitic ferrite rather than the original proposition of 80 % transformed. The lower interrupt temperature would provide a smaller amount of austenite that could be enriched in carbon as a result of the interrupted thermal treatment process.

Since the results presented in this work focussed exclusively on the transformation products and resulting mechanical behaviour of samples that were thermally treated under no-strain conditions, the effect of deformation was not investigated. Deformation is an important strengthening mechanism and is also utilized in current mill TMCP practices; as a result, a suggestion for future work is to repeat the ITT experiments using strain during thermal treatment. The repeated ITT trials under strain conditions would provide a direct comparison with the zero-strain samples and would also reflect real life mill conditions better than the ITT samples that were generated without strain. At the current stage, the relationships between thermal history, microstructure and mechanical properties are incomplete; it is necessary to compare the ITT results to those resulting from samples that are mechanically

deformed in order to determine the effect of deformation on microstructure development.

Another area of this work that requires further analysis is related to microstructure characterization. Although the TEM investigation led to successful identification of a few grains that were previously indistinguishable in SE SEM micrographs, this process was time consuming and did not reveal a clear distinction between bainitic ferrite and martensite. A more efficient and reproducible method must be explored to ease the identification and subsequent quantification of the microconstituents present in these steels. One way to achieve this goal is to increase the number of regions in the 'grain characterization database'. Distinguishing features may be noticed when comparing several (e.g., ten or more) confirmed regions for each constituent rather than just a few confirmed regions. In this work, only three grains of martensite and three grains of bainitic ferrite were identified, which was a small database to draw conclusions from. Once the database is expanded and any distinguishing features are identified, image processing techniques could be developed to separate the grains individually rather than simultaneously processing the images for multiple constituents. A specific macro could be created to analyze the SEM SE images in segments; i.e., the martensite grains would be identified first and removed from the image, then the bainitic ferrite grains would be isolated and removed followed by the M-A particles. The remaining microstructure would then contain 100 % ferrite. This automated and segmented approach might improve the reproducibility in phase quantification as well as grain size determination since the errors associated with manual image processing would be removed.

When considering the effect of microstructure on mechanical behaviour, the results of this thesis were unclear. The relationship between hardness and UTS did not agree with the expected trend; this may have been due to the small sample

thickness that was subjected to large indent loads in macrohardness testing. In order to verify these trends, the hardness values should be repeated on samples with a sufficient thickness suitable for hardness testing. In order to maintain consistency between microstructure, hardness and tensile behaviour, the same sample must be investigated as was done in this work. Therefore, a thicker strip specimen must be thermally treated in the Gleeble 3500 to ensure that the resulting hardness values can be obtained from the strip specimen before it is machined into sub-size tensile specimens. Alternatively, regular-sized tensile specimens could be tested at full thickness; however, suitable grips would be required for the Gleeble thermomechanical simulators in order to thermally treat the samples.

This page was intentionally left blank

Appendix A

Transformation Kinetics of ITT Specimens

An isothermal hold at 585 °C was conducted to verify that the transformation from austenite to a lower temperature product (bainitic ferrite) occurred in less than a minute, thus justifying the subsequent ITT tests where samples were immediately re-heated to 750 °C. A second isothermal hold at 750 °C was performed to determine whether re-austenitization was occurring during the 5 and 10 minute holds at the re-heat temperature.

As discussed in Section 3.3.2, the Gleeble 3800 had two different jaw configurations. Table A.1 describes the isothermal experiments using the regular and the low-force jaws. The samples were austenitized at 945 °C for 5 min. Table A.1 describes the post-austenitization treatment, starting with the cooling rate from 945 °C. Samples K1 and K2 were performed using the regular jaw configuration whereas samples K3 and K4 used the low-force jaws. Furthermore, samples K3 and K4 included isothermal holds at both the lower temperature (585 °C) and the higher temperature (750 °C for sample K3 and 675 °C for K4). The re-heat temperature

Table A.1: Thermal schedule for isothermal hold experiments using both the regular and low-force jaw configurations.

Sample ID	Cooling Rate (°C/s)	Interrupt Temperature (°C)	Hold Time (min)	Re-heat Temperature (°C)	Hold Time (min)	Cooling Rate (°C/s)	Jaw Type
K1	10	585	30	-	-	3	regular
K2	10	585	0	750	30	3	regular
K3	10	585	30	750	30	3	low-force
K4	10	585	30	675	30	3	low-force

for sample K4 was lowered to 675 °C to directly compare the dilation behaviour with that at the higher temperature. The aim of lowering the re-heat temperature was to determine whether the original temperature was below or above the A_{c1} temperature.

The dilation results from sample K1 and K2 are shown in Figure A.1 and Figure A.2, respectively. The data is presented as dilation and temperature on the ordinate axes versus time on the abscissa in Figure A.1a and Figure A.2a. Furthermore, dilation is plotted against temperature in Figure A.1b and Figure A.2b.

Figure A.1a and Figure A.2a show the overall dilation behaviour as a function of temperature. The transformation to austenite during the isothermal hold at 945 °C is evident by the sharp dilation drop within the first 200 seconds, followed by the slight dilation decrease at the constant temperature. The onset of austenitization is also evident in Figure A.1b and Figure A.2b as the change in curvature beginning at roughly 700 °C. Figure A.1b and Figure A.2b illustrate the 'stress relaxation' phenomenon during the isothermal hold at 945 °C, which will be discussed in further detail below. The transformation to a second product is illustrated in Figure A.1 as the sharp increase in dilation at approximately 800 sec in Figure A.1a and the dilation increase in Figure A.1b at approximately 610 °C. The transformation be-

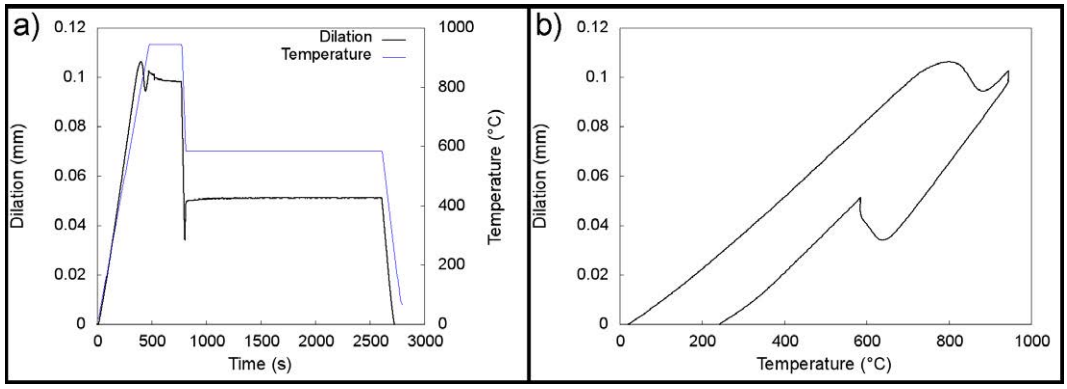

Figure A.1: Dilation data for sample K1 which includes an isothermal hold at 585 °C for 30 min using standard jaws: a) dilation versus time with temperature superimposed on a second axis; b) dilation as a function of temperature.

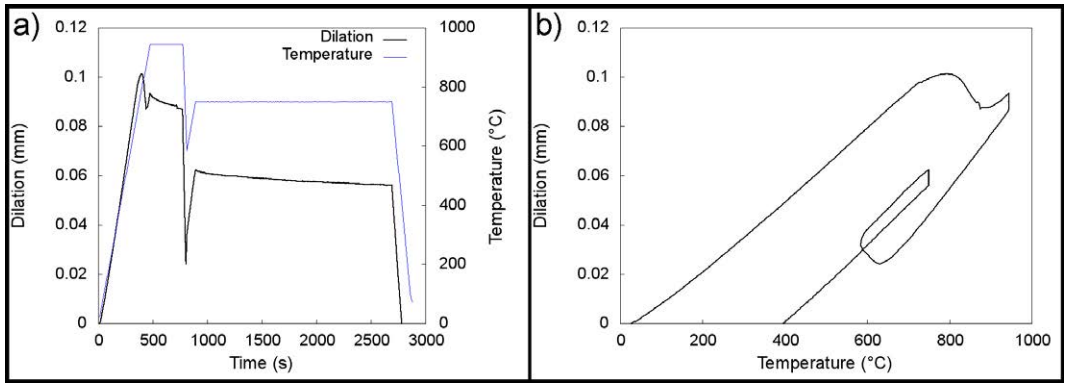

Figure A.2: Dilation data for sample K2 which includes an isothermal hold at 750 °C for 30 minutes using standard jaws: a) dilation versus time with temperature superimposed on a second axis; b) dilation as a function of temperature.

haviour in Figure A.2 is similar; more specifically, the transformation from austenite to a lower temperature product begins at approximately 610 °C as shown in Figure A.2b. The decrease in dilation during the isothermal hold at 750 °C is evident in both Figure A.2a and b; Figure A.2a shows a slight decrease in dilation during the 1500 sec hold whereas Figure A.2b displays the dilation decrease as a vertical line at 750 °C.

Figure A.3 shows an expanded view of the dilation data during austenitization for samples K1 and K2. The resulting dilation plots from samples K1 and K2 (performed on the regular jaws) showed a similar contraction during austenitization at 945 °C to the CCT curve specimens as shown in Figure 3.3. The contraction was also observed during the isothermal holds at 585 °C (sample K1) and 750 °C (sample K2). Similar to Figure 3.3, K1 and K2 both exhibit constant contraction during the isothermal hold at 945 °C rather than obeying a horizontal line as expected. These tests were combined into a single test (K3) and repeated on the low-force jaws, which will be discussed below.

The dilation data during the isothermal hold at 585 °C, shown in Figure A.1a, was investigated further in order to verify the test conditions chosen for the entire ITT trial test matrix that was previously presented. More specifically, it was important to confirm that the transformation from austenite to a lower temperature constituent was completed almost instantaneously as the ITT trials (4, 5, 6, 7, 8 and 9) involved re-heating the sample to a re-heat temperature of 750 °C after a 0 minute hold at the interrupt temperature of 585 °C. Figure A.4 shows the dilation behaviour from the tail end of austenitization to roughly the first minute of the isothermal hold at 585 °C. The transformation from austenite to a second product (ferrite or bainitic ferrite) as shown in Figure A.4 reveals an almost instantaneous transformation. The transformation begins at approximately 670 °C (indicated by

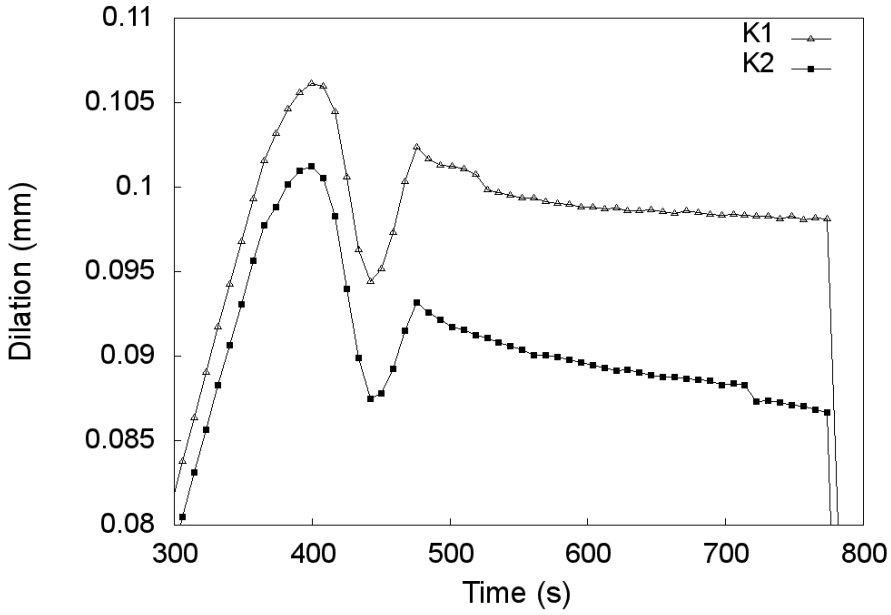

Figure A.3: Transformation behaviour during austenitization at 945 °C for samples K1 and K2.

point 1 in Figure A.4) and is complete within 20 seconds (corresponding to point 2). This indicates that the transformation kinetics from (almost homogenous) austenite to bainitic ferrite/bainite is very fast and will not continue as the hold time at 585 °C increases. This data confirms that the amount of transformation that is thermodynamically possible at 585 °C (80 % of the available austenite after austenitization) is complete within 30 seconds of an isothermal hold, leaving the remaining 20 % of austenite to transform to another product upon further cooling.

The overall transformation behaviour for sample K2 is shown in Figure A.2 and an expanded view of the isothermal hold at 750 °C is shown in Figure A.5. Figure A.5 reveals that the transformation does not appear to be complete at 750 °C as indicated by the slight and continuous contraction with increasing hold time. The dilation curve becomes almost horizontal near the end of the isothermal hold, how-

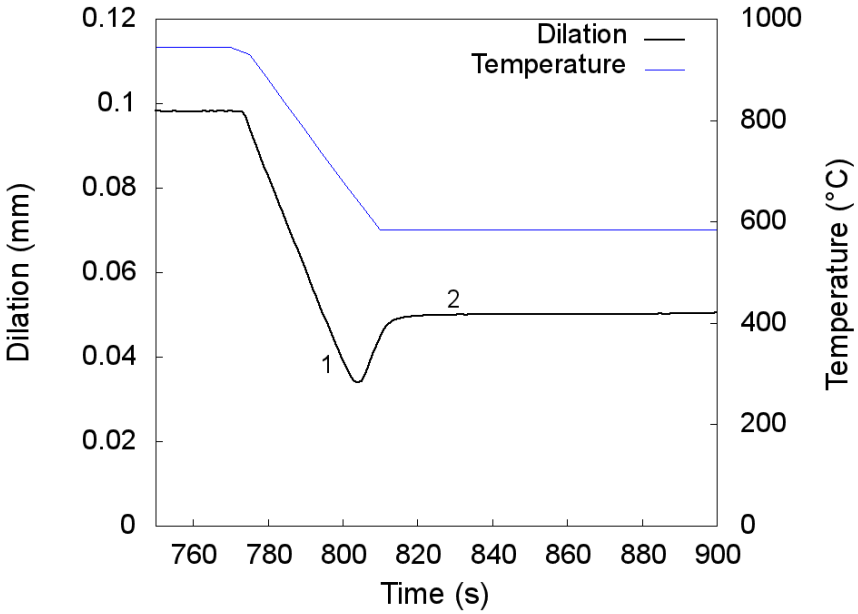

Figure A.4: Transformation behaviour during the isothermal hold at 585 °C for sample K1.

ever, and therefore complete transformation is obtained after the 30 min isothermal hold at 750 °C. The region of interest in Figure A.5 is identified and expanded in Figure A.6, with points 1, 2 and 3 labeled for illustration. Point 1 corresponds to the onset of transformation, which occurs at approximately 705 °C. The transformation begins during the cooling process from 945 °C to 585 °C. For sample K1, the transformation to bainitic ferrite/bainite occurs at 670 °C which is 35 °C different than the transformation temperature identified in sample K2 using the data in Figure A.6. As mentioned in Section 3.3.3, there is significant error when determining transformation temperatures from dilation data based on the tangent line selected to fit the data. As this issue was previously presented, it will not be discussed further in this section. Point 2 in Figure A.6 corresponds to the end of phase transformation to bainitic ferrite/bainite after approximately 15 sec. At this point, 80 % of the available austenite has transformed to bainitic ferrite/bainite. The sample linearly expands as the temperature increases to the re-heat temperature of 750 °C, which can be attributed to thermal expansion effects rather than a phase change. As hold time increases at 750 °C (point 3 in Figure A.6), the sample experiences a slight but continuous contraction as shown in Figure A.5. A phase transformation was not observed at this temperature, which means that the ferrite/bainitic ferrite is not re-austenitizing at 750 °C (note that the A_{c1} temperature was previously determined to be 740 °C as detailed in Section 3.3.1).

Based on the results shown in Figures A.3, A.4, A.5 and A.6, the test conditions for samples K1 and K2 were combined into a single test K3. K3 involved 30 minute holds at both 585 °C and 750 °C and was performed on the low-force jaws to to assess whether or not the contraction at the isothermal hold temperatures (945 °C, 750 °C and 585 °C) is caused by pressure exerted on the sample from the jaws during stress relaxation. Figure A.7 shows the results from K3.

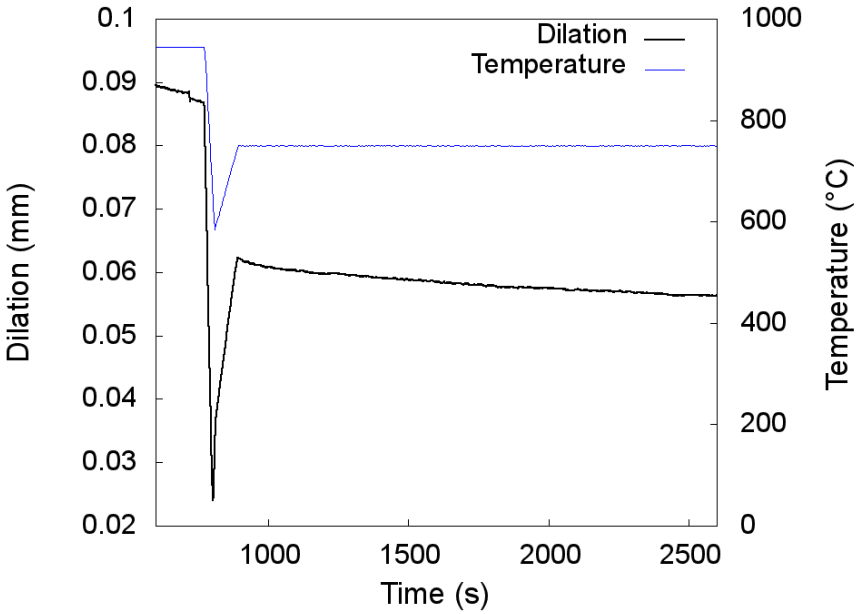

Figure A.5: Transformation behaviour during the isothermal hold at 750 °C for sample K2.

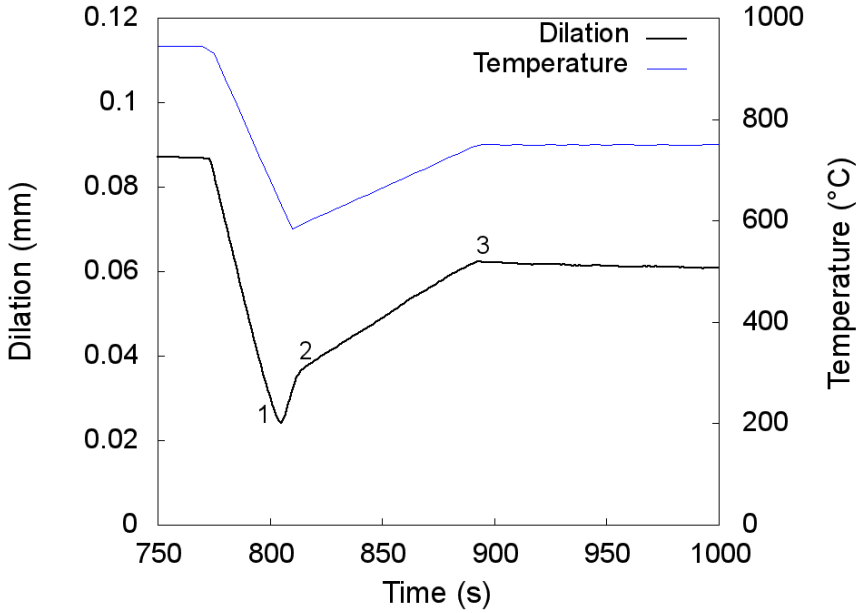

Figure A.6: Magnified view of the transformation behaviour at the onset of the isothermal hold at 750 °C for sample K2.

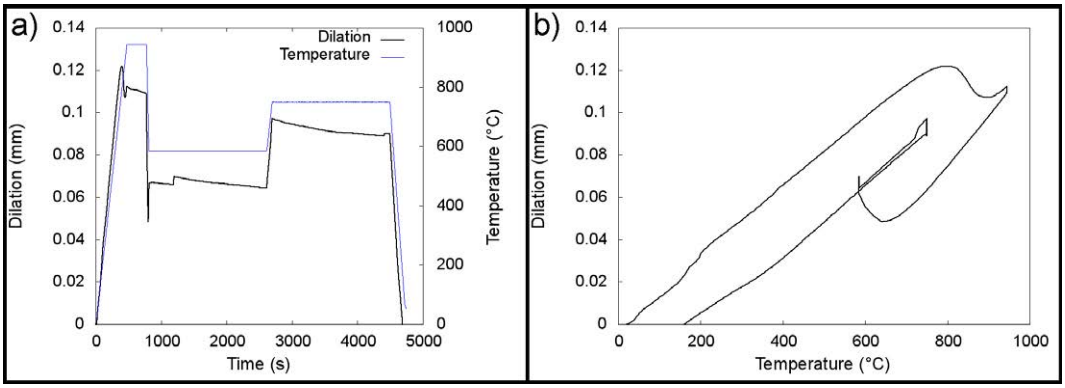

Figure A.7: Dilation data for sample K3 subjected to two isothermal holds: 585 °C for 30 minutes and 750 °C for 30 minutes using low-force jaws.

The overall transformation behaviour shown in Figure A.7a shows the same relaxation behaviour at 945 °C and at 750 °C as was observed in samples K1 and K2. The dilation behaviour during the isothermal hold at 585 °C showed an uncharacteristic bump at approximately 1200 sec, which can be attributed to dilatometer slippage during the experiment. The slippage is also apparent in Figure A.7b. The bump in dilation data did not have an impact on the final results, however, as the transformation behaviour at 585 °C had already been investigated in sample K1 using the regular jaws and it was determined that the transformation was complete in well under one minute. Furthermore, the isothermal hold at 585 °C was also studied on the low-force jaws in sample K4, which will be discussed below. As a result, the bump observed in Figure A.7 was considered an inconsequential anomaly. The important result from this experiment was that the sample still experienced relaxation (or a decrease in dilation) during the isothermal hold at 750 °C using the low-force jaws.

A final isothermal test was performed to replicate the test conditions of test K3 to verify the behaviour during the isothermal hold at 585 °C and to investigate the dilation behaviour at a lower re-heat temperature of 675 °C instead of 750 °C. As shown in Table A.1, test K4 is almost identical to K3 with the exception of the re-heat temperature; all other parameters are identical. The dilation data for K4 is shown in Figure A.8.

Figure A.8a shows the transformation behaviour as a function of time and temperature. As observed for samples K1, K2 and K3, the dilation data for sample K4 showed a dilation decrease during the isothermal hold at 945 °C; however, no dilation decrease was noted during the isothermal hold at 675 °C. The sample is neither expanding nor contracting at 675 °C, which confirms that no transformation is occurring at this temperature. As a result, a new set of ITT trials were proposed

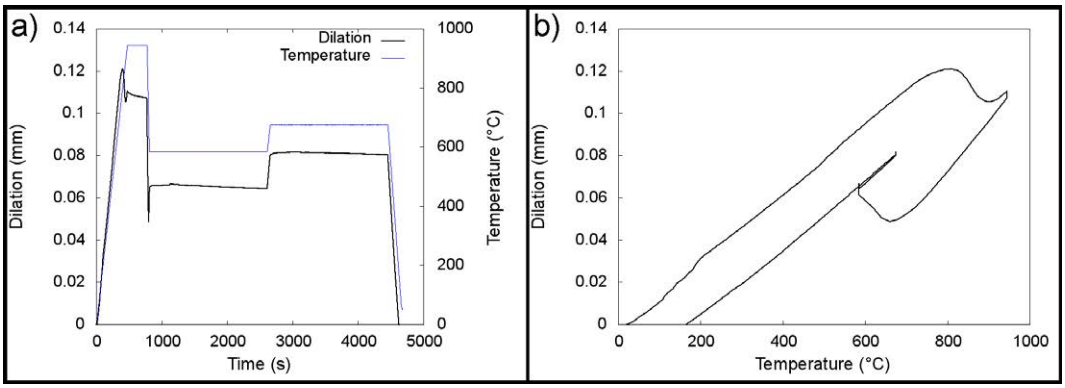

Figure A.8: Dilation data for sample K4 subjected to two isothermal holds: 585 °C for 30 minutes and 650 °C for 30 minutes using low-force jaws.

to incorporate the results from the isothermal transformation kinetics study. The re-engineered trials included a heat treatment at the lower temperature of 675 °C and will be discussed in Section 4.6.

As previously mentioned, the test conditions for sample K4 were chosen to verify the behaviour during the isothermal hold at 585 °C for sample K3; more specifically, to determine whether the bump in dilation data in Figure A.7a was an anomaly or an actual event that was reproducible. As shown in Figure A.8a, there was no bump in the dilation data, which verifies that the results shown for K3 during the 585 °C isothermal hold are not representative.

This page was intentionally left blank

Appendix B

Color Metallography and Ion Etching

This section includes supplementary information that was not included in the body of the thesis. Section B.1 includes a brief investigation into ion etching of a CCT curve specimen and section B.2 presents the results from color metallography.

B.1 Ion Etching

In the process of making TEM samples in the FIB, a brief side investigation into ion imaging was conducted to assess whether it would be a plausible technique to image the X80 steel with ions rather than using conventional etching and imaging techniques. Ion imaging in the FIB SEM was conducted using Ga^+ ions to bombard the sample surface, which create SE that are collected and used to generate an image. CCT curve sample D11 was pre-etched with 2 % Nital and then bombarded with Ga^+ ions. As a result, the micrographs in Figure B.1 show the effect of both chemical etching and physical etching with Ga^+ ions in the FIB. The small box that is observed in the center of Figure B.1b is the result of ion damage during ion

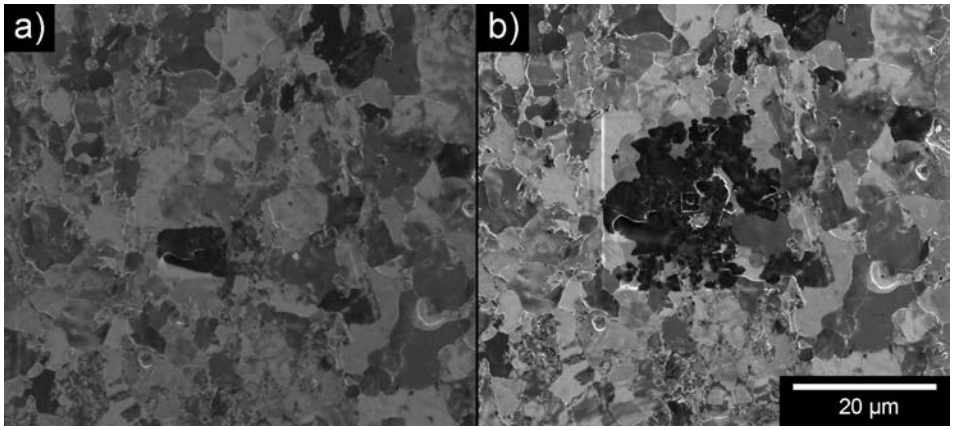

Figure B.1: FIB SE images of CCT sample D11, which was chemically etched with 2 % Nital and then ion etched with Ga^+ ions.

imaging. The surface was bombarded with Ga^+ ions before this image was collected using SE; therefore, the white box in Figure B.1 corresponds to the area on the sample surface that interacted with the ion beam prior to imaging with SE.

The initial ion images looked promising, so more images were taken with the FIB-SEM specifically to experiment with ion imaging on unetched samples. Theoretically, a sample does not need to be chemically etched, since the ion etching reveals differences in grain orientations and, hence, shows the microstructural features of interest. Figure B.2 shows micrographs obtained from the CCT sample D11 (the same sample as shown in Figure B.1) that was introduced as an unetched sample, physically etched with Ga^+ ions and then imaged with the SE generated from ion bombardment. The sample was not chemically etched with 2 % Nital as was the case in Figure B.1.

The micrographs in Figure B.2 are fuzzy and difficult to interpret, although there is a noticeable difference in contrast between individual grains that could be associated with a change in orientation. The features are much finer in Figure B.2 than Figure B.1 (which were taken from a sample that was chemically etched and ion

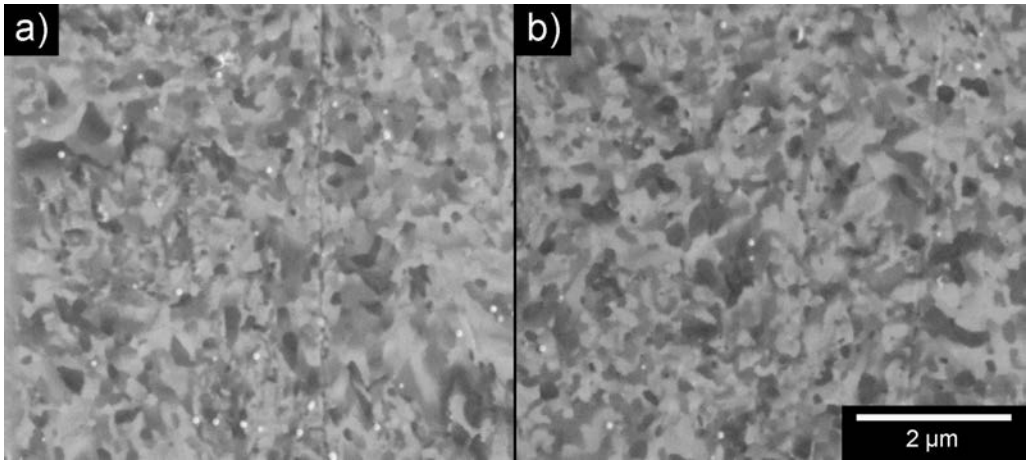

Figure B.2: FIB SE images of CCT sample D11, which was ion etched with Ga^+ ions

etched). One possible explanation is that the ion channeling is capable of imaging smaller features, like sub-grains. The small white dots in Figure B.2 are most likely small silicon carbide particles resulting from the grinding and/or polishing procedure during sample preparation. Regardless, the images were difficult to interpret and unreliable. Since ion etching was not a viable technique for imaging, the study was not pursued further.

B.2 Color Metallography Experiments

The ITT specimens were prepared according to Section 3.1.2, etched with 2 % Nital and subsequently imaged using the optical microscope described in Section 3.2. As previously mentioned, color metallography was performed in order to aid microstructure quantification. Color metallography involves using a modified version of LePerra's etch (described in Section 4.1.2) to preferentially color grains based on their structure; more specifically, bainite grains should appear black, ferrite is tinted a tan color and M-A is white. This etch was very difficult to perform correctly.

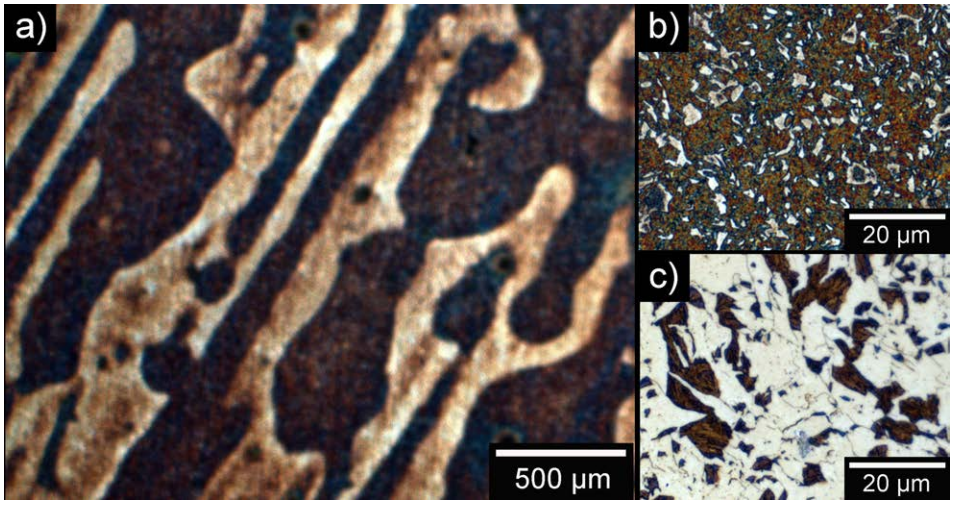

Figure B.3: Typical attempt of color metallography (sample 1): a) low magnification image; b) high magnification images of the red and white bands observed in a)

Numerous attempts were made over a period of several months with little success. Figure B.3 shows a typical optical micrograph after etching with modified LePerra's etch. A low magnification image is shown in Figure B.3a and higher magnification images, from the red and white bands, are shown in Figure B.3b and B.3c, respectively. The microstructures in Figure B.3b and Figure B.3c are extremely different even though they were taken from neighboring regions. The grains in Figure B.3b are relatively small and dark in color. The grains in Figure B.3c are large, jagged and predominantly white. These two micrographs were obtained from neighboring regions but show completely different microstructures. As a result, neither image can be considered representative and the experiment was not successful for this sample.

Figure B.4 shows another unsuccessful attempt at color metallography. Instead of the expected black, tan and white grains, Figure B.4a shows blue, green, black and orange regions. Similarly, Figure B.4b displays red, orange and blue regions. These two micrographs were taken from the same sample that was re-polished and

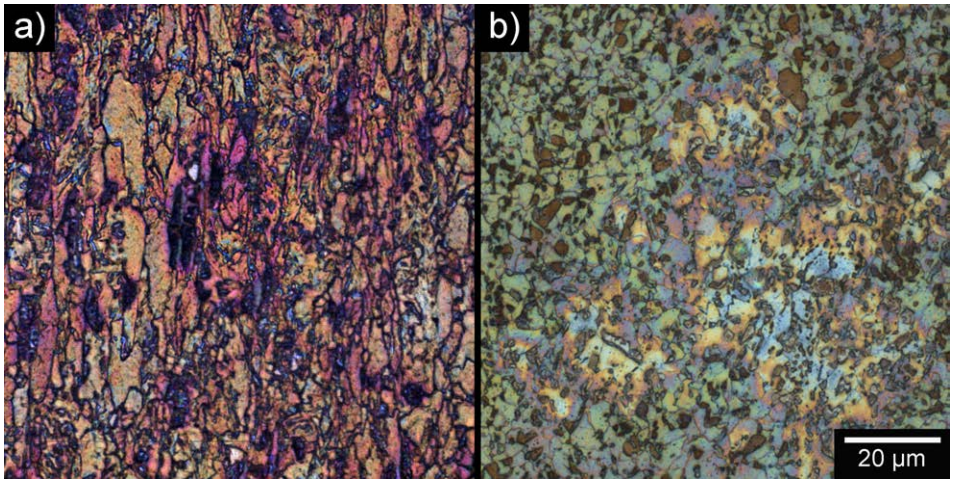

Figure B.4: Color metallography failure (sample 6): a) optical micrograph after one attempt with LePerra's etch; b) representative micrograph from a repeated etching procedure

re-etched. The variability in results with color metallography proved to be very frustrating and challenging.

After several fruitless attempts at color metallography, one successful color etch was performed and is shown in Figure B.5. The sample was polished and etched in the exact same manner as the previous samples, but the technique was successful during this experiment. These images were taken from the same sample in various regions across the sample surface. The black, tan and white grains are clearly distinguishable and the grain sizes are more realistic and consistent between micrographs. This particular image required several iterations of polishing and etching and was not reproducible.

The phase fractions from the successful color metallography experiment shown in Figure B.5 were compared with the phase quantification results using the SEM and TEM method for the same sample (ITT trial 6). The comparison is shown in Table B.1. The color metallography reveal that the structure is dominated by

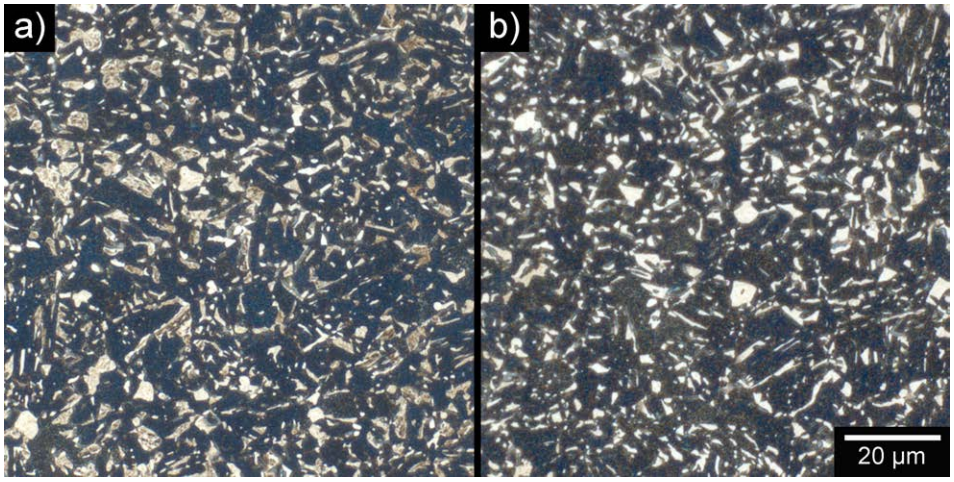

Figure B.5: Successful color metallography experiment for ITT sample 6. The white, black and tan grains are clearly distinguishable.

Table B.1: Phase fraction comparison between color metallography and the joint SEM/TEM method for ITT sample 6.

Method	Ferrite (%)	Bainitic Ferrite/Martensite (%)	M-A (%)	Bainite (%)
Color Metallography	18.1	-	11.5	70.4
SEM/TEM	67.5	32.1	0.4	-

dark-tinted phase (bainite), which is not consistent with the SEM/TEM results. A possible explanation is that the LePerra's etch preferentially tints bainite grains, whereas the SEM/TEM analysis showed the grains to be bainitic ferrite.

Due to the significant amount of difficulty in successfully performing the LePera etch, color metallography was not pursued further. Color metallography was attempted for several months before one sample yielded positive results which were only obtained once and were unfortunately not reproducible. Several ITT samples were repeatedly polished, etched and imaged - Figures B.3 to B.5 only illustrate the typical failed experiment results and the one successful experiment. Due to the

incredible time investment with little success, color metallography was abandoned as a feasible and viable technique for phase quantification.

This page was intentionally left blank

Appendix C

Nanoindentation Experiments

As mentioned in Section 4.5.1, nanoindentation tests were performed on ITT sample 1 in an attempt to determine the relative hardness of a martensite/bainitic ferrite grain relative to the surrounding ferrite matrix. Three separate nanoindentation experiments were performed and will be discussed in this section. The experimental conditions were chosen based on the requirement that the indent depth be approximately 100 nm. Based on some preliminary trials varying the indentor load on the sample surface, the first experiment used an indentor load of 2000 μN, which did not sufficiently indent the sample surface. The second and third experiments used an indentor load of 4000 μN. Although this indentor load was sufficient, only one indent in the second experiment successfully hit the region of interest. The final experiment was successful in indenting the region of interest and the surrounding grains; however, the results were scattered. A possible reason for the experimental error is related to the sample surface roughness: the surface roughness was determined using AFM to be approximately 130 nm. As a result, the average indent depth was very similar to the surface roughness; therefore, the results are inconclusive.

The first attempt at nanoindentation was performed on a grain that was selected

because of its preliminary classification as martensite according to the results from TEM analysis on similar-looking grains. More specifically, the grain of interest shown in Figure C.1b is similar to the region shown in Figure 4.28e which was confirmed to be martensite through TEM analysis. Once the appropriate grain was located in the FIB-SEM instrument, three lines were milled into the sample surface that branched out from the grain of interest (i.e., the grain was at the center of the three lines which served to 'point' in the direction of the specified region). A large box (100 μm by 100 μm) was milled around the lines to act as a guide for visual inspection. The box was milled so that the grain of interest was located in the direct center of the box. Figure C.1a shows the box and three indicator lines pointing to the grain of interest, which is magnified in Figure C.1b. The micrograph in Figure C.1a was taken at an oblique angle; therefore, the box does not look like it is square but in fact it was milled from the FIB at a perfect vertical orientation. The dark regions in Figure C.1 are surface contamination due to improper sample cleaning or local corrosion from the etching procedure; these regions do not affect the nanoindentation experiment and therefore are irrelevant artifacts.

Since the magnification limit in the Hysteron Triboindenter machine was 100 x, the box acted as the macro-scale indicator of the grain's location within the sample microstructure. Once the box was located and the position of the instrument was calibrated to coincide with the exact center of the box, the experimental conditions for the nanoindention experiment were set and the test was performed. A maximum load of 2000 μN was chosen to apply an indent that would penetrate the sample surface to a depth of approximately 100 μm. 30 individual indents were programmed to penetrate the sample surface at 2 μm intervals, thereby covering a 60 μm wide region that would hopefully contain the grain of interest as well as a significant portion of surrounding ferrite matrix to provide a direct observation of the varying

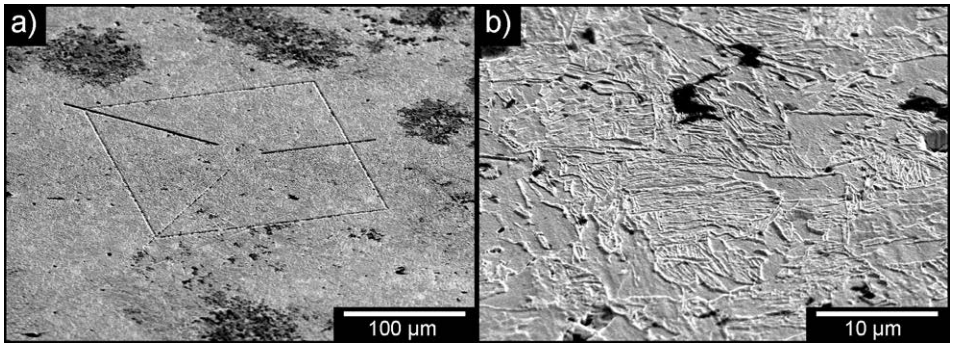

Figure C.1: First attempt at nanoindentation: a) low magnification SEM SE image showing the 100 μm by 100 μm box outlining the three indication lines pointing to the grain of interest located at the center (image taken prior to the nanoindentation experiment); b) high magnification image of the grain of interest that was subjected to nanoindentation.

hardness across the constituents.

The first attempt at nanoindentation was not successful as the indenter load was insufficient to indent the sample surface. Figure C.1 shows the grain of interest that was subjected to nanoindentation both before (Figure C.1a) and after (Figure C.1b) indentation. Figure C.1a is a lower magnification image that illustrates the region of interest enclosed in a milled box, whereas Figure C.1b is a higher magnification image showing the grain of interest that was subjected to nanoindentation. No indents were visible in Figure C.1b and, as a result, the indentation measurements were irrelevant and the process had to be repeated.

The second attempt at nanoindentation was much more successful. A higher peak load of 4000 μN was chosen and fifty indents were taken at a separation of 2 μm. Figure C.2a is a low magnification SEM SE image of the grain of interest surrounded by two larger 'indicator' boxes, with a high magnification image of the grain shown in Figure C.2b.

Figure C.3 shows the results from the nanoindentation experiment. The fifty indents that were taken across the sample surface are faintly distinguishable in the

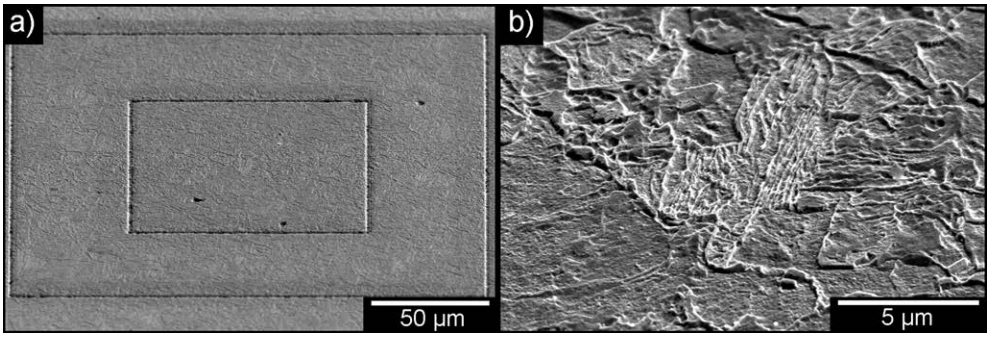

Figure C.2: Second attempt at nanoindentation: a) low magnification SEM SE image showing the two boxes marking the region of interest at the center of the boxes; b) high magnification image of the grain of interest that was subjected to nanoindentation.

SEM SE image as the white horizontal lines. The indents are labeled with numerical values to show the position of each indent relative to the grain of interest (which is located directly between points 20 and 30 in Figure C.3 and is circled in red). Figure C.3 shows the correct location of each indent from the initial indent (point 1) to the final indent (point 50); however, the individual indents are difficult to see clearly in Figure C.3 due to the large area that was covered in the experiment. The images were re-configured in Figure C.4 to better display the individual indents as they appeared across the sample surface. Although the overall picture and 'snapshot' of the microstructure were compromised in Figure C.4, each indent is more clearly distinguishable and, as such, each indent was correlated with the microconstituent that it indented. Unfortunately, only one indent (number 25, circled in red) successfully hit the grain of interest that was shown in Figure C.2b. The remaining 49 indents measured the hardness values for the surrounding ferrite grains or grain boundaries, as previously mentioned.

The hardness results from the nanoindentation experiment are shown in Table C.1. The experimental hardness values were recorded in GPa and subsequently

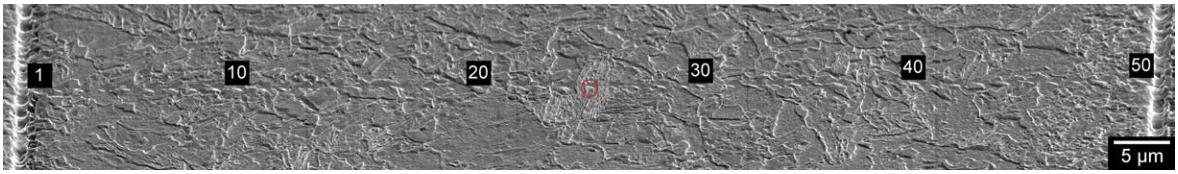

Figure C.3: SEM SE image of the post-indentation sample surface after the second attempt at nanoindentation (the numerical labels represent the indent number across the sample surface). The indent that successfully hit the grain of interest is circled in red.

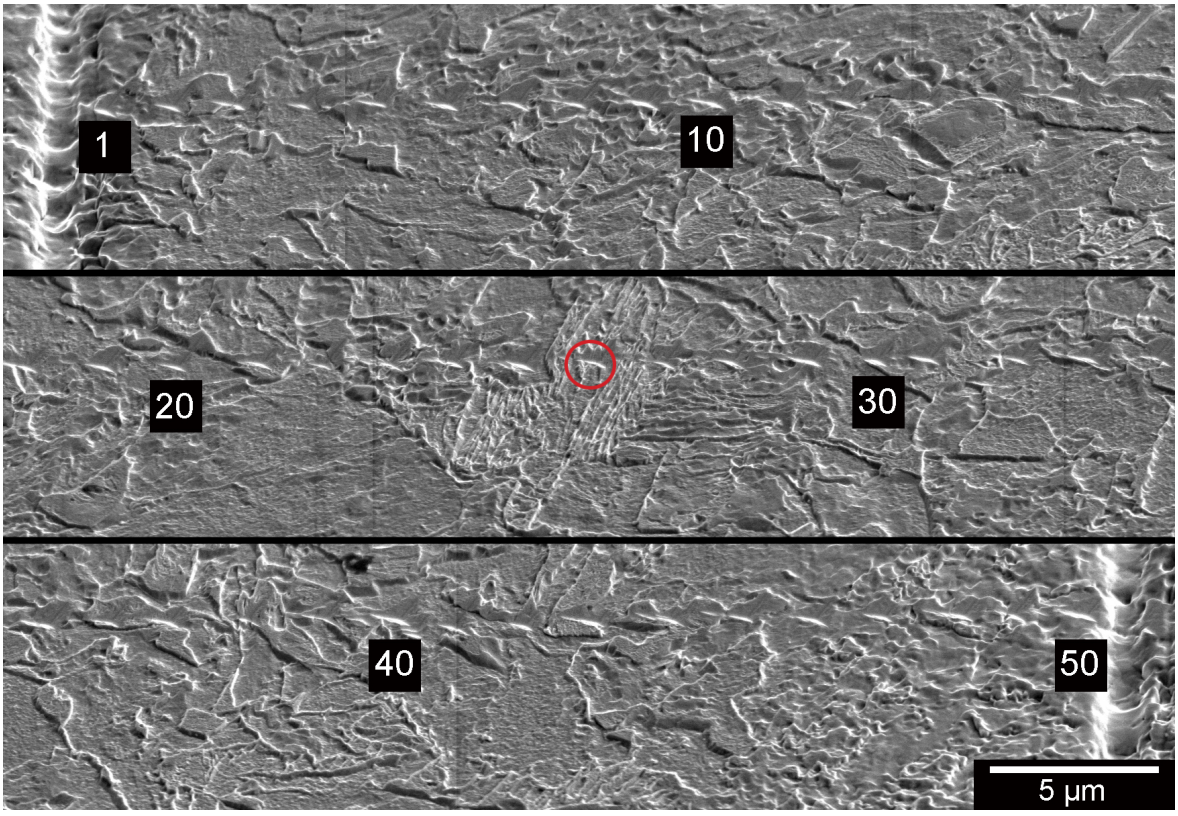

Figure C.4: Re-formatted view of the nanoindentation results presented in Figure C.3. The indent that successfully hit the grain of interest is circled in red.

converted to HV; more specifically, 1 MPa is equivalent to 9.807 HV [Yovanovich 06]. Indent 1 has the lowest hardness value, whereas indent 11 has the highest value. The hardness values are very high for this material and do not make sense.

As previously mentioned, only one indent successfully hit the bainitic ferrite/martensite grain; the expectation of this experiment was that the indents would hit the grain of interest in multiple locations and, thus, provide a range of data values that could be considered representative hardness measurements for a martensite grain. This unfortunately did not occur as only one value was correctly attributed to the martensite grain. Furthermore, the nanoindentation results from the surrounding material had significant variability. More specifically, indents that were performed on the surrounding material occasionally had higher hardness values than the grain that was tentatively labeled as martensite. Interestingly, the region with the highest hardness for the entire test (indent 11) corresponds to a rough surface that could be labeled as ferrite since no clear or definite laths are observed where the indent penetrated the surface. A few indents indented grain boundaries (numbers 13, 33, 36 and 43) rather than the grain interiors. The hardness values for the 'grain boundary indents' range from 349 HV to 842 HV, so these values cannot be considered reliable as there is significant scatter in the data. Considering the variability in the results, no direct comparison could be made between the hardness of the martensite grain and the surrounding material.

Figure C.5 displays the results from the nanoindentation experiments as hardness (HV) as a function of indentation number. The results can be directly compared with Figure C.4 which shows the indents more clearly than Figure C.3. There is no distinct trend in the data. As a result, a third experiment was performed to test the viability of nanoindentation to determine the hardness of a baintic ferrite/martensite grain relative to a ferrite grain.

Table C.1: Hardness results from the second nanoindentation experiment (indent numbers correspond to the labels in Figure C.3).

Indent	Hardness (GPa)	Hardness (HV)	Indent	Hardness (GPa)	Hardness (HV)
1	0.7	17	26	6.20	632
2	2.35	240	27	2.21	225
3	7.06	720	28	4.83	493
4	2.37	242	29	6.40	653
5	6.03	615	30	4.85	495
6	4.21	429	31	6.71	684
7	4.11	419	32	8.83	900
8	3.96	404	33	5.58	569
9	4.69	478	34	7.63	778
10	3.72	379	35	4.50	459
11	11.45	1168	36	8.26	842
12	3.11	317	37	6.78	691
13	4.03	411	38	5.72	583
14	6.70	683	39	2.90	296
15	3.07	313	40	4.08	416
16	6.34	647	41	3.90	398
17	3.16	322	42	3.51	358
18	3.38	345	43	3.42	349
19	4.91	501	44	4.75	484
20	7.23	737	45	7.84	799
21	3.45	352	46	3.35	342
22	4.47	456	47	6.88	702
23	3.66	373	48	4.82	492
24	5.27	537	49	8.60	877
25	6.00	612	50	4.41	450

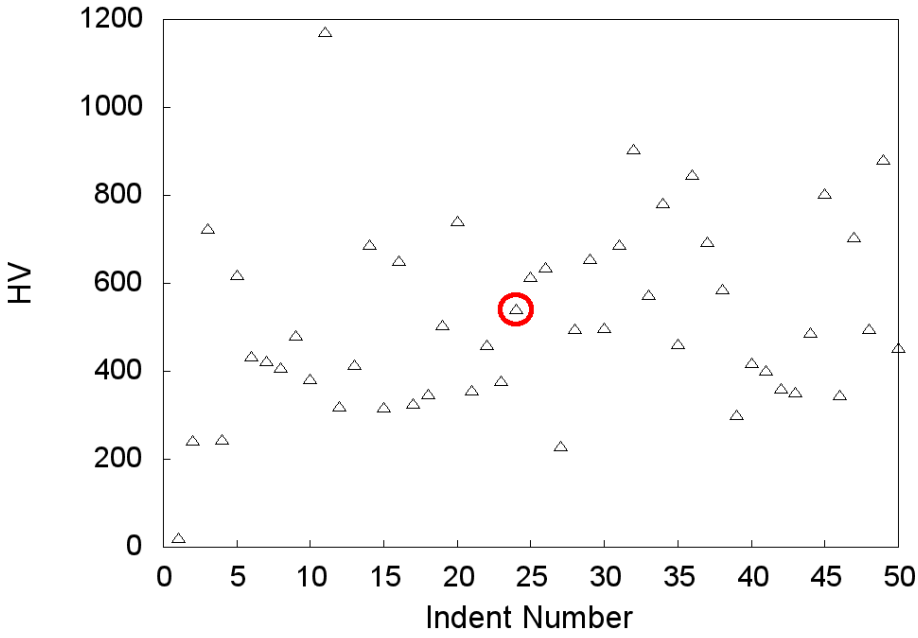

Figure C.5: Graphical interpretation of the nanoindentation results listed in Table C.1. The hardness values correspond to the indent numbers shown in Figure C.3.

The third nanoindentation experiment involved indenting the surface in two opposite diagonal directions, forming an 'x' pattern rather than a linear horizontal pattern. The same grain as shown in Figure C.2b was tested with the intent that the diagonal criss-cross pattern would be centered on the grain of interest. The post-indentation SEM SE micrographs are shown in Figure C.6. The same peak load of 4000 μN was used for 19 individual indents that were programmed to penetrate the sample surface at intervals of 2 μm (10 indents on one diagonal and 9 indents on the other). Figure C.6a shows a low magnification SEM SE micrograph of the sample surface. The indication box that was used as a visual guide to locate the region of interest within the overall microstructure is clearly visible in Figure C.6, as are the indents from both the second and third nanoindentation experiments. The horizontal line of indents observed in Figure C.6a are the result of the second nanoindentation experiment and are indicated in Figure C.6a by the white box. The indents from the third nanoindentation test are distinguished in Figure C.6a with the black box and are shown at a higher magnification in Figure C.6b. Points 1 through 19 in Figure C.6b correspond to the indent number.

The results of the third nanoindentation experiment are tabulated in Table C.2. The indent numbers correspond to the number labels in Figure C.6b and, as a result, a direct comparison of hardness and microstructure can be made. Indent 1 had the highest hardness value; in fact, this value is so extreme that it can be considered erroneous data and will not be included in the analysis. The size of indent 1 is comparable with the other indents; therefore, the high hardness cannot be attributed to a different indent size.

Indents 7 through 10 successfully indented the grain of interest shown in Figure C.6b. The remaining indents indented the neighboring ferrite grain as intended. The results shown in Table C.2 can be compared directly with Figure C.6b. The

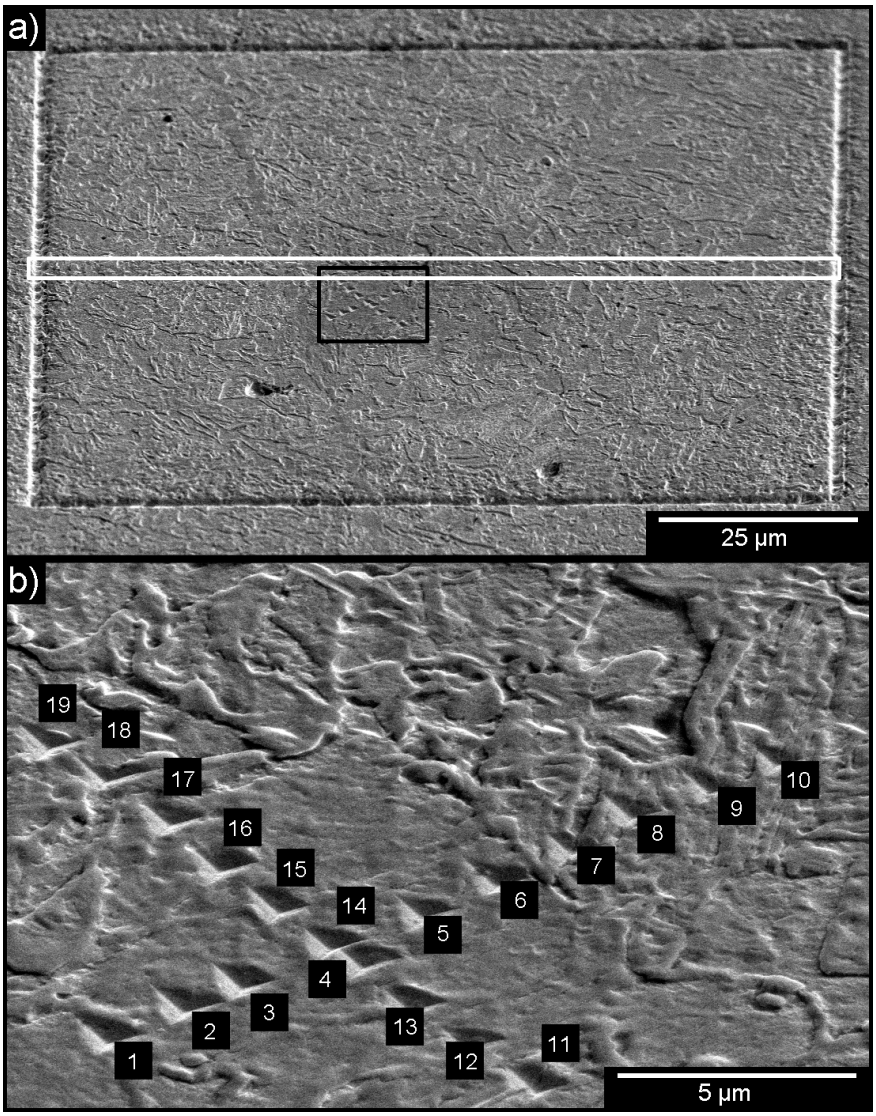

Figure C.6: Third and final attempt at nanoindentation: a) SEM SE image of the post-indentation sample surface at low magnification to show the position of the grain and indents relative to the overall box; b) high magnification image showing the position of the individual indents in the microstructure (the numerical labels represent the indent number across the sample surface).

Table C.2: Hardness results from the second nanoindentation experiment (indent numbers correspond to the labels in Figure C.6.

Indent	Hardness (GPa)	Hardness (HV)	Indent	Hardness (GPa)	Hardness (HV)
1	13.21	1347	11	3.80	387
2	6.68	681	12	4.35	444
3	6.05	617	13	4.39	448
4	4.96	506	14	3.53	360
5	5.55	566	15	4.66	475
6	5.46	557	16	3.81	388
7	5.80	591	17	3.98	406
8	4.06	414	18	4.04	412
9	4.77	486	19	4.04	412
10	5.48	559	-	-	-

hardness values for the ferrite grain (all indents except for 7-10 in Table C.2) ranged from 360 HV to 681 HV (excluding indent 1 as this value is significantly higher than all the other data points). Indents 4 and 14 may not be accurate as the indents are almost overlapping. The average ferrite hardness value was calculated to be 474 ± 49 HV, and the average hardness for the grain of interest was 513 ± 39 HV. This experiment was successful in terms of correctly indenting the grain of interest and a neighboring ferrite grain; however, no distinction could be made between the hardness for the ferrite grain and that of the grain of interest since the values were very similar (within standard deviation of each other). As a result, nanoindentation experiments were not pursued further as the experimental data could not identify a significant difference in hardness between the various constituents.

Three nanoindentation experiments were conducted with very little success. There was no evident correlation between the hardness and the indented microstructure, as the data was very scattered and misleading. As mentioned, the indents that resulted in the highest hardness values were occasionally associated with ferrite grains rather than the expected bainitic ferrite/martensite grain. Since the data

was not reproducible nor trustworthy, the nanoindentation tests were stopped and the results were not used to conclusively identify the relative hardness of a bainitic ferrite/martensite grain.

Appendix D

SEM SE Micrographs for CCT Curve Samples

As mentioned in Section 3.4.2, ten different micrographs were collected from each CCT specimen. One representative image from each sample was shown in Figure 3.30, and the other nine micrographs were combined into a single compilation image for each sample, as shown in Figures D.1 to D.9. The dark regions correspond to ferrite and the white regions are bainitic ferrite/martensite or M-A. The SEM SE micrographs were obtained using the Philips XL Series DX4-i XL-30 microscope at the Research facility at EVRAZ Inc. NA, as detailed in Section 3.2.

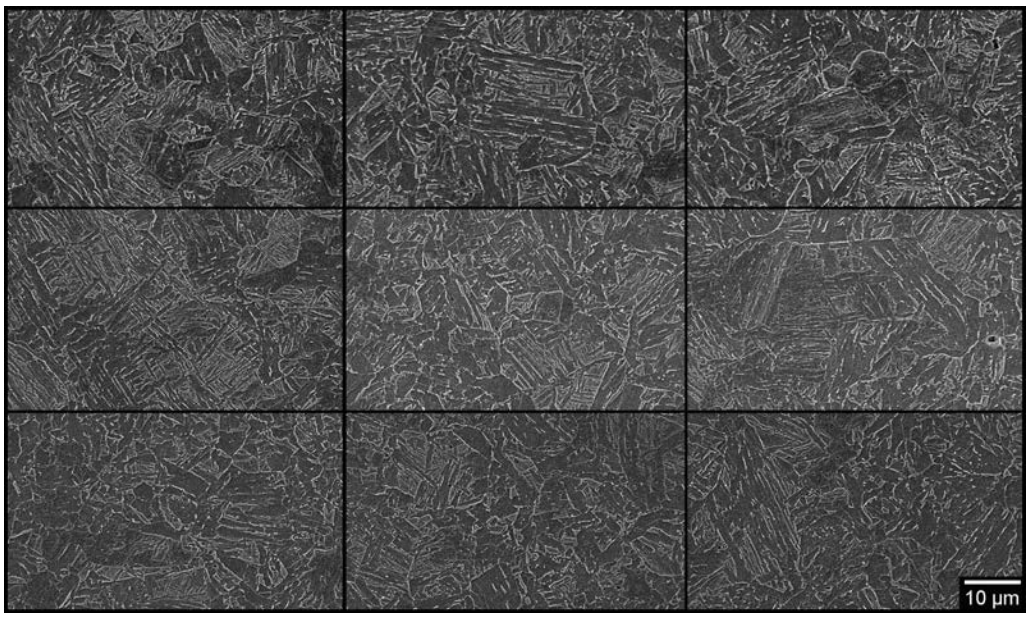

Figure D.1: Nine representative SEM SE micrographs for CCT sample D3 (50 °C/s).

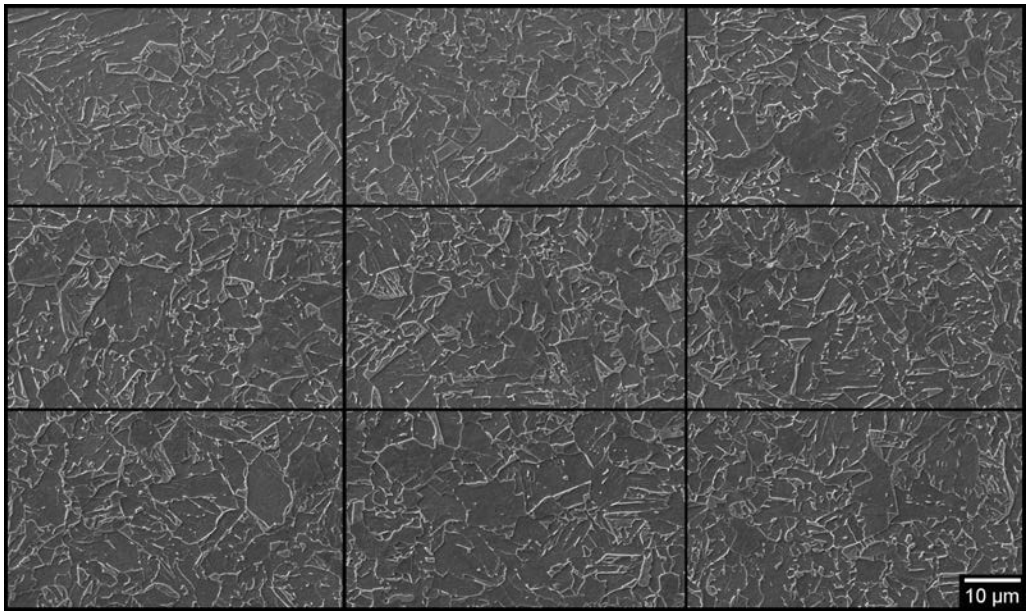

Figure D.2: Nine representative SEM SE micrographs for CCT sample D4 (20 °C/s).

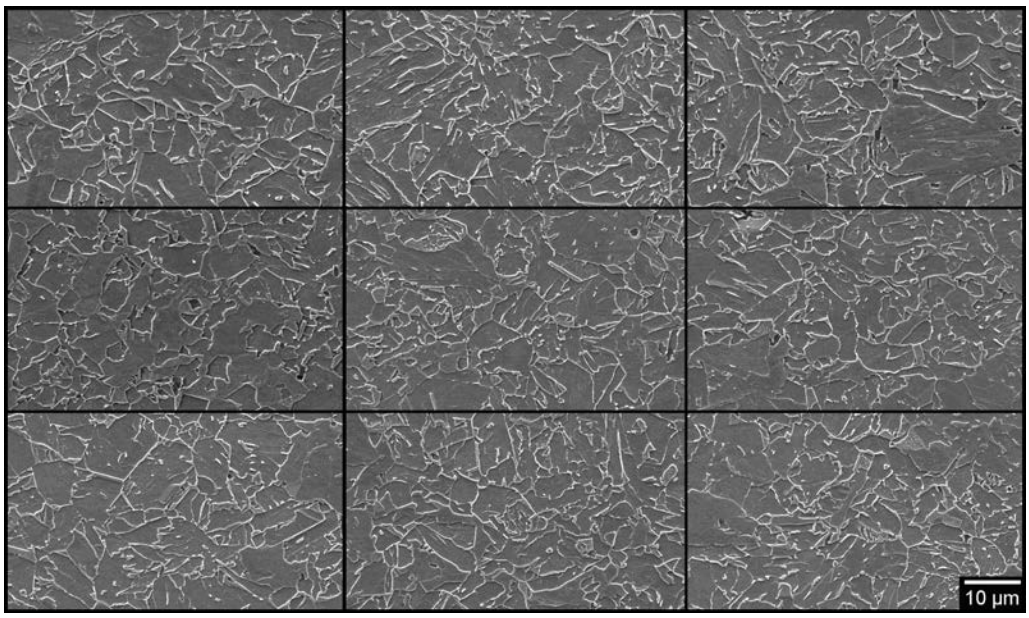

Figure D.3: Nine representative SEM SE micrographs for CCT sample D6 (10 °C/s).

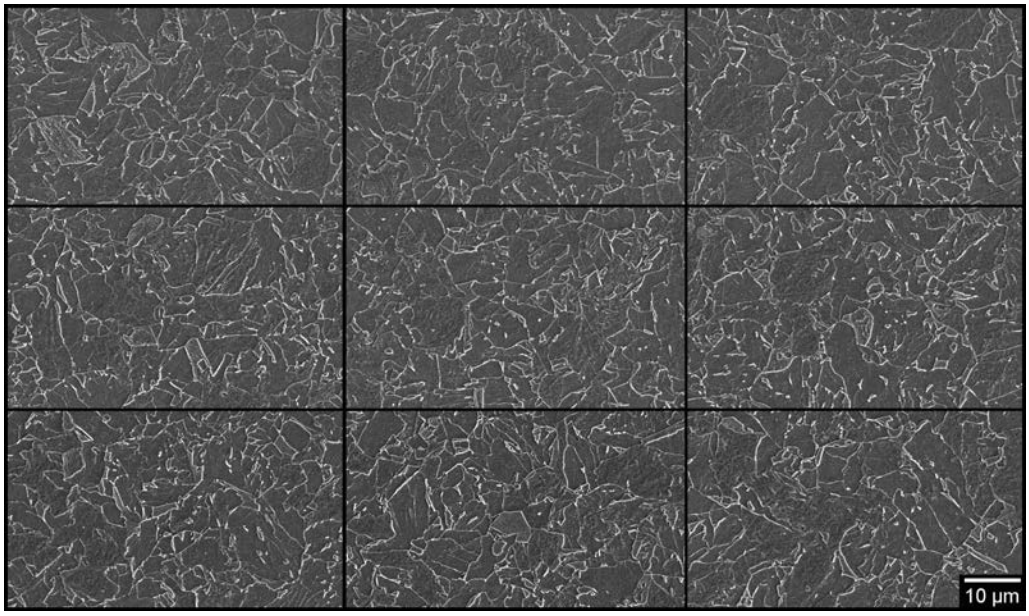

Figure D.4: Nine representative SEM SE micrographs for CCT sample D7 (7 °C/s).

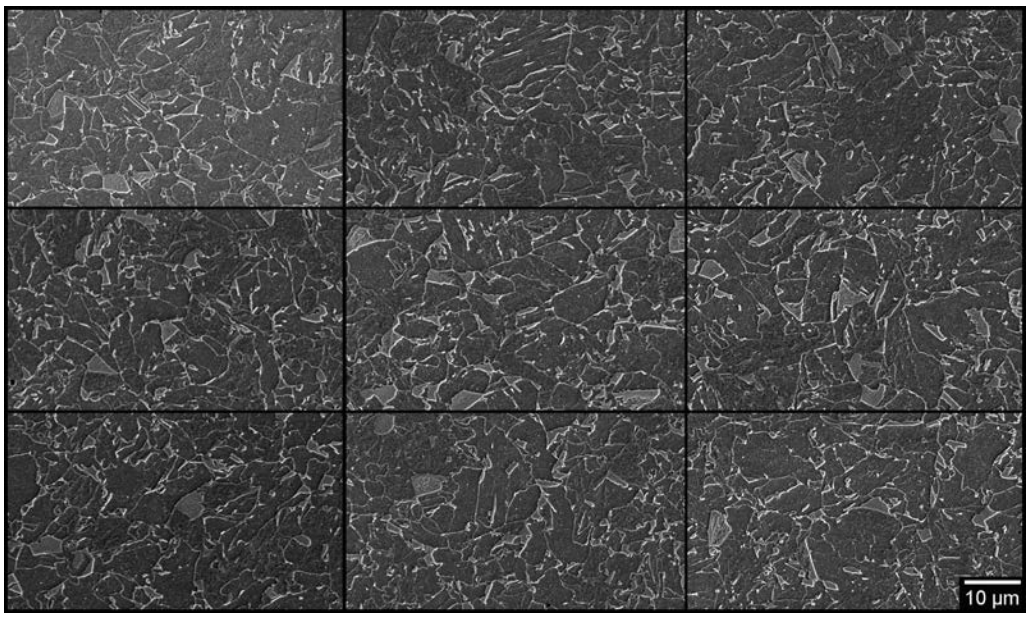

Figure D.5: Nine representative SEM SE micrographs for CCT sample D8 (5 °C/s).

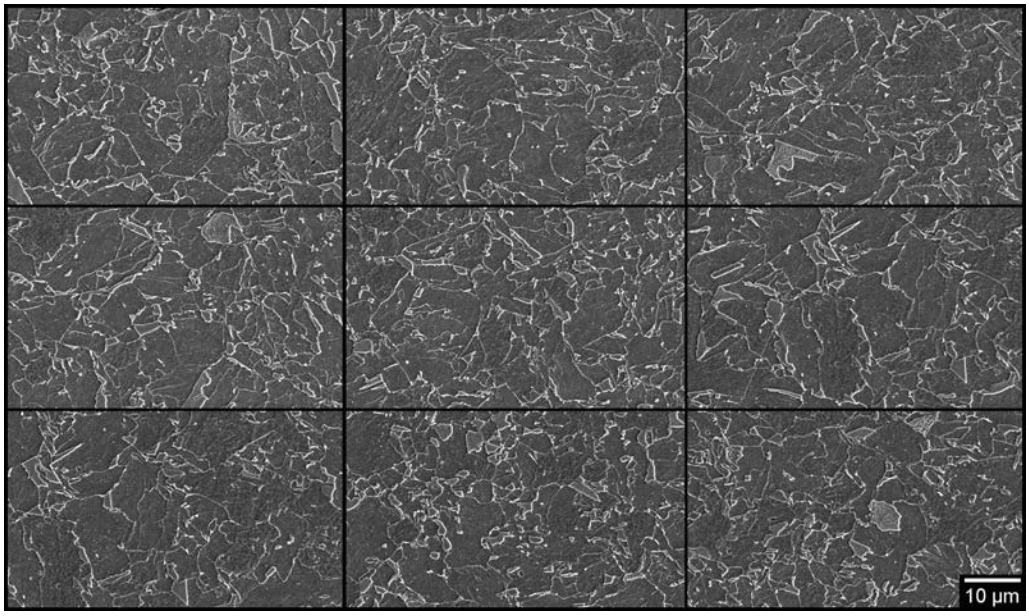

Figure D.6: Nine representative SEM SE micrographs for CCT sample D9 (3 °C/s).

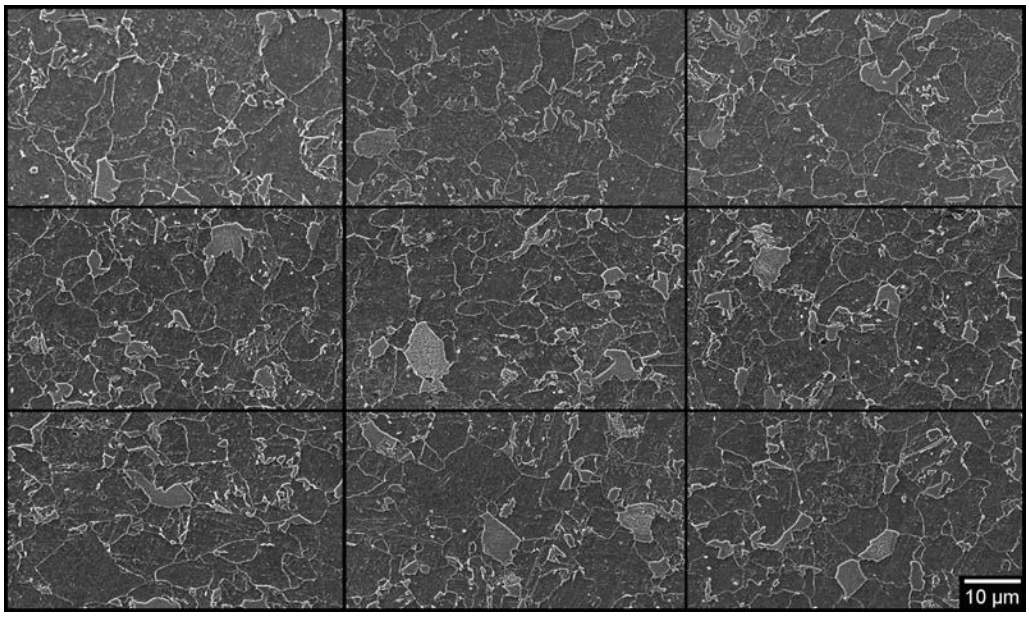

Figure D.7: Nine representative SEM SE micrographs for CCT sample D12 (1 °C/s).

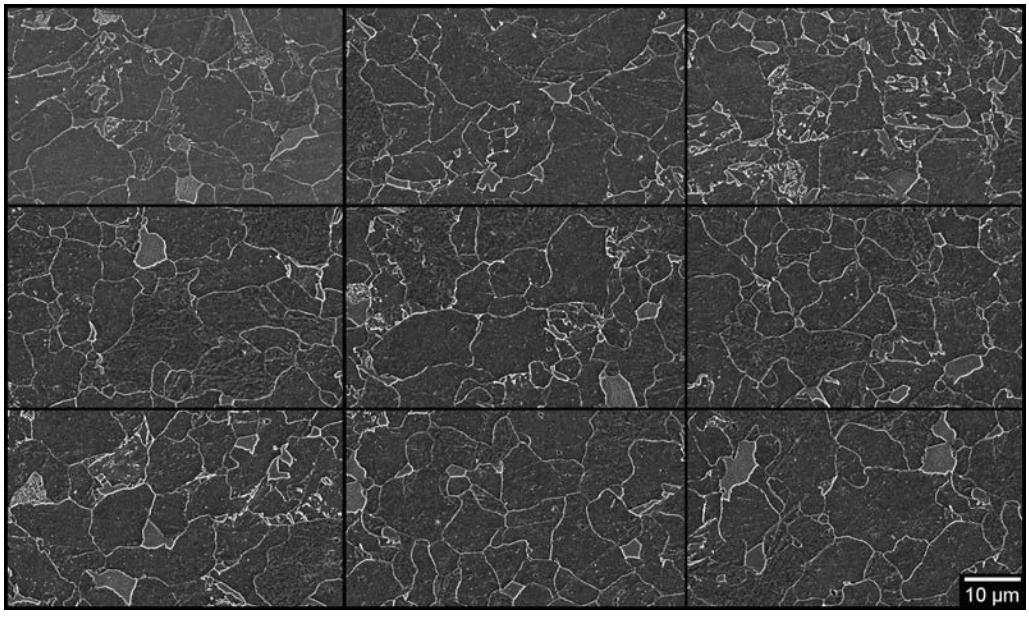

Figure D.8: Nine representative SEM SE micrographs for CCT sample D10 (0.5 °C/s).

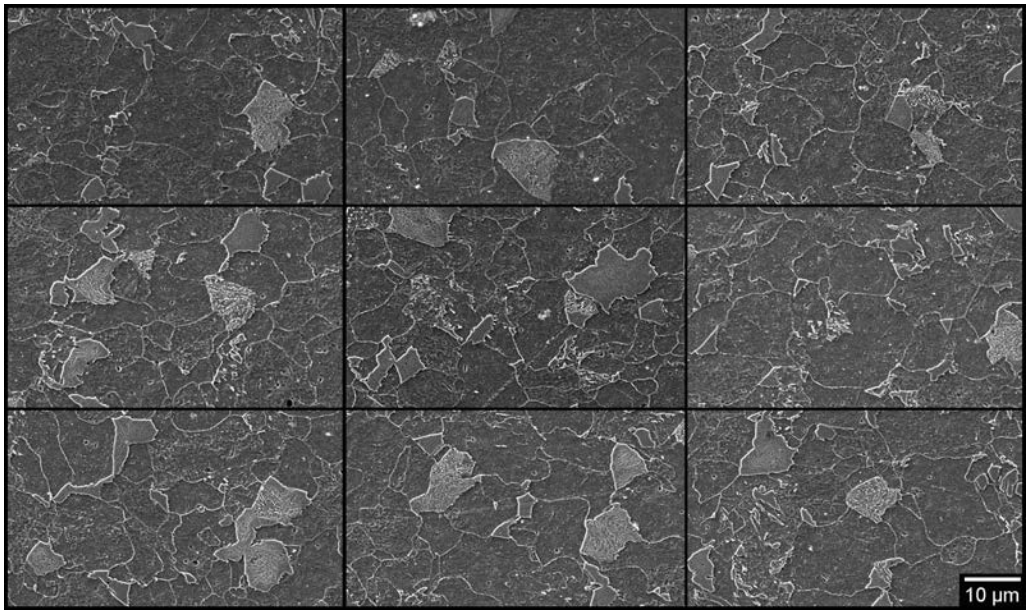

Figure D.9: Nine representative SEM SE micrographs for CCT sample D11 (0.3 °C/s).

Appendix E

SEM SE Micrographs for ITT Trial Samples

The strip samples that were subjected to the ITT schedule detailed in Table /reftable:ITT sample ID were imaged with the Philips XL Series DX4-i XL-30 microscope as detailed in Section 4.1.3. Figures E.1 to E.9 show SEM SE micrographs for the nine ITT trials that were conducted on the strip samples. As for Section 4.4.1, the dark regions correspond to ferrite and the white regions are bainitic ferrite/martensite or M-A. Similar to the CCT curve specimens, the SEM SE micrographs were obtained using the Philips XL Series DX4-i XL-30 microscope at the Research facility at EVRAZ Inc. NA, detailed in Section 3.2.

The SEM SE images were used to calculate the phase fraction of each constituent, which will be discussed in the next section.

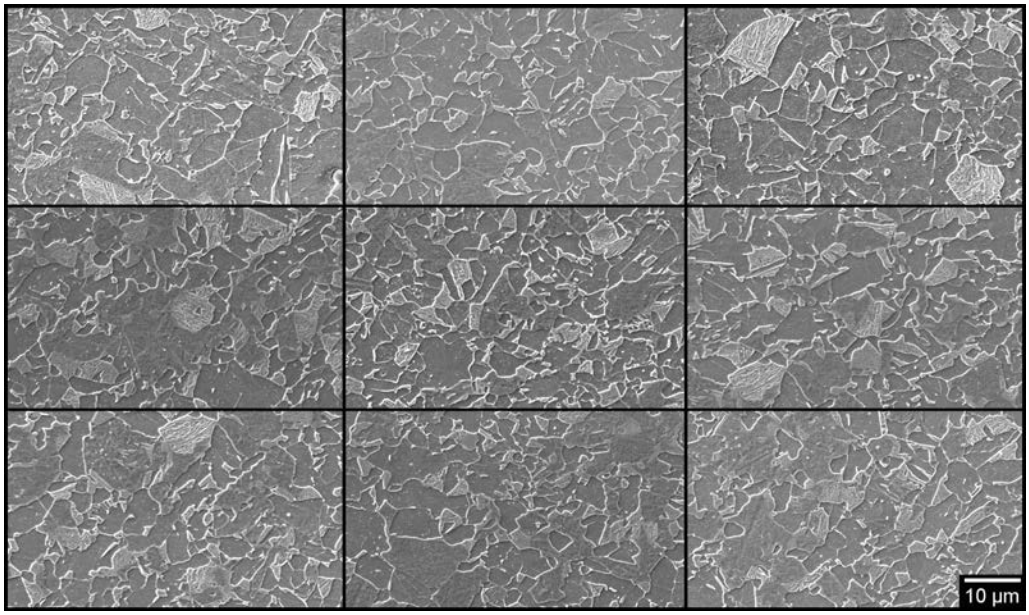

Figure E.1: Nine representative SEM SE micrographs for ITT sample 1.

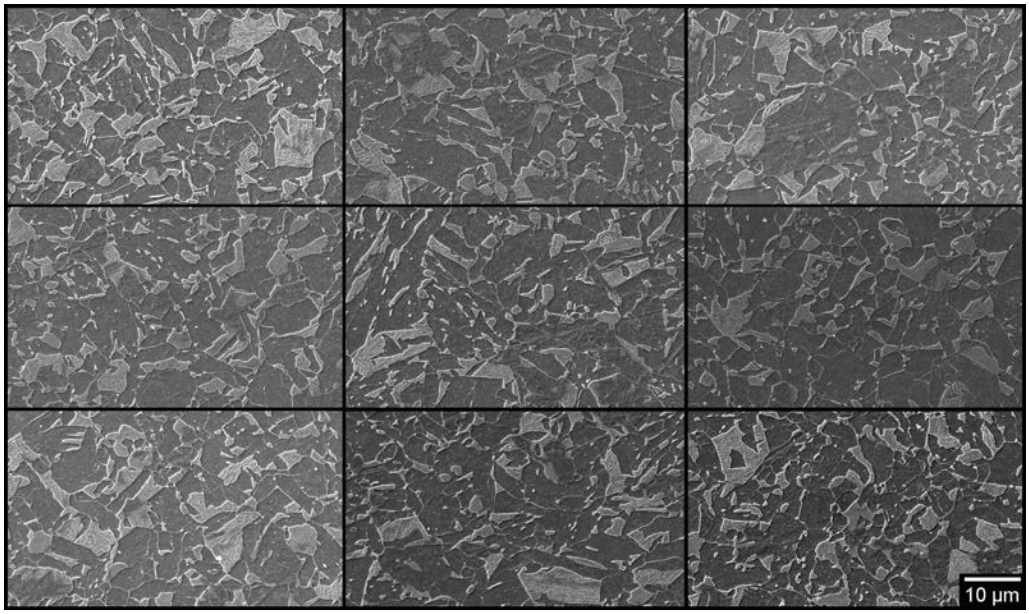

Figure E.2: Nine representative SEM SE micrographs for ITT sample 2.

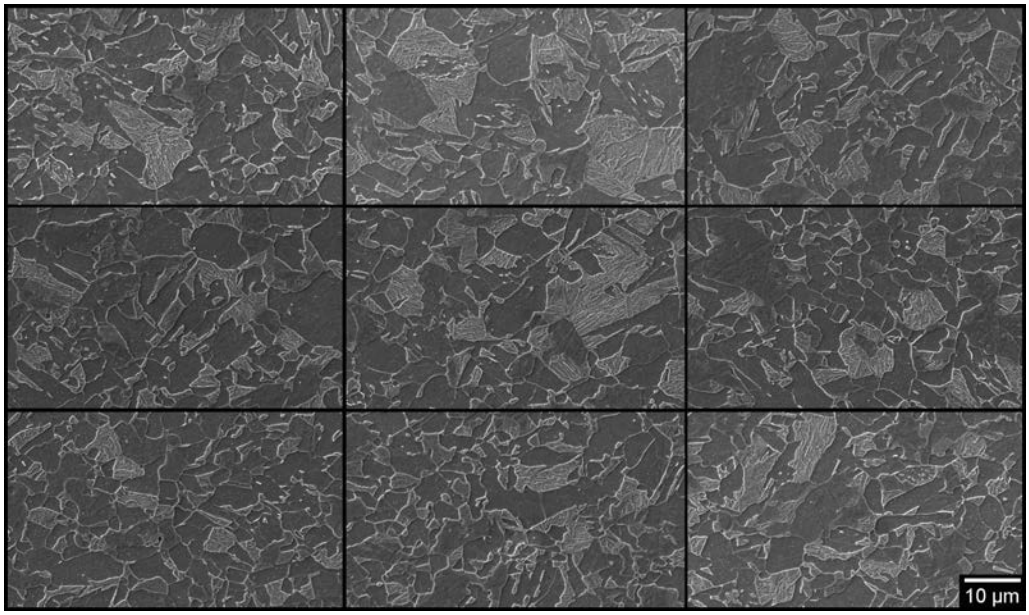

Figure E.3: Nine representative SEM SE micrographs for ITT sample 3.

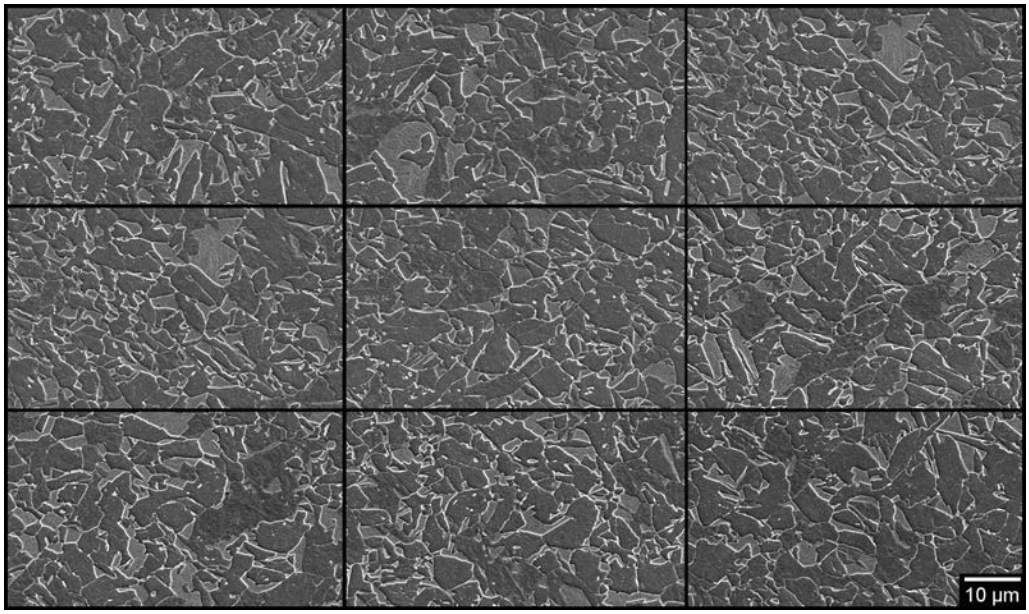

Figure E.4: Nine representative SEM SE micrographs for ITT sample 4.

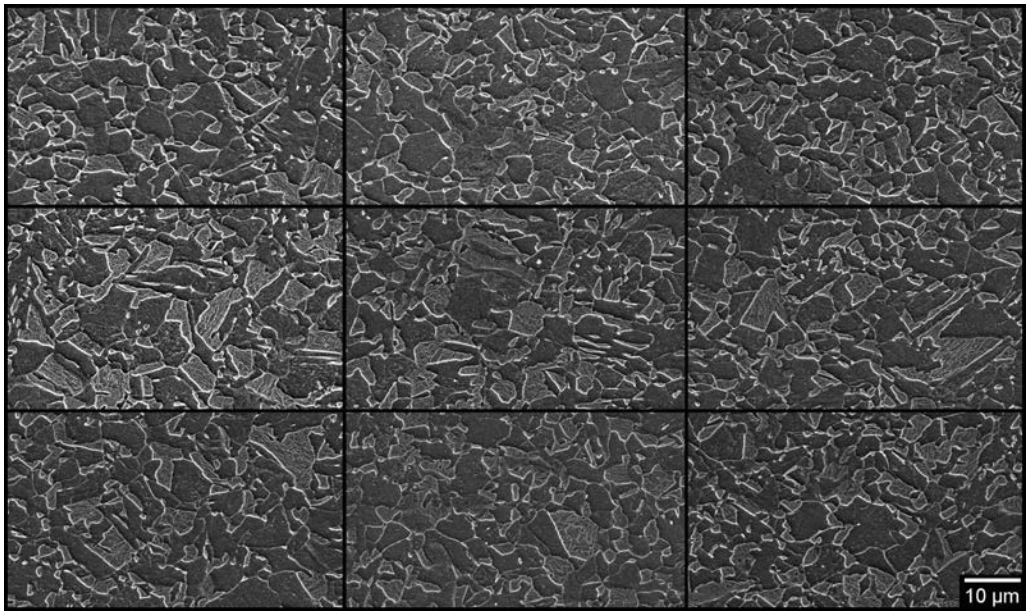

Figure E.5: Nine representative SEM SE micrographs for ITT sample 5.

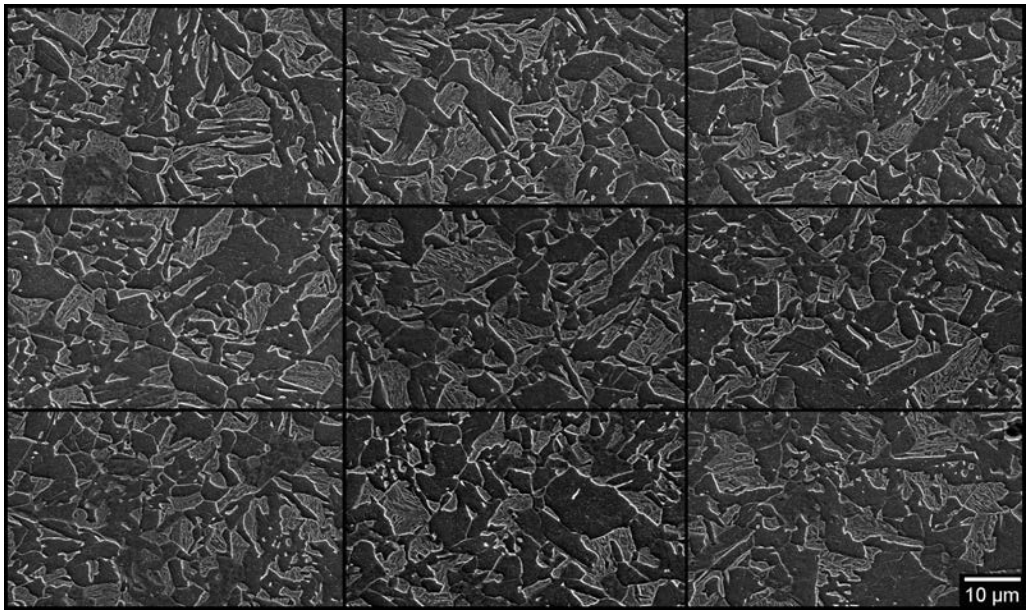

Figure E.6: Nine representative SEM SE micrographs for ITT sample 6.

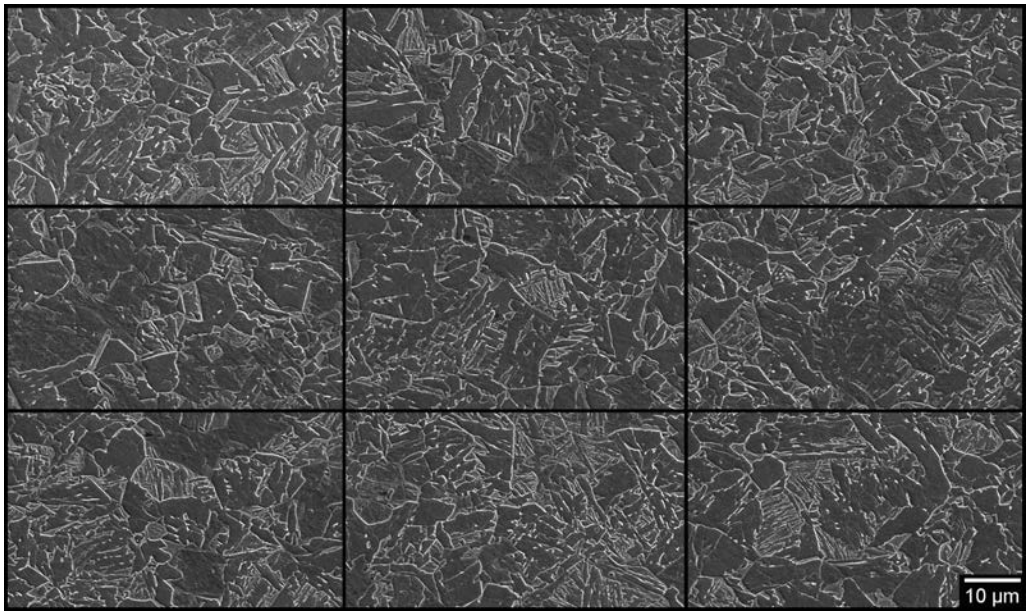

Figure E.7: Nine representative SEM SE micrographs for ITT sample 7.

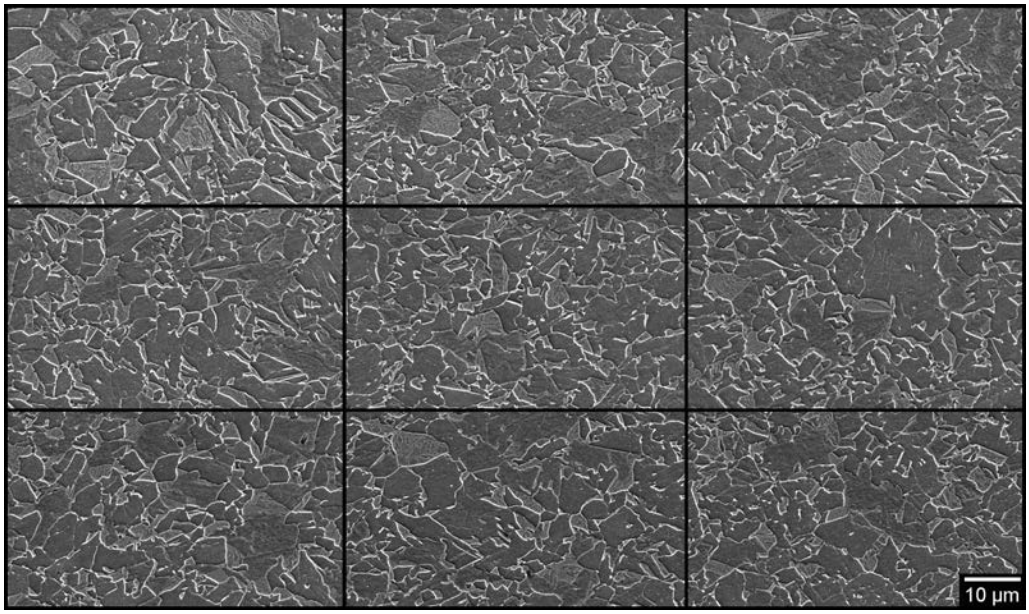

Figure E.8: Nine representative SEM SE micrographs for ITT sample 8.

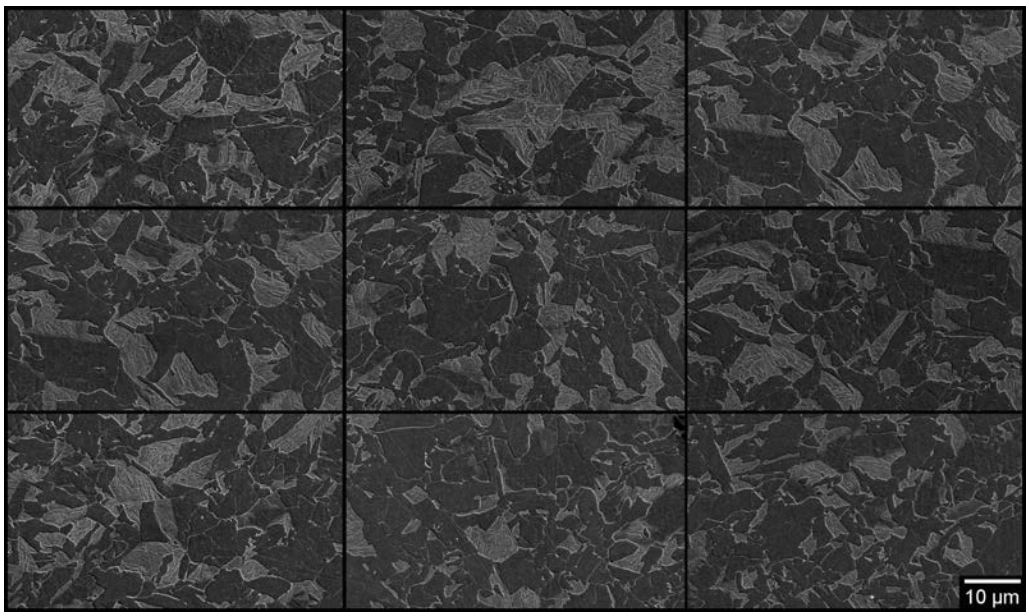

Figure E.9: Nine representative SEM SE micrographs for ITT sample 9.

Appendix F

Image Processing Procedure

Section 4.4.1 presented the image analysis technique and results for quantifying the ITT specimen microstructures. The automated steps for image processing (i.e., the image processing macro) are outlined in Table F.1. Each step was performed to incrementally segment the image into a binary image for subsequent quantification.

After the median filter was applied, the threshold was manually adjusted to optimize the histogram. The threshold was adjusted manually as each image was slightly different after the automated image processing macro and manual adjustments resulted in better binary images than a consistent threshold value applied to each individual image. As mentioned in Section 4.4.1, the next step was to invest the image after thresholding, then subtract the inverted image from the original image.

Table F.1: Detailed image processing procedure for ITT sample phase quantification.

Process Step	Parameter
Remove Dark Outliers	r = 5.0, thresh = 1.0
Remove Bright Outliers	r = 4.0, thresh = 1.0
Enhance Contrast	0.5 %
Apply Median Filter	r = 5.0

This page was intentionally left blank

References

[Abbaschian 94] R. Abbaschian & R.E. Reed-Hill. Physical metallurgy principles. PWS Publishing Company, third edition, 1994.

[API 12] ANSI/API specification 5L: Specification for line pipe. API, fourty-fourth edition, 2012.

[AST 0] ASTM E1382–97(2010): Standard test methods for determining average grain size using semiautomatic and automated image analysis. ASTM, 1997 (2010).

[AST 04] ASTM E8M–04: Standard test methods for tension testing of metallic materials [metric]. ASTM, 2004.

[AST 10] ASTM E112–10: Standard test methods for determining average grain size. ASTM, 2010.

[Beeston 72] B.E.P. Beeston, R.W. Horne & R. Markham. Electron diffraction and optical diffraction techniques. North-Holland/American Elsevier, 1972.

[Benscoter 02] A.O. Benscoter & B.L. Bramfitt. *Metallographer's Guide: Practices and Procedures for Irons and Steels.* ASM International, page 221, 2002.

[Bhadeshia 98] H.K.D.H. Bhadeshia. *Alternatives to te Ferrite-Pearlite Microstructure*. Materials Science Forum, vol. 284–286, pages 39–50, 1998.

[Bhadeshia 10] H.K.D.H. Bhadeshia. *Nanostructured bainite*. Proceedings of The Royal A Society, pages 3–18, 2010.

[Bramfitt 98] B.L. Bramfitt. Metals handbook desk edition. ASM International, second edition, 1998.

[Caballero 05] F.G. Caballero, C. Garcia-Mateo & C. Garcia de Andres. *Dilatometric Study of Reaustenitisation of High Silicon Bainitic Steels: Decomposition of Retained Austenite*. Materials Transactions, vol. 46, no. 3, pages 581–586, 2005.

[Callister 03] W. Callister. Materials science and engineering an introduction. John Wiley and Sons, Inc., sixth edition, 2003.

[Carboni 08] A. Carboni & A. Pigani. *Casting and rolling of API X70 grades for arctic applications in a thin slab rolling plant*. Milenium Steel, pages 131–136, 2008.

[Chapra 02] S.C. Chapra & R.P. Canale. Numerical methods for engineers. McGraw Hill, fourth edition, 2002.

[Cizek 01] P. Cizek. *Transformation Behaviour and Microstructure of an API X80 Linepipe Steel Subjected to Simulated Thermomechanical Processing*. Metal 2001, vol. 15, pages 1–8, 2001.

[Collins 01] L.E. Collins. *Processing of Niobium-Containing Steels by Steckel Mill Rolling*. Niobium, Science and Technology, pages 527–542, 2001.

[Collins 09] L.E. Collins, R. Klein & D. Bai. *Development of High Strength Line Pipe for Arctic Applications.* Canadian Metallurgical Quarterly, vol. 48, no. 3, pages 261–270, 2009.

[Dieter 00] G. Dieter. Mecahnical behaviour under tensil and compressive loads, volume 8. ASM International, first edition, 2000.

[Eldis 78] G.T. Eldis. *A Critical Review of Data Sources for Isothemal Transformation and Continuous Cooling Transformation Diagrams.* AIME, pages 126–157, 1978.

[Freitag 08] B. Freitag & C. Kisielowski. *Determining resolution in the transmission electron microscope: object-defined resolution below 0.5 A.* C. EMC 2008, vol. 1, pages 21–22, 2008.

[Fujibayashi 05] A. Fujibayashi & K. Omata. *JFE Steel's Advanced Manufacturing Technologies for High Performance Steel Plates.* JFE Technical Report, no. 5, pages 10–15, March 2005.

[Garcia 12] C.I. Garcia, M.J. Hua, X. Liang, P. Suikannen & A.J. DeArdo. *On the Microstructure of Plate Steels for API 5–L X120 Applications.* Materials Science Forum, vol. 706–709, pages 17–23, 2012.

[Gasko 11] M. Gasko & G. Rosenburg. *Correlation between Hardness and Tensile Properties in Ultra-high Strength Dual Phase Steels - Short Communication.* Materials Engineering, vol. 18, no. 3, pages 155–159, 2011.

[Gladman 97] T. Gladman. The physical metallurgy of microalloyed steels. The Institute of Materials, 1997.

[Goldstein 03] J. Goldstein, D. Newbury, D. Joy, C. Lyman, P. Echlin, E. Lifshin, L. Sawyer & J. Michael. Scanning and electron microscopy and x-ray microanalysis. Springer, third edition, 2003.

[Han 12] S.Y. Han, S.S. Sohn, S.Y. Shin, J. Bae, H. Kim & S. Lee. *Effects of microstructure and yield ratio on strain hardening and Bauschinger effect in two API X80 linepipe steels.* Materials Science and Engineering A, vol. 551, pages 192–199, 2012.

[Hiroshi 08] N. Hiroshi, K. Chikara & M. Nobuyuki. *Development of API X80 Grade Electric Resistance Welding Line Pipe with Excellent Low Temperature Toughness.* JFE Technical Report, no. 12, pages 27–31, October 2008.

[Inc. 12] Dynamic Systems Inc. *Gleeble Systems.* 2012.

[Krauss 05] G. Krauss. Carbon and low-alloy steels, volume 1. ASM International, second edition, 2005.

[Lan 12] L. Lan & D. Qiu C. Zhao. *Analysis of martensite-austenite constituent and its effect on toughness in submerged arc welded joint of low carbon bainitic steel.* J Mater Sci, pages 4732–4742, 2012.

[LePera 79] E.S. LePera. *Improved Etching Technique for the Determination of Percent Martensite in High-Strength Dual-Phase Steels.* . Metallography 12, pages 263–268, 1979.

[Lu 12] J. Lu, O. Omotos, J.B. Wiskel, D.G Ivey & H. Henein. *Strengthening Mechanisms and Their Relative Contributions to the Yield Strength of Microalloyed Steels.* Metallurgical and Materials Transactions A, March 2012. Online Publication.

[Matlock 01] D.K. Matlock, G. Krauss & J.G. Speer. *Microstructures and properties of direct-cooled microalloy forging steels.* Journal of Materials Processing Technology, vol. 117, no. 13, pages 324–328, November 2001.

[Mayer 07] J. Mayer, L. Giannuzzi, T. Kamino & J. Micheal. *TEM Sample Preparation and FIB-Induced Damage.* MRS Bulletin, vol. 32, pages 400–407, 2007.

[Mitsuhiro 08] O. Mitsuhiro, S. Nobuo & J. Kondo. *Development of a High-Deformability Linepipe with Resistance to Strain-aged Hardening by HOP (Heat-treatment On-line Process).* JFE Technical Report, no. 12, pages 8–14, October 2008.

[Nastich 07] S.Y. Nastich, Y.D. Morozov, L.I Efron & M.Y. Matrosov. *Steels with Ferrite-Bainite Microstructure with Improved Weldability and Cold Resistance for Main Pipelines.* Materials Science Forum, vol. 539–543, pages 4744–4749, 2007.

[Nobuyuki 06] I. Nobuyuki, S. Endo & J. Kondo. *High Performance UOE Linepipes.* JFE Technical Report, no. 7, pages 20–26, January 2006.

[Nobuyuki 08] I. Nobuyuki, N. Shikanai & J. Kondo. *Development of Ultra-High Strength Linepipes with Dual-Phase Microstructure for High Strain Application.* JFE Technical Report, no. 12, pages 15–19, October 2008.

[Oberholzer 96] M. Oberholzer, M. Ostreicher, H. Christen & M. Bruhlmann. *Methods in quantitative image analysis.* Histochem Cell Biol, vol. 105, pages 333–355, 1996.

[Onsien 09] M.I. Onsien, M. M'Hamdi & A. Mo. *A CCT diagram for an offshore pipeline steel of X70 type.* Welding Journal, vol. 88, no. 1, pages 1S–6S, January 2009.

[Revankar 00] G. Revankar. Hardness testing, volume 8. ASM International, first edition, 2000.

[Shikanai 08] N. Shikanai, S. Mitao & S. Endo. *Recent Development in Microstructural Control Technologies through the Termo-Mechanical Control Process (TMCP) with JFE Steel's High Performance Plates.* JFE Technical Report, no. 11, pages 1–6, March 2008.

[Vander Voort 92] G.F. Vander Voort, H.E Exner & M. Ruhle. Metallographic techniques, volume 9. ASM International, fifth edition, 1992.

[Vander Voort 01] G.F. Vander Voort. *Etching Isothermally Treated Steels.* Heat Treating Progress, April/May 2001.

[Wiskel 08] J.B. Wiskel, D.G. Ivey & H. Henein. *The Effects of Finish Rolling Temperature and Cooling Interrupt Conditions on Precipitation in Microalloyed Steels Using Small Angle Neutron Scattering.* Metallurgical and Materials Transactions B, vol. 39B, pages 116–124, February 2008.

[Yovanovich 06] M.M. Yovanovich. *Micro and Macro Hardness Measurements, Correlations, and Contact Models*. 44th AIAA Aeorspace Sciences Meeting and Exhibit, pages 11702–11729, 2006.